

Pnp-Switchable Coinage-Metal Thermoelectrics for the Development of One-Compound Diodes

Alfred Horst Leopold Rabenbauer

Vollständiger Abdruck der von der TUM School of Natural Sciences der Technischen
Universität München zur Erlangung eines
Doktors der Naturwissenschaften (Dr. rer. nat.)
genehmigten Dissertation.

Vorsitz: Prof. Dr. Thomas F. Fässler

Prüfer*innen der Dissertation:

1. Prof. Dr. Tom Nilges
2. Prof. Dr. Klaus Köhler

Die Dissertation wurde am 09.08.2023 bei der Technischen Universität München eingereicht
und durch die TUM School of Natural Sciences am 30.10.2023 angenommen.

„Für den gläubigen Menschen steht Gott am Anfang,
für den Wissenschaftler am Ende aller seiner Überlegungen“

Max Planck

Danksagung

Mein herzlichster Dank geht an Alle, die meinen persönlichen und akademischen Werdegang über die letzten Jahre begleitet und mich stets unterstützt und mir tatkräftig zur Seite gestanden haben. Besonders anzumerken sind dabei folgende Personen:

- Mein Doktorvater **Prof. Dr. Tom Nilges**, der diese Arbeit und die komplexe Themenstellung überhaupt erst möglich gemacht hat. Die vielen fachlichen Diskussionen, sein stets offenes Ohr, aber auch die über die Wissenschaft hinausgehenden Erlebnisse möchte ich dabei besonders hervorheben.
- **Lucia Weissenborn**, die unsere gesamte Gruppe immer tatkräftig bei allen Angelegenheiten im bürokratischen Dschungel unterstützt hat und immer zur Stelle war, wenn man eine Person zum Reden brauchte. Luci, du wirst für immer in unseren Herzen sein!
- **Dr. Patrick Walke**, welcher mich für die Arbeit in unserer Gruppe begeistern konnte und mich sowohl während meines Forschungspraktikums als auch meiner Masterarbeit betreute und an die wissenschaftliche Arbeit heranführte.
- **Dr. Claudia Ott**, welche mich ebenfalls während meiner Masterarbeit unterstützte und mir viele dafür nötige Arbeitsweisen und Tricks beibrachte.
- **Dr. Felix Reiter**, der immer engagiert und hilfsbereit war, wenn man eine neue Technik von ihm erlernen wollte.
- **Dr. Anna Vogel**, die immer mit Rat und Tat zur Seite stand, wenn die Einkristalle mal wieder nicht so wollten, wie man es gerne hätte und die durch Ihre vorangegangene Forschung dieses Projekt zum großen Teil erst mit möglich gemacht hat.
- **Dr. Janio Venturini**, der stets seine Erfahrungen rund um Publikationen mit mir teilte und das Projekt rund um die Diode, sowie alle anderen Arbeiten im Labor in seiner Zeit bei uns vorantrieb.
- **Philipp Deng**, der sowohl sein Forschungspraktikum als auch seine Masterarbeit bei mir absolvierte und mit seinem Engagement maßgeblich zu dieser Arbeit beigetragen hat.
- **Matthias Hoffmann**, der ebenfalls seine Masterarbeit bei mir durchgeführt hat und sowohl im Labor als auch bei anderen Aktivitäten unsere Gruppe bereichert.
- **Ruben Steib**, welcher mich permanent im gemeinsamen Büro ertragen musste und immer ein offenes Ohr für mich hatte.
- **Kathrin Vosseler**, die immer fleißig SEM-Aufnahmen für mich angefertigt hat und sich ebenfalls zu uns in unser Büro gesellte.
- **Allen aktuellen und ehemaligen Mitgliedern des AK Nilges**, die stets ein freundliches und hilfsbereites Arbeitsklima geschaffen haben. Sie alle sind der Grund dafür, dass man stets gut gelaunt bei uns in der Gruppe erscheint, man sowohl die

Arbeit als auch natürlich die unzähligen Kaffeepausen genießt und auch außerhalb der Universität viel Spaß hat.

- **Meinen Eltern**, die mich schon seit frühester Kindheit immer in meinen Zielen unterstützt und mir sämtliche Freiheiten ermöglicht haben.
- **Milena Heller**, welche mich als meine Lebensgefährtin durch die gesamte Promotion begleitet hat und sich alle meine Probleme anhören musste.

Table of Contents

1.	Introduction	1
1.1	Pnp-switchable thermoelectrics.....	3
1.1.1	Ag ₁₀ Te ₄ Br ₃ and related compounds.....	4
1.1.2	AgCuS.....	7
1.1.3	Schottky Diode	10
1.1.4	pn-Junction Diode	12
2	Experimental	16
2.1	Chemicals.....	16
2.2	Solid State Synthesis.....	16
2.2.1	Ag ₁₈ Cu ₃ Te ₁₁ Cl ₃	17
2.2.2	AgCuS.....	17
2.2.3	Cu _{1.5} Se _y Te _{1-y}	17
2.2.4	Pellet Preparation.....	18
2.3	Analytical Methods.....	19
2.3.1	Powder X-ray Diffraction	19
2.3.2	Single Crystal X-ray Diffraction	19
2.3.3	Seebeck Coefficient and Electrical Conductivity	20
2.3.4	Laser Flash Analysis (LFA)	23
2.3.5	Diode measurements	23
2.3.6	Bulk modulus determinations	25
2.3.7	Solid State Nuclear Magnetic Resonance (NMR)	25
2.3.8	Differential Scanning Calorimetry (DSC)	26
2.3.9	Semi-quantitative Phase Analysis and Scanning Electron Microscopy (SEM).....	26
2.3.10	Photoluminescence Spectroscopy (PL)	26
2.3.11	X-ray Photoelectron Spectroscopy (XPS).....	26
3	Results.....	28
3.1	A Switchable One-Compound Diode	28
3.2	AgCuS: A Single Material Diode with Fast Switching Times	74

3.3	$\text{Cu}_{1.5}\text{Se}_y\text{Te}_{1-y}$ ($y = 0.2 - 0.7$): A Series of Narrow Band Gap Semiconductors with Low Thermal Conductivity at Ambient Temperature	92
4	Summary.....	111
	Publications.....	113
	Literature.....	115

Abstract

Coinage-metal chalcogenides and chalcogenide halides are mixed ionic and electrical semiconductors with low thermal conductivities. They show a high potential for thermoelectric applications. Despite these general aspects, a small number of those materials is known to show a reversible switching from p-type to n-type semiconduction and back during a temperature induced phase transition. This switching enables a widespread potential for applications in one-compound diodes and transistors, as well as solar cells or electrocatalysis, due to the generation of p-type and n-type regions in one single material.

In this work, $\text{Ag}_{18}\text{Cu}_3\text{Te}_{11}\text{Cl}_3$, AgCuS and $\text{Cu}_{1.5}\text{Se}_{1-y}\text{Te}_y$ are synthesized in standard solid-state approaches in a muffle furnace. The chemical composition is assessed by powder and single crystal X-ray diffraction and substantiated by energy-dispersive X-ray spectroscopy. To monitor the temperature dependent behavior, differential scanning calorimetry is used, and the thermoelectric properties are examined by Seebeck coefficient and electrical conductivity measurements as well as laser flash analysis. For the pnp-switching materials AgCuS and $\text{Ag}_{18}\text{Cu}_3\text{Te}_{11}\text{Cl}_3$, the change in conduction mechanism is reassessed during those measurements. They are therefore identified as possible candidates for the construction of one-compound diode devices, where a pn-junction is created by a simple temperature gradient within a uniform material without any additional doping. A new measurement setup is created, allowing conductivity measurements on single crystalline samples with specifically applied temperature gradients on them. The existence of the rectifying diode behavior is proven by UI-curve measurements, and Schottky-like behavior is ruled out by the assessment of switching times and the electronic response of the system under isothermal conditions.

Both materials are successfully utilized as one-compound diode devices. $\text{Ag}_{18}\text{Cu}_3\text{Te}_{11}\text{Cl}_3$ shows a phase transition accompanied by a pnp-switch at around 295 K, allowing its use in one compound diodes at room temperature (RT) with switching times of ~ 9 s. AgCuS can be used at slightly elevated temperatures. A heat gradient of 333/368 K enables the creation of a one-compound diode with a faster switching time of 2.7 s due to the accelerated carrier mobility.

The proof of the generated pn-junction in a single material enables a wide new field of electrical applications, from one-compound diodes and transistors to solar cells or electrocatalysis.

Kurzzusammenfassung

Münzmetallchalcogenide und chalcogenid-halogenide sind Halbleiter mit gemischter ionischer und elektrischer Leitfähigkeit sowie niedriger thermischer Leitfähigkeit. Sie besitzen ein hohes Potential für thermoelektrische Anwendungen. Neben diesen generellen Eigenschaften zeigt eine kleine Anzahl dieser Materialien während einem temperatur-induzierten Phasenübergang eine reversible Schaltung von einem p-halbleitenden Zustand in einen n-halbleitenden Zustand und wieder zurück. Dieses Schalten wird durch die Erzeugung von p-Typ und n-Typ Regionen in einem einzelnen Material ermöglicht, was ein weitgefächertes Anwendungspotential von Einkomponentendioden bzw. -transistoren bis hin zu Solarzellen und Elektrokatalyse eröffnet.

In dieser Arbeit werden die Materialien $\text{Ag}_{18}\text{Cu}_3\text{Te}_{11}\text{Cl}_3$, AgCuS und $\text{Cu}_{1.5}\text{Se}_{1-y}\text{Te}_y$ in Standard-Festkörpersynthesen in einem Muffelofen hergestellt. Die chemische Zusammensetzung wird durch Pulver- und Einkristall-Röntgendiffraktometrie bestimmt und durch energiedispersive Röntgenspektroskopie bestätigt. Dynamische Differenz-Kalorimetrie wird benutzt, um das temperaturabhängige Verhalten zu beobachten, und die thermoelektrischen Eigenschaften werden durch Messungen des Seebeckkoeffizienten und der elektrischen Leitfähigkeit, sowie durch Laser-Flash Analyse untersucht. Für die pnp-schaltbaren Materialien AgCuS und $\text{Ag}_{18}\text{Cu}_3\text{Te}_{11}\text{Cl}_3$ wird die Änderung des Leitungsmechanismus durch diese Messungen neu bewertet. Dies identifiziert sie als mögliche Kandidaten zum Bau von Einkomponentendioden, in welchen ein pn-Übergang in einem gleichförmigen Material und ohne zusätzliche Dotierung durch einen einfachen Temperaturgradienten erzeugt wird. Ein neues Messsetup wird entworfen, welches Leitfähigkeitsmessungen an einkristallinen Proben erlaubt, an welchen ein spezifischer Temperaturgradient angelegt werden kann. Die Existenz von rektifizierenden pn-Dioden wird durch Spannungs-Strom Kennlinien bewiesen. Hier wird ein Schottky-Verhalten durch Messung der Schaltzeiten und der Analyse der elektronischen Antwort des Systems unter isothermen Bedingungen ausgeschlossen.

Beide Materialien werden erfolgreich als Einkomponentendioden eingesetzt. $\text{Ag}_{18}\text{Cu}_3\text{Te}_{11}\text{Cl}_3$ zeigt einen reversiblen Phasenübergang bei 295 K, welcher von einer pnp-Schaltung begleitet wird. Dieses Material eignet sich dadurch für die Anwendung als reversibel zu generierende Dioden nahe Raumtemperatur, mit Schaltzeiten von ~9 s. AgCuS kann bei leicht erhöhten Temperaturen mit einem Gradienten von 333/368 K eingesetzt werden, was aufgrund der erhöhten Ladungsträgermobilität die Erzeugung einer Einkomponentendioden mit einer schnelleren Schaltzeit von 2.7 s ermöglicht.

Der Nachweis des erzeugten pn-Übergangs in einem einzelnen Material ermöglicht ein breites, neues Feld an möglichen Anwendungen, von Einkomponentendioden und -transistoren über Solarzellen hin zur Elektrokatalyse.

Abbreviations

BV	breakdown voltage
Conc.	concentrated
DFT	density functional theory
DSC	differential scanning calorimetry
EDX	energy-dispersive X-ray spectroscopy
IC	integrated circuit
LED	light emitting diode
LFA	laser flash analysis
MAS	magic angle spinning
NMR	nuclear magnetic resonance
PCB	printed circuit board
PL	photo luminescence
PXRD	powder X-ray diffraction
RT	room temperature
SC	single crystal
SEM	scanning electron microscopy
SMU	source measure unit
XPS	X-ray photoelectron spectroscopy

1. Introduction

Our everyday life is getting more and more technologized over the last decades, and a stop of the growth is not foreseeable. The raise in population, paired with the need for a more effective use of resources – human and material – pushes the need for new, economic and green energy applications. Apart from reducing the general amount of the needed energy, more efficient possibilities of conversion are another approach to avoid a possible lack of energy.

Thermoelectric materials, capable of generating electrical energy from an applied heat gradient, offer a suitable approach to reduce losses in the production of any kind of energy.¹

Coinage-metal chalcogenides and chalcogenide halides were under extensive research during the last decade, since they combine three major characteristics which are beneficial for a good thermoelectric material.²⁻⁷ Most of them are semiconducting materials, combining ionic as well as electronic conductivities, so they are capable of reaching high electrical conductivities. On the other hand, the mobility of the coinage metal atoms is beneficial for phonon scattering processes, reducing the overall thermal conductivity of the material.^{3, 8} This perfectly matches the general requirements for high performance thermoelectrics, which demands reasonable electrical conductivities to increase the generated electrical energy, while on the other hand a low thermal conductivity is needed to preserve the thermal gradient.⁹

During this extensive research, another major feature was revealed in one of those materials. $\text{Ag}_{10}\text{Te}_4\text{Br}_3$, discovered in 2006, is the first compound of a new class, the pnp-switchable materials, which show a reversible transformation from p- to n-type semiconduction and back during a structural phase transition.¹⁰ The underlying phase transition takes place at 390 K. Three other materials were added to this class after 2009, which are described in more detail later, but only one of them shows a lower transition temperature than $\text{Ag}_{10}\text{Te}_4\text{Br}_3$, namely AgCuS at 361 K.¹¹ Since then, it should in general be possible to create a pn-junction in a single material by applying a specific heat gradient, allowing a versatile application potential, since these junctions are widely used in all kinds of electronic devices. The simplest application would be the creation of a pn-junction diode in a single material without the need for differently doped regions. To allow the use under ambient conditions, the transition temperature should be as close to room temperature as possible. In this work, the new compound $\text{Ag}_{18}\text{Cu}_3\text{Te}_{11}\text{Cl}_3$ is discovered and characterized, featuring a pnp-switch directly at room temperature. The material is probed in the creation of a one-compound diode, which can be thermally turned on and off.

Additional, the feasibility of these one-compound diodes is substantiated by the use of a second material, AgCuS , at slightly higher temperatures. The material is tested under various switching conditions, verifying the versatility of those materials in electronic applications. Those

features enable a huge field for further research, due to the various devices and techniques where a pn-junction is needed. Besides the use in electronic devices, the exploitation in electrocatalysis or solar cells is imaginable.

1.1 Pnp-switchable thermoelectrics

Coinage-metal (poly)chalcogenide halides are promising candidates for thermoelectric applications and were therefore under excessive research during the last decades. Thermoelectric materials are characterized by the dimensionless figure of merit ZT:

$$ZT = \frac{S^2 \sigma}{\kappa} T \quad (1)$$

With S the Seebeck coefficient, σ the electrical conductivity and κ the thermal conductivity.¹² It is clearly visible that a material is therefore defined by three major properties to gain high performance in thermoelectric applications: it needs to provide high Seebeck coefficients, high electrical conductivities and at the same time low thermal conductivities.^{7, 13} Coinage-metal chalcogenide halides are mixed ionic and electric conductors, they combine the ionic conductivity of coinage-metal halides in the coinage metal substructure with the electrical conductivity of coinage-metal chalcogenides.^{2, 5, 6, 14, 15} This offers a high potential to enable good electrical conductivity, and at the same time, the mobile coinage-metals enable high phonon scattering, suppressing the lattice part of the thermal conductivity.³ The thermal conductivity consists of two major contributions, the electronic part connected to the moving electrons, and the lattice part connected to lattice vibrations. The Wiedemann-Franz Law therefore describes the dependency between the electronic contribution to the thermal conductivity and the electrical conductivity in a metal as follows:

$$\frac{\kappa}{\sigma} = L \times T \quad (2)$$

With κ the electronic part of the thermal conductivity, σ the electrical conductivity, the Lorenz number and T the temperature.¹⁶ Since thermoelectrics need reasonable electrical conductivities, one can only reduce the overall thermal conductivity without losing electrical conductivity by decreasing the lattice part, so the ion conducting coinage-metal chalcogenide halides offer a high potential for reaching high ZT. Unfortunately, at the same time the mobility of the coinage metals induces problems concerning their temperature and cycling stability, e.g. by electromigration, causing an irreversible decomposition of the material.⁴

Another intriguing property of those materials, connected to their high ion mobility as well as versatile cationic substructure, is their tendency to show polymorphism. The polymorphic compound $\text{Ag}_{10}\text{Te}_4\text{Br}_3$ was found in 2006, as the first representative of ternary coinage-metal chalcogenide halides containing partially covalent chalcogen units.⁶ The existence of three order-disorder phase transitions in a temperature range from 223 – 410 K, enabled both through the high silver ion mobility and the rearrangement of the covalently bound chalcogen units, was afterwards reported in 2007.⁵ Interestingly, the $\beta - \alpha$ phase transition at 390 K is

accompanied by a switch of the semiconductor type from p-type to n-type and back, first proven by the change of the Seebeck coefficient sign in 2009 by Lange *et al.*¹⁰ This effect, which was shown for the first time, enables a large field of possible applications for that kind of semiconductors. In the following decade, only three other materials showing this pnp-switch were identified: AgCuS, $\text{Tl}_2\text{Ag}_{12}\text{Se}_7$ and AgBiSe_2 .^{11, 17, 18} AgCuS shows pnp-switching at 364 K, $\text{Tl}_2\text{Ag}_{12}\text{Se}_7$ at 410 K and AgBiSe_2 at 580 K, and the switch is initiated by a temperature-induced phase transition for all of them. Another concept to enable this switching was shown for CuFeS_2 , where a pressure induced phase transition at ~ 8 GPa is used to generate an n-conducting state in a p-type semiconductor.¹⁹

Diodes and transistors are the main technical building units which need p- and n-type semiconductors in close contact.²⁰ Through local heating of a pnp-switchable compound to the right temperature, the reversible creation of a n-type region within the material could be feasible. This should create a local pn-junction, showing rectifying behavior if a potential is applied, and should make it in general possible to create a one-compound diode. The realization of this kind of device is a major part of this work. To assure an uncomplicated application, as well as enable operation at ambient conditions, the pnp-switching temperature should be as close to room temperature as possible. The two candidates with the best options are therefore AgCuS and $\text{Ag}_{10}\text{Te}_4\text{Br}_3$, which are described in more detail concerning the switching mechanisms as well as the optimization of the switching temperature in the following.

1.1.1 $\text{Ag}_{10}\text{Te}_4\text{Br}_3$ and related compounds

$\text{Ag}_{10}\text{Te}_4\text{Br}_3$ was the first compound showing a switch between p- and n-type semiconduction during a temperature-induced phase transition.¹⁰ To gain further insights into the mechanism of this new property, a closer look into the structural changes during this phase transition is needed. Four different polymorphs of this compound are known, starting with the low temperature δ -phase at 223 K up to the high temperature α -phase at 410 K. Since the transition from β to α is the one accompanied by the pnp-switch, the following part focuses on the description of these two polymorphs. Because of the high complexity of the compound's structure, the easiest way is to separately define the anion and the cation substructures and additionally use a topological description of the anionic one. The anion substructure consists of Kagomé-like 3.6.3.6 nets of Br⁻ ions, stacked alternately along the c-axes with 6³ honeycomb nets of isolated Te²⁻ ions. Additional tellurium is arranged in strands of so-called Te₄ units, where each consists of a covalently bound [Te₂]²⁻ dumbbell and two additional Te²⁻ ions. Those strands interpenetrate the aforementioned stacked nets along their stacking direction and are centered in the voids of the 6³ Te²⁻ nets. The arrangement of those units is representatively depicted in the top of Figure 1 for a single unit cell. While in the δ - and γ - phase the [Te₂]²⁻

dumbbells of neighboring strands are shifted by a translation vector of $\frac{1}{2}c$, one third of the strands is structurally frustrated in the β -polymorph, and is completely frustrated in the high temperature α -polymorph. This frustration in the strands is reflected by half-occupied Te positions. It is mainly caused by the increased silver ion mobility at higher temperatures and therefore by the depopulation of position Ag1, which is coordinating two neighboring Te_4 units in a linear arrangement in the low temperature polymorphs. At the same time, the silver population in the other positions, which are located around the 6^3 Te-nets, increases, and the linear Te_4 chains have to be re-arranged, resulting in the described structural frustration which is very similar to a Peierls distortion in the chain, see bottom of Figure 1. The coordination of the silver atoms can be described as a nearly linear arrangement of silver around the Te_4 -strands along its stacking direction, forming $[\text{Te}_4\text{Ag}]_n$ strands.^{5, 10}

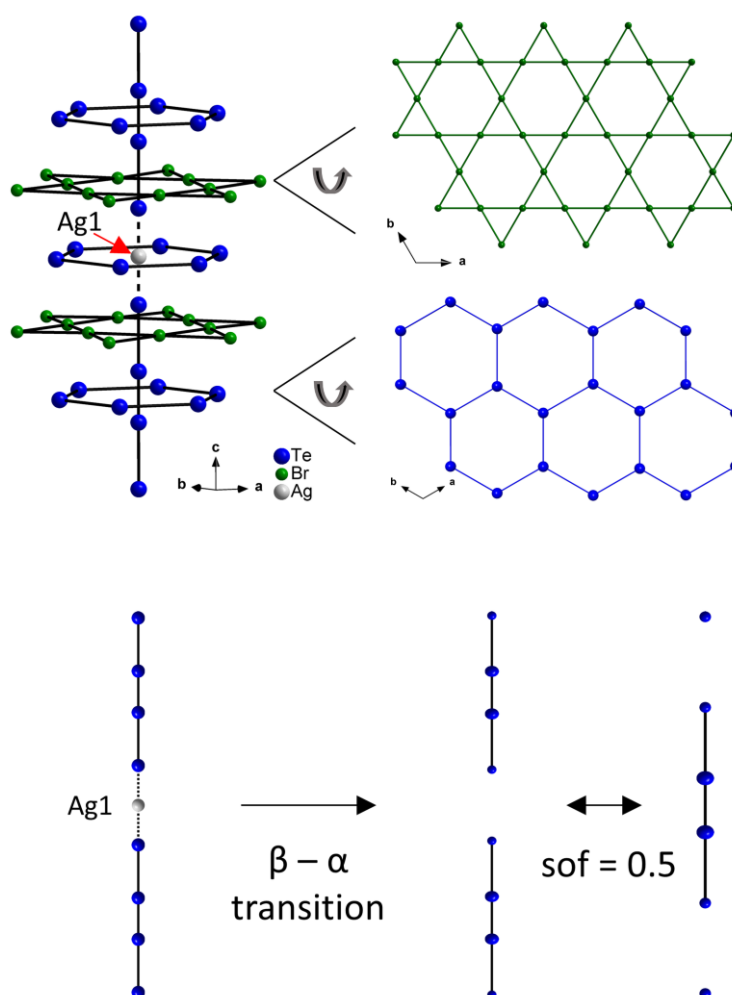


Figure 1: Top: Structure motif of $\beta\text{-Ag}_{10}\text{Te}_4\text{Br}_3$. The cation substructure is removed for better understanding, except for Ag1, separating two different Te_4 units. The right side shows the Br 6.3.6.3 Kagomé net (green) and Te 6^3 honeycomb net (blue). The rearrangement from the separated Te_4 units in the beta phase to the frustrated, half occupied Te-strand by depopulation of the Ag1 position is depicted in the bottom.

When one now takes a look at the Seebeck coefficient in relation to the DSC measurement, it is clearly visible that the Seebeck coefficient starts to decrease from $+310 \mu\text{V K}^{-1}$ at around

360 K, which is the exact same region where the broad endothermic effect, depicting the β - α phase transition, starts. The Seebeck coefficient even changes its sign at 380 K to negative, reaching its minimum of $-940 \mu\text{V K}^{-1}$ at 390 K. A significant and important structural change during this phase transition is the continuous depopulation of the silver position between the Te_4 units, giving rise to the very broadened signal in the DSC curve. This leads to the afore described rearrangement from a Peierls like distorted Te_4 chain to an equidistant one. Band gap calculations showed that this transformation leads to an upwards shift of the Fermi level, narrowing the band gap and in fact, generating freely propagating electrons within the one-dimensional arrangement of the Te_4 strands. This generation of mobile electrons is correlated with an internal redox process, namely the formation and breaking of the $[\text{Te}_2]^{2-}$ groups into Te^{2-} ions, which causes the dominant semiconductor type change from p-type to n-type conduction.¹⁰

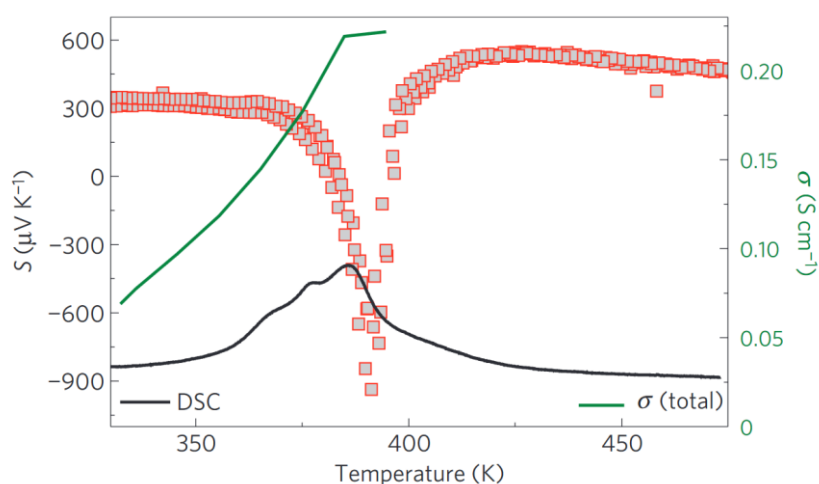


Figure 2: Temperature dependent Seebeck coefficient, electrical conductivity and DSC curve for $\text{Ag}_{10}\text{Te}_4\text{Br}_3$. A reversible change in sign of Seebeck coefficient can clearly be seen at around 390 K. Reproduced with permission from Springer Nature.¹⁰

Since this pnp-switch can enable possible semiconductor switching applications or sensor devices by a simple temperature increase, different approaches were conducted to change the temperature of the pnp-switch in this material. Different substitutions, either within the halide substructure from Br to Cl or I, in the chalcogenide substructure from Te to Se and S, or in the cationic substructure from Ag to Cu, showed potential to tune the temperature of the β - α phase transition in a broad range. While the introduction of Cu, Cl, S and Se shift the transition towards room temperature, the substitution with I leads to a slight increase of the temperature.²¹⁻²³ Unfortunately, most times the shift of the transition temperature is accompanied by a loss of the pnp-switch. To enable pnp-switching closer to room temperature, other compounds in this new class of materials were investigated, showing similar building units to $\text{Ag}_{10}\text{Te}_4\text{Br}_3$: Manifold other compounds were added to the group of the coinage metal (poly)chalcogenide halides, also presenting high ionic motilities and the combination of

covalently bonded $[\text{Te}_2]^{2-}$ and ionically bond Te^{2-} anions, like $\text{Ag}_{23}\text{Te}_{12}\text{Cl}$, $\text{Ag}_{23}\text{Te}_{12}\text{Br}$ and $\text{Ag}_{20}\text{Te}_{10}\text{BrI}$.^{15, 24} Unfortunately, those materials didn't show any hints of pnp-switching. $\text{Ag}_5\text{Te}_2\text{Cl}$ was a promising candidate, which showed a similar modulation of the Seebeck coefficient during the phase transition, but unfortunately, this change wasn't pronounced enough to enable a switch of the sign and therefore a change of the conduction type.²⁵ Various substitutions in this material were able to change the temperature of the modulation as well as its magnitude, but a shift from p- to n-type conduction was not possible.²⁶⁻²⁹ Encouraged by this findings, Anna Vogel added two new compounds to the group of coinage-metal chalcogenide halides, $\text{Cu}_{9.1}\text{Te}_4\text{Cl}_3$ and $\text{Cu}_{20}\text{Te}_{11}\text{Cl}_3$.^{3, 4} Unfortunately, none of the compounds showed pnp-switching abilities, but polymorphism is present in all of them. In $\text{Cu}_{20}\text{Te}_{11}\text{Cl}_3$, a new building unit was identified in the structure, where covalently bonded Te_2^{2-} groups are not only distributed linearly, like in $\text{Ag}_{10}\text{Te}_4\text{Br}_3$, but are organized in a layered arrangement. They form a Kagomé like 6363 network, which was reported for the halide substructure in some of the materials mentioned before. The structure is built up of a regular stack of these layers: In the middle, a 6363 Cl net is present, surrounded by a 6^3 honeycomb Te net above and underneath it. On top and below this honeycomb net, there follows the new 6363 Te Kagome net, which isn't interpenetrated by any of the Te_4 units. This inhibits the formation of a linear Te strand and the Peierl's like distortion of it, a one dimensional CDW like in $\text{Ag}_{10}\text{Te}_4\text{Br}_3$ can't be formed. Since no pnp- switching is observed in this material, no CDW is present during the structural transition, but in general, it should be possible to introduce a new kind of two dimensional CDW in the Kagomé like arrangement of tellurium. In the present work, it is shown that the substitution of nearly every Cu by Ag in $\text{Cu}_{20}\text{Te}_{11}\text{Cl}_3$ leads to the introduction of a pnp-switch close to room temperature, which is explained in the discussion part, and the possible application of such a compound in one-compound diode devices is investigated.

1.1.2 AgCuS

The second compound supplying a pnp-switch close to room temperature at ~ 364 K is the semiconducting AgCuS, which is also used for diode applications in this work. It is known as the mineral stromeyerite, and its four different polymorphs have been characterized in 2007 by Trots et al..^{30, 31} In 2014, Biswas et al. were the first ones to show that the phase transition from the orthorhombic β -phase to the hexagonal α -phase at 364 K is also accompanied by a pnp switch. Since the high temperature δ -phase is not involved in the pnp-switching mechanism, it is not explained in this thesis.

At room temperature, the orthorhombic β -polymorph is stable, crystallizing in space group $Cmc2_1$ (36). The silver and copper atoms are fully ordered at this point, occupying two different

Wyckoff sites 4a. During heating, the material undergoes a phase transition to the hexagonal α -phase at 364 K, crystallizing in space group $P6_3/mmc$. Driven by an enhanced cation mobility, 25% of the copper ions start to share same sites with silver (orange spheres in Figure 3, 12k site). As a result, a partial disorder in the cationic substructure occurs. In the high temperature δ -polymorph, the cations are fully disordered on Wyckoff sites 8c and 32f.³⁰

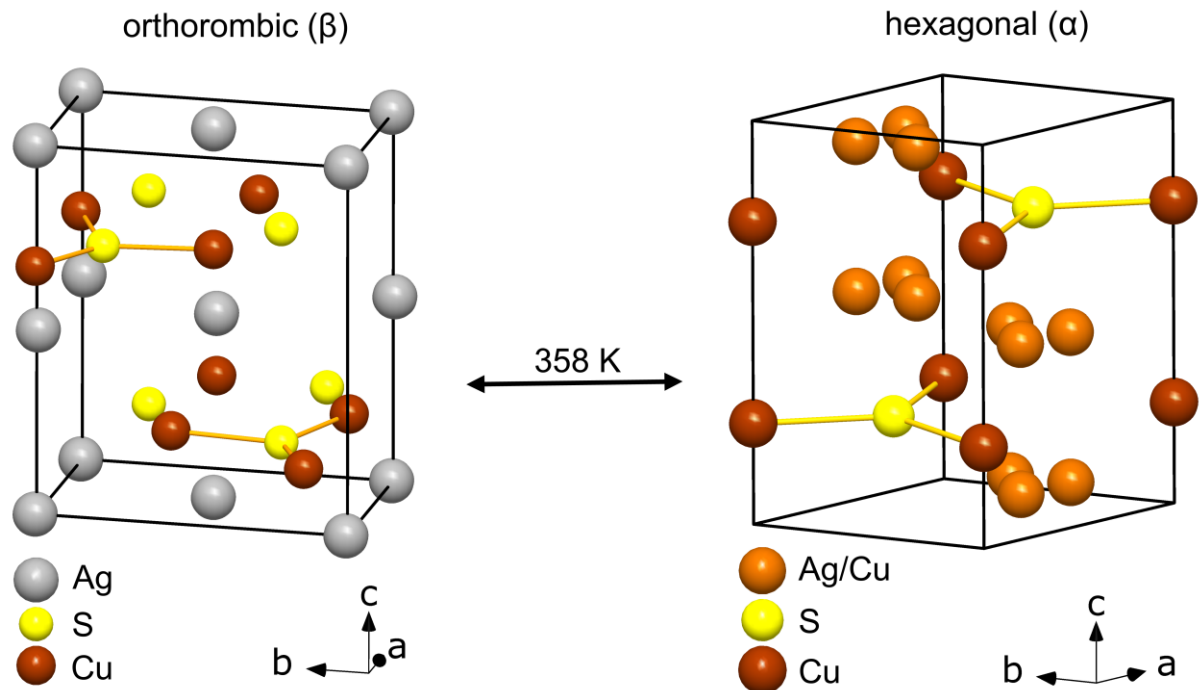


Figure 3: Representative unit cells of the orthorhombic low temperature β - and the hexagonal high temperature α -phase of AgCuS. A S-Cu₃ structure motive is added for an easier understanding of the transition (represented by yellow sticks). Structure data taken from Trots *et al.*³⁰

The reported Seebeck coefficient drop during this phase transition reaches from 1757 $\mu\text{V K}^{-1}$ to -840 $\mu\text{V K}^{-1}$ right after the β - α phase transition. Density functional theory (DFT) calculations were conducted to identify the processes which enable the pnp switching. While the Cu-S bonds stay unchanged during the phase transition, the movement of parts of the copper ions leads to a shift of the energy bands, and during the transition path of the cationic substructure, semimetallic intermediate states are generated by hybrid Cu-S orbitals. This loss of the bandgap during the transition allows the flow of conducting electrons, and hence transfers the material to an n-type conductive state.^{11, 32}

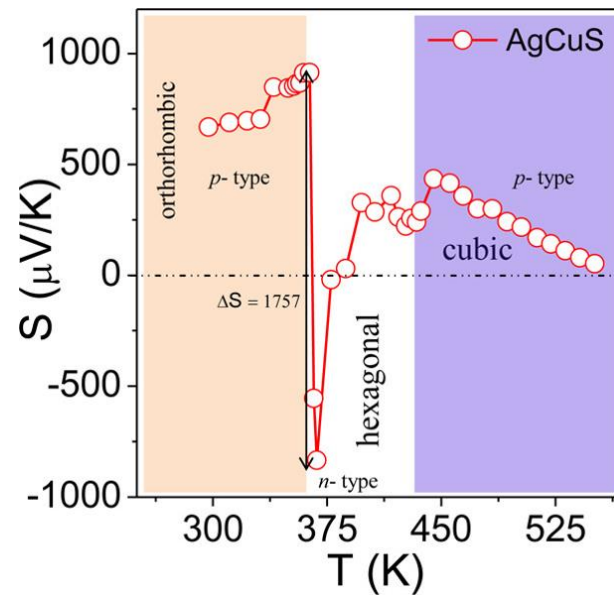


Figure 4: Temperature-dependent Seebeck coefficient measurement of AgCuS. The switch between p- and n-type conductivity is clearly visible right after the β - α phase transition at ~ 360 K. Reprinted with permission from [11] © 2014, American Chemical Society.

Approaches to tune the material properties, like the switching temperature and the electrical conductivity by reducing the material size from bulk to the nanometer-regime resulted in a loss of the pnp-switching ability.³² Furthermore, also the application of certain vacancies in the Cu substructure by reducing the copper content ($\text{AgCu}_{1-x}\text{S}$, $x = 0.01 - 0.04$) hinders a successful pnp-switch. Only changes in the Ag-content (up to -10% Ag) enable the material to keep the pnp-switching ability, but the magnitude of the Seebeck coefficient modulation is less pronounced than in stoichiometric AgCuS.³³

Rectifying Devices

A high electrical conductivity is one of the main characteristic properties of a metal, since there is no band gap present and the electrons can freely flow throughout the material.³⁴ Therefore, metals are used in modern integrated circuits (ICs) and all resulting electronic devices as non-rectifying conductors. The dependence between voltage and current flow linear, according to Ohm's law:

$$I = \frac{U}{R} \quad (3)$$

With I the current, U the voltage and R the resistance of the material.³⁵ Since the resistance of a metal is material-specific and constant, the resulting current is linearly increasing with an increasing potential, and the direction of the current flow is determined by the polarity of the applied voltage.

For any kind of IC or electrical device, the current flow has to be directed at some point. Therefore, current should only go in one specific direction, but not in the other. Devices with a non-linear U/I dependence are needed, which are called rectifying devices. Those devices are also named diodes, and they can for instance be used to convert alternating current into direct current, since they only allow a current flow in a specific direction. Two major kinds of diodes are used as rectifying devices, the simplest one is a so-called Schottky diode, and the other one is a pn-junction diode. These two types are explained in more detail in the following.^{36, 37}

1.1.3 Schottky Diode

The simplest form of a rectifying contact is developed by contacting a metal with a semiconductor. Those interfaces are called Schottky contacts or Schottky diodes, which were first found by F.Braun in 1874, and Schottky & Mott were the ones to explain this effect in the first half of the 20th century.^{38, 39} When a metal is contacted by a semiconductor, the Fermi levels E_F of both materials align to each other in a thermodynamic equilibrium, since this energy level cannot have two different values at the same point, see Figure 5. For the explanation of this process, an n-type semiconductor is considered in contact with a metal. The Fermi level of the metal E_{Fm} is then lower than the Fermi level of the semiconductor E_{Fsc} . Furthermore, at ambient conditions, there are electrons excited from the valence band with a considered energy of E_V to the conduction band with an energy E_C , which is the highest occupied energy state in the semiconductor. As a result of the energy difference, electrons of the n-type semiconductor move into the metal to reach a lower energetic state, leaving behind an equal amount of positive holes. There, a space charge region called depletion region is formed in the semiconductor near the metal contact, with a width of W_0 . The region in the metal, where the electrons are located, can be considered as infinitely thin, since the metal behaves as a perfect

conductor, and is called a “charge sheet” due to the charge distribution. Due to the alignment of the energy levels, the energy bands in the semiconductor get bent, inducing a curvature of the band between the semiconductor and the metal, see Figure 5b. This directly corresponds to a potential barrier V_i hindering further electrons from moving into the metal, while on the other side the electrons in the metal face a potential barrier Φ_b ; with an amplitude corresponding to V_i and $E_C - E_F$.

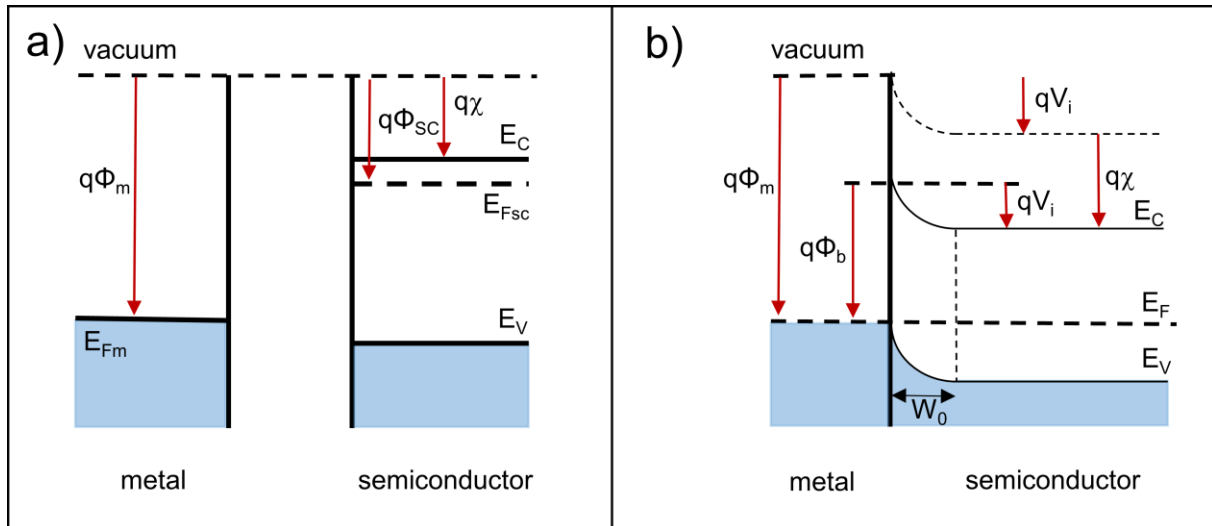


Figure 5: Energy band diagram of a) a separated metal and semiconductor and b) a metal-semiconductor (Schottky) contact.³⁶ E_{Fm} is the energy of the Fermi level in a metal, E_{Fsc} the energy of the Fermi level in a semiconductor, $q\chi$ the electron affinity, $Q\phi$ the work function of the metal, $Q\phi_{sc}$ the work function of the semiconductor, E_V the energy of the valence band, E_C the energy of the conduction band, W_0 the width of the depletion region, Φ_b the potential barrier for electrons in the metal and qV_i the potential barrier for electrons in the semiconductor.

Without an external gradient applied to the system, only a few electrons have enough energy to overcome this barrier and flow from the semiconductor to the metal, and this flow is equilibrated with the same amount of charges going into the opposite direction. If now an external potential is applied to the junction, with $V_a > 0$, so the positive side is connected to the metal and the negative to the semiconductor, the potential barrier V_i is reduced by V_a , and more electrons can move to the metal. At the same time, Φ_b on the metal side remains unchanged, so the electron flow to the semiconductor is constant. The sum of electrons is moving from the semiconductor (-) to the metal, the current can flow without rectification. This is called the forward bias mode of a diode. The opposite is called reverse biased, when + is connected to the semiconductor and - to the metal, inducing a negative voltage $V_a < 0$. In this case, the barrier on the semiconductor side is increased by V_a , less electrons flow from the semiconductor to the metal. In the opposite direction, the flow still remains unchanged, causing a small net current flow from the metal to the semiconductor, which is called leakage current.³⁶

In a Schottky diode, only majority carriers, here electrons, contribute to the discussed effect. The electrons in the n-type semiconductor have a higher energy than in the metal, so they are called “hot carriers”, also giving the Schottky diode the alternative name “hot carrier diode”. Additionally, those majority carriers react to the electrical fields in a very fast way. This allows the diode to switch in very small amounts of time, down to picoseconds, enabling their use in high frequency rectification applications.³⁶ Another advantage is the relatively low forward voltage of 0.3 V, which will be compared to the pn-junction diode in the next chapter.

1.1.4 pn-Junction Diode

As already implicated by the name, a pn-junction diode is made by the combination of a p-type and an n-type semiconductor. When the same material is used with different doping levels (e.g. n-doped and p-doped silicon), the created junction is called a homojunction. When two different materials, like n-type silicon and p-type germanium are used, it is called a heterojunction. For a better understanding, only homojunctions are explained in more detail. In comparison to a resistance, which shows a linear current-voltage dependence, the pn-junction diode shows a strongly rectifying behavior. It behaves in the same way like the Schottky diode, the current can flow in one bias direction (so-called forward direction), but not in the opposite one (reverse direction). The applied voltage V_a is positive in forward direction, meaning that the potential at the p-type semiconductor is higher (+ pole) than in the n-type semiconductor.³⁶

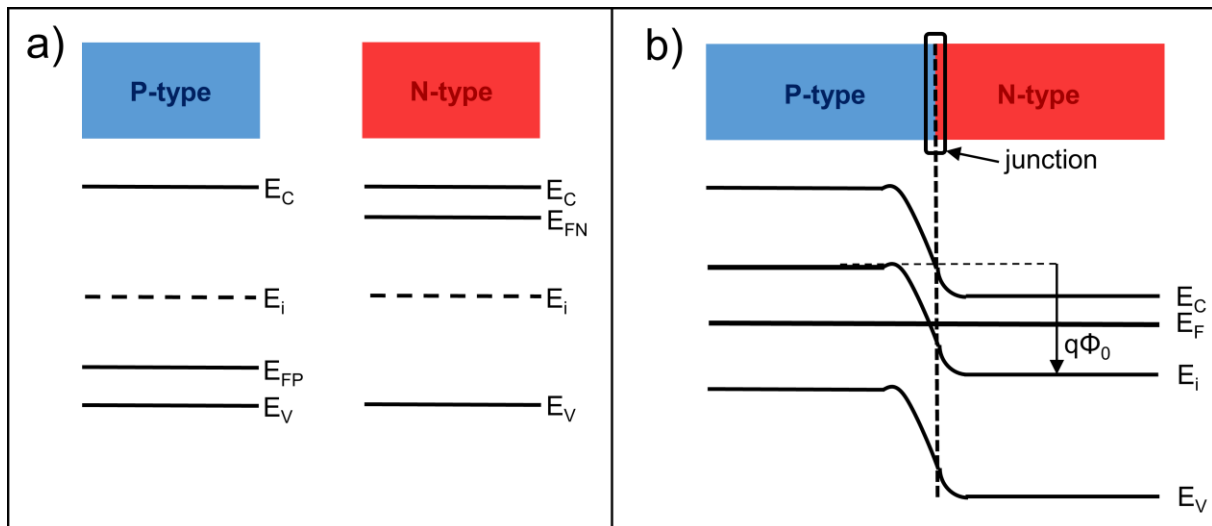


Figure 6: Energy band diagram of a) a separated p- and n-type semiconductor and b) metallurgically connected pn-junction. ³⁶ E_F is the energy of the Fermi level, E_{FN} the energy of the Fermi level in a n-type semiconductor, E_{FP} the energy of the Fermi level in a p-type semiconductor, E_V the energy of the valence band, E_C the energy of the conduction band, E_i the intrinsic energy level, and $q\phi_0$ the junction potential

The Fermi level of a n-type semiconductor is located closer to the conduction band (an excess of electrons is introduced by the dopant), while it is closer to the valence band in a p-type

semiconductor due to the generation of positive vacancies. This is schematically depicted in Figure 6a. When the materials are now contacted to each other in the so-called metallurgic junction, the Fermi levels are aligned, since it has to be constant over the whole material under thermodynamic equilibrium, see Figure 6b. This leads to a transport of electrons from the n-type semiconductor to the electron-poor p-type semiconductor, and of positive holes in the opposite way. Both of the carriers leave behind oppositely-charged donor atoms which can't move since they're fixed in the crystal structure, and as a consequence an internal potential called the junction potential Φ_0 is formed in the device due to the curvature of the bands. The region of the remaining ionized donor atoms is called depletion region (see Figure 7), and in equilibrium, the charge of this region creates an attractive force which exactly balances the one from the diffusing electrons or holes, respectively. ^{41, 42}

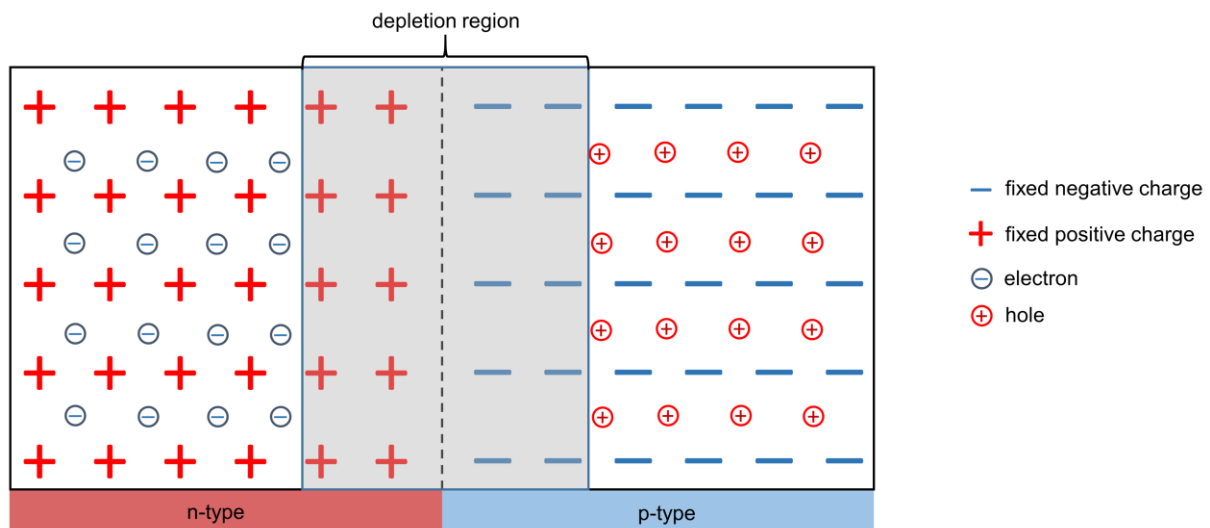
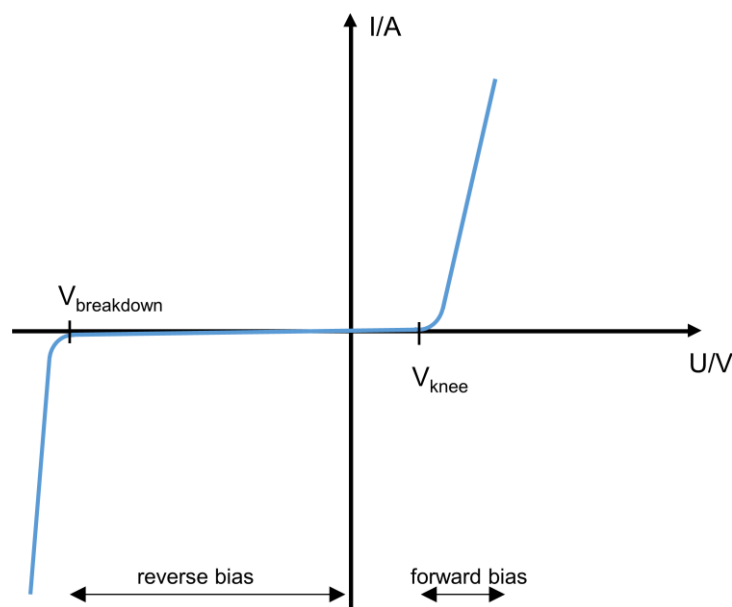


Figure 7: Creation of a depletion region in a pn-junction without an applied voltage. Figure adopted from ³⁶.

When an external voltage V_a is applied to the diode, the depletion zone is strongly influenced by the occurring electrical field, resulting in the characteristic, direction-dependent current-voltage behavior. When the negative pole is applied to the n-type semiconductor, the voltage is defined as positive, with $U_a > 0$, and is so-called forward biased. In this case, the depletion region is getting smaller, so the resulting energy barrier is decreasing for the amount of V_a , so $\Phi = \Phi_0 - V_a$. The flow of the diffusing carriers and the electric field forces of the remaining donor atoms is then no longer balanced, the holes can diffuse from the p-type semiconductor into the n-type one and the electrons in the opposite direction. Those injected excess minority carriers, here the holes from the p-type semiconductor, can then recombine with an electron in the n-type region. Those electrons needed for recombination are constantly fed into this region by the applied external potential, resulting in an overall electron flow through the device. This is also supported by the opposite effect, the recombination of the electrons from the n-type region

with the holes in the p-type region, resulting in a hole current with opposite direction. Overall, in the forward direction, an extensive increase in current flow is observed when the external potential is higher than the junction potential, leading to the characteristic UI curve of a pn-diode.³⁶

If the external voltage V_a is negative, the diode is reverse-biased, and the value of the energy barrier Φ is increased, leading to an increased size of the depletion zone. The diffusion of the electrons into the p-type region and of the holes into the n-type region is decreased, and therefore, only a very small net current is observed. This current is directly correlated to the drift of the holes from the n-type region into the p-type region and from electrons in the opposite direction, and since these are only minority carriers, the current, known as leakage current, is extremely low. In this case, the diode is in reverse mode, allowing nearly no current flow.³⁶ A characteristic U/I curve for a pn-junction diode is shown in Figure 8.



Figur 8: Characteristic U/I curve of a pn-junction diode. Figure adopted from ³⁶.

As every device, also diodes have certain limits. In the reverse mode, the current is nearly independent of an increase in U_a . At a certain level, the electrical field build up from the depletion region gains enough energy to accelerate the carriers to very high kinetic energies. Due to collisions, those carriers can then generate electron-hole pairs in an impact ionization process. Those pairs are then accelerated themselves, and can create even more carriers by impact ionization. This effect is known as the avalanche effect, and the voltage at which this occurs is generally called the breakdown voltage BV of a diode.⁴³ In general, the breakdown voltage of a diode is defined as the voltage in reverse bias at which a sudden increase of current flow occurs, and it is not necessarily given that the diode is destroyed at this point. But if the diode is operated in the breakdown regime, it is highly likely that damage to the system is induced by thermal effects, if no safety precautions are made. Another mechanism observed

in diodes is the Zener breakdown, which only occurs in diodes with two highly doped semiconductors.⁴⁴ At high doping levels, the depletion region is very narrow, and electrons can directly move from the p-type valence- into the n-type conduction band by the tunnel effect. This effect can be used in so-called Zener diodes for voltage references, as the doping level and therefore the breakdown voltage can be controlled easily.^{40, 45}

In comparison to Schottky diodes, the switching time (the time needed to switch the diode from forward bias into reverse bias) is much higher. In the moment when the external field is switched, the minority carriers start to move in the opposite direction. The resulting current $-I_R$ is way higher than the saturation current I_S , and it remains unchanged until all excess minority carriers at the transition region vanish. This time is called switching time T_s , where the current through the device stays nearly linear. Afterwards, the so called fall regime starts, where the current decreases exponentially, since the stored charge is no longer sufficient to supply the current I_R . The end of the fall time t_f is defined as the value when the current reaches 10% of the initial I_R , and the complete time $t_s + t_f$ is called the reverse recovery time. Since the switching time t_s is directly dependent on the movement of minority carriers, it is way slower than in Schottky contacts, where electrons as majority carriers contribute to the diode behavior.^{36, 46, 47}

Diodes can not only be used as rectifying devices. Other types of diodes which are commonly used would be e.g. light emitting diodes (LED), where the recombination of electrons and holes in a direct band gap semiconductor is accompanied by the emission of a photon, which can be seen as a light correlated to the band gap energy.^{48, 49} Furthermore, pn-junctions can be utilized in solar cells, where the excitation of electrons through light is used. In solar cells, electron-hole pairs are generated, and the junction is used to separate the charges and make them usable in form of electrical energy.^{50, 51}

2 Experimental

2.1 Chemicals

Table 1: List of used chemicals with respective supplier and purity grades.

Chemical	Supplier	Grade [%]
Copper, powder, -20,+50 mesh	CHEMPUR	99.95
Copper(I) chloride	ALFA AESAR	97
Indium	ALFA AESAR	99.999
Selenium, granules, 2-4 mm	CHEMPUR	99.999
Silver, shots, 2-3 mm	THERMO SCIENTIFIC	99.999
Sulfur, pieces	ALFA AESAR	99.999
Tellurium, lumps	THERMO SCIENTIFIC	99.999+
HCl, 37%	VWR CHEMICALS	<99.9
Ethanol	MERCK	<99.8
¹²⁵ Tellurium	STB ISOTOPE GERMANY	94% ¹²⁵ Te

Copper(I) chloride is purified by re-crystallization in conc. HCl prior to use. Therefore, about 5 mg of CuCl are dissolved in the lowest possible amount of 37% HCl in a 2 l Erlenmeyer flask. Afterwards, the solution is diluted with demineralized water until all CuCl dissipates. The residue is collected with the aid of a Buchner funnel and immediately washed with pure ethanol for three times. The powder is then transferred into a *Schlenk*-tube and dried for at least 12 h under a vacuum of $< 10^{-2}$ mbar. The purified CuCl, silver, copper and tellurium are stored in a glovebox (Unilab, MBRAUN, O₂ < 2 ppm, H₂O < 0.1 ppm) until use. To allow precise weighing, silver is cut into pieces with a side cutter, and selenium and tellurium are slightly ground with an agate mortar.

2.2 Solid State Synthesis

For all solid state synthesis of pnp-switchable thermoelectrics, stoichiometric amounts of the starting materials are weighed on an analytical balance (AX224, SARTORIUS AG, with a precision of 0.1 mg). For the copper-chalcogenide samples, additional CuCl is added as a transport agent. The approaches are performed in batches of 1 g if not stated differently in the following. The starting materials are transferred into silica ampoules (10 mm diameter, 1 mm thickness) which were dried for at least 12 h prior to use, evacuated on a *Schlenk*-line to $< 2 \times 10^{-3}$ mbar and flushed with argon (WESTFALEN AG, grade 4.8, 99.998%, dried over titanium sponge) for three times. When CuCl is used, the time at air is kept as short as possible due to its moisture sensitivity. The evacuated ampoules are then closed with the aid of an

oxyhydrogen burner. If not stated differently in detail, the starting materials are then heated up to 1323 K in a muffle furnace (NABERTHERM, type L 3/11, equipped with a B310 controller) within 2 h, kept at this temperature for at least 2 h and then immediately quenched in an ice bath to produce homogeneous mixed precursors.

2.2.1 $\text{Ag}_{18}\text{Cu}_3\text{Te}_{11}\text{Cl}_3$

To form single- and polycrystalline samples of the coinage-metal chalcogenide halide $\text{Ag}_{18}\text{Cu}_3\text{Te}_{11}\text{Cl}_3$, the air-sensitive precursor is ground in an agate mortar for better homogenization and immediately re-sealed into a new silica ampoule. The material is then tempered in a muffle furnace. The ampoules are placed in the furnace at a 90° angle to the heating elements with the material located close to the hot side. The oven is heated to 663 K within 12 h and kept at this temperature between 7 and 21 days depending on the recommended crystal size. After 7 days, crystals with sizes ≤ 1 mm are achieved after natural cooling of the oven, which are predominantly used for powder- or single crystal X-ray diffraction (SC-XRD). With longer tempering times, crystals up to the cm range are grown, which are needed for the diode experiments.

2.2.2 AgCuS

To form the pnp-switchable material AgCuS , no homogenization step is needed. The material is synthesized in a one-step approach by a defined heating program like described by Biswas *et al.*¹¹ In difference to the other approaches, the material is produced on a 7 g scale in 14 mm silica ampoules with a wall thickness of 1 mm. The ampoule is placed nearly vertically in a muffle furnace and heated to 773 K in 12 h, then to 1223 K in 5 h and kept there for 24 h. The material is then quenched to RT by atmosphere exposure. The uniform ingot is stored under air until further use.

2.2.3 $\text{Cu}_{1.5}\text{Se}_y\text{Te}_{1-y}$

The copper chalcogenide thermoelectrics are produced according to the synthesis of $\text{Ag}_{18}\text{Cu}_3\text{Te}_{11}\text{Cl}_3$. Only the tempering process is slightly different: The ground precursor is re-sealed into new ampoules of 7 – 9 cm length. Up to five of them are then put into a ceramic tube of 5 cm length. This tube is then placed into the muffle furnace, with the starting materials located close to the hot wall, and heated to 723 K in 12 h and kept at this temperature for 7 days before natural cooling. The pure sample is produced on the hot side of the ampoule, while the excess CuCl is transported to the cold side. A clear gradient can be seen in the product, with pure, black material on the hot end and a greyish color (from residual CuCl) on the cold end, which can be separated and discarded. Only the pure black sample is used for further processing.

2.2.4 Pellet Preparation

For thermoelectric measurements, bulk samples are prepared in the form of pellets. Finely ground material is transferred into a P/OWEBER 10 H high precision hot-pressing tool (10 mm diameter for LFA measurements, 13 mm diameter for Seebeck and electrical conductivity measurements). The tool is afterwards transferred into a MAASSEN MP150 hydraulic press and evacuated to a pressure of $<10^{-2}$ mbar with an EDWARDS RV 12 rotary vacuum pump. The tool is heated to 373 K by the aid of an P/OWEBER TRG 1 temperature controller. When a constant temperature is reached, the pressure is increased to 2 t for the 10 mm tool and to 3 t for the 13 mm tool and held for 1 h. The sample is then cooled down slowly to RT by turning off the heater and the pressure is carefully released to remove the pellet.

2.3 Analytical Methods

2.3.1 Powder X-ray Diffraction

For compositional analysis and cell parameter determinations, powder X-ray diffraction (PXRD) experiments are performed. Small amounts of finely ground sample are placed between two stripes of SCOTCH[®] Magic[™] Tape, 3M and fixed in a flatbed holder. This is transferred to a STOE Stadi P powder diffractometer, attached with a DECTRIS Mythen 1K detector, in transmission geometry and a curved Ge(111) monochromator. The sample is measured with Cu-K_{α1} radiation ($\lambda = 1.54056 \text{ \AA}$) in a range from 5 to 80° 2 θ (step 0.015). For compositional analysis, a standard measurement time of 15 min is used. The time is increased to 1h for Ag₁₈Cu₃Te₁₁Cl₃ samples due to the high amount of theoretical reflections and for indexing. Phase analysis, indexing and cell parameter refinements (for Cu_{1.5}Se_yTe_{1-y}) are performed in the STOE WinXPow software package.⁵² For comparison with known materials, cif-files taken from the Pearson Crystallographic Database are used to calculate theoretical reflection patterns.⁵³

2.3.2 Single Crystal X-ray Diffraction

Single crystal X-ray diffraction is used for structure model determinations. Suitable single crystals are either directly selected or cut from bigger parts with a scalpel under an optical microscope (NIKON SMZ645). The crystallinity is checked by a polarization filter, which is attached to a ZEISS Stemi 508 microscope equipped with a ZEISS Axiocam 105 color. For experiments below 400 K, the crystals are mounted onto a glass fiber either with the aid of colorless nail polish or bee's wax. Due to the limited operating range of those gluing agents, a different method is used for the high temperature measurements. For the tests, the crystal is placed into a glass capillary and fixed in this position by putting another, slightly smaller capillary into it. The bigger capillary is then sealed under vacuum prior to measurement. The measurements are performed on a STOE StadiVari single crystal diffractometer equipped with a 2-D DECTRIS Pilatus 3R 110K detector and a XENOCs Genix 3D^X microfocus X-ray source (Mo-K_{α1/2} radiation, $\lambda = 0.71073 \text{ \AA}$). The temperature is controlled by an OXFORD Cryostream plus heating/cooling system. Data reduction and unit cell determinations are performed with the Stoe X-Area software package.⁵⁴ A numerical absorption correction is applied based on optimized crystal shapes generated from symmetry-equivalent reflections using the XRed and XShape software.^{55, 56} The structures are solved using a charge-flipping algorithm which is implemented in the Jana 2006 software suite.⁵⁷⁻⁵⁹ For the mobile species present in ion conductors, the displacement parameters were refined anharmonically to provide a suitable structure description.⁶⁰⁻⁶⁴

2.3.3 Seebeck Coefficient and Electrical Conductivity

Since the behavior of the Seebeck coefficient with temperature is the most straightforward way to detect if a semiconductor is p- or n-type conducting, its measurement plays a crucial role in this work. The possible materials for applications as one-compound diodes need the ability to switch their conduction type through the thermal induction of a phase transition. Therefore, this work focuses very strongly on the thermoelectric and electric characterization of the used materials and those methods are explained in more detail.

To measure the Seebeck coefficient, as well as the overall electrical conductivity of the samples, a NETZSCH SBA 458 Nemesis measurement unit is used. The AgCuS and Ag₁₈Cu₃Te₁₁Cl₃ samples are therefore hot-pressed into pellets of 13 mm diameter, with a height between 1 – 2 mm and reaching at least 84% of the material's theoretical density. This pellet is then placed onto the sample carrier, which consists of an alumina plate with one integrated micro heater on each side, as well as four holes containing two type K thermocouples as well as two rhodium electrodes, schematically depicted in Figure 9. The whole measurement chamber can be heated to a specific temperature, while the inside is flooded with argon (60 ml/min) to provide an inert atmosphere.

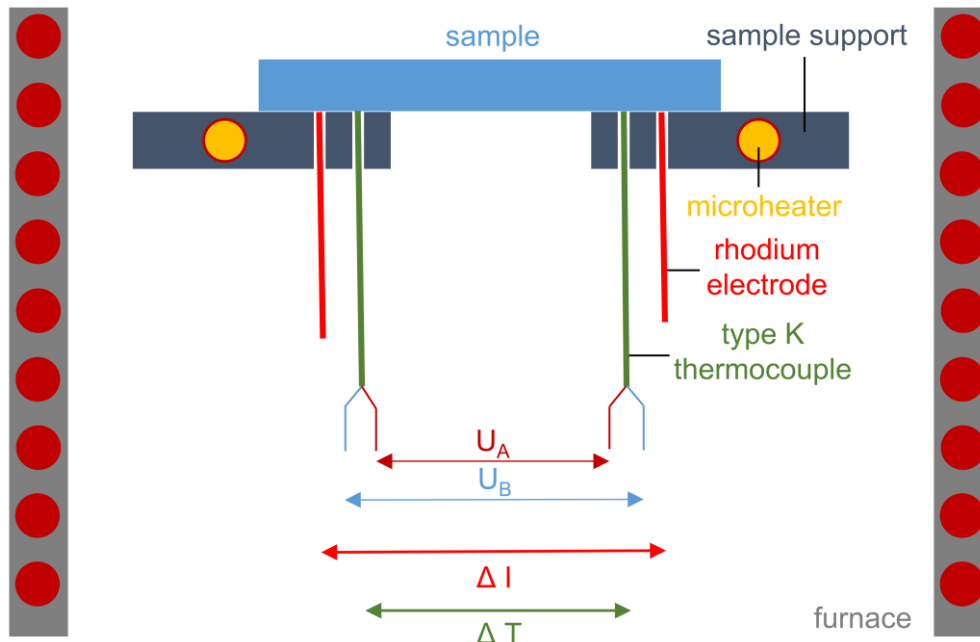


Figure 9: Schematic structure of the Seebeck and conductivity measurement cell in the Netzsch SBA 458 Nemesis. Graphic adopted from Netzsch SBA 458 manual.⁶⁵

For the determination of the electrical sheet resistivity of the samples, the pellet is measured in a so-called linear four terminal measurement arrangement. The outer rhodium contacts are

used to apply a defined current. For semiconductors, the standard range is set between 50 and -50 mA and a total of six steps is used (at 1/3, 2/3 and 3/3 of the maximum current, respectively). The resulting voltage over the sample is then measured via the thermocouples in between the rhodium contacts. Taking the distance $s_1 = s_3 = 1.625$ mm between a rhodium contact and a thermocouple and $s_2 = 8.25$ mm between the two thermocouples into account, according to Smits and Valdes the resistivity of a quasi-infinite sample is calculated by:

$$\rho = \frac{\Delta V}{I} \times \frac{\pi}{\left(\frac{1}{s_1} - \frac{1}{s_1 + s_2}\right)} \quad (4)$$

With ρ as the sheet resistivity, ΔV the voltage difference and I the applied current.^{66, 67}

Since the measured samples are not of infinite sample geometry, the resistivity is internally corrected for scattering depending on the sample's shape.

To measure the Seebeck coefficients, a heat gradient has to be applied in a defined region of the samples. Therefore, the micro heaters are operated with a heating voltage of 7 V to generate a temperature difference of some K. The thermocouples are then at the same time used to measure the temperature and the resulting voltage difference generated by the Seebeck effect. The voltage between two arms of one thermocouple directly correlates to the exact temperature in the point where the potential is measured, while the thermo voltage of the sample is measured between each pair of same thermo wires (U_A and U_B). During the measurement of each temperature point, alternating sides of the sample are heated and therefore a high amount of measurement points is generated during the cycle. Those values for the thermo voltages are then drawn up against the temperature difference ΔT for both pairs of thermo wires. The resulting Seebeck coefficient of the sample can be calculated by the slope of this two curves α_A and α_B (determined by linear regression) with knowledge of the Seebeck coefficients of the used thermo wires S_A and S_B by using following equation:

$$S = \frac{1}{2} \times \left(\frac{\alpha_A + \alpha_B}{\alpha_B - \alpha_A} \right) \times S_{AB} + S_A + S_B \quad (5)$$

With S the Seebeck coefficient of the measured sample, α_A and α_B the slopes of the two curves, S_{AB} the Seebeck coefficient of the type K thermocouple and S_A and S_B the Seebeck coefficients of the two different thermo wires. The collected data is analyzed using the NETZSCH SBA Measurement software package.⁶⁸

The slope of the curves directly describes the type of conduction within a semiconductor material. If the slope is negative, a negative Seebeck coefficient is calculated, defining the material as n-type conductive. In this kind of materials, negative charge carriers, more specifically electrons, are the dominant carrier type which can move to the side of lower energy when a heat gradient is applied. For positive Seebeck coefficients, positive charge carriers

(holes in the semiconductor) are the main carrier type, identifying the material as p-type conductive.⁶⁹ This fact renders the measurement of the Seebeck coefficient the most convenient and practicable way to determine the conduction type in a semiconductor, and for this work, it makes it possible to correlate structural changes to the dominant charge carrier type and identify new materials as possible candidates for one-compound diode or transistor applications.

2.3.4 Laser Flash Analysis (LFA)

The thermal diffusivity α of the samples is determined on a NETZSCH HyperFlash 467 Laser Flash Apparatus equipped with a mercury cadmium telluride (MCT) detector. The measurement atmosphere is pure nitrogen (5.0, WESTFALEN AG) to avoid oxidation reactions. The samples are hot-pressed into pellets of 10 mm diameter and 1 – 2 mm thickness and afterwards spray-coated with graphite (CRAMOLIN Graphit) on both sides to enhance emissivity. The ignition voltage of the flash lamp is set to 250 V and the pulse width is 600 μs . Heat loss and finite pulse corrections are applied using Dusza's model.⁷⁰ The data is analysed using the NETZSCH Protheus Thermal Analysis software package using an improved version of the model provided by Cape and Lehman to calculate the thermal diffusivity.⁷¹⁻⁷³ The thermal conductivity was calculated by using following equation:

$$\kappa = \alpha \times \rho \times C_p \quad (6)$$

With α the thermal diffusivity, ρ the density of the material and C_p the specific heat capacity of the material, which is approximated by the Dulong-Petit rule in the case of $\text{Ag}_{18}\text{Cu}_3\text{Te}_{11}\text{Cl}_3$.⁷⁴

For $\text{Cu}_{1.5}\text{Se}_y\text{Te}_{1-y}$ the specific molar heat capacity was determined on a Linseis LFA1000 laser flash device equipped with a InSb detector. A CuS sample is used as reference.

2.3.5 Diode measurements

To prove the rectifying behavior of diode devices, UI-measurements are the method of choice. A KEITHLEY source-measure unit SMU 2450 is used to apply a potential to single crystals of the chosen material and collect the resulting current response. Data is processed by the aid of the KEITHLEY Kickstart I-V Characterizer App.⁷⁵ The UI-curve are collected between 1 V and -1 V with a scanning speed of 0.06 V s^{-1} . To ohmically contact the materials and enable a heat gradient within the crystal to generate p- and n-regions at the same time, self-designed printed circuit boards (PCB) with gold-plated contacts are used. The PCBs are designed with the aid of the Eagle software package available in AUTODESK Fusion 360 and manufactured by MULTI LEITERPLATTEN GmbH, Brunnthal.^{76, 77}

For the $\text{Ag}_{18}\text{Cu}_3\text{Te}_{11}\text{Cl}_3$ sample, design 1 shown in Figure 10a is used to prove the existence of a thermally operated one compound diode. Therefore, two 49 Ω resistors are placed right next to one of the contact sides to allow local heating up to 363 K. While located in a fridge with a temperature of 281 K, the temperature gradient over the sample can be adjusted to 295 K on the cold and 308 K on the hot side by applying a potential gradient to the resistor with the aid of a QJE PS6005 switching power supply. The temperature is controlled at the contacts with a Ni/Cr/Ni thermocouple equipped to a RSpro thermometer device, allowing the

cold side safely to be in the β -regime and using the hot side to transform it to the α -phase. This process provides stable conditions to gain a pn-junction right in the crystal, causing a depletion layer between those regions, and finally show rectifying behavior in the obtained UI-curve. To allow ohmic contacts, indium is used to realize the interconnection between the gold-plated pads and the sample.

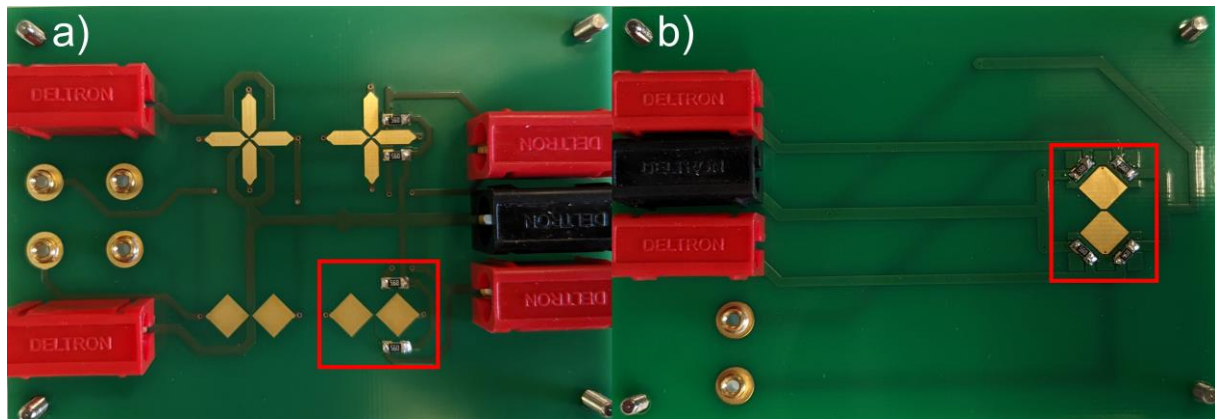


Figure 10: a) PCB design 1 used for diode measurements with $\text{Ag}_{18}\text{Cu}_3\text{Te}_{11}\text{Cl}_3$ enabling only one sided heating. b) PCB design 2 used for measurements with AgCuS , featuring independent resistive heating on both contact sides. The red rectangles represent the areas used during successful operation.

Ingots of AgCuS are cut into bar-shaped samples to perform further electrical experiments. Since the temperature for the pn-transition of 358 K is well above room temperature in those samples, the experiments can be performed at ambient conditions. Additional to the proof of a second one-compound diode, the reproducible on- and off-switching of the diode as well as its direction-independent behavior should be shown. To realize this switching of the forward direction of the diode without any changes in the contacts, the temperature gradient has to be inverted. For this purpose, another type of PCB is designed, using one pair of 56Ω resistances on each contact side of the ingot, see Figure 10b They can be contacted and heated independently from each other, so the n-type region can be formed alternately on both sides. As contacting medium, tin-lead solder (STANNOL, Sn:Pb:Cu 60:39:1 wt%) is used to ensure ohmic behavior. The applied heat gradient ranges from 338 K to 363 K.

In addition, the temperature profile on the crystal is visualized and verified using a INFRATEC VarioCam HD head 980 S microbolometer system equipped with a JENOPTIK M = 1.0x precision microscope objective. The obtained thermograms are processed using the Irbis 3.1 professional software package.⁷⁸

To undoubtedly prove the formation of a pn-diode, the switching time of the devices is accessed. A potential of 1 V is applied to the system, which is then instantly switched to the reverse potential of -1 V after a defined time. The current decrease is monitored during this

process, which is directly correlated to the dominant carrier type in the diode. For Schottky contacts, the switching to the blocking mode would be almost instantaneous, in a time frame of nano- to picoseconds), because majority carriers are the predominant form there.

2.3.6 Bulk modulus determinations

To determine the resistance of $\text{Ag}_{18}\text{Cu}_3\text{Te}_{11}\text{Cl}_3$ and $\text{Cu}_{1.5}\text{Se}_{0.5}\text{Te}_{0.5}$ against compressive stress, high-pressure P-XRD experiments were performed at Diamond Light Source Beamline I15, Didcot, Great Britain. The samples are measured in a LeToulllec-style membrane diamond anvil cell (DAC) with an applied X-ray wavelength of $\lambda = 0.4246 \text{ \AA}$ for $\text{Ag}_{18}\text{Cu}_3\text{Te}_{11}\text{Cl}_3$ and 0.4959 \AA for $\text{Cu}_{1.5}\text{Se}_{0.5}\text{Te}_{0.5}$. The diamond anvils have 300 micron culets and rhenium is used as gasket material. A 2D CdTe area detector DECTRIS Pilatus 2M is used for data collection and the sample-detector distance is calibrated by the aid of a LaB_6 standard prior to measurement. The applied pressure ranges from ambient to 8 GPa, with daphne oil as pressure transmitting medium for $\text{Ag}_{18}\text{Cu}_3\text{Te}_{11}\text{Cl}_3$. For $\text{Cu}_{1.5}\text{Se}_{0.5}\text{Te}_{0.5}$, an ethanol/methanol mixture (1:4, volume fraction) is used to measure from ambient pressure up to 9.5 GPa. The pressure is calibrated by the aid of an internal ruby standard using the ruby fluorescence scale.⁷⁹⁻⁸¹ The ruby modes are collected before and after each pressure step, with an equilibration time of 10 min. The 2D diffraction data is converted to 1D high pressure P-XRD data by using DAWN and the ruby modes are fitted with a pseudo-Voigt profile using FITYK for exact pressure evaluations.^{82, 83} Therefore, the pre- and post-measurement pressures are averaged for each data point. The unit cells are refined using the JANA 2006 software routine to track the behavior under compressive stress.⁵⁷

2.3.7 Solid State Nuclear Magnetic Resonance (NMR)

To access the mobility in the anionic and cationic substructure and the bonding situation, ^{65}Cu -, ^{109}Ag - and ^{125}Te -solid-state NMR is performed by Dr. Renée Siegel at the university of Bayreuth. Samples with enriched ^{125}Te are prepared to reduce measurement time.

To avoid a temperature gradient during ^{125}Te solid state magic angle spinning (MAS) NMR, the samples are placed in the middle third of the rotor and spun with a frequency of 62.5 kHz on a BRUKER 1.3 mm double-resonance MAS probe. $(\text{CH}_3)_2\text{Te}$ and $\text{Te}(\text{OH})_2$ are used as a reference. Data is collected on a BRUKER 400 Advance III HD spectrometer operated with a frequency of 126.1 MHz ($B_0 = 9.4 \text{ T}$).

For ^{65}Cu and ^{109}Ag a BRUKER 600 Advance III HD spectrometer is used at a field of $B_0 = 14.1 \text{ T}$ resulting in a frequency of 170.5 and 28.0 MHz for Cu and Ag, respectively. A Bruker 1.3 mm double resonance probe is operated at 62.5 (Cu) and 40.0 kHz (Ag). Static experiments are

performed with a triple-resonance wide-line probe. An AgNO_3 solution and CuCl powder are used as reference for ^{109}Ag and ^{65}Cu experiments and temperature is calibrated with the aid of $\text{Pb}(\text{NO}_3)_2$.

Data is analyzed with the Bruker TopSpin 3.6.3 software package.⁸⁴

2.3.8 Differential Scanning Calorimetry (DSC)

The thermal behavior of the samples is monitored using differential scanning calorimetry (DSC). About 50 mg of powdered sample are therefore transferred into an aluminum crucible, NETZSCH GmbH, and sealed under air with the corresponding NETZSCH press. The measurements are conducted on a NETZSCH DSC 200 F3 Maja calorimeter with a standard heating speed of 10 K min^{-1} in a nitrogen atmosphere. Appearing phase transitions (endothermal signal) are determined by onset-temperatures, and enthalpies by integration of the signal area in the NETZSCH Protheus Thermal Analysis software package.⁸⁵

2.3.9 Semi-quantitative Phase Analysis and Scanning Electron Microscopy (SEM)

To clarify the sample composition and homogeneity, energy dispersive X-ray spectroscopy (EDX) is performed on a JEOL JSM-IT200 InTouchScope™ with an integrated JEOL JED-2300 EDX unit. The samples are fixed on a steel holder with the aid of conductive adhesive tape from PLANO GmbH. EDX results are averaged from at least three different points randomly distributed over the sample surface. An acceleration voltage of 10 kV is used as standard setting.

2.3.10 Photoluminescence Spectroscopy (PL)

To access the band gap of $\text{Ag}_{18}\text{Cu}_3\text{Te}_{11}\text{Cl}_3$, photoluminescence spectra are recorded on a WITec alpha300R equipped with an Olympus LMPlanFL N 50x / 0.5 objective. A pressed pellet is therefore excited with a 532 nm laser operated at power of 0.15 mW and with a 300 g mm^{-1} grating. Three accumulations with an integration time of 30 s are performed for each measurement.

2.3.11 X-ray Photoelectron Spectroscopy (XPS)

To identify the present oxidation state of Cu in $\text{Cu}_{1.5}\text{Se}_{0.5}\text{Te}_{0.5}$, X-ray photoelectron spectroscopy is conducted on a freshly prepared crystal, which is broken up to measure on the inside. The spectra are acquired on a Kratos Axis Supra spectrometer using monochromatic Al K_α radiation ($h\nu = 1486.6 \text{ eV}$) with a total power of 225 W under high vacuum ($<10^{-9}$ Torr). The emission current is set to 15 mA and a pass energy for the detector of 160 eV for the wide scans and 40 eV for the detailed regions is used. The step size and

dweltimes are 0.1 eV and 300 ms for the detailed spectra and 1 eV and 200 ms for the wide scan, respectively. Binding energies are calibrated to the C 1s photoemission peak of adventitious carbon at 284.8 eV. A filament current of 0.45 A, a filament bias of 1 V and a charge balance of 3 V (all empirical values) are used, while the instrument's charge neutralizer is set as active.

3 Results

3.1 A Switchable One-Compound Diode

Anna Vogel¹, **Alfred Rabenbauer**¹, Philipp Deng¹, Ruben Steib¹, Thorben Böger², Wolfgang G. Zeier², Renée Siegel³, Jürgen Senker³, Dominik Daisenberger⁴, Katharina Nisi⁵, Alexander W. Holleitner⁵, Janio Venturini¹, and Tom Nilges¹

¹ Technical University Munich, School of Natural Sciences (NAT), Department of Chemistry, Synthesis and Characterization of Innovative Materials Group, Lichtenbergstraße 4, 85748 Garching bei München, Germany

² University of Münster, Institute for Inorganic and Analytical Chemistry Corrensstraße 30, 48149 Münster, Germany

³ University of Bayreuth, Faculty of Chemistry, Universitätsstraße 30, 95447 Bayreuth, Germany

⁴ Diamond Light Source, Harwell Science and Innovation Campus, Didcot, OX11 0DE Oxfordshire, Great Britain.

⁵ Technical University Munich, Walter Schottky Institute and Physics Department, Am Coulombwall 4a, 85748 Garching, Germany

Adv. Mater. **2022**, 2208698

First published: October 25th 2022

The aim of this project was the search for a pnp-switchable material with a switching temperature located around room temperature, as well as its application in the first thermally controlled one-compound diode. $\text{Ag}_{18}\text{Cu}_3\text{Te}_{11}\text{Cl}_3$ is developed for this purpose, as the endpoint of a cationic substitution series derived from $\text{Cu}_{20}\text{Te}_{11}\text{Cl}_3$. The latter was examined by Anna Vogel in an earlier project, but unfortunately, the material didn't show pnp-switching, even if its complex structural chemistry includes several phase transitions.⁴

As a first step, the crystal structure of $\text{Ag}_{18}\text{Cu}_3\text{Te}_{11}\text{Cl}_3$ is derived from single crystal XRD. It crystallizes as a superstructure of $\text{Cu}_{20}\text{Te}_{11}\text{Cl}_3$, in comparison the 6.3.6.3 Te nets appear ordered in form of distorted Kagomé nets. DSC experiments accompany the thermoelectric characterization, and reveal two phase transitions at 216(3) and 288(3) K. During the β - α phase transition, a huge Seebeck coefficient drop from around +950 to -2700 and back to +1800 $\mu\text{V K}^{-1}$ appears, revealing the ability to switch between p- and n-type conduction at around 288 K, so directly at room temperature. Two main contributions are then discussed to these switching mechanisms, namely a 2D-CDW which is created during the order-disorder

phase transition, as well as the d^{10} - d^{10} interactions in the cation substructure. As detected by single crystal XRD, the 6.3.6.3 Te net consist of $[\text{Te}_2]^{2-}$ dumbbells, as well as Te^{2-} anions, which also is the reason for the increased amount of charges in the $[\text{Te}_{11}\text{Cl}_3]$ unit and therefore higher number of cations compared to $\text{Cu}_{20}\text{Te}_{11}\text{Cl}_3$. This enables an internal redox process during the phase transition and therefore the switch in sign of the Seebeck coefficient, similar to the mechanism proposed for $\text{Ag}_{10}\text{Te}_4\text{Br}_3$.¹⁰ As a second point, some Ag-Cu distances are detected to move closer together during the transition, instead of following the thermal expansion. This sign of attractive d^{10} - d^{10} interactions is further substantiated by solid state NMR experiments, and the combination of both effects is clearly identified as the reason for the enormous Seebeck coefficient modulations. LFA analysis show extremely low thermal conductivities, which on the one hand would be beneficial for thermoelectric applications, and on the other hand are crucial for the creation of a stable temperature gradient across the material, which would be needed for the creation of a thermally controlled one-compound diode, which doesn't need any doping like classical pn-junction diodes.

The last part of the project reveals the feasibility of the aforementioned one-compound diodes. Therefore, single crystalline material is contacted on a PCB and a specially tuned heat gradient of 295 to 308 K is applied to the material to form a p- and n-region in close contact. U/I curves are measured under these conditions, which clearly show rectifying diode behavior, whereas without a heat gradient, the material behaves like a classical resistor. Those measurements are the unambiguous proof for the creation of a one-compound diode.

Author contributions: A.V. characterized the compound, conducted DSC, EDX, powder as well as single crystal-XRD and solved the crystal structures. A.R. synthesized the materials for electrical characterizations. A.V. and A.R. performed the thermoelectric characterization, with the friendly support of Dr. Ekkehard Post from Netzsch GmbH, Selb, Germany, which provided access to their low temperature Seebeck apparatus. R.St. and A.R. designed and revised the PCB design. T.B and W.Z. conducted the LFA measurements. R.Si and J.S performed the solid state NMR. A.R. and D.D. analyzed the material's performance under high pressure and calculated the bulk modulus. K.N. and A.H. collected the PL data. A.R. and P.D. conducted the current/voltage measurements and proofed the diode-like behavior. All authors discussed the results and contributed to the final manuscript.

Reprint from Vogel, A.; Rabenbauer, A.; Deng, P.; Steib, R.; Böger, T.; Zeier, W.; Siegel, R.; Senker, J.; Deisenberger, D.; Nisi, K.; Holleitner, A.; Venturini, J.; Nilges, T. 'A switchable one-component diode', *Adv. Mater.* **2022**, 2208698. This work is licensed under the Creative Commons Attribution – Non Commercial- No Derivatives 4.0 International License. To view a copy of this license, visit <https://creativecommons.org/licenses/by-nc-nd/4.0/legalcode> or send a letter to Creative Commons, PO Box 1866, Mountain View, CA 94042, USA.

A Switchable One-Compound Diode

Anna Vogel, Alfred Rabenbauer, Philipp Deng, Ruben Steib, Thorben Böger, Wolfgang G. Zeier, Renée Siegel, Jürgen Senker, Dominik Daisenberger, Katharina Nisi, Alexander W. Holleitner, Janio Venturini,* and Tom Nilges*

A diode requires the combination of p- and n-type semiconductors or at least the defined formation of such areas within a given compound. This is a prerequisite for any IT application, energy conversion technology, and electronic semiconductor devices. Since the discovery of the pnp-switchable compound $\text{Ag}_{10}\text{Te}_4\text{Br}_3$ in 2009, it is in principle possible to fabricate a diode from a single material without adjusting the semiconduction type by a defined doping level. Often a structural phase transition accompanied by a dynamic change of charge carriers or a charge density wave within certain substructures are responsible for this effect. Unfortunately, the high pnp-switching temperature between 364 and 580 K hinders the application of this phenomenon in convenient devices. This effect is far removed from a suitable operation temperature at ambient conditions. $\text{Ag}_{18}\text{Cu}_3\text{Te}_{11}\text{Cl}_3$ is a room temperature pnp-switching material and the first single-material position-independent diode. It shows the highest ever reported Seebeck coefficient drop that takes place within a few Kelvin. Combined with its low thermal conductivity, it offers great application potential within an accessible and applicable temperature window. $\text{Ag}_{18}\text{Cu}_3\text{Te}_{11}\text{Cl}_3$ and pnp-switching materials have the potential for applications and processes where diodes, transistors, or any defined charge separation with junction formation are utilized.

solar cells, to name a few. Currently, two different materials with opposite majority carriers are used to create a pn-junction. Nevertheless, some selected materials have previously been shown to switch between p- and n-conduction due to variations in temperature. In this context, the utilization of a single-material, thermally-controlled pn-junction would allow direct control of the character of these semiconducting devices including the position of the junction or its properties. Today, four different semiconducting materials are known to be capable of changing the mechanism of charge carrier transport between p- and n-type conduction. The first reported compound was $\text{Ag}_{10}\text{Te}_4\text{Br}_3$.^[1–3] This material switches reversibly between p-type to n-type conduction at $T_{\text{pnp}} = 390$ K during an order-disorder phase transition of the cation substructure, driven by a charge density wave within the telluride substructure. Upon further heating or cooling down below the phase transition temperature the material switches back from n-type to p-type conduction. Later, AgBiSe_2 ($T_{\text{pnp}} = 580$ K), AgCuS ($T_{\text{pnp}} = 364$ K), and $\text{Tl}_2\text{Ag}_{12}\text{Se}_7$ ($T_{\text{pnp}} = 410$ K) were also discovered to show a comparable pnp-switch at elevated temperatures.^[4–6] In all reported cases, the interplay of a highly

1. Introduction

The pn-junction is the most elementary building block of semiconducting devices, being found in diodes, transistors, sensors, and

switches back from n-type to p-type conduction. Later, AgBiSe_2 ($T_{\text{pnp}} = 580$ K), AgCuS ($T_{\text{pnp}} = 364$ K), and $\text{Tl}_2\text{Ag}_{12}\text{Se}_7$ ($T_{\text{pnp}} = 410$ K) were also discovered to show a comparable pnp-switch at elevated temperatures.^[4–6] In all reported cases, the interplay of a highly

A. Vogel, A. Rabenbauer, P. Deng, R. Steib, J. Venturini, T. Nilges
School of Natural Sciences (NAT)
Department of Chemistry
Synthesis and Characterization of Innovative Materials group
Technical University of Munich
Lichtenbergstraße 4, 85748 Garching b. München, Germany
E-mail: janio.venturini@tum.de; tom.nilges@tum.de
T. Böger, W. G. Zeier
Institute of Inorganic and Analytical Chemistry
University of Münster
Corrensstraße 28/30, 48149 Münster, Germany

 The ORCID identification number(s) for the author(s) of this article can be found under <https://doi.org/10.1002/adma.202208698>.

© 2022 The Authors. Advanced Materials published by Wiley-VCH GmbH. This is an open access article under the terms of the Creative Commons Attribution-NonCommercial-NoDerivs License, which permits use and distribution in any medium, provided the original work is properly cited, the use is non-commercial and no modifications or adaptations are made.

T. Böger
International Graduate School for Battery Chemistry, Characterization, Analysis, Recycling and Application (BACCARA)
University of Münster
Corrensstraße 40, 48149 Münster, Germany

R. Siegel, J. Senker
Inorganic Chemistry III
University of Bayreuth
Universitätsstraße 30, 95447 Bayreuth, Germany

D. Daisenberger
Diamond Light Source
Harwell Science and Innovation Campus
Didcot, Oxfordshire OX11 0DE, UK

K. Nisi, A. W. Holleitner
Walter Schottky Institute and Physics Department
TU Munich, Am Coulombwall 4a, 85748 Garching b. München, Germany

DOI: 10.1002/adma.202208698

dynamic substructure and the rearrangement of complementary structural units causes a modulation of the entire defect configuration and a switch of the semiconducting mechanism. A common building principle of all known pnp-switching materials is that they contain mobile d^{10} ions and a chalcogenide substructure, which interact with each other in a synergistic manner. Following this concept, the utilization of pn-switching materials in applications requires energy-friendly access to the switch close to the application temperature. Here, we report on a silver chalcogenide halide where the pn switch can be operated at room temperature without a huge and complex energy demand.

2. Results and Discussion

2.1. Structure Chemistry of $\text{Ag}_{18}\text{Cu}_3\text{Te}_{11}\text{Cl}_3$

Our group has recently prepared a material that shows pnp-switching close to room temperature: $\text{Ag}_{18}\text{Cu}_3\text{Te}_{11}\text{Cl}_3$.

The crystal structures of the relevant polymorphs of this compound were determined from single crystals by temperature-dependent X-ray diffraction measurements (XRD). The structures can be described by a simple topological approach where neighboring anions are connected in such a way that different layers are realized: a $\text{Te } 6^3$ honeycomb net, a $\text{Cl } 6.3.6.3$ kagomé net, and a distorted $\text{Te } 6.3.6.3$ kagomé net (see Figure 1a). The layers are stacked along one crystallographic axis in the following sequence: $\text{Te } 6^3 - \text{Cl } 6.3.6.3 - \text{Te } 6^3 - \text{Te } 6.3.6.3$. While the $\text{Te } 6^3$ and the $\text{Cl } 6.3.6.3$ nets consist only of isolated Te^{2-} or Cl^- ions, the distorted $\text{Te } 6.3.6.3$ net is composed of $[\text{Te}_2]^{2-}$ dumbbells and additional coordinating Te^{2-} ions (see Figure 1b). More details concerning the structure are denoted in Figure S1 (Supporting Information). A similar $\text{Te } 6.3.6.3$ layer can also be found in the mineral stützite ($\text{Ag}_{55-x}\text{Te}_3$, Figure S2, Supporting Information).^[7] Another feature of the anion substructure is the polyanionic Te_4 unit that vertically interpenetrates the $\text{Te } 6^3$ and $\text{Cl } 6.3.6.3$ nets. These units consist of a covalently-bonded $[\text{Te}_2]^{2-}$ dumbbell and two linearly

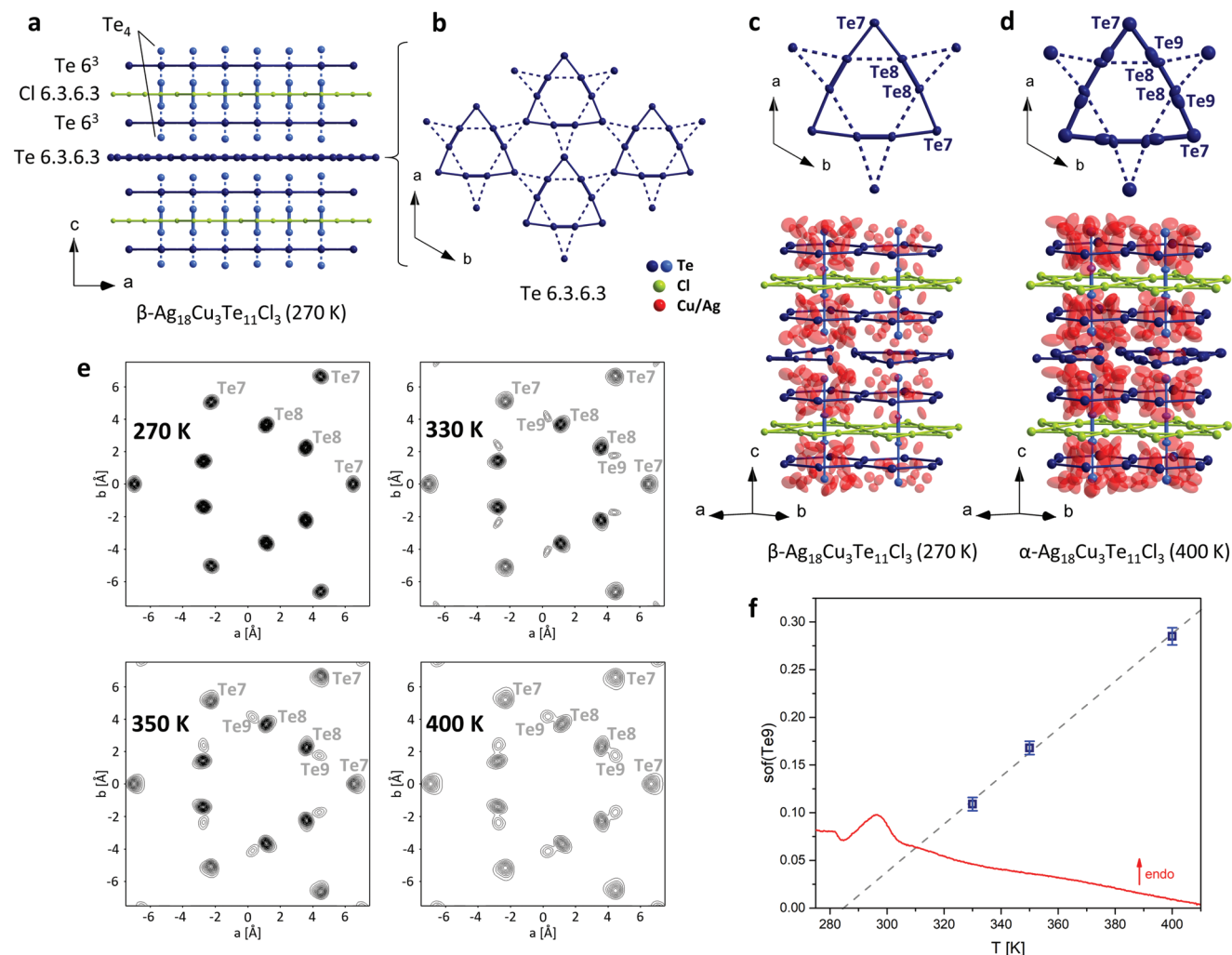


Figure 1. a) Scheme of anion substructure of $\beta\text{-Ag}_{18}\text{Cu}_3\text{Te}_{11}\text{Cl}_3$. b) Distorted $\text{Te } 6.3.6.3$ net. c, d) Structure sections of β - and $\alpha\text{-Ag}_{18}\text{Cu}_3\text{Te}_{11}\text{Cl}_3$. Te nets are drawn in dark blue and Te_4 units in light blue for better differentiation. Displacement parameters are drawn at 70% probability. e) Joint probability density function (jpdf) images of sections of the $\text{Te } 6.3.6.3$ net at 270, 330, 350, and 400 K. One contour line represents $0.3 \text{ e } \text{\AA}^{-3}$. f) Site occupancy factors (sof) of Te9 plotted against temperature (blue), linear fit (grey), and DSC (red).

coordinating Te^{2-} ions. The latter are located at distances closer than twice the van der Waals radius of tellurium ($d_{\text{vdW}}(\text{Te}) = 2.06 \text{ \AA}$),^[8] illustrating a certain attractive bonding interaction. All other anions are well-separated from each other without showing any kind of bonding interaction. Similar Te_4 units can be found in $\text{Ag}_{10}\text{Te}_4\text{Br}_3$, the first ever described pnp-switching material (see Figures S2 and S3, Supporting Information).^[1–3] The anion substructure of $\text{Ag}_{10}\text{Te}_4\text{Br}_3$ is closely related to that of $\text{Ag}_{18}\text{Cu}_3\text{Te}_{11}\text{Cl}_3$ – stacked Te_6^3 and Br_6^3 nets with interpenetrating Te_4 units – but the mechanisms of pnp-switching that will be discussed in the following are utterly different. The mobile and highly disordered d^{10} cations in $\text{Ag}_{18}\text{Cu}_3\text{Te}_{11}\text{Cl}_3$ are distributed in a liquid-like manner within the Te substructure (see Figure 1c,d) while the Cl_6^3 net acts as a separator for the mobile d^{10} ions. No silver or copper cations are distributed or located within this layer. All cation positions (red spheres in Figure 1c,d) in $\text{Ag}_{18}\text{Cu}_3\text{Te}_{11}\text{Cl}_3$ are mixed (by variable amounts of Cu^+ and Ag^+) and partially occupied. $\text{Ag}_{18}\text{Cu}_3\text{Te}_{11}\text{Cl}_3$ exhibits a high 2D ion mobility parallel to the (001) layer. This feature is substantiated by solid-state nuclear magnetic resonance (NMR) spectroscopy (as shown in Figure 4). Structural similarities to the mineral stützite and other coinage metal chalcogenide halides, like previously published $\text{Cu}_{20}\text{Te}_{11}\text{Cl}_3$, $\text{Cu}_{9,1}\text{Te}_4\text{Cl}_3$, and $\text{Ag}_{10}\text{Te}_4\text{Br}_3$, are discussed in the Supporting Information (shown in Figures S1 and S2, Supporting Information).^[1–3,7,9,10]

2.2. Polymorphism

$\text{Ag}_{18}\text{Cu}_3\text{Te}_{11}\text{Cl}_3$ is a polymorphic compound that shows two reversible order-disorder phase transitions at 216(3) and 288(3) K (onset values from differential scanning calorimetry (DSC), Figure 2a). The important phase transition for the pnp-switch is the latter, where $\beta\text{-Ag}_{18}\text{Cu}_3\text{Te}_{11}\text{Cl}_3$ – stable between 216 and 288 K – converts to $\alpha\text{-Ag}_{18}\text{Cu}_3\text{Te}_{11}\text{Cl}_3$, the phase present above room temperature. Single crystal structure determinations revealed that the symmetry and therefore also the space group does not change and the cell volume increases continuously without a significant volume discontinuity while undergoing the transition (see Table 1). While some physical properties, like the total electrical conductivity, increase continuously without any abrupt change in the temperature window around room temperature, the Seebeck coefficient drops significantly right after the $\beta\text{-}\alpha$ phase transition (Figure 2a). The origin of this intriguing Seebeck modulation effect needs to be identified and discussed. In $\beta\text{-Ag}_{18}\text{Cu}_3\text{Te}_{11}\text{Cl}_3$, a triangular arrangement of Te_2 dumbbells (Te_8 sites) and additional coordinating Te neighbors (Te_7 sites) create an ordered Te_6^3 net. Right after the phase transition to $\alpha\text{-Ag}_{18}\text{Cu}_3\text{Te}_{11}\text{Cl}_3$ at 288 K, we observe emerging disorder in the Te_6^3 net (Figure 1d). While the net is fully ordered in the β -polymorph, the occurrence of additional Te sites (Te_9) in close vicinity to the Te_2 dumbbells can be identified after the transition. Temperature-dependent joint probability density function (jpdf) plots are given in Figure 1e, where the population of the Te_9 site close to the dumbbell sites is represented. The distance between Te_9 and Te_7 (2.96(4) \AA at 330 K) is very similar to the dumbbell distance between two Te_8 (2.795(7) \AA at 330 K), from which we can

conclude that a new dumbbell is formed at this position. Temperature-dependent single crystal XRD measurements for $\alpha\text{-Ag}_{18}\text{Cu}_3\text{Te}_{11}\text{Cl}_3$ at 330(1), 350(1) and 400(1) K illustrate that the occupation of Te_9 increases linearly with temperature, while that of Te_8 decreases. The linear fit crosses the x -axis right at the onset of the phase transition. Further details concerning the temperature-dependent structure analysis are summarized in the Supporting Information section.

2.3. Physical Properties and Possible Applications

The most striking feature during this transition is the variation of the thermopower or Seebeck coefficient. $\text{Ag}_{18}\text{Cu}_3\text{Te}_{11}\text{Cl}_3$ displays a gigantic drop of the Seebeck coefficient of over 3000 $\mu\text{V K}^{-1}$ (at $\approx 295 \text{ K}$) followed by an increase of the thermopower by 4500 $\mu\text{V K}^{-1}$ (320 to 360 K) within a small temperature window of only 50 K (see Figure 2a). Such huge thermopower modulations within 50 K of more than 4 mV K^{-1} close to ambient temperature have never been observed before. This feature should enable the utilization of $\text{Ag}_{18}\text{Cu}_3\text{Te}_{11}\text{Cl}_3$ in sensors and power applications at room temperature. The previously mentioned materials show changes of only 1400 $\mu\text{V K}^{-1}$ in $\text{Ag}_{10}\text{Te}_4\text{Br}_3$, 750 $\mu\text{V K}^{-1}$ in AgBiSe_2 , 700 $\mu\text{V K}^{-1}$ in AgCuS , and 400 $\mu\text{V K}^{-1}$ in $\text{Tl}_2\text{Ag}_{12}\text{Se}_7$ during the pnp-switch.^[1,4–6] $\text{Ag}_{18}\text{Cu}_3\text{Te}_{11}\text{Cl}_3$ is able to create large voltage drops in a temperature window close to room temperature where manifold applications – e.g. solar cells, catalysts, and sensors – operate. Photoluminescence measurements of $\text{Ag}_{18}\text{Cu}_3\text{Te}_{11}\text{Cl}_3$ show two Lorentzian emission lines at 1.35 and 1.5 eV, located in the infrared (Figure 2b). Thermal activation and initiation of the pnp-effect are thus possible by light irradiation. This optical behavior may allow the utilization in solar cells since the band gaps are close to the maximal efficiency for single junction solar cells, as defined by the Shockley–Queisser limit (Figure S7, Supporting Information).^[11] The material also shows an extremely low thermal diffusivity, which is beneficial for the application of $\text{Ag}_{18}\text{Cu}_3\text{Te}_{11}\text{Cl}_3$ as diodes/transistors due to the maintenance of the thermal gradient and therefore the p- and n- regions (Figure 2c). The thermal diffusivity of $\text{Ag}_{18}\text{Cu}_3\text{Te}_{11}\text{Cl}_3$ of 0.08 $\text{mm}^2 \text{ s}^{-1}$ is lower than the values of water (0.135 $\text{mm}^2 \text{ s}^{-1}$) and polymers like polycarbonate (0.148 $\text{mm}^2 \text{ s}^{-1}$), polyethylene (0.283 $\text{mm}^2 \text{ s}^{-1}$), and polystyrene (0.137 $\text{mm}^2 \text{ s}^{-1}$).^[12,13] The thermal conductivity does not change significantly between 260 and 380 K and varies around $\approx 0.14 \text{ W m}^{-1} \text{ K}^{-1}$ (Figure 2c). This very low and rather temperature-independent thermal conductivity of $\text{Ag}_{18}\text{Cu}_3\text{Te}_{11}\text{Cl}_3$ is either caused by its excellent phonon scattering capability due to the intrinsic high cation mobility or by diffuson-mediated thermal transport. The latter mechanism has been recently identified and discussed for silver-ion conducting argyrodites.^[14] The calculated thermoelectric figure of merit ZT of 10^{-2} at 320 K is rather low due to the poor electrical conductivity (see Figure 2d). Due to possible applications as thin-layer and bulk material we determined the bulk modulus of this compound via high-pressure XRD experiments. Using a 3rd-order Birch–Murnaghan equation of state fit we derived a bulk modulus of 28.2(11) GPa (Figure 2 e,f, and Figure S4 a,b, Supporting Information).^[15] This value is slightly higher than the calculated bulk modulus of

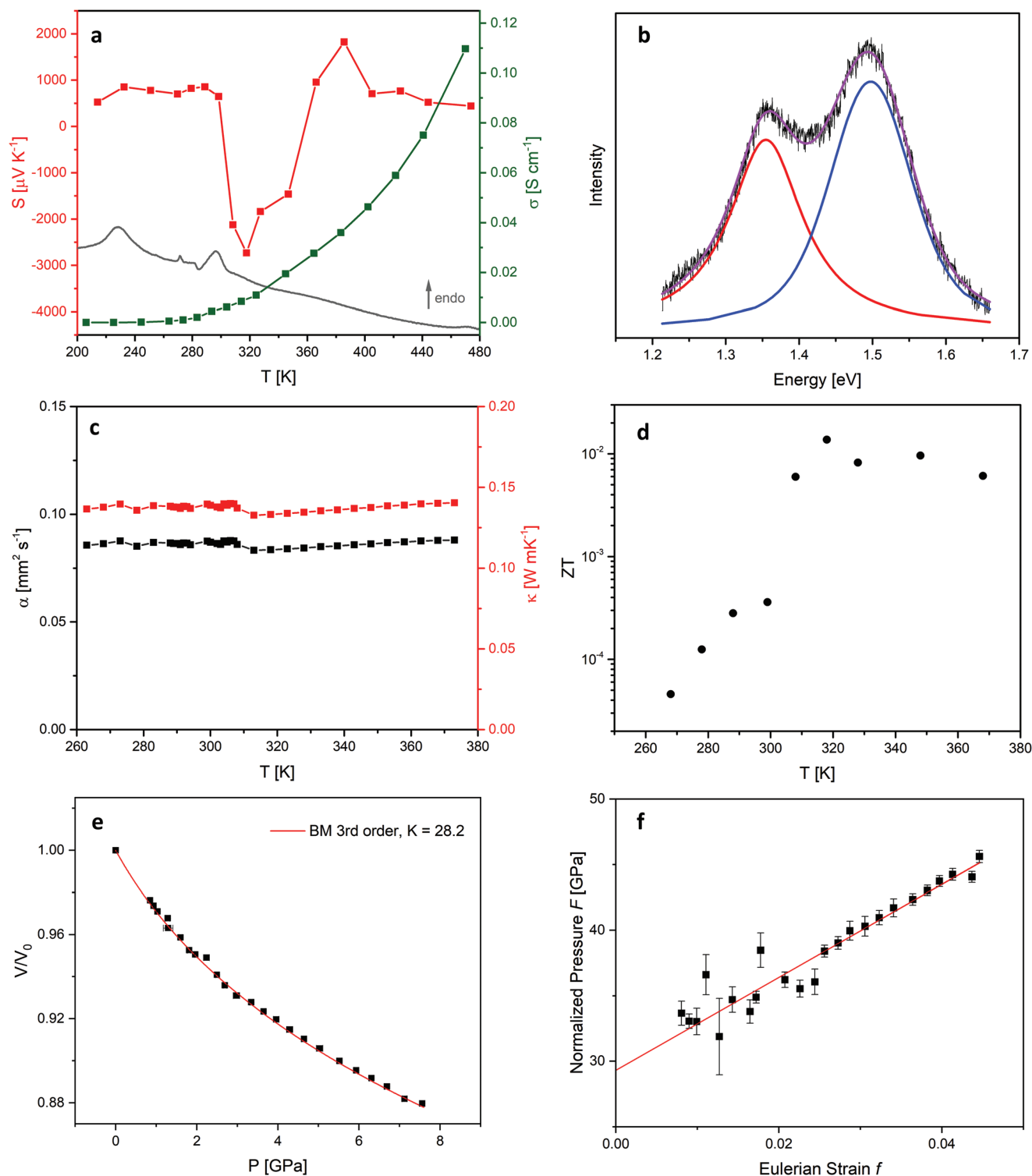


Figure 2. Physical properties of $\text{Ag}_{18}\text{Cu}_3\text{Te}_{11}\text{Cl}_3$. a) The Seebeck coefficient (red) varies between $625 \mu\text{V K}^{-1}$ (298 K) before, and $-2731 \mu\text{V K}^{-1}$ (317 K) and $1824 \mu\text{V K}^{-1}$ (386 K) directly after the β - α phase transition. DSC (grey) illustrates the reversible endothermic thermal effects at 216(3) and at 288(3) K (onset values, the small effect at 273 K is due to water impurity in liquid nitrogen). The total electrical conductivity (green) varies between 6 mS cm^{-1} (300 K) and 110 mS cm^{-1} (470 K). b) Photoluminescence measurements (black) show Lorentzian emissions at 1.35 (red) and 1.50 eV (blue). c) Thermal conductivities (red) calculated from thermal diffusivity (black) measurements cumulate in very low values of $\approx 0.14 \text{ W m}^{-1} \text{ K}^{-1}$ around the β - α phase transition. Effective phonon scattering takes place around room temperature. d) Calculated thermoelectric figure of merit ZT value of $\text{Ag}_{18}\text{Cu}_3\text{Te}_{11}\text{Cl}_3$. The error was estimated to 10%. e) Bulk modulus determination of α - $\text{Ag}_{18}\text{Cu}_3\text{Te}_{11}\text{Cl}_3$ from a 3rd-order fit using the Birch–Murnaghan equation of state resulting in $K_0 = 28.2(11) \text{ GPa}$ and $K' = 12.7(8)$. An F - f plot is given in (f).

Table 1. Single crystal XRD data of α - and β -Ag₁₈Cu₃Te₁₁Cl₃ at 270, 330, 350, and 400 K.

	β -Ag ₁₈ Cu ₃ Te ₁₁ Cl ₃	α -Ag ₁₈ Cu ₃ Te ₁₁ Cl ₃	α -Ag ₁₈ Cu ₃ Te ₁₁ Cl ₃	α -Ag ₁₈ Cu ₃ Te ₁₁ Cl ₃
Temperature [K]	270(1)	330(1)	350(1)	400(1)
Refined composition	Ag _{17.1(3)} Cu _{2.85(6)} Te ₁₁ Cl ₃	Ag _{17.2(5)} Cu _{2.87(8)} Te ₁₁ Cl ₃	Ag _{17.2(4)} Cu _{2.86(6)} Te ₁₁ Cl ₃	Ag _{16.4(5)} Cu _{2.74(9)} Te ₁₁ Cl ₃
Molar mass [g mol ⁻¹]	3537.7	3548.3	3542.4	3455.8
Crystal size [mm]		0.1 × 0.05 × 0.05		0.2 × 0.1 × 0.1
Crystal shape/color			block/black	
Crystal system	hexagonal		hexagonal	
Space group	<i>P6₃/mcm</i>		<i>P6₃/mcm</i>	
Z	6		6	
a [Å]	13.4709(12)	13.5506(12)	13.5651(12)	13.5775(12)
c [Å]	30.818(2)	30.7723(19)	30.8198(12)	30.822(3)
V [Å ³]	4843.1(7)	4893.4(7)	4911.4(6)	4920.7(8)
ρ_{calc} [g cm ⁻³]	7.2777	7.2246	7.186	6.9971
Diffractionmeter		STOE Stadivari		
Radiation [Å]		0.71073 (Mo K $_{\alpha 1/2}$)		
μ [cm ⁻¹]	22.16	21.771	21.656	21.114
F[000]	9061	9089	9074	8847
θ range [°]	3.04 – 30.13	3.01 – 29.99	3 – 30	3 – 29.99
hkl range	-18/ +9, 0/ +9, 0/ +43	-19/ +9, 0/ +19, 0/ +38	-19/ +9, 0/ +19, -43/ +43	-18/ +19, -18/ +19, -43/ +41
No. of reflections	8811	8099	17785	67811
R_{int}	0.0431	0.0613	0.0938	0.1913
Data/parameters	2053 / 275	1736 / 285	2154 / 301	2330 / 308
R / ω R [$> 3\sigma$ (I)]	0.0375 / 0.0637	0.0370 / 0.0598	0.0378 / 0.0625	0.0370 / 0.0726
R / ω R [all]	0.0887 / 0.0794	0.1169 / 0.1169	0.1117 / 0.0839	0.1476 / 0.1238
Goodness of fit	1.23	0.98	1.13	1.12
Res. elec. dens. max / min [e Å ⁻³]	-1.84 / +1.56	-1.47 / +1.26	-1.62 / +0.88	-1.53 / +1.30

Cu₂Te K₀ = 22.9 GPa.^[16] We observed no further phase transitions; at room temperature α -Ag₁₈Cu₃Te₁₁Cl₃ maintains the same structure up to \approx 8 GPa.

2.4. Mechanism of the pnp-Switch

An important point to elucidate is the mechanism of the pnp-transition in Ag₁₈Cu₃Te₁₁Cl₃. The Seebeck coefficient is defined by the Mott equation:^[17,18]

$$S = -\frac{\pi^2 k_B^2 T}{3e} \left[\frac{1}{n} \frac{dn(E)}{dE} + \frac{1}{\mu} \frac{d\mu(E)}{dE} \right]_{E=E_F} \quad (1)$$

where S , k_B , e , n , and μ are the Seebeck coefficient, Boltzmann constant, electron charge, charge carrier concentration, and carrier mobility, respectively. This equation may be understood as the partial derivative of the density of states (DOS) analyzed at the Fermi energy. As such, changes in the magnitude and signal of the Seebeck coefficient represent variation in the local state of the DOS at E_F . Two effects in Ag₁₈Cu₃Te₁₁Cl₃ are responsible for such modulation of the DOS and the resulting pn-switch that occurs right after the β - α phase transition.

One is localized in the heaviest atom (Te) substructure, and the other in the d¹⁰ cation substructure. The effect in the Te substructure can be regarded as a local 2D charge density wave (CDW) within the 6.3.6.3 Te kagomé net. The disorder phenomenon and the occupancy of additional Te sites within the kagomé net lead to significant atomic rearrangements and charge fluctuations. In **Figure 3a**, the proposed mechanism of the atomic rearrangement in the Te 6.3.6.3 net is illustrated. A partial local rearrangement of Te₂ dumbbells causes the observed variation in occupancy of Te8 and Te9 sites in the kagomé net. The Te₂ dumbbell – which is fully localized in β -Ag₁₈Cu₃Te₁₁Cl₃ – is shifted toward the corners of the Te triangle (see **Figure 3a**) within the kagomé net. This dynamic rearrangement is only possible through internal redox processes with charge fluctuation. Electron delocalization and transport are thus enabled via this dynamic process within the Te substructure in α -Ag₁₈Cu₃Te₁₁Cl₃. The temporary excess of free electrons leads to an upward shift of the Fermi level. As even small amounts of free electrons have a considerable impact on the electron-hole balance in semiconductors, the temporary availability of electrons leads to pn-switching during the phase transition. The observed broad Seebeck modulation and drop – in comparison to the other known pnp-compounds – might be explained by the continuous temperature-driven

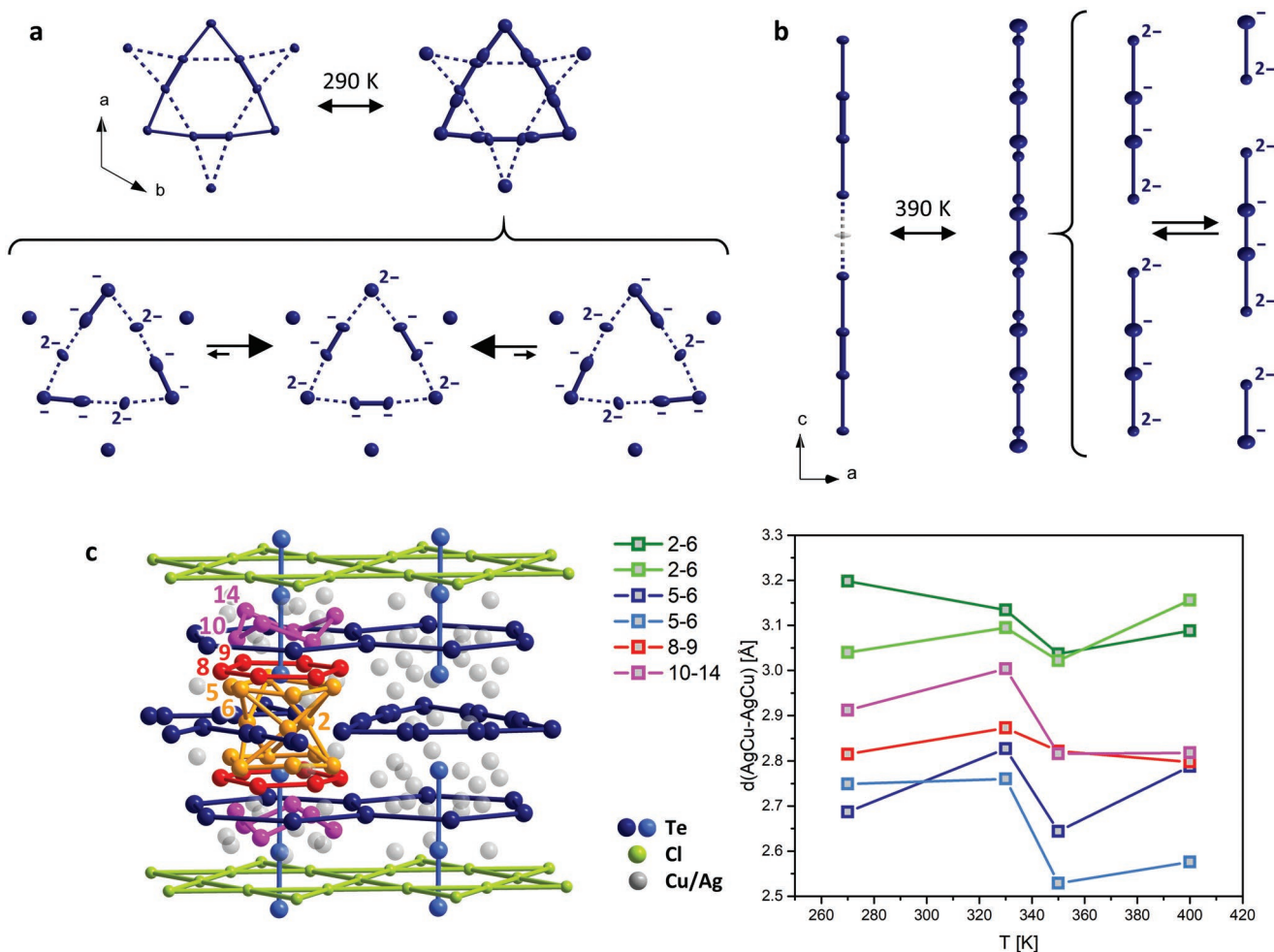


Figure 3. Mechanism of pnp-switching. a) Structure sections of Te 6.3.6.3 in β - and α - $\text{Ag}_{18}\text{Cu}_3\text{Te}_{11}\text{Cl}_3$. Proposed mechanism of dumbbell rearrangement in α - $\text{Ag}_{18}\text{Cu}_3\text{Te}_{11}\text{Cl}_3$. b) Structure sections of the isolated Te_4 strands and the equidistant Te chain that is formed during the β - to α - $\text{Ag}_{10}\text{Te}_4\text{Br}_3$ phase transition. c) Mixed occupied Ag/Cu sites in $\text{Ag}_{18}\text{Cu}_3\text{Te}_{11}\text{Cl}_3$. d^{10} - d^{10} interactions in the coinage metal substructure shorten the coinage metal distances. After the β - α phase transition, the d^{10} ions interact with each other and show reduced bond distances upon heating. Four different cation site couples are selected to illustrate this phenomenon, and their bond lengths are given as a function of temperature. Ag/Cu bond distances are defined by the maxima of electron density derived from the so-called mode positions, which were identified after the integration of the probability density functions of non-harmonically refined displacements for each ion.

occupation of the Te9 site that is necessary to induce the pn-transition.^[1,4-6] A comparable mechanism of atomic rearrangements in the Te substructure can be found in pnp-switching $\text{Ag}_{10}\text{Te}_4\text{Br}_3$. In this case, the rearrangement of strands of Te_4 units leads to a 1D CDW. The reorganization from a strand of oligomeric Te_4 units to a dynamically disordered equidistant Te-chain (shown in Figure 3b) occurs in a similar manner via internal redox processes. This phenomenon in $\text{Ag}_{10}\text{Te}_4\text{Br}_3$ also allows the delocalization of electrons along the equidistant Te chain and the temporary generation of extra conduction electrons in higher band states, resulting in an upward shift of the Fermi level, and consequently causing the observed pn-switching after the phase transition temperature of 390 K. In the $\text{Ag}_{10}\text{Te}_4\text{Br}_3$ high-temperature α -polymorph, the mobility within the Te-strands becomes too high to enable constructive delocalization of electrons and therefore the system switches back to p-type conduction.^[1]

In $\text{Ag}_{18}\text{Cu}_3\text{Te}_{11}\text{Cl}_3$ a partial 2D CDW occurs. According to our single crystal structure determination data, we see a temperature-dependent population of an additional Te site (Te9) at the onset of the β - α phase transition (Figure 1e). The population increases linearly with temperature up to 28.5% at 400 K, which is a clear indicator of a dynamic process instead of a static disorder.

To further investigate this phenomenon, ^{125}Te solid-state MAS NMR experiments were acquired at various temperatures (Figure 4a). As reported previously, the isolated Te^{2-} ions are located in the chemical shift range between 1600 and 1900 ppm (referenced to $(\text{CH}_3)_2\text{Te}$), while resonances for the polytelluride $[\text{Te}_n]^{m-}$ units in the kagomé net occur at chemical shifts ranging from 600 to 900 ppm.^[1,19] These atoms are also characterized by a much larger chemical shift anisotropy (≈ 800 ppm vs 300 ppm for the isolated species) due to the anisotropic environment originated by the Te-Te bond. The resonances between

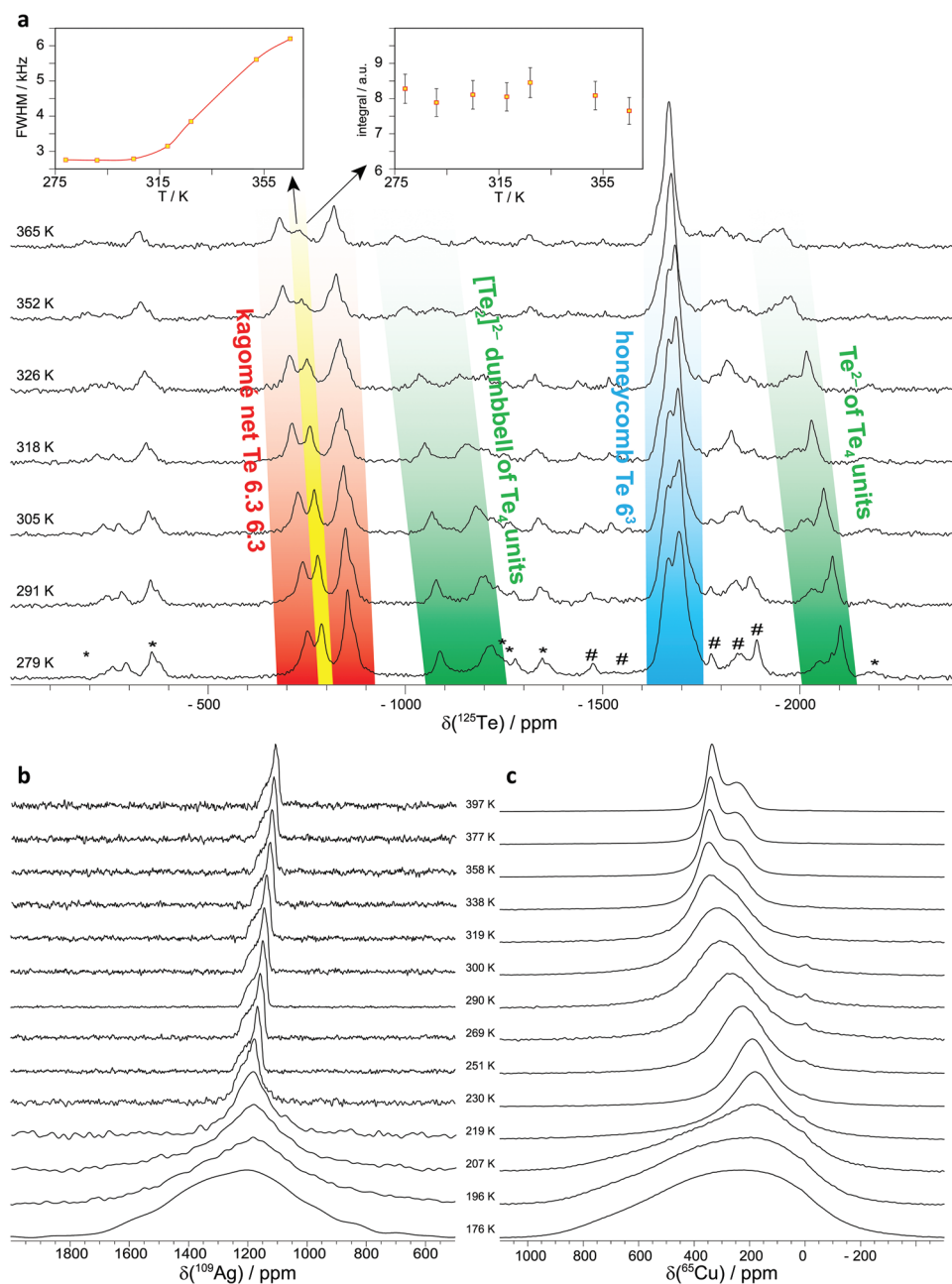


Figure 4. Solid-state NMR spectra of $\text{Ag}_{18}\text{Cu}_3\text{Te}_{11}\text{Cl}_3$ at different temperatures. a) ^{125}Te MAS spectra with color-coded assignment of the characteristic Te subunits. The resonance where coalescence occurs is marked in yellow. The corresponding typical trends for the full width at half maximum (FWHM) and integral for this resonance are given in the insets. The asterisks marks spinning sidebands and the hashtags the impurities. b) ^{109}Ag and c) ^{65}Cu static spectra.

1000 and 1200 ppm as well as the ones between 1900 and 2100 ppm could be assigned to the atoms in Te_4 units, the former corresponding to the $[\text{Te}_2]^{2-}$ dumbbells and the latter to the Te^{2-} of the Te_4 units. Except for the isolated Te^{2-} within the honeycomb layer (1600 to 1800 ppm), all the other ^{125}Te resonances shift downfield significantly with increasing temperature (Figure 4a; Figure S5a, Supporting Information). Within the group of resonances assigned to the kagome net (700 to 900 ppm), the Te atoms drifting the most are the ones at 750 and 790 ppm. In addition, the amplitude of the change

with temperature for the resonance at 790 ppm is particularly striking. While constant below 315 K, its full width at half maximum (FWHM), almost doubles while retaining the overall integral up to 365 K. This behavior is characteristic of the onset of a coalescence phenomenon under MAS conditions.^[20] For a ^{125}Te enriched sample, we observed that the magnitude of the chemical shift anisotropy (CSA) for the same resonance (see Figure S5b, Supporting Information) decreases within the same temperature range, supporting the hypothesis of coalescence. This phenomenon substantiates the onset of dynamic

disorder of the Te atoms within the kagomé net with correlation times on the order of tens of kHz. The disorder corresponds to a chemical exchange between isolated Te^{2-} atoms and $[\text{Te}_2]^{2-}$ dumbbells as suggested by the diffraction data (Figure 1e). As the onset temperature for the dynamic exchange coincides with the initiation of the pnp-switch, both effects are likely linked.

Temperature-dependent XRD and ^{109}Ag and ^{65}Cu solid-state NMR data suggest that the pnp-switch is also connected to changes in the dynamic disorder of the d^{10} ion substructure. The first phase transition observed at 216(3) K is accompanied by a pronounced narrowing of the ^{109}Ag and ^{65}Cu resonances (Figure 4b,c). Thus, above 220 K, both cations exhibit fast motion. The remaining narrow shape for the ^{109}Ag NMR spectra, typical for an almost axially symmetric chemical shift anisotropy, is in line with a restriction of the ion mobility in two dimensions parallel to the (001) layer.^[21] Diffraction data suggest that silver and copper are mixed within these layers. Nevertheless, the presence of two resonances at 1160 and 1164 ppm in the ^{109}Ag MAS NMR spectrum, at chemical shifts comparable to similar compounds, suggests two slightly different environments in the cation layers.^[1]

In contrast to the lineshape of the ^{109}Ag NMR spectra, which is temperature-independent above 270 K, the lineshape of the ^{65}Cu NMR signal in the temperature range of the pnp-switch is temperature-dependent and even develops an anisotropic shape (quadrupolar and chemical shift interaction) toward higher temperatures. This effect is most likely caused by the attraction of the silver and copper ions right after the β - α phase transition, as also indicated by the drop in bond lengths between the d^{10} ions observed in temperature-dependent single crystal structure determinations at 270, 330, 350, and 400 K (Figure 3c). Usually, bond lengths tend to extend upon temperature increase; instead, we see a significant decrease upon heating. This effect may tune the Seebeck coefficient as already shown for $\text{Ag}_5\text{Te}_2\text{Cl}$, a system in which d^{10} - d^{10} interactions were identified as the only source for thermopower modulations.^[22] The occurrence of lineshape changes only in the ^{65}Cu resonance suggests a drastic additional change in the Cu mobility around the room temperature β - α phase transition and the consequently stronger d^{10} - d^{10} interactions in the copper sub-ensemble. As discussed earlier on, this feature should also contribute to the modulation of the DOS close to the Fermi level. The sum of both discussed aspects causes the enormous Seebeck coefficient drop, with an unprecedented intensity of $4,500 \text{ mV K}^{-1}$.

2.5. The Position-Independent, Switchable One-Component Diode

The most intriguing property of $\text{Ag}_{18}\text{Cu}_3\text{Te}_{11}\text{Cl}_3$ is the pnp-switch at room temperature. It may allow the generation of diodes and transistors by a simple change of temperature. In order to verify the diode behavior of $\text{Ag}_{18}\text{Cu}_3\text{Te}_{11}\text{Cl}_3$, we investigated the system at two different temperature conditions and setups. A crystal was mounted onto gold pads with metallic indium so that both ends of the sample are contacted (see Figure 5a,b). The first setup was chosen so that the system operates in the β - $\text{Ag}_{18}\text{Cu}_3\text{Te}_{11}\text{Cl}_3$ phase, slightly below

room temperature. The second setup includes a temperature gradient to bring the system into the pn-transition regime, already in the α - $\text{Ag}_{18}\text{Cu}_3\text{Te}_{11}\text{Cl}_3$ phase. Here we used a 295 to 308 K gradient where the hot side is supposedly n- and the cold side p-conducting.

At 283 K we find a linear U/I curve upon polarization between $\pm 1.5 \text{ V}$ (Figure 5c). The absence of a Schottky diode behavior indicates that the indium contact is ohmic. After unilaterally increasing the temperature, we were able to apply a temperature gradient of 308 to 295 K to the crystal. Now, the U/I curve is significantly different. The hot side should transition to the electron-conducting n-phase while, at the opposite end, holes remain as majority carriers, effectively creating a pn-junction across the semiconductor. Indeed, a rectifying behavior can be seen in the U/I curves measured under a temperature gradient, with a forward current over 10 times larger than the reverse current at $\pm 1.0 \text{ V}$, as can be seen in Figure 5c. A junction potential of 0.3 V is determined for the transitory diode. Upon cooling back to 283 K, the system transitions to its starting configuration (the β -phase), and measurements yield the same linear U/I curve as before the application of the gradient. This reversibility clearly rules out the formation of additional semiconducting phases between the indium solder and $\text{Ag}_{18}\text{Cu}_3\text{Te}_{11}\text{Cl}_3$ during our measurements upon polarization or temperature treatment. To further substantiate this assumption, we used a different solder material to contact $\text{Ag}_{18}\text{Cu}_3\text{Te}_{11}\text{Cl}_3$. Using lead/tin solder we find the same behavior and diode formation as in the case of the indium solder (Figure S6a, Supporting Information).

If U/I measurements are performed isothermally (without an applied, defined temperature gradient) the material behaves ohmically even in the pn-transition range. This observation rules out the formation of a Schottky diode at higher temperatures (299 to 331 K, see Figure 5e). Furthermore, the curves also indicate the absence of effects caused by polarization and mass transport due to the mobile Ag and Cu ions.

These findings substantiate the creation of a thermally-induced single-material pn-junction. Before we step into the discussion, the type of junction that is formed here needs to be addressed and defined. A heterojunction is generated by contacting two dissimilar materials where one is a p- and the other an n-type semiconductor, as is the case of GaAs/GaAlAs lasers. On the other hand, a homojunction is generated by different doping characters in a given material without affecting its structure, such as an n-Si/p-Si junction. As shown earlier, the defect structure of the studied compound varies during the pn-switch but the symmetry and general structural units remain virtually unchanged. Therefore, according to symmetry considerations, the interface between the two phases could be defined as a homojunction. However, regarding the defined property change, the thermal signature in DSC, and the significant changes in defect and electronic structure, the term heterojunction may also partially explain the electronic situation. Neither of the current terms correctly encompasses the real structure of this novel system. Thus, we define a new type of junction, an ambijunction, to illustrate the ambivalent character in this new material.

The switching time of this single crystal diode (forward-reverse direction) has been assessed via the application of

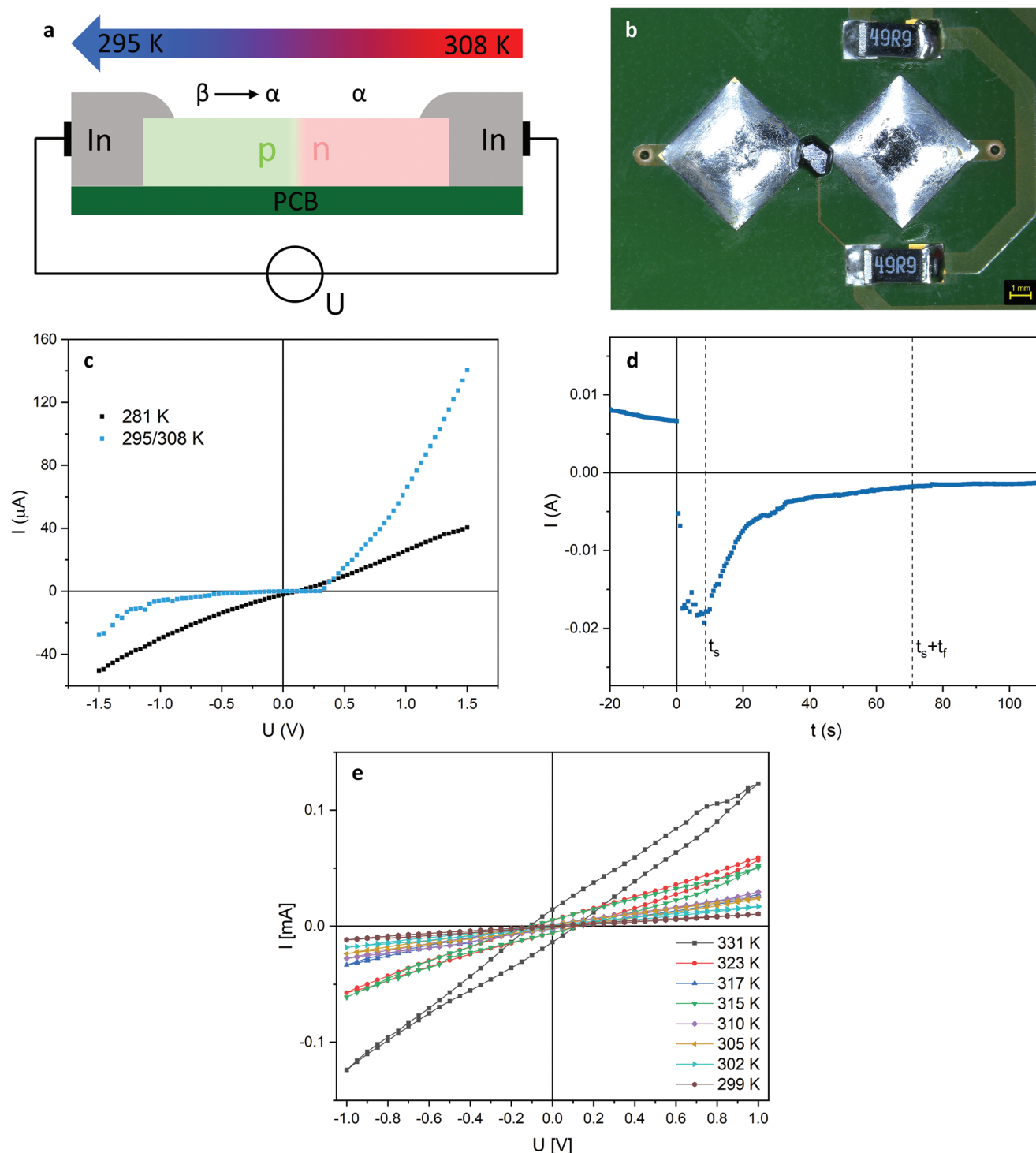


Figure 5. Diode fabrication and U/I characterization. a) Scheme of the measurement set-up. b) Single crystal of $\text{Ag}_{18}\text{Cu}_3\text{Te}_{11}\text{Cl}_3$ mounted on top of Au electrodes and contacted with metallic In. The $49\ \Omega$ resistances used to apply a temperature gradient via resistivity heating can be found next to the right contact. c) U/I plot measured at 281 K within $\beta\text{-Ag}_{18}\text{Cu}_3\text{Te}_{11}\text{Cl}_3$ (black line) and after applying temperature to the system to create a gradient of 13 K between 295(1) and 308(1) K (blue line). d) Switching time of the diode under the same thermal gradient. A 5 V forward was applied, followed by a $-5\ \text{V}$ reverse current at $t = 0$. The errors of the measured values are located within the points. e) To ensure that no Schottky diode is being formed in the applied temperature ranges, we also measured isothermal U/I curves for $\text{Ag}_{18}\text{Cu}_3\text{Te}_{11}\text{Cl}_3$ up to 331 K. When the entire crystal was held at the same temperature, no rectifying character was found. A conductivity increase was seen at higher temperatures as is expected for a semiconductor. The errors of the measured values are located within the points.

a 5 V forward potential for 60 s to induce the build-up of the minority carrier at the quasi-neutral regions surrounding the junction (Figure 5d). Subsequently, the device was turned off via the application of a reverse -5 V potential. The linear removal of the excess minority carrier leads to a steady current that is much larger than the saturation current of the device. The switching time t_s for the removal of the excess carriers in this system was ≈ 8.7 s. After this time, the current decays exponentially toward the saturation limit of the device. The fall time t_f – needed to reach 10% of the initial reverse current – was estimated at 62.4 s.

The initiation of this diode effect is determined in our experimental setup as a sum of the time constants of the several different thermal transport phenomena taking place. Heat must be transferred from the resistance via the metallic contact to the sample. This non-optimized process takes a while, generally a few minutes. This aspect of the measurement setup will be optimized in the future. The full inversion of the p- and n-regions in the given experiment can be realized in minutes in this experimental setup for a mm-sized crystal. This secondary switching process (change of direction besides on-off states) may also be optimized by downscaling of the crystals.

The observed switching is a further indication that the thermal gradient successfully induces the creation of a pn-junction, as this is the only likely source for the shape of the current decay displayed by the device. Furthermore, the long times associated with t_s and t_f again rule out the creation of a Schottky diode instead of a true pn-junction, as the operation in the first is associated with majority carriers, which display higher mobilities, leading to very fast switching. These measurements unambiguously illustrate the creation of the first-ever single-material functional pn-junction, without the need for nanostructuring or advanced architectures, as the diode behavior is an intrinsic property of the bulk material itself. In the future, we intend to downscale the device and material size from the mm to the μ meter regime. This will speed up temperature dissipation and operating speed drastically.

The question arises if the pn-junction formation is unique for $\text{Ag}_{18}\text{Cu}_3\text{Te}_{11}\text{Cl}_3$. We selected another pnp-switching material, AgCuS , with a higher switching temperature of 364 K to verify if a diode can also be formed for this material. This is indeed the case: in a temperature gradient of 333(1) to 365(1) K, this material also forms a diode at room temperature while its behavior is ohmic. The measurement can be found in Figure S6b (Supporting Information).

2.6. Impact on Electronics and Energy-Related Science

With the simple and defined creation of a working pn-junction and the consequent diode formation, the process in general, and the compound, in particular, have huge application potential in energy-related science. A single-junction solar cell might be realizable, wherein the pn-junction is generated in a certain temperature gradient directly on the device. Such pn-ambijunction formation and the intrinsic charge separation might be a source for effective water splitting purposes, either stand-alone or as a tandem photoelectrochemical (PEC)-thermoelectrical (TE) device.^[23] One step further from the position-independent

or position-variable diode is the generation of a position-independent bipolar junction transistor (BJT) with a larger gradient also encompassing the other p-conducting temperature region of $\text{Ag}_{18}\text{Cu}_3\text{Te}_{11}\text{Cl}_3$. Similarly, a field effect transistor (FET) may be constructed with the application of heat at the source and drain regions, with the channel below the transition temperature. With the appropriate design, a single device could work as a resistance, a diode, or a transistor, depending on the temperature gradient and the position of the connections. A variation of the FET could also be realized where the role of the regular gate is substituted by a thermal gate. The inversion layer at the interface between the channel and gate would be created and controlled by temperature instead of local polarization. Such thermal effect transistor (TET) could also be exploited in the recycling of thermal waste generated in the normal operation of FETs, leading to the creation of even more processing units. Due to the possibility of generating a diode or transistor at the place where it is occasionally needed, a new IT architecture might be possible, not demanding the preparation of different p- and n-doped regions to form rectifying devices, or a pre-adjustment of the architecture to manipulate the charge carrier density by gate biasing.^[24–26] Recently AgI was used to program WSe_2 devices that can be reversibly transformed into transistors with reconfigurable carrier types. Homojunctions with switchable polarities were generated using superionic silver iodide as a medium to polarize WSe_2 by van der Waals or dispersive interactions via an ion gradient in AgI. Unfortunately, such a device requires the deposition and alignment of several materials and a high-temperature treatment of 147 °C to reverse the polarization by initiating silver ion conductivity in AgI.^[27] Instead, in the case of $\text{Ag}_{18}\text{Cu}_3\text{Te}_{11}\text{Cl}_3$, only one material needs to be deposited, and external stimuli that are able to increase the temperature by a few Kelvin may be used to address the necessary junction formation. This junction may either be kept present in a stable temperature gradient or canceled by its removal. The observed effect is also intrinsic to the bulk material, without the need for nanostructuring or complex architectures. The temperature range in which the effect occurs is also very convenient. For comparison, Wu, Wang, and collaborators recently reported superconducting heterostructures, so-called field-free Josephson diodes, with rectifying character.^[28] Although impressive, the diode behavior is only observed close to 0 K, hindering the viability of these devices in most practical applications. In our system, the application temperature at ambient conditions is more beneficial and useful.

Another huge field for semiconductors and the utilization of opposite charge carriers is electrocatalysis. Using the described diode formation effect in electrocatalytic reactions can open a wide field of applications. Recently, it has been shown that ultra-thin semiconductors can be used as effective electrocatalysts, although they suffer from low intrinsic carrier concentrations.^[29]

3. Conclusion

In this work, the polymorphic compound $\text{Ag}_{18}\text{Cu}_3\text{Te}_{11}\text{Cl}_3$, a newly discovered addition to the class of coinage metal chalcogenide halides, was successfully synthesized. The β - α phase

transition takes place close to room temperature, and at the same time enables reversible switching from an n- to p-type semiconductor and back. For the first time, this allows the fabrication of a commercially viable, easily accessible single-material diode. In our case, we are able to generate opposite charge carriers and n- or p-type semiconductor regions in bulk materials by a simple temperature gradient and at positions where opposite charge carriers are needed. With an appropriate setup, electrocatalysis can be initiated where a suitable temperature gradient is provided on one side and the reaction takes place on the opposite side of a thin-layer device. Future optimization in temperature control should enable the realization of a single-material transistor, potentially leading to novel applications and devices. The newly described phenomenon of the temperature gradient-induced, position-independent, and switchable pn-junction should lead to the observation of emergent anomalous effects. Thus, the nascent field of single-material electronic devices begins.

4. Experimental Section

Synthesis: $\text{Ag}_{18}\text{Cu}_3\text{Te}_{11}\text{Cl}_3$ was prepared from a stoichiometric mixture of silver (Chempur, 99.999%), copper(I) chloride (Alfa Aesar, 97%), and tellurium (Chempur, 99.999%) on a gram scale. The starting materials were sealed into evacuated silica glass ampules, heated to 1320(1) K, held at this temperature for 3 h, and quenched in an ice bath. The crude product was finely ground and annealed for 7 days at 660(1) K followed by slow cooling to room temperature. This synthesis route led to phase pure black crystalline products.

XRD Experiments: Powder XRD data were collected with a Stoe STADI P powder diffractometer equipped with a position-sensitive Mythen 1K detector using $\text{Cu } K_{\alpha 1}$ radiation ($\lambda = 1.54060 \text{ \AA}$, curved Ge(111) monochromator). Data analysis was performed using the STOE WinXpow software package.^[30] Single crystal XRD measurements were performed at 200(1), 270(1), 330(1), 350(1), and 400(1) K on a Stoe STADIVARI diffractometer fitted with $\text{Mo } K_{\alpha 1/2}$ radiation ($\lambda = 0.71073 \text{ \AA}$), a Dectris hybrid pixel detector and an Oxford Cryostream plus system. Data reduction was performed using the Stoe X-AREA package.^[31] Structures were solved using the charge-flipping algorithm implemented in the Jana 2006 program suite.^[32,33] Numerical absorption correction was performed based on an optimized crystal shape derived from symmetry-equivalent reflections. Space groups were determined by careful analysis of Laue symmetry and extinction conditions. While the structure of $\gamma\text{-Ag}_{18}\text{Cu}_3\text{Te}_{11}\text{Cl}_3$ (200 K) was still not solved due to severe twinning, the data for $\beta\text{-Ag}_{18}\text{Cu}_3\text{Te}_{11}\text{Cl}_3$ (270 K) and $\alpha\text{-Ag}_{18}\text{Cu}_3\text{Te}_{11}\text{Cl}_3$ (at 330 K, 350 K, and 400 K) were deposited with the Cambridge Structure Database (<https://www.ccdc.cam.ac.uk/structures/>): CSD 2201919 (270 K); CSD 2201916 (330 K); CSD 2201917 (350 K); CSD 2201918 (400 K)

Thermal Analysis: Phase pure crystalline material was transferred to an aluminum crucible and differential scanning calorimetry (DSC) was performed with a Netzsch DSC 200 F3 Maia device. The measurement was conducted under N_2 atmosphere in the temperature range of 143 to 523 K with a heating-cooling rate of 10 K min^{-1} . The thermal effects were derived from the onset temperatures. Data analysis was performed using the Netzsch Proteus Thermal Analysis software package.^[34]

Measurements of Electrical Conductivity and Seebeck Coefficient: Finely ground phase pure $\text{Ag}_{18}\text{Cu}_3\text{Te}_{11}\text{Cl}_3$ was pressed under vacuum to a pellet of 13 mm diameter and 1.23 mm thickness reaching 90% of the crystallographic density. The Seebeck coefficient and the electric conductivity were measured simultaneously directly at Netzsch with a Netzsch SBA 458 Nemesis under a continuous helium flow. The electrical conductivity was determined using the four-point probe.

The technical measurement error was $\pm 7\%$ for the Seebeck coefficient and $\pm 5\%$ for the electrical conductivity. Data analysis was performed with the Netzsch SBA-measurement software package.^[35]

Thermal Diffusivity Measurements: Thermal diffusivity was measured by laser flash analysis (LFA) on an LFA 467 HyperFlash setup (Selb, Germany) in an atmosphere of pure nitrogen. The ignition voltage of the flash lamp was set to 250 V and the pulse width was 600 μs . The hot-pressed pellet with a diameter of 10 mm and a thickness of 2.0 mm was spray-coated with a graphite layer to enhance emissivity. An improved version of the model proposed by Cape and Lehman was employed to calculate the thermal diffusivity.^[36,37] Data analysis was performed using the Netzsch Proteus Thermal Analysis software package.^[38] Thermal conductivity was obtained from thermal diffusivity measurements using the following equation:

$$\kappa = \alpha \times \rho \times c_p \quad (2)$$

with α = thermal diffusivity of the material, ρ = density of the material, c_p = specific heat capacity, and κ = thermal conductivity. The Dulong-Petit rule was applied to approximate the specific molar heat capacity of the material in the given temperature range of 260 to 380 K.

Photoluminescence Spectroscopy: Photoluminescence spectra were recorded at room temperature using a WITec alpha300R equipped with an Olympus LMPlanFL N $50 \times / 0.5$ objective. The pressed pellet was irradiated with a 532 nm laser with 0.15 mW and a 300 g mm^{-1} grating. Each measurement was integrated for 30 s with 3 accumulations.

Solid-State NMR: In order to reduce measuring time for solid-state ^{125}Te NMR spectroscopy, $\text{Ag}_{18}\text{Cu}_3\text{Te}_{11}\text{Cl}_3$ using enriched ^{125}Te (STB Isotope Germany, ^{125}Te content 94%) was prepared. The crude ^{125}Te powder was purified in a hydrogen stream at 673 K to remove traces of tellurium oxide. The same synthesis protocol reported earlier on was followed, taking the different molecular weights of the enriched ^{125}Te into account.

^{125}Te MAS NMR experiments were carried out on a Bruker 400 Avance III HD spectrometer ($B_0 = 9.4 \text{ T}$) working at a ^{125}Te frequency of 126.1 MHz. The samples were confined in the middle third of the rotor to minimize temperature gradients and were spun at 62.5 kHz using a Bruker double resonance 1.3 mm MAS probe. The single-pulse MAS spectra were obtained after a 90° pulse of 0.95 μs with recycling delays of 0.5 – 4.0 s. ^{125}Te was referenced to $(\text{CH}_3)_2\text{Te}$, using $\text{Te}(\text{OH})_2$ as a secondary reference. The chemical shift anisotropies were extracted from the profiles of the MAS spectra using TopSpin 3.6.3. ^{109}Ag and ^{65}Cu were acquired on a Bruker 600 Avance III HD spectrometer ($B_0 = 14.1 \text{ T}$) working at 28.0 and 170.5 MHz for ^{109}Ag and ^{65}Cu , respectively. For ^{109}Ag and ^{65}Cu MAS experiments, the samples were spun at 40.0 and 62.5 kHz, using a Bruker 1.3 mm double resonance probe. ^{109}Ag single-pulse experiment was acquired after a 90° pulse of 5.5 μs and a recycle delay of 2.0 s. ^{65}Cu MAS spectra were obtained using a rotor-synchronized spin-echo experiment with a 90° pulse of 1.2 μs and a recycle delay of 10 ms. ^{109}Ag and ^{65}Cu static experiments were acquired with a triple-resonance wideline probe using a spin echo experiment with 90° pulses of 7.5 and 2.1 μs , respectively, and echo delays of 40 and 10 μs , respectively. Recycle delays ranged from 5 to 300 s for ^{109}Ag and from 5 to 20 ms for ^{65}Cu . ^{109}Ag was referenced to AgNO_3 solution and ^{65}Cu to powdered CuCl . All temperatures were calibrated using $\text{Pb}(\text{NO}_3)_2$.

Diode Measurements: A single crystal was mounted onto a printed circuit board (PCB) with the aid of indium (Alfa Aesar, 99.999%) or tin/lead (Stannol, composition Sn:Pb:Cu = 60:39:1 wt.%) contacts (Figure 5a,b). To apply a temperature gradient to the crystal, two 49 Ω resistances were placed next to one of the In contacts to create localized heating on one side of the mounted crystal and thus induce a temperature gradient across the device.

$\beta\text{-Ag}_{18}\text{Cu}_3\text{Te}_{11}\text{Cl}_3$: Measurements were conducted inside a refrigerator set to 281(1) K, to start the experiment safely within the $\beta\text{-Ag}_{18}\text{Cu}_3\text{Te}_{11}\text{Cl}_3$ phase. This temperature was chosen to be also in a certain thermal distance to the $\beta\text{-}\alpha$ phase transition. A temperature gradient of 295 to 308 K was applied to the sample by using an external current passing through the 49 Ω resistances. The external current was supplied by a QJE PS6005 switching power supply.

AgCuS: For AgCuS the isothermic temperature point was room temperature (298(1) K) and the temperature gradient of 333(1) to 365(1) K was generated using the aforementioned procedure.

Temperature was controlled by an external thermocouple (RSpro Thermometer device, Ni/Cr/Ni type thermocouple, accuracy ± 1 K) at the contacts during the measurements. Conductivity measurements were performed using a Keithley 2450 SourceMeter. Voltage errors are $\pm 0.015\%$ and current errors are $\pm 0.03\%$. This digital multimeter was operated with the aid of KickStart I - V Characterizer App. Measurements were performed at a scanning speed of 0.06 V s^{-1} . Data analysis was performed with the Keithley Kickstart I - V Characterizer App software package.^[39]

Semi-Quantitative Phase Analyses: Energy dispersive X-ray spectroscopy (EDX) was performed using a JOEL JCM-6000 NeoScop with an integrated JOEL JED-2200 EDX unit. The acceleration voltage was set to 15 kV. The EDX results were averaged from at least three different points, selected randomly on the crystal surface. The samples were fixed on a graphite holder with a conductive adhesive polymer tape from PLANO GmbH. More details in the Supporting Information section.

Bulk Modulus Determination: Pressure-dependent determinations of the $\text{Ag}_{18}\text{Cu}_3\text{Te}_{11}\text{Cl}_3$ cell parameters were conducted at the I15 beamline at Diamond light source, Ditcot, Great Britain. The applied X-ray wavelength was set to $\lambda = 0.4246 \text{ \AA}$. A LeToullec-style membrane diamond anvil cell was used to apply pressure in the range from ambient to 8 GPa. The diamond anvils had 300-micron culets and the gasket material was rhenium. Ruby was used as the internal pressure calibration standard and daphne oil was used as a pressure transmitting medium.^[40] Ruby fluorescence was measured with a laser system, and the diffractometer raw data were transferred into a processable format with DAWN.^[41] The pressure of each data point was measured by collecting ruby spectra before and after the XRD measurement. A pressure equilibration time of 10 min was applied prior to the pressure and XRD data acquisition. A peak fitting routine with Pseudo-Voigt profiles embedded in the FITYK software suite was used to achieve exact pressure data.^[42] XRD data were refined using the JANA 2006 program suite.^[33] The determined cell parameters at ambient pressure were used as starting model. A LeBail fitting routine, a Legendre polynomial function with 18 background parameters, and a Pseudo-Voigt profile were used to refine the XRD data profile. Cell parameters were determined for each data point with an unrestricted refinement of the cell parameters. The space group $P6_3/mcm$ determined at ambient pressure was applied in the entire pressure range. No change in symmetry in this pressure regime was detected. For each new cell refinement, the previous cell parameters were used as a starting model. Data after the cell parameter refinements are summarized in Table S18 (Supporting Information).

The acquired pressure data was fitted with a Birch–Murnaghan equation of state (EoS):^[15]

$$P = \frac{3}{2}K_0 \left[\left(\frac{V}{V_0} \right)^{\frac{7}{3}} - \left(\frac{V}{V_0} \right)^{\frac{5}{3}} \right] \left\{ 1 + \frac{3}{4}(K' - 4) \left[\left(\frac{V}{V_0} \right)^{\frac{2}{3}} - 1 \right] \right\} \quad (3)$$

with P = applied pressure in GPa, K_0 = bulk modulus in GPa, K' = pressure derivate of bulk modulus, V_0 = cell volume at ambient pressure in \AA^3 , and V = cell volume at a given pressure P in \AA^3 to determine the bulk modulus K_0 . The software EoSFit7c was used for the fitting.^[43]

Using the cell volume at ambient pressure of $V_0 = 4898(4) \text{ \AA}^3$, which was determined by single crystal structure determination experiments, values of $K_0 = 28.2(11) \text{ GPa}$ and $K' = 12.7(8)$ from a 3rd-order EOS fit was calculated. In order to verify the significance of the fit the Eulerian strain f :

$$f = \frac{1}{2} \left[\left(\frac{V}{V_0} \right)^{\frac{2}{3}} - 1 \right] \quad (4)$$

was plotted against the normalized pressure F :

$$F = \frac{P}{3f \times (1 + 2f)^{\frac{5}{2}}} \quad (5)$$

which is shown in Figure 2f. According to the F - f plot values of $K_0 = 29.3 \text{ GPa}$ and $K' = 12.1$ were found. The F - f plot substantiates the significance of K' in the EOS which significantly deviates from a 2nd-order representation of $K' = 4$. More details are in the Supporting Information section in chapter 3.

[CCDC 2201916/2201917/2201918 /2201919 contains the supplementary crystallographic data for this paper. These data can be obtained free of charge from The Cambridge Crystallographic Data Centre via www.ccdc.cam.ac.uk/data_request/cif.]

Supporting Information

Supporting Information is available from the Wiley Online Library or from the author.

Acknowledgements

A.V., A.R., and P.D. contributed equally to this work. The authors thank Dr. Ekkehard Post from Netzsch, Selb, Germany for the temperature-dependent measurement of the Seebeck coefficient, and the electric conductivity on their in-house equipment and Sylvio Richter from InfraTec, Dresden, Germany for high-resolution IR camera measurements. The conduction of EDX measurements by Katia Rodewald at the Wacker Chair of Macromolecular Chemistry, TUM, is gratefully acknowledged. A.V., A.R., P.D., and R.S. thank the TUM Graduate School for their support. J.V. thanks for a stipend funded by the TUM Talent Factory program. Funded by the Deutsche Forschungsgemeinschaft (DFG, German Research Foundation) under Germany's Excellence Strategy EXC 2089/1-390776260. The authors also thank Diamond Light Source, UK, for the provision of beamtime at beamline I15 under proposal number CY30094.

Open access funding enabled and organized by Projekt DEAL.

Conflict of Interest

The authors declare no conflict of interest.

Data Availability Statement

The data that support the findings of this study are available from the corresponding author upon reasonable request.

Keywords

coinage metals, diodes, ion conductors, pnp-switches, polymorphism

Received: September 21, 2022

Revised: October 11, 2022

Published online: November 24, 2022

[1] T. Nilges, S. Lange, M. Bawohl, J. M. Deckwart, M. Janssen, H.-D. Wiemhöfer, R. Decourt, B. Chevalier, J. Vannahme, H. Eckert, R. Wehrich, *Nat. Mater.* **2009**, *8*, 101.

[2] S. Lange, T. Nilges, *Chem. Mater.* **2006**, *18*, 2538.

- [3] S. Lange, M. Bawohl, D. Wilmer, H.-W. Meyer, H.-D. Wiemhöfer, T. Nilges, *Chem. Mater.* **2007**, *19*, 1401.
- [4] C. Xiao, X. Qin, J. Zhang, R. An, J. Xu, K. Li, B. Cao, J. Yang, B. Ye, Y. Xie, *J. Am. Chem. Soc.* **2012**, *134*, 18460.
- [5] S. N. Guin, J. Pan, A. Bhowmik, D. Sanyal, U. V. Waghmare, K. Biswas, *J. Am. Chem. Soc.* **2014**, *136*, 12712.
- [6] Y. Shi, A. Assoud, C. R. Sankar, H. Kleinke, *Chem. Mater.* **2017**, *29*, 9565.
- [7] J. Peters, O. Conrad, B. Bremer, B. Krebs, *Z. Anorg. Allg. Chem.* **1996**, *622*, 1823.
- [8] L. Pauling, *The Nature of the Chemical Bond*, 3rd ed., Cornell University Press, Ithaca, NY **1960**.
- [9] A. Vogel, T. Nilges, *Inorg. Chem.* **2021**, *60*, 15233.
- [10] A. Vogel, T. Miller, C. Hoch, M. Jakob, O. Oeckler, T. Nilges, *Inorg. Chem.* **2019**, *58*, 6222.
- [11] W. Shockley, H. J. Queisser, *J. Appl. Phys.* **1961**, *32*, 510.
- [12] D. W. James, *J. Mater. Sci.* **1968**, *3*, 540.
- [13] X. Zhang, M. Fujii, *Polym. Eng. Sci.* **2003**, *43*, 1755.
- [14] T. Bernges, R. Hanus, B. Wankmiller, K. Imasato, S. Lin, M. Ghidui, M. Gerlitz, M. Peterlechner, S. Graham, G. Hautier, Y. Pei, M. R. Hansen, G. Wilde, G. J. Snyder, J. George, M. T. Agne, W. G. Zeier, *Adv. Energy Mater.* **2022**, *12*, 2200717.
- [15] F. Birch, *Phys. Rev.* **1947**, *71*, 809.
- [16] S. Hasan, P. Adhikari, K. Baral, W.-Y. Ching, *AIP Adv.* **2020**, *10*, 75216.
- [17] Q. Yang, J. Lee, B. Feng, Y. Ikuhara, G. Kim, H. J. Cho, H. Jeon, H. Ohta, *ACS Appl. Electron. Mater.* **2020**, *2*, 2250.
- [18] M. Cutler, N. F. Mott, *Phys. Rev.* **1969**, *181*, 1336.
- [19] K. J. D. MacKenzie, M. E. Smith, *Multinuclear Solid-State Nuclear Magnetic Resonance of Inorganic Materials*, Pergamon, Oxford, UK **2002**.
- [20] A. D. Bain, *Prog. Nucl. Magn. Reson. Spectrosc.* **2003**, *43*, 63.
- [21] C. D. Keenan, M. M. Herling, R. Siegel, N. Petzold, C. R. Bowers, E. A. Rössler, J. Breu, J. Senker, *Langmuir* **2013**, *29*, 643.
- [22] T. Nilges, O. Ostera, M. Bawohl, J.-L. Bobet, B. Chevalier, R. Decourt, R. Wehrich, *Chem. Mater.* **2010**, *22*, 2946.
- [23] J.-Y. Jung, D. Woong Kim, D.-H. Kim, T. Joo Park, R. B. Wehrspohn, J.-H. Lee, *Sci. Rep.* **2019**, *9*, 9132.
- [24] D. Li, M. Chen, Z. Sun, P. Yu, Z. Liu, P. M. Ajayan, Z. Zhang, *Nat. Nanotechnol.* **2017**, *12*, 901.
- [25] R. Cheng, F. Wang, L. Yin, Z. Wang, Y. Wen, T. A. Shifa, J. He, *Nat. Electron.* **2018**, *1*, 356.
- [26] J.-W. Chen, S.-T. Lo, S.-C. Ho, S.-S. Wong, T.-H.-Y. Vu, X.-Q. Zhang, Y.-D. Liu, Y.-Y. Chiou, Y.-X. Chen, J.-C. Yang, Y.-C. Chen, Y.-H. Chu, Y.-H. Lee, C.-J. Chung, T.-M. Chen, C.-H. Chen, C.-L. Wu, *Nat. Commun.* **2018**, *9*, 3143.
- [27] S.-J. Lee, Z. Lin, J. Huang, C. S. Choi, P. Chen, Y. Liu, J. Guo, C. Jia, Y. Wang, L. Wang, Q. Liao, I. Shakir, X. Duan, B. Dunn, Y. Zhang, Y. Huang, X. Duan, *Nat. Electron.* **2020**, *3*, 630.
- [28] H. Wu, Y. Wang, Y. Xu, P. K. Sivakumar, C. Pasco, U. Filippozzi, S. S. P. Parkin, Y.-J. Zeng, T. McQueen, M. N. Ali, *Nature* **2022**, *604*, 653.
- [29] Y. He, Q. He, L. Wang, C. Zhu, P. Golani, A. D. Handoko, X. Yu, C. Gao, M. Ding, X. Wang, F. Liu, Q. Zeng, P. Yu, S. Guo, B. I. Yakobson, L. Wang, Z. W. Seh, Z. Zhang, M. Wu, Q. J. Wang, H. Zhang, Z. Liu, *Nat. Mater.* **2019**, *18*, 1098.
- [30] Stoe, *WinXPOW*, Stoe & Cie GmbH, Darmstadt, Germany, **2011**.
- [31] Stoe, *X-AREA*, Stoe & Cie GmbH, Darmstadt, Germany, **2015**.
- [32] L. Palatinus, G. Chapuis, *J. Appl. Crystallogr.* **2007**, *40*, 786.
- [33] V. Petricek, M. Dušek, L. Palatinus, *The Crystallographic Computing System*, Institute of Physics, Praha, Czech Republic **2006**.
- [34] Netzsch GmbH, *Proteus Thermal Analysis*, Netzsch Gerätebau GmbH, Selb, Germany **2010**.
- [35] Netzsch GmbH, *NetzschSBA-Measurement*, Netzsch Gerätebau GmbH, Selb, Germany **2016**.
- [36] J. A. Cape, G. W. Lehman, *J. Appl. Phys.* **1963**, *34*, 1909.
- [37] J. Blumm, J. Opfermann, *High Temp.-High Pressures* **2002**, *34*, 515.
- [38] Netzsch GmbH, *Proteus LFA Analysis*, Netzsch Gerätebau GmbH, Selb, Germany **2021**.
- [39] Keithley Instruments LLC, *Kickstart I-V Characterizer App*, Tektronix Inc., Beaverton, United States, **2021**.
- [40] K. Syassen, *High Pressure Res.* **2008**, *28*, 75.
- [41] J. Filik, A. W. Ashton, P. C. Y. Chang, P. A. Chater, S. J. Day, M. Drakopoulos, M. W. Gerring, M. L. Hart, O. V. Magdysyuk, S. Michalik, A. Smith, C. C. Tang, N. J. Terrill, M. T. Wharmby, H. Wilhelm, *J. Appl. Crystallogr.* **2017**, *50*, 959.
- [42] M. Wojdyr, *J. Appl. Crystallogr.* **2010**, *43*, 1126.
- [43] R. J. Ross, M. Alvaro, J. Gonzalez-Platas, *Z. Kristallogr. Cryst. Mater.* **2014**, *229*, 405.

Supporting Information

A switchable one-compound diode

Anna Vogel, Alfred Rabenbauer, Philipp Deng, Ruben Steib, Thorben Böger, Wolfgang G. Zeier, Renée Siegel, Jürgen Senker, Dominik Daisenberger, Katharina Nisi, Alexander W. Holleitner, Janio Venturini, Tom Nilges**

Structure chemistry of coinage metal (poly)chalcogenide

The structures of coinage metal (poly)chalcogenides are complex and hard to describe with standard procedures like a) close packing arrangement of atoms with void filling procedures, or b) the definition of cluster or other complex subunits and their connection or distribution, or other recent and frequently used procedures. The cations in coinage metal (poly)chalcogenides show a dynamic disorder in general due to the intrinsic high cation mobility of d^{10} ions. Polymorphism is a general property caused by order-disorder phenomena of the cations. Anions are often ordered except for covalently-bonded substructures which also tend to show ion dynamics under certain circumstances. We describe the complexity of the structure by using a topologic description of the anion substructure by the definition of anion layers of isolated anions without any homoatomic bonding interactions (isolated ions), and the illustration of partially and fully covalently bonded polyanion subunits in the structure. In the following we will discuss the ‘evolution’ of the title compound $\text{Ag}_{18}\text{Cu}_3\text{Te}_{11}\text{Cl}_3$ by successive substitution of Cu by Ag in $\text{Cu}_{20}\text{Te}_{11}\text{Cl}_3$.

Cu₂₀Te₁₁Cl₃, the Ag_xCu_{21-x}Te₁₁Cl₃ substitution series, and the end member Ag₁₈Cu₃Te₁₁Cl₃

The title compound has been discovered finally after a long-lasting evolution and optimization process from more simple systems. To understand the idea behind our title compound one has to start with an also rather complex compound, Cu₂₀Te₁₁Cl₃. Similar to the other coinage metal (poly)chalcogenide halides, the anionic substructure of recently published Cu₂₀Te₁₁Cl₃ can be topologically described by stacked anion nets that are interpenetrated by polyanionic Te₄ units (Te···Te⁻ Te···Te).^[1] These nets were defined by connecting neighboring anions of the same type on certain layers in the unit cell. The distances of the anions within the nets are generally above two times the van-der-Waals radii according to Pauling and the connecting lines do not represent chemical bonds but are only drawn based on topological grounds. In the case of Cu₂₀Te₁₁Cl₃ every second anion net is a Te 6³ honeycomb net and every second net between the Te 6³ nets is a Cl 6.3.6.3 kagomé net. Both net types have already been observed in Ag₁₀Te₄Br₃ and Cu_{9,1}Te₄Cl₃ where they are stacked alternately.^[2-4] However, in α -Cu₂₀Te₁₁Cl₃ every second position between two Te 6³ nets is occupied by a disordered Te 6.3.6.3 net. The polyanionic Te₄ units are built by a [Te₂]²⁻ dumbbell and two linearly coordinating Te²⁻ anions and interpenetrate the Te 6³ and Cl 6.3.6.3 nets but are separated by the disordered Te 6.3.6.3 net.^[1] A scheme of the anion sublattice of the crystal structure is shown in **Figure S1c**. A full section of the crystal structure is given in **Figure S3**.

In our previously published study we discussed two models that describe the chemical nature of the disordered Te 6.3.6.3 net: disordered dumbbells and two statistically distributed stützite-type distorted kagomé nets in opposing orientations. For Cu₂₀Te₁₁Cl₃ we strongly favor the statistic distribution of [Te₂]²⁻ dumbbells because the resulting total charge of the anionic substructure [Te₁₁Cl₃]²⁰⁻ composed of ([Te₂]²⁻)_{2.5}(Te²⁻)₆(Cl)₃ is in good accordance

with the refined composition of $\text{Cu}^{20+}[\text{Te}_{11}\text{Cl}_3]^{20-}$ and a dynamic fluctuation within the network would provoke a charge density wave (CDW) that would lead to a defined drop of the Seebeck coefficient, which was not observed.^[1]

In order to release ordering of the disordered Te 6.3.6.3 net by enlargement of the unit cell, Cu was substituted stepwise by Ag in $\text{Cu}_{20}\text{Te}_{11}\text{Cl}_3$. The synthesis led to phase pure products up to an Ag:Cu ratio of 6:1. Higher Ag:Cu ratios led to the formation of $\text{Ag}_5\text{Te}_2\text{Cl}$ as side product.^[5,6] **Figure S1a** denotes powder diffraction pattern of the stepwise substitution of Cu by Ag. Indexing of the main reflections shows a linear increase of the unit cell volume but splitting of some weaker reflections (highlighted in grey in **Figure S1a**) points toward the formation of a super structure.

Single crystal XRD of $\text{Ag}_{18}\text{Cu}_3\text{Te}_{11}\text{Cl}_3$ confirms that assumption. The formation of a ($\sqrt{3} \times \sqrt{3} \times 2$) super structure (in relation to $\alpha\text{-Cu}_{20}\text{Te}_{11}\text{Cl}_3$) is released by the ordering of the disordered Te 6.3.6.3 net (see **Figure S1d**). While in $\text{Cu}_{20}\text{Te}_{11}\text{Cl}_3$ it can be described by statistically distributed $[\text{Te}_2]^{2-}$ dumbbells, in $\text{Ag}_{18}\text{Cu}_3\text{Te}_{11}\text{Cl}_3$ the Te-Te distances are too long for the formation of dumbbells only. The formerly disordered net orders to a distorted Te 6.3.6.3 kagomé net similar to the one found in synthetic stützite.^[7] The transition from $[\text{Te}_2]^{2-}$ dumbbells to dumbbells and non-bonded Te^{2-} ions in the net causes the increase of the total negative charge of the anion substructure from $[\text{Te}_{11}\text{Cl}_3]^{20-}$ in $\text{Cu}_{20}\text{Te}_{11}\text{Cl}_3$ to $[\text{Te}_{11}\text{Cl}_3]^{21-}$ in $\text{Ag}_{18}\text{Cu}_3\text{Te}_{11}\text{Cl}_3$. Hence, the real coinage metal content of the products of the substitution series ranges between $\text{M}_{20}\text{Te}_{11}\text{Cl}_3$ and $\text{M}_{21}\text{Te}_{11}\text{Cl}_3$ with $\text{M} = \text{Ag}, \text{Cu}$ and can be written as $(\text{Ag}_x\text{Cu}_{1-x})_{20+\delta}\text{Te}_{11}\text{Cl}_3$ with $\delta = 0-1$ and $x = 0$ to $\frac{6}{7}$ (**Figure S1b**). Nevertheless, the starting composition for all samples was chosen as $\text{Ag}_x\text{Cu}_{21-x}\text{Te}_{11}\text{Cl}_3$, as the exact coinage metal content is defined by the bonding situation in the anion substructure. The very small amount of spare MCl which results from this small deviation between the starting composition and the realized composition would deposit separated from the main product on the cooler side of the

ampoule during synthesis. The composition $\text{Ag}_{18}\text{Cu}_3\text{Te}_{11}\text{Cl}_3$ of the end member of the series was substantiated by EDX measurements that can be withdrawn from **Table S17**.

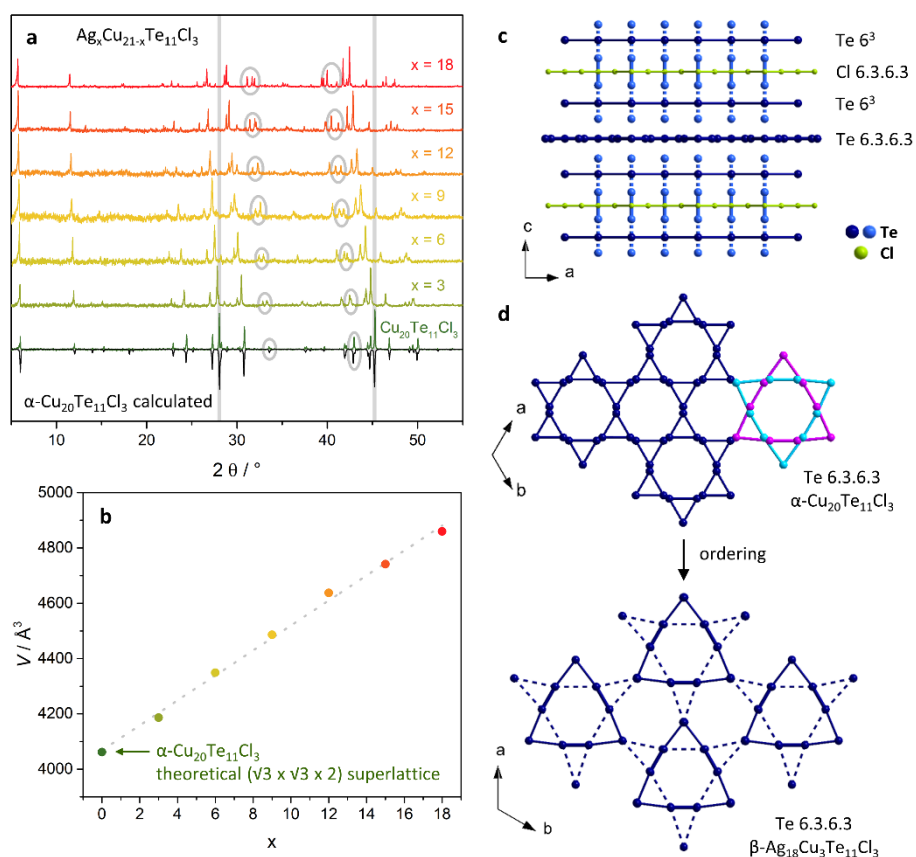


Figure S1. $\text{Ag}_{18}\text{Cu}_3\text{Te}_{11}\text{Cl}_3$ was first synthesized by substituting Cu by Ag in recently published $\text{Cu}_{20}\text{Te}_{11}\text{Cl}_3$.⁹ The elongation of Te-Te-distances causes the formation of a $(\sqrt{3} \times \sqrt{3} \times 2)$ super structure and an increase in anion charge from $[\text{Te}_{11}\text{Cl}_3]^{20-}$ to $[\text{Te}_{11}\text{Cl}_3]^{21-}$. a) Powder XRD pattern of $\text{Cu}_{20}\text{Te}_{11}\text{Cl}_3$ and $\text{Ag}_x\text{Cu}_{21-x}\text{Te}_{11}\text{Cl}_3$ with $x = 3 - 18$. Calculated diffractograms are drawn downwards for clarity. b) Evolution of unit cell volume of $\text{Ag}_x\text{Cu}_{21-x}\text{Te}_{11}\text{Cl}_3$ with increasing x from $x = 3$ to 18 compared to the volume of a theoretical $(\sqrt{3} \times \sqrt{3} \times 2)$ super cell of $\alpha\text{-Cu}_{20}\text{Te}_{11}\text{Cl}_3$. c) Scheme of anionic substructure of $\text{Cu}_{20}\text{Te}_{11}\text{Cl}_3$ and $\text{Ag}_{18}\text{Cu}_3\text{Te}_{11}\text{Cl}_3$. d) Disordered Te $6.3.6.3$ net of $\alpha\text{-Cu}_{20}\text{Te}_{11}\text{Cl}_3$ and ordered Te $6.3.6.3$ net of $\beta\text{-Ag}_{18}\text{Cu}_3\text{Te}_{11}\text{Cl}_3$.

Structure similarities

To set the very complex crystal chemistry of $\text{Ag}_{18}\text{Cu}_3\text{Te}_{11}\text{Cl}_3$ and $\text{Cu}_{20}\text{Te}_{11}\text{Cl}_3$ into some context, we compare the structure to related compounds. Besides the mineral stützite the

compounds are related to the other coinage metal polytelluride halides $\text{Cu}_{9,1}\text{Te}_4\text{Br}_3$ and $\text{Ag}_{10}\text{Te}_4\text{Br}_3$, the first reported pnp material.^[2-4,7] All structures can be described by a simple topological approach where the anion substructure is defined by different layers stacked along a crystallographic axis, interpenetrated by polyanionic Te units (see **Figure S2**). In stützite ($\text{Ag}_{5-x}\text{Te}_3$), only Te 6³ and Te 6.3.6.3 nets exist that are stacked alternately, interpenetrated by elongated Te_2 dumbbells. The Te 6.3.6.3 net is built of $[\text{Te}_2]^{2-}$ dumbbells and additional coordinating Te^{2-} ions. The replacement of the Te 6.3.6.3 nets by Cl 6.3.6.3 kagomé nets results in the anion substructure of $\text{Cu}_{9,1}\text{Te}_4\text{Cl}_3$. The smaller Cl atoms in comparison to Te induce the bond length decrease of the elongated dumbbells. While they are still slightly elongated in $\text{Cu}_{9,1}\text{Te}_4\text{Cl}_3$ (the reason of the slight excess of coinage metal), they are able to coordinate to strands of dumbbells. The replacement of the Cl by larger Br leads to the anion substructure of $\text{Ag}_{10}\text{Te}_4\text{Br}_3$. Here, another important structural feature emerges: oligomeric Te_4 units (built up of $\text{Te}^{2-}-[\text{Te}_2]^{2-}-\text{Te}^{2-}$) that switch to dynamically disordered equidistant Te-chains during the pnp switch. Those units interpenetrate the two other anion nets. In $\text{Ag}_{18}\text{Cu}_3\text{Te}_{11}\text{Cl}_3$, every second halide 6.3.6.3 net is again replaced by a Te 6.3.6.3 net as in stützite. Here, the Te 6.3.6.3 net separates the Te_4 units and they are arranged in a parallel manner on the same height (regarding the c-axis) unlike the zigzag arrangement in $\text{Ag}_{10}\text{Te}_4\text{Br}_3$ where they interpenetrate all layers. All mentioned anion substructures and anion layers are shown in **Figure S2**.

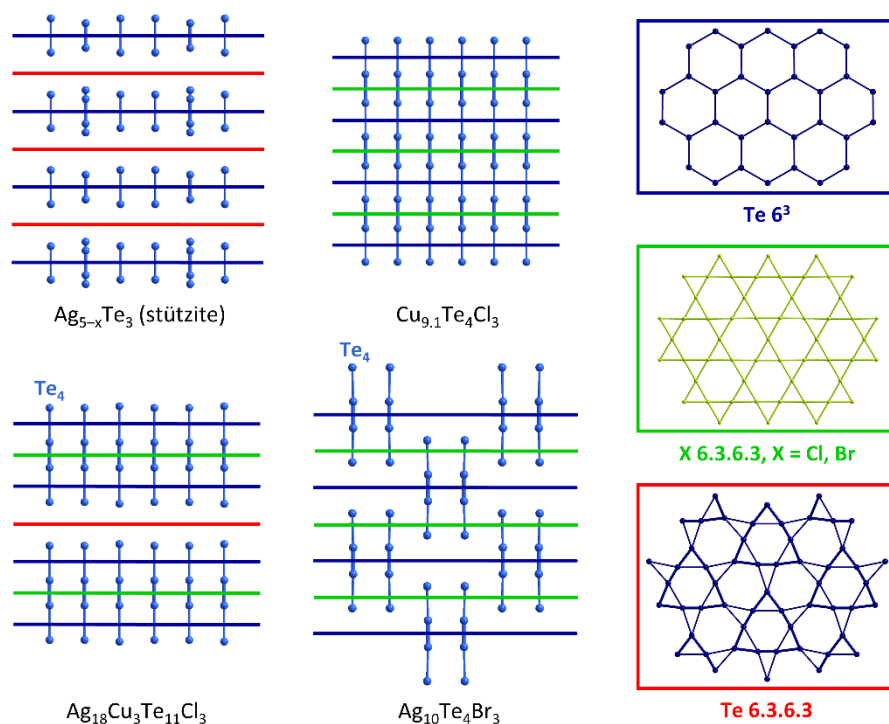


Figure S2. Building units and related structures: schemes of the anion substructures of synthetic stützite $\text{Ag}_{5-x}\text{Te}_3$, $\text{Cu}_{9.1}\text{Te}_4\text{Cl}_3$, $\text{Ag}_{18}\text{Cu}_3\text{Te}_{11}\text{Cl}_3$ and $\text{Ag}_{10}\text{Te}_4\text{Br}_3$.^[2,3,7,10] The anion building units of all four compounds are stacked $\text{Te } 6^3$ honeycomb nets, halide 6.3.6.3 kagomé nets and distorted $\text{Te } 6.3.6.3$ kagomé nets that consist of $[\text{Te}_2]^{2-}$ dumbbells and coordinating Te^{2-} anions with interpenetrating strands of $[\text{Te}_2]^{2-}$ dumbbells or Te_4 units (built up of Te^{2-} - $[\text{Te}_2]^{2-}$ - Te^{2-}). Distances are represented proportional.

Related pnp-switch in $\text{Ag}_{10}\text{Te}_4\text{Br}_3$

In $\text{Ag}_{10}\text{Te}_4\text{Br}_3$ a rearrangement of the Te_4 units is responsible for the pnp-switch.^[8] In γ - $\text{Ag}_{10}\text{Te}_4\text{Br}_3$ stable between 290 and 317 K all Te_4 units are fully ordered. In β - $\text{Ag}_{10}\text{Te}_4\text{Br}_3$ (317 to approx. 390 K) one third of the strands is rearranged to equidistant mobile Te-chains, and in α - $\text{Ag}_{10}\text{Te}_4\text{Br}_3$ (realized above 390 K) only equidistant mobile Te-chains exist. The rearrangement of the strands is triggered by increasing Ag mobility. The Ag1 position that separates two Te_4 units in γ - $\text{Ag}_{10}\text{Te}_4\text{Br}_3$ becomes partially occupied and the coordinating Te^{2-} ions of the Te_4 units are able to approach each other to form a new dumbbell. Structure sections of the α - and β -polymorph as well as the Seebeck-drop are shown in **Figure S3**.

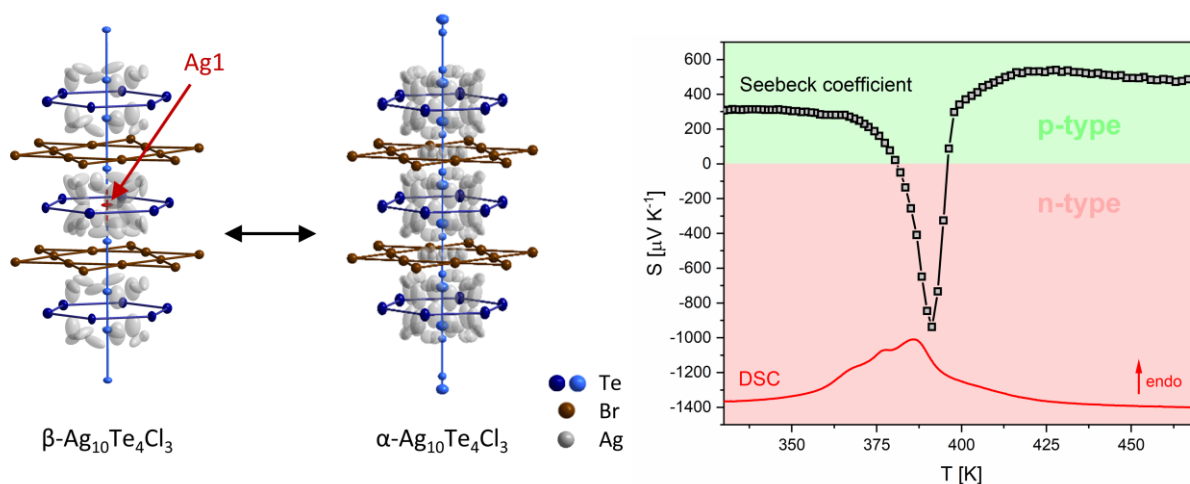


Figure S3. Structure sections of β - and α - $\text{Ag}_{10}\text{Te}_4\text{Br}_3$ and Seebeck-drop.

Structure refinement and extended crystal chemistry discussion

All refinements were performed using 3rd order displacement parameters (so called non-harmonic refinement). This procedure is necessary to reduce residual electron density if crystalline solid ion conductors feature a high grade of ion dynamics and disorder. This procedure typically leads to a high number of parameters and therefore to a poor data/parameter ratio. To decrease the number of parameters, insignificant 3rd order parameters were set to 0 and fixed in the last refinement step. Atomic coordinates, site occupancy factors, and displacement parameters are given for all refinements in **Table S1-S12**. In the case of mixed Ag/Cu sites, Ag and Cu were constrained to have the same positional and displacement parameters. As it is not possible to differentiate between Ag and Cu on partially occupied sites with large displacement parameters, the Ag:Cu ratio was constrained at 6:1, reflecting the initial composition as substantiated by EDX measurements (represented in **Table S17**).

According to DSC measurements, $\text{Ag}_{18}\text{Cu}_3\text{Te}_{11}\text{Cl}_3$ exhibits two broad phase transitions at 216(3) K and at 288(3) K, with the latter extending over a temperature interval around room temperature. The polymorphs are assigned γ -, β - and α - $\text{Ag}_{18}\text{Cu}_3\text{Te}_{11}\text{Cl}_3$ with increasing temperature. Similar to the other pnp-switching compounds, the drop of thermopower in

$\text{Ag}_{18}\text{Cu}_3\text{Te}_{11}\text{Cl}_3$ is initiated by an order-disorder phase transition, in that case the β - α transition around room temperature.

Single crystal XRD measurements have been performed at 200(1), 270(1), 330(1), 350(1), and 400(1) K in order to evaluate the structural changes upon and after the β - α transition in more detail.

In the structure refinement, third order anharmonic replacement parameters are used for Ag/Cu due to high ion mobility. As in α - $\text{Ag}_{18}\text{Cu}_3\text{Te}_{11}\text{Cl}_3$, mobility in the Te 6.3.6.3 net is released, third order anharmonic replacement parameters are also used for the Te atoms in the net, namely Te7, Te8, and Te9. In order to discuss atomic distances in the right manner, mode positions have been determined by calculating probability density functions (pdf). The mode position represents the true maximum of electron density of a given position that can differ from the refined position due to the anharmonicity of the displacement. A brief explanation for this procedure is given elsewhere.^[9,10] Mode positions are shown in **Table S14-S17** and are used in the following discussion.

β - $\text{Ag}_{18}\text{Cu}_3\text{Te}_{11}\text{Cl}_3$ crystallizes in hexagonal symmetry in space group $P6_3/mcm$, with $a = 13.4709(12)$ Å and $c = 30.818(2)$ Å at 270 K. Details of the single crystal XRD measurements can be withdrawn from **Table 1**. The structural features of the anion substructure, excluded the Te 6.3.6.3 net, are similar to those of $\text{Cu}_{20}\text{Te}_{11}\text{Cl}_3$: three parallel anion nets (a Cl 6.3.6.3 net between two Te 6³ nets) vertically interpenetrated by linear Te_4 units that are built by a $[\text{Te}_2]^{2-}$ dumbbell and two coordinating Te^{2-} ions.^[1] Unlike in $\text{Cu}_{20}\text{Te}_{11}\text{Cl}_3$, those structure units are not separated by a fully disordered Te 6.3.6.3 net but by a distorted ordered one (see **Figure S1c**). Similar to the Te 6.3.6.3 net in synthetic stützite, it consists of $[\text{Te}_2]^{2-}$ dumbbells and additional coordinating Te^{2-} anions (see **Figure S1d**).^[7] The dumbbell Te-Te distance is 2.81 Å and the distance to the coordinating Te^{2-} anion is 3.67 Å. These correspond well to values for $[\text{Te}_2]^{2-}$ at room temperature that can be found in literature: 2.84 Å in the Te 6.3.6.3

net in stützite, 2.70 Å in MgTe₂, 2.86 Å in α-K₂Te₂, or the dumbbell distance in the Te₄ units in β-Ag₁₈Cu₃Te₁₁Cl₃ with 2.81 - 2.83 Å.^[7,11,12] The distance of the coordinating Te²⁻ anion to the [Te₂]²⁻ dumbbell in the 6.3.6.3 net is comparable to the appropriate distance in stützite (3.61 Å) and the distance of the coordinating Te²⁻ anion in the Te₄ units in β-Ag₁₈Cu₃Te₁₁Cl₃ (3.85 – 4.05 Å).^[7]

The cations are very mobile and flow around the anion substructure as a quasi-liquid. The electron density is distributed over multiple partially occupied positions with large displacement parameters. As it is not possible to differentiate between Ag and Cu under these circumstances, the ratio Ag:Cu = 6:1 is constrained in every position. That ratio was gathered from the initial weight and substantiated by EDX measurements. Under that requirement, the site occupancy factors were refined without restrictions. This approach resulted in the refined sum formula Ag_{17.1(3)}Cu_{2.85(6)}Te₁₁Cl₃ that meets the expectations. The mixed Ag/Cu positions are located around the Te₄ strands between the anion nets and in the voids of the Te nets. The displacement parameters indicate mobility in two dimensions. As no Ag/Cu probability can be found within the Cl 6.3.6.3 net, this net seems to hinder a three-dimensional distribution of the d¹⁰ ions and the third direction (along the c-axis) is blocked.

Similar to β-Ag₁₈Cu₃Te₁₁Cl₃, α-Ag₁₈Cu₃Te₁₁Cl₃ crystallizes in *P6₃/mcm* with *a* = 13.5775 Å and *c* = 30.822 Å at 400 K. The main difference to β-Ag₁₈Cu₃Te₁₁Cl₃ can be found in the Te 6.3.6.3 net, where disorder emerges. Even after careful examination of the diffraction pattern we found no hints for a symmetry change which would lead to another space group. The dumbbell position Te8 splits into two positions. At 400 K the original dumbbell distance Te8-Te8 is 2.83 Å, the distance between the split positions Te8-Te9 is 0.98 Å, and the distance between the newly emerging position Te9 and the originally coordinating Te7 is 2.82 Å, which corresponds to a proper [Te₂]²⁻ dumbbell bond length as well.

The cation substructure is very similar to the β -polymorph. As expected, the displacement parameters increase with increasing temperature and ion mobility.

The crystal structure of γ -Ag₁₈Cu₃Te₁₁Cl₃ is more complex than those of α - and β -Ag₁₈Cu₃Te₁₁Cl₃ as we assume twinning. It is still under examination and, as it is not involved in pnp-switching. This structure will be published in an upcoming study.

Table S1. Positional parameters of β -Ag₁₈Cu₃Te₁₁Cl₃ at 270 K.

Atom	Wyckhoff position	site	sof	x	y	z
Te1	4e	3.m	1	1	1	0.04584(4)
Te2	8h	3..	1	0.6667	0.3333	0.04563(3)
Te3	4e	3.m	1	1	1	0.17736(6)
Te4	8h	3..	1	0.6667	0.3333	0.17046(4)
Te5	12k	..m	1	0.66206(6)	0.66206(6)	0.11342(3)
Te6	12k	..m	1	1	0.66866(8)	0.11287(3)
Te7	6g	m2m	1	0.56757(8)	0	0.25
Te8	12j	m..	1	0.31161(6)	0.12031(6)	0.25
Cl1	6f	..2/m	1	0.5	0	0
Cl2	12i	..2	1	0.83559(10)	0.6712(2)	0
Ag1	6g	m2m	0.241(9)	1	0.9043(13)	0.25
Cu1	6g	m2m	0.0401(14)	1	0.9043(13)	0.25
Ag2	12j	m..	0.662(5)	0.6501(2)	0.4484(2)	0.25
Cu2	12j	m..	0.1103(9)	0.6501(2)	0.4484(2)	0.25
Ag3	12k	..m	0.25(2)	0.574(2)	0.574(2)	0.1883(8)
Cu3	12k	..m	0.042(3)	0.574(2)	0.574(2)	0.1883(8)
Ag4	12k	..m	0.467(5)	1	0.7922(4)	0.19141(9)
Cu4	12k	..m	0.0779(8)	1	0.7922(4)	0.19141(9)
Ag5	24l	1	0.155(5)	0.6282(8)	0.5096(9)	0.1989(4)
Cu5	24l	1	0.0259(9)	0.6282(8)	0.5096(9)	0.1989(4)
Ag6	24l	1	0.254(6)	0.5506(6)	0.8516(14)	0.1777(4)
Cu6	24l	1	0.0424(11)	0.5506(6)	0.8516(14)	0.1777(4)
Ag7	24l	1	0.301(4)	1.1141(5)	0.8549(5)	0.1610(2)
Cu7	24l	1	0.0501(7)	1.1141(5)	0.8549(5)	0.1610(2)
Ag8	24l	1	0.263(8)	0.4761(10)	0.5438(6)	0.1701(4)
Cu8	24l	1	0.0439(13)	0.4761(10)	0.5438(6)	0.1701(4)
Ag9	24l	1	0.393(5)	0.5843(3)	0.7844(4)	0.16429(10)
Cu9	24l	1	0.0654(9)	0.5843(3)	0.7844(4)	0.16429(10)
Ag10	24l	1	0.252(6)	0.5623(7)	0.4331(9)	0.1132(5)
Cu10	24l	1	0.0419(10)	0.5623(7)	0.4331(9)	0.1132(5)
Ag11	24l	1	0.425(5)	0.8857(4)	0.8240(4)	0.11922(11)
Cu11	24l	1	0.0709(8)	0.8857(4)	0.8240(4)	0.11922(11)
Ag12	24l	1	0.210(6)	0.7639(10)	0.5222(11)	0.1222(7)
Cu12	24l	1	0.0350(11)	0.7639(10)	0.5222(11)	0.1222(7)
Ag13	24l	1	0.252(6)	0.5326(11)	0.4191(12)	0.0674(3)
Cu13	24l	1	0.0419(11)	0.5326(11)	0.4191(12)	0.0674(3)
Ag14	24l	1	0.292(7)	0.767(2)	0.5558(6)	0.0696(3)
Cu14	24l	1	0.0487(11)	0.767(2)	0.5558(6)	0.0696(3)

Ag15	12k	..m	0.724(5)	1	0.8055(3)	0.0542(2)
Cu15	12k	..m	0.1207(9)	1	0.8055(3)	0.0542(2)
Ag16	24l	1	0.369(7)	0.6707(3)	0.5325(4)	0.0524(3)
Cu16	24l	1	0.0615(12)	0.6707(3)	0.5325(4)	0.0524(3)

Table S2. Anisotropic displacement parameters of β -Ag₁₈Cu₃Te₁₁Cl₃ at 270 K.

Atom	U_{11}	U_{22}	U_{33}	U_{12}	U_{13}	U_{23}
Te1	0.0378(3)	0.0378(3)	0.0211(5)	0.0189(2)	0	0
Te2	0.0553(3)	0.0553(3)	0.0227(4)	0.0277(2)	0	0
Te3	0.0507(5)	0.0507(5)	0.0545(9)	0.0254(2)	0	0
Te4	0.0478(3)	0.0478(3)	0.0450(5)	0.0239(2)	0	0
Te5	0.0458(3)	0.0458(3)	0.0511(5)	0.0121(3)	-0.0073(3)	-0.0073(3)
Te6	0.0525(5)	0.0660(4)	0.0453(5)	0.0263(2)	0	0.0055(4)
Te7	0.0351(4)	0.0434(6)	0.0829(9)	0.0217(3)	0	0
Te8	0.0353(3)	0.0299(3)	0.0349(3)	0.0129(3)	0	0
Ag1	0.078(6)	0.127(8)	0.154(11)	0.039(3)	0	0
Cu1	0.078(6)	0.127(8)	0.154(11)	0.039(3)	0	0
Ag2	0.0501(8)	0.0483(9)	0.097(2)	0.0266(7)	0	0
Cu2	0.0501(8)	0.0483(9)	0.097(2)	0.0266(7)	0	0
Ag3	0.179(14)	0.179(14)	0.140(11)	0.095(11)	0.081(9)	0.081(9)
Cu3	0.179(14)	0.179(14)	0.140(11)	0.095(11)	0.081(9)	0.081(9)
Ag4	0.072(2)	0.0727(14)	0.062(2)	0.0361(8)	0	0.0041(9)
Cu4	0.072(2)	0.0727(14)	0.062(2)	0.0361(8)	0	0.0041(9)
Ag5	0.057(4)	0.093(5)	0.132(7)	0.012(3)	0.017(3)	-0.061(5)
Cu5	0.057(4)	0.093(5)	0.132(7)	0.012(3)	0.017(3)	-0.061(5)
Ag6	0.144(7)	0.131(7)	0.157(10)	-0.032(5)	-0.012(3)	0.056(7)
Cu6	0.144(7)	0.131(7)	0.157(10)	-0.032(5)	-0.012(3)	0.056(7)
Ag7	0.062(2)	0.075(2)	0.088(3)	0.027(2)	-0.011(2)	-0.015(2)
Cu7	0.062(2)	0.075(2)	0.088(3)	0.027(2)	-0.011(2)	-0.015(2)
Ag8	0.148(7)	0.056(3)	0.137(5)	0.033(3)	0.093(4)	0.028(3)
Cu8	0.148(7)	0.056(3)	0.137(5)	0.033(3)	0.093(4)	0.028(3)
Ag9	0.0553(13)	0.061(2)	0.070(2)	0.0219(10)	0.0065(10)	0.0091(11)
Cu9	0.0553(13)	0.061(2)	0.070(2)	0.0219(10)	0.0065(10)	0.0091(11)
Ag10	0.053(3)	0.148(7)	0.29(2)	0.048(3)	0.054(5)	0.069(7)
Cu10	0.053(3)	0.148(7)	0.29(2)	0.048(3)	0.054(5)	0.069(7)
Ag11	0.0673(14)	0.082(2)	0.081(2)	-0.0082(12)	0.0083(10)	0.0004(10)
Cu11	0.0673(14)	0.082(2)	0.081(2)	-0.0082(12)	0.0083(10)	0.0004(10)
Ag12	0.109(6)	0.068(5)	0.39(2)	-0.001(3)	-0.106(9)	0.066(8)
Cu12	0.109(6)	0.068(5)	0.39(2)	-0.001(3)	-0.106(9)	0.066(8)
Ag13	0.215(10)	0.254(10)	0.111(5)	0.198(9)	0.062(4)	0.055(4)
Cu13	0.215(10)	0.254(10)	0.111(5)	0.198(9)	0.062(4)	0.055(4)
Ag14	0.244(12)	0.074(3)	0.087(4)	0.023(5)	0.066(7)	0.004(2)
Cu14	0.244(12)	0.074(3)	0.087(4)	0.023(5)	0.066(7)	0.004(2)
Ag15	0.102(2)	0.0695(8)	0.130(3)	0.0510(8)	0	0.0343(11)
Cu15	0.102(2)	0.0695(8)	0.130(3)	0.0510(8)	0	0.0343(11)
Ag16	0.093(3)	0.084(2)	0.123(4)	0.046(2)	0.008(2)	-0.048(2)
Cu16	0.093(3)	0.084(2)	0.123(4)	0.046(2)	0.008(2)	-0.048(2)

Table S3. Anharmonic displacement parameters of β -Ag₁₈Cu₃Te₁₁Cl₃ at 270 K.

Atom	C_{111}	C_{112}	C_{113}	C_{122}	C_{123}
Ag1	0	0.021(3)	0	0.021(3)	0
Cu1	0	0.021(3)	0	0.021(3)	0
Ag2	-0.0016(4)	-0.0029(3)	0	-0.0033(3)	0
Cu2	-0.0016(4)	-0.0029(3)	0	-0.0033(3)	0
Ag3	-0.021(9)	-0.027(7)	-0.009(2)	-0.027(7)	0
Cu3	-0.021(9)	-0.027(7)	-0.009(2)	-0.027(7)	0
Ag4	0	0	-0.0025(2)	0	-0.00123(10)
Cu4	0	0	-0.0025(2)	0	-0.00123(10)
Ag5	0	0.0042(13)	-0.0018(4)	-0.0058(13)	0
Cu5	0	0.0042(13)	-0.0018(4)	-0.0058(13)	0
Ag6	0	0.016(2)	-0.0067(13)	0	0.0043(7)
Cu6	0	0.016(2)	-0.0067(13)	0	0.0043(7)
Ag7	-0.0084(11)	-0.0065(7)	0.0016(3)	-0.0043(7)	0.0013(2)
Cu7	-0.0084(11)	-0.0065(7)	0.0016(3)	-0.0043(7)	0.0013(2)
Ag8	0.026(4)	-0.0038(9)	0	0	0
Cu8	0.026(4)	-0.0038(9)	0	0	0
Ag9	0	-0.0023(3)	0	-0.0036(4)	0
Cu9	0	-0.0023(3)	0	-0.0036(4)	0
Ag10	0.0060(11)	0.0055(8)	-0.0034(6)	0	-0.0011(7)
Cu10	0.0060(11)	0.0055(8)	-0.0034(6)	0	-0.0011(7)
Ag11	0.0052(7)	0.0033(6)	0.0014(2)	-0.0082(6)	-0.00206(13)
Cu11	0.0052(7)	0.0033(6)	0.0014(2)	-0.0082(6)	-0.00206(13)
Ag12	-0.036(5)	-0.0051(11)	0.019(3)	0	0
Cu12	-0.036(5)	-0.0051(11)	0.019(3)	0	0
Ag13	0.035(5)	0.021(3)	-0.0138(13)	0	-0.0162(13)
Cu13	0.035(5)	0.021(3)	-0.0138(13)	0	-0.0162(13)
Ag14	-0.040(12)	-0.029(4)	-0.012(2)	0.009(2)	-0.0034(5)
Cu14	-0.040(12)	-0.029(4)	-0.012(2)	0.009(2)	-0.0034(5)
Ag15	0	0.0031(4)	0.0047(2)	0.0031(4)	0.00237(12)
Cu15	0	0.0031(4)	0.0047(2)	0.0031(4)	0.00237(12)
Ag16	0	-0.0043(6)	0.0043(4)	-0.0052(5)	0.0024(3)
Cu16	0	-0.0043(6)	0.0043(4)	-0.0052(5)	0.0024(3)
	C_{133}	C_{222}	C_{223}	C_{233}	C_{333}
Ag1	0	0.043(7)	0	0	0
Cu1	0	0.043(7)	0	0	0
Ag2	0	-0.0032(4)	0	0	0
Cu2	0	-0.0032(4)	0	0	0
Ag3	-0.0013(4)	-0.021(9)	-0.009(2)	-0.0013(4)	0
Cu3	-0.0013(4)	-0.021(9)	-0.009(2)	-0.0013(4)	0
Ag4	0	-0.0057(7)	0	0	0
Cu4	0	-0.0057(7)	0	0	0
Ag5	0	-0.026(3)	0.016(2)	-0.0075(7)	0.0025(3)
Cu5	0	-0.026(3)	0.016(2)	-0.0075(7)	0.0025(3)
Ag6	0	-0.014(5)	-0.007(2)	-0.0034(8)	-0.0035(6)
Cu6	0	-0.014(5)	-0.007(2)	-0.0034(8)	-0.0035(6)
Ag7	-0.00114(10)	-0.0038(10)	0.0009(2)	0	0
Cu7	-0.00114(10)	-0.0038(10)	0.0009(2)	0	0
Ag8	-0.0026(3)	-0.0028(9)	0.0019(3)	0	-0.0013(2)

Cu8	-0.0026(3)	-0.0028(9)	0.0019(3)	0	-0.0013(2)
Ag9	0	-0.0080(7)	0	0	0
Cu9	0	-0.0080(7)	0	0	0
Ag10	-0.0021(7)	0.027(5)	0.000(2)	0.0060(8)	-0.0034(8)
Cu10	-0.0021(7)	0.027(5)	0.000(2)	0.0060(8)	-0.0034(8)
Ag11	0	0.0050(10)	0.0016(2)	0	0
Cu11	0	0.0050(10)	0.0016(2)	0	0
Ag12	-0.010(2)	0.008(3)	0.007(2)	0.0076(14)	0.010(2)
Cu12	-0.010(2)	0.008(3)	0.007(2)	0.0076(14)	0.010(2)
Ag13	-0.0032(3)	-0.028(4)	-0.020(2)	-0.0038(4)	0
Cu13	-0.0032(3)	-0.028(4)	-0.020(2)	-0.0038(4)	0
Ag14	-0.0012(3)	0	0	0	0
Cu14	-0.0012(3)	0	0	0	0
Ag15	0	0.0020(4)	0.0020(2)	0.00123(9)	0.00133(10)
Cu15	0	0.0020(4)	0.0020(2)	0.00123(9)	0.00133(10)
Ag16	0	0	0.0026(3)	-0.0020(2)	0.0013(2)
Cu16	0	0	0.0026(3)	-0.0020(2)	0.0013(2)

Table S4. Positional parameters of α -Ag₁₈Cu₃Te₁₁Cl₃ at 330 K.

Atom	Wyckhoff position	site	sof	x	y	z
Te1	4e	3.m	1	1	1	0.04590(6)
Te2	8h	3..	1	0.6667	0.3333	0.04569(4)
Te3	4e	3.m	1	1	1	0.17394(8)
Te4	8h	3..	1	0.6667	0.3333	0.17098(6)
Te5	12k	..m	1	0.66136(8)	0.66136(8)	0.11399(5)
Te6	12k	..m	1	1	0.66844(8)	0.11352(5)
Te7	6g	m2m	1	0.5632(3)	0	0.25
Te8	12j	m..	0.891(9)	0.3147(2)	0.1191(4)	0.25
Te9	12j	m..	0.109(9)	0.331(2)	0.186(3)	0.25
Cl1	6f	..2/m	1	0.5	0	0
Cl2	12i	..2	1	0.83474(14)	0.6695(3)	0
Ag1	6g	m2m	0.424(11)	1	0.8976(9)	0.25
Cu1	6g	m2m	0.071(2)	1	0.8976(9)	0.25
Ag2	12j	m..	0.657(10)	0.6504(2)	0.4464(4)	0.25
Cu2	12j	m..	0.110(2)	0.6504(2)	0.4464(4)	0.25
Ag3	12k	..m	0.39(2)	0.576(3)	0.576(3)	0.1867(11)
Cu3	12k	..m	0.065(3)	0.576(3)	0.576(3)	0.1867(11)
Ag4	12k	..m	0.460(10)	1	0.7894(8)	0.1925(2)
Cu4	12k	..m	0.077(2)	1	0.7894(8)	0.1925(2)
Ag5	24l	1	0.245(10)	0.6370(13)	0.512(2)	0.1979(7)
Cu5	24l	1	0.041(2)	0.6370(13)	0.512(2)	0.1979(7)
Ag6	24l	1	0.277(9)	0.572(2)	0.8607(14)	0.1845(3)
Cu6	24l	1	0.0461(14)	0.572(2)	0.8607(14)	0.1845(3)
Ag7	24l	1	0.327(6)	1.1134(6)	0.8619(5)	0.1612(2)
Cu7	24l	1	0.0545(10)	1.1134(6)	0.8619(5)	0.1612(2)
Ag8	24l	1	0.200(11)	0.4625(11)	0.5365(13)	0.1683(4)
Cu8	24l	1	0.033(2)	0.4625(11)	0.5365(13)	0.1683(4)
Ag9	24l	1	0.316(6)	0.5821(5)	0.7857(6)	0.1649(2)
Cu9	24l	1	0.0527(11)	0.5821(5)	0.7857(6)	0.1649(2)
Ag10	24l	1	0.242(10)	0.5435(8)	0.4049(13)	0.1082(9)

Cu10	24l	1	0.040(2)	0.5435(8)	0.4049(13)	0.1082(9)
Ag11	24l	1	0.369(7)	0.8882(5)	0.8093(4)	0.1088(3)
Cu11	24l	1	0.0616(12)	0.8882(5)	0.8093(4)	0.1088(3)
Ag12	24l	1	0.264(9)	0.7560(10)	0.5358(10)	0.1116(5)
Cu12	24l	1	0.044(2)	0.7560(10)	0.5358(10)	0.1116(5)
Ag13	24l	1	0.219(9)	0.5477(10)	0.4256(12)	0.0723(7)
Cu13	24l	1	0.037(2)	0.5477(10)	0.4256(12)	0.0723(7)
Ag14	24l	1	0.174(7)	0.7839(10)	0.5523(9)	0.0701(5)
Cu14	24l	1	0.0289(11)	0.7839(10)	0.5523(9)	0.0701(5)
Ag15	12k	..m	0.709(10)	1	0.8060(4)	0.05309(13)
Cu15	12k	..m	0.118(2)	1	0.8060(4)	0.05309(13)
Ag16	24l	1	0.455(8)	0.6712(4)	0.5310(6)	0.0529(3)
Cu16	24l	1	0.0758(13)	0.6712(4)	0.5310(6)	0.0529(3)

Table S5. Anisotropic displacement parameters of α -Ag₁₈Cu₃Te₁₁Cl₃ at 330 K.

Atom	U_{11}	U_{22}	U_{33}	U_{12}	U_{13}	U_{23}
Te1	0.0501(5)	0.0501(5)	0.0346(10)	0.0251(2)	0	0
Te2	0.0603(4)	0.0603(4)	0.0339(7)	0.0302(2)	0	0
Te3	0.0596(6)	0.0596(6)	0.071(2)	0.0298(3)	0	0
Te4	0.0612(4)	0.0612(4)	0.0627(10)	0.0306(2)	0	0
Te5	0.0576(4)	0.0576(4)	0.0663(10)	0.0222(5)	-0.0048(4)	-0.0048(4)
Te6	0.0600(6)	0.0638(5)	0.0658(10)	0.0300(3)	0	0.0032(5)
Te7	0.0555(7)	0.0592(9)	0.0872(13)	0.0296(4)	0	0
Te8	0.0462(7)	0.038(2)	0.0493(8)	0.0154(10)	0	0
Te9	0.111(11)	0.09(2)	0.054(8)	0.088(12)	0	0
Ag1	0.072(4)	0.133(6)	0.157(8)	0.036(2)	0	0
Cu1	0.072(4)	0.133(6)	0.157(8)	0.036(2)	0	0
Ag2	0.077(2)	0.074(2)	0.127(3)	0.0409(11)	0	0
Cu2	0.077(2)	0.074(2)	0.127(3)	0.0409(11)	0	0
Ag3	0.29(2)	0.29(2)	0.24(2)	0.09(2)	0.15(2)	0.15(2)
Cu3	0.29(2)	0.29(2)	0.24(2)	0.09(2)	0.15(2)	0.15(2)
Ag4	0.129(4)	0.138(4)	0.100(4)	0.065(2)	0	-0.001(3)
Cu4	0.129(4)	0.138(4)	0.100(4)	0.065(2)	0	-0.001(3)
Ag5	0.147(8)	0.154(8)	0.186(13)	0.077(5)	-0.009(6)	-0.069(8)
Cu5	0.147(8)	0.154(8)	0.186(13)	0.077(5)	-0.009(6)	-0.069(8)
Ag6	0.27(2)	0.167(8)	0.100(6)	0.057(9)	-0.002(5)	0.035(6)
Cu6	0.27(2)	0.167(8)	0.100(6)	0.057(9)	-0.002(5)	0.035(6)
Ag7	0.088(3)	0.090(2)	0.111(4)	0.043(2)	-0.019(2)	-0.023(2)
Cu7	0.088(3)	0.090(2)	0.111(4)	0.043(2)	-0.019(2)	-0.023(2)
Ag8	0.146(7)	0.047(3)	0.117(8)	0.043(3)	0.061(6)	0.019(4)
Cu8	0.146(7)	0.047(3)	0.117(8)	0.043(3)	0.061(6)	0.019(4)
Ag9	0.075(2)	0.077(3)	0.081(3)	0.030(2)	0.003(2)	-0.003(2)
Cu9	0.075(2)	0.077(3)	0.081(3)	0.030(2)	0.003(2)	-0.003(2)
Ag10	0.126(6)	0.159(8)	0.58(3)	0.103(6)	0.191(9)	0.199(12)
Cu10	0.126(6)	0.159(8)	0.58(3)	0.103(6)	0.191(9)	0.199(12)
Ag11	0.073(2)	0.101(2)	0.280(7)	0.017(2)	0.002(2)	0.050(3)
Cu11	0.073(2)	0.101(2)	0.280(7)	0.017(2)	0.002(2)	0.050(3)
Ag12	0.130(8)	0.106(6)	0.64(3)	-0.007(4)	0.002(9)	0.028(6)
Cu12	0.130(8)	0.106(6)	0.64(3)	-0.007(4)	0.002(9)	0.028(6)
Ag13	0.119(6)	0.171(9)	0.158(12)	0.101(6)	0.058(7)	0.051(6)
Cu13	0.119(6)	0.171(9)	0.158(12)	0.101(6)	0.058(7)	0.051(6)

Ag14	0.191(10)	0.075(5)	0.086(7)	0.019(4)	0.003(4)	0.021(4)
Cu14	0.191(10)	0.075(5)	0.086(7)	0.019(4)	0.003(4)	0.021(4)
Ag15	0.151(3)	0.103(2)	0.136(3)	0.0754(14)	0	0.0348(14)
Cu15	0.151(3)	0.103(2)	0.136(3)	0.0754(14)	0	0.0348(14)
Ag16	0.152(4)	0.117(3)	0.149(4)	0.078(3)	0.006(3)	-0.043(3)
Cu16	0.152(4)	0.117(3)	0.149(4)	0.078(3)	0.006(3)	-0.043(3)

Table S6. Anharmonic displacement parameters of α -Ag₁₈Cu₃Te₁₁Cl₃ at 330 K.

Atom	C_{111}	C_{112}	C_{113}	C_{122}	C_{123}
Te7	-0.0027(4)	-0.0016(2)	0	-0.0016(2)	0
Te8	0.0007(4)	-0.0007(3)	0	-0.0003(3)	0
Te9	-0.06(2)	-0.044(14)	0	-0.038(14)	0
Ag1	0	0.0032(12)	0	0.0032(12)	0
Cu1	0	0.0032(12)	0	0.0032(12)	0
Ag2	0	-0.0026(4)	0	-0.0038(5)	0
Cu2	0	-0.0026(4)	0	-0.0038(5)	0
Ag3	-0.11(2)	0.071(12)	-0.017(3)	0.071(12)	0.020(4)
Cu3	-0.11(2)	0.071(12)	-0.017(3)	0.071(12)	0.020(4)
Ag4	0	0	0	0	0
Cu4	0	0	0	0	0
Ag5	0	-0.015(2)	0	-0.022(3)	0.0026(7)
Cu5	0	-0.015(2)	0	-0.022(3)	0.0026(7)
Ag6	0.10(2)	0.063(9)	0	0.053(6)	0.0077(13)
Cu6	0.10(2)	0.063(9)	0	0.053(6)	0.0077(13)
Ag7	-0.013(2)	-0.0042(7)	0.0020(4)	0	0.0015(2)
Cu7	-0.013(2)	-0.0042(7)	0.0020(4)	0	0.0015(2)
Ag8	0	-0.015(2)	0.0050(9)	-0.0069(13)	0
Cu8	0	-0.015(2)	0.0050(9)	-0.0069(13)	0
Ag9	0	0	0	-0.0027(5)	0
Cu9	0	0	0	-0.0027(5)	0
Ag10	-0.043(6)	-0.036(5)	-0.047(5)	-0.027(5)	-0.027(4)
Cu10	-0.043(6)	-0.036(5)	-0.047(5)	-0.027(5)	-0.027(4)
Ag11	0.0087(11)	0.0071(7)	0	-0.0048(7)	-0.0018(3)
Cu11	0.0087(11)	0.0071(7)	0	-0.0048(7)	-0.0018(3)
Ag12	-0.051(7)	0	0	-0.009(3)	0.013(2)
Cu12	-0.051(7)	0	0	-0.009(3)	0.013(2)
Ag13	0	-0.018(3)	-0.0075(11)	-0.040(6)	-0.0140(13)
Cu13	0	-0.018(3)	-0.0075(11)	-0.040(6)	-0.0140(13)
Ag14	0	-0.051(5)	-0.024(2)	0	0
Cu14	0	-0.051(5)	-0.024(2)	0	0
Ag15	0	0.0067(7)	0.0053(4)	0.0067(7)	0.0026(2)
Cu15	0	0.0067(7)	0.0053(4)	0.0067(7)	0.0026(2)
Ag16	0	-0.0083(12)	0.0057(6)	-0.0099(14)	0.0035(3)
Cu16	0	-0.0083(12)	0.0057(6)	-0.0099(14)	0.0035(3)
	C_{133}	C_{222}	C_{223}	C_{233}	C_{333}
Te7	0.00011(5)	0	0	0	0
Te8	0.00008(3)	-0.0009(6)	0	-0.00009(4)	0
Te9	-0.0016(6)	-0.04(2)	0	-0.0014(6)	0
Ag1	0	0.038(5)	0	0	0
Cu1	0	0.038(5)	0	0	0

Ag2	0	-0.0048(7)	0	0	0
Cu2	0	-0.0048(7)	0	0	0
Ag3	0	-0.11(2)	-0.017(3)	0	0
Cu3	0	-0.11(2)	-0.017(3)	0	0
Ag4	0	-0.019(2)	0.0012(4)	0.0009(2)	0
Cu4	0	-0.019(2)	0.0012(4)	0.0009(2)	0
Ag5	0	-0.027(5)	0.015(2)	-0.0079(13)	0.0033(8)
Cu5	0	-0.027(5)	0.015(2)	-0.0079(13)	0.0033(8)
Ag6	0.0017(5)	0.015(5)	0	0	0
Cu6	0.0017(5)	0.015(5)	0	0	0
Ag7	-0.0010(2)	-0.0049(10)	0	0	0
Cu7	-0.0010(2)	-0.0049(10)	0	0	0
Ag8	0.0012(3)	-0.002(2)	0	0	0
Cu8	0.0012(3)	-0.002(2)	0	0	0
Ag9	0	-0.0056(12)	0.0013(2)	0	0
Cu9	0	-0.0056(12)	0.0013(2)	0	0
Ag10	-0.039(4)	-0.017(6)	-0.005(4)	-0.014(3)	-0.027(3)
Cu10	-0.039(4)	-0.017(6)	-0.005(4)	-0.014(3)	-0.027(3)
Ag11	0	0	-0.0097(7)	-0.0152(6)	-0.0110(5)
Cu11	0	0	-0.0097(7)	-0.0152(6)	-0.0110(5)
Ag12	0	0.005(4)	0	0.037(3)	0
Cu12	0	0.005(4)	0	0.037(3)	0
Ag13	0	-0.077(10)	-0.022(2)	-0.0023(5)	0.0016(4)
Cu13	0	-0.077(10)	-0.022(2)	-0.0023(5)	0.0016(4)
Ag14	0.0018(4)	0	-0.0038(6)	0	0.0015(2)
Cu14	0.0018(4)	0	-0.0038(6)	0	0.0015(2)
Ag15	0	0.0029(8)	0	0	0
Cu15	0	0.0029(8)	0	0	0
Ag16	0	-0.003(2)	0	0	0
Cu16	0	-0.003(2)	0	0	0

Table S7. Positional parameters of α -Ag₁₈Cu₃Te₁₁Cl₃ at 350 K.

Atom	Wyckhoff position	site	sof	x	y	z
Te1	4e	3.m	1	1	1	0.04590(3)
Te2	8h	3..	1	0.6667	0.3333	0.04561(2)
Te3	4e	3.m	1	1	1	0.17336(5)
Te4	8h	3..	1	0.6667	0.3333	0.17085(3)
Te5	12k	..m	1	0.66143(5)	0.66143(5)	0.11392(3)
Te6	12k	..m	1	1	0.66857(6)	0.11352(3)
Te7	6g	m2m	1	0.5602(2)	0	0.25
Te8	12j	m..	0.832(7)	0.3155(2)	0.1181(4)	0.25
Te9	12j	m..	0.168(7)	0.3377(14)	0.178(2)	0.25
Cl1	6f	..2/m	1	0.5	0	0
Cl2	12i	..2	1	0.83379(9)	0.6676(2)	0
Ag1	6g	m2m	0.390(9)	1	0.8964(6)	0.25
Cu1	6g	m2m	0.065(2)	1	0.8964(6)	0.25
Ag2	12j	m..	0.541(8)	0.6509(2)	0.4463(3)	0.25
Cu2	12j	m..	0.0901(13)	0.6509(2)	0.4463(3)	0.25
Ag3	12k	..m	0.252(11)	0.594(2)	0.594(2)	0.1948(3)

Cu3	12k	..m	0.042(2)	0.594(2)	0.594(2)	0.1948(3)
Ag4	12k	..m	0.383(7)	1	0.7856(6)	0.1932(2)
Cu4	12k	..m	0.0638(12)	1	0.7856(6)	0.1932(2)
Ag5	24l	1	0.242(7)	0.6399(8)	0.5076(8)	0.1979(4)
Cu5	24l	1	0.0403(11)	0.6399(8)	0.5076(8)	0.1979(4)
Ag6	24l	1	0.249(5)	0.5498(12)	0.845(2)	0.1839(3)
Cu6	24l	1	0.0415(9)	0.5498(12)	0.845(2)	0.1839(3)
Ag7	24l	1	0.436(6)	1.1184(3)	0.8700(4)	0.16349(11)
Cu7	24l	1	0.0726(10)	1.1184(3)	0.8700(4)	0.16349(11)
Ag8	24l	1	0.364(8)	0.4627(6)	0.5486(7)	0.1676(2)
Cu8	24l	1	0.0606(13)	0.4627(6)	0.5486(7)	0.1676(2)
Ag9	24l	1	0.429(7)	0.5793(6)	0.7838(6)	0.16452(12)
Cu9	24l	1	0.0715(12)	0.5793(6)	0.7838(6)	0.16452(12)
Ag10	24l	1	0.246(7)	0.5451(6)	0.4007(10)	0.1044(3)
Cu10	24l	1	0.0409(11)	0.5451(6)	0.4007(10)	0.1044(3)
Ag11	24l	1	0.356(5)	0.8884(4)	0.8059(3)	0.1083(2)
Cu11	24l	1	0.0594(9)	0.8884(4)	0.8059(3)	0.1083(2)
Ag12	24l	1	0.213(7)	0.7584(9)	0.5346(7)	0.1053(4)
Cu12	24l	1	0.0354(11)	0.7584(9)	0.5346(7)	0.1053(4)
Ag13	24l	1	0.211(6)	0.5327(12)	0.4197(12)	0.0693(4)
Cu13	24l	1	0.0352(10)	0.5327(12)	0.4197(12)	0.0693(4)
Ag14	24l	1	0.207(7)	0.7757(8)	0.5556(8)	0.0729(5)
Cu14	24l	1	0.0346(11)	0.7757(8)	0.5556(8)	0.0729(5)
Ag15	12k	..m	0.570(7)	1	0.8063(3)	0.0543(2)
Cu15	12k	..m	0.0951(12)	1	0.8063(3)	0.0543(2)
Ag16	24l	1	0.367(7)	0.6664(9)	0.5288(7)	0.0533(2)
Cu16	24l	1	0.0611(12)	0.6664(9)	0.5288(7)	0.0533(2)

Table S8. Anisotropic displacement parameters of α -Ag₁₈Cu₃Te₁₁Cl₃ at 350 K.

Atom	U_{11}	U_{22}	U_{33}	U_{12}	U_{13}	U_{23}
Te1	0.0516(3)	0.0516(3)	0.0249(4)	0.0258(2)	0	0
Te2	0.0595(3)	0.0595(3)	0.0262(3)	0.0297(2)	0	0
Te3	0.0590(4)	0.0590(4)	0.0623(7)	0.0295(2)	0	0
Te4	0.0611(3)	0.0611(3)	0.0562(5)	0.0306(2)	0	0
Te5	0.0583(3)	0.0583(3)	0.0588(5)	0.0225(3)	-0.0042(3)	-0.0042(3)
Te6	0.0617(4)	0.0645(4)	0.0568(5)	0.0308(2)	0	0.0009(3)
Te7	0.0619(6)	0.0645(7)	0.0703(6)	0.0323(3)	0	0
Te8	0.0462(6)	0.0382(11)	0.0413(8)	0.0119(5)	0	0
Te9	0.096(8)	0.18(2)	0.043(4)	0.106(10)	0	0
Ag1	0.069(3)	0.123(4)	0.153(5)	0.0346(13)	0	0
Cu1	0.069(3)	0.123(4)	0.153(5)	0.0346(13)	0	0
Ag2	0.0736(12)	0.0682(12)	0.112(2)	0.0412(8)	0	0
Cu2	0.0736(12)	0.0682(12)	0.112(2)	0.0412(8)	0	0
Ag3	0.178(10)	0.178(10)	0.135(7)	0.074(10)	0.079(6)	0.079(6)
Cu3	0.178(10)	0.178(10)	0.135(7)	0.074(10)	0.079(6)	0.079(6)
Ag4	0.121(3)	0.167(5)	0.092(3)	0.060(2)	0	-0.008(2)
Cu4	0.121(3)	0.167(5)	0.092(3)	0.060(2)	0	-0.008(2)
Ag5	0.138(5)	0.160(5)	0.186(7)	0.079(4)	-0.022(4)	-0.082(5)
Cu5	0.138(5)	0.160(5)	0.186(7)	0.079(4)	-0.022(4)	-0.082(5)
Ag6	0.173(7)	0.154(9)	0.102(4)	0.006(4)	-0.007(3)	0.021(5)
Cu6	0.173(7)	0.154(9)	0.102(4)	0.006(4)	-0.007(3)	0.021(5)
Ag7	0.098(2)	0.110(2)	0.105(2)	0.0431(13)	-0.0120(11)	-0.0194(12)
Cu7	0.098(2)	0.110(2)	0.105(2)	0.0431(13)	-0.0120(11)	-0.0194(12)
Ag8	0.165(4)	0.115(3)	0.117(3)	0.068(3)	0.066(3)	0.020(2)
Cu8	0.165(4)	0.115(3)	0.117(3)	0.068(3)	0.066(3)	0.020(2)
Ag9	0.109(2)	0.111(2)	0.093(2)	0.055(2)	0.013(2)	0.009(2)
Cu9	0.109(2)	0.111(2)	0.093(2)	0.055(2)	0.013(2)	0.009(2)
Ag10	0.139(4)	0.183(6)	0.406(11)	0.125(4)	0.156(5)	0.157(7)
Cu10	0.139(4)	0.183(6)	0.406(11)	0.125(4)	0.156(5)	0.157(7)
Ag11	0.074(2)	0.091(2)	0.297(5)	0.0124(11)	0.024(2)	0.050(2)
Cu11	0.074(2)	0.091(2)	0.297(5)	0.0124(11)	0.024(2)	0.050(2)
Ag12	0.144(5)	0.090(3)	0.368(12)	0.000(3)	0.011(3)	-0.060(5)
Cu12	0.144(5)	0.090(3)	0.368(12)	0.000(3)	0.011(3)	-0.060(5)
Ag13	0.157(7)	0.182(7)	0.172(7)	0.141(6)	0.071(5)	0.065(5)
Cu13	0.157(7)	0.182(7)	0.172(7)	0.141(6)	0.071(5)	0.065(5)
Ag14	0.119(7)	0.075(3)	0.169(10)	0.020(3)	-0.010(4)	0.000(4)
Cu14	0.119(7)	0.075(3)	0.169(10)	0.020(3)	-0.010(4)	0.000(4)
Ag15	0.166(3)	0.0973(13)	0.134(2)	0.083(2)	0	0.0400(10)
Cu15	0.166(3)	0.0973(13)	0.134(2)	0.083(2)	0	0.0400(10)
Ag16	0.163(6)	0.110(3)	0.137(3)	0.084(4)	0.019(3)	-0.042(2)
Cu16	0.163(6)	0.110(3)	0.137(3)	0.084(4)	0.019(3)	-0.042(2)

Table S9. Anharmonic displacement parameters of α -Ag₁₈Cu₃Te₁₁Cl₃ at 350 K.

Atom	C_{111}	C_{112}	C_{113}	C_{122}	C_{123}
Te7	-0.0055(3)	-0.0034(2)	0	-0.0034(2)	0
Te8	0.0005(3)	-0.0005(2)	0	0.0003(2)	0
Te9	-0.031(9)	-0.047(12)	0	-0.07(2)	0

Ag1	0	0.0063(8)	0	0.0063(8)	0
Cu1	0	0.0063(8)	0	0.0063(8)	0
Ag2	0	-0.0039(3)	0	-0.0055(4)	0
Cu2	0	-0.0039(3)	0	-0.0055(4)	0
Ag3	-0.007(4)	-0.009(3)	0	-0.009(3)	0
Cu3	-0.007(4)	-0.009(3)	0	-0.009(3)	0
Ag4	0	-0.0020(10)	-0.0026(4)	-0.0020(10)	-0.0013(2)
Cu4	0	-0.0020(10)	-0.0026(4)	-0.0020(10)	-0.0013(2)
Ag5	0	-0.009(2)	-0.0029(7)	-0.025(3)	0.0040(9)
Cu5	0	-0.009(2)	-0.0029(7)	-0.025(3)	0.0040(9)
Ag6	0.018(4)	0.015(2)	0	0.017(3)	0.0056(7)
Cu6	0.018(4)	0.015(2)	0	0.017(3)	0.0056(7)
Ag7	-0.0075(9)	-0.0034(4)	0.0032(2)	0	0.0025(2)
Cu7	-0.0075(9)	-0.0034(4)	0.0032(2)	0	0.0025(2)
Ag8	0.009(2)	0	0.0077(6)	0.0052(9)	0.0041(4)
Cu8	0.009(2)	0	0.0077(6)	0.0052(9)	0.0041(4)
Ag9	0.0028(10)	-0.0030(7)	0	-0.0083(8)	0
Cu9	0.0028(10)	-0.0030(7)	0	-0.0083(8)	0
Ag10	-0.058(5)	-0.062(6)	-0.052(3)	-0.063(7)	-0.051(4)
Cu10	-0.058(5)	-0.062(6)	-0.052(3)	-0.063(7)	-0.051(4)
Ag11	0.0087(7)	0.0067(5)	0	-0.0062(5)	-0.0023(3)
Cu11	0.0087(7)	0.0067(5)	0	-0.0062(5)	-0.0023(3)
Ag12	-0.029(6)	0.019(3)	-0.022(3)	-0.023(2)	0.0120(12)
Cu12	-0.029(6)	0.019(3)	-0.022(3)	-0.023(2)	0.0120(12)
Ag13	-0.029(5)	-0.040(5)	-0.016(2)	-0.053(6)	-0.021(2)
Cu13	-0.029(5)	-0.040(5)	-0.016(2)	-0.053(6)	-0.021(2)
Ag14	0.009(3)	-0.012(2)	-0.0120(13)	0	0.0023(5)
Cu14	0.009(3)	-0.012(2)	-0.0120(13)	0	0.0023(5)
Ag15	0	0.0129(7)	0.0118(5)	0.0129(7)	0.0059(3)
Cu15	0	0.0129(7)	0.0118(5)	0.0129(7)	0.0059(3)
Ag16	-0.013(4)	-0.019(3)	0.0091(8)	-0.017(2)	0.0047(4)
Cu16	-0.013(4)	-0.019(3)	0.0091(8)	-0.017(2)	0.0047(4)
	C_{133}	C_{222}	C_{223}	C_{233}	C_{333}
Te7	0.00010(2)	0	0	0	0
Te8	0.00009(2)	-0.0011(3)	0	-0.00015(2)	0
Te9	-0.0008(3)	-0.12(3)	0	-0.0013(5)	0
Ag1	0	0.041(3)	0	0	0
Cu1	0	0.041(3)	0	0	0
Ag2	0	-0.0060(6)	0	0	0
Cu2	0	-0.0060(6)	0	0	0
Ag3	0	-0.007(4)	0	0	0
Cu3	0	-0.007(4)	0	0	0
Ag4	0	-0.051(4)	0.0041(5)	0	0
Cu4	0	-0.051(4)	0.0041(5)	0	0
Ag5	-0.0014(4)	-0.051(4)	0.021(2)	-0.0101(8)	0.0041(4)
Cu5	-0.0014(4)	-0.051(4)	0.021(2)	-0.0101(8)	0.0041(4)
Ag6	0	-0.026(7)	-0.011(2)	-0.0016(4)	0
Cu6	0	-0.026(7)	-0.011(2)	-0.0016(4)	0
Ag7	0	0.0035(7)	0.0027(2)	0	0
Cu7	0	0.0035(7)	0.0027(2)	0	0
Ag8	0.0016(2)	0.009(2)	0.0039(5)	0.0014(2)	0
Cu8	0.0016(2)	0.009(2)	0.0039(5)	0.0014(2)	0
Ag9	-0.00052(8)	-0.0091(10)	0.0024(2)	0	0
Cu9	-0.00052(8)	-0.0091(10)	0.0024(2)	0	0

Ag10	-0.040(2)	-0.063(8)	-0.044(4)	-0.035(3)	-0.028(2)
Cu10	-0.040(2)	-0.063(8)	-0.044(4)	-0.035(3)	-0.028(2)
Ag11	-0.0031(3)	0	-0.0074(5)	-0.0148(5)	-0.0130(6)
Cu11	-0.0031(3)	0	-0.0074(5)	-0.0148(5)	-0.0130(6)
Ag12	0	0.003(2)	-0.007(2)	0.023(2)	-0.024(2)
Cu12	0	0.003(2)	-0.007(2)	0.023(2)	-0.024(2)
Ag13	-0.0036(4)	-0.066(7)	-0.026(2)	-0.0054(6)	0
Cu13	-0.0036(4)	-0.066(7)	-0.026(2)	-0.0054(6)	0
Ag14	0	0	0	0	0
Cu14	0	0	0	0	0
Ag15	0	0.0080(7)	0.0028(2)	0	0
Cu15	0	0.0080(7)	0.0028(2)	0	0
Ag16	0	-0.007(2)	0.0012(3)	0	0
Cu16	0	-0.007(2)	0.0012(3)	0	0

Table S10. Positional parameters of α -Ag₁₈Cu₃Te₁₁Cl₃ at 400 K.

Atom	Wyckhoff position	site	sof	x	y	z
Te1	4e	3.m	1	1	1	0.04577(5)
Te2	8h	3..	1	0.6667	0.3333	0.04573(4)
Te3	4e	3.m	1	1	1	0.17211(6)
Te4	8h	3..	1	0.6667	0.3333	0.17103(4)
Te5	12k	..m	1	0.66184(7)	0.66184(7)	0.11400(5)
Te6	12k	..m	1	1	0.66894(8)	0.11389(5)
Te7	6g	m2m	1	0.5513(4)	0	0.25
Te8	12j	m..	0.715(9)	0.3174(5)	0.1162(7)	0.25
Te9	12j	m..	0.285(9)	0.339(2)	0.184(3)	0.25
Cl1	6f	..2/m	1	0.5	0	0
Cl2	12i	..2	1	0.83382(14)	0.6676(3)	0
Ag1	6g	m2m	0.506(10)	1	0.8876(9)	0.25
Cu1	6g	m2m	0.084(2)	1	0.8876(9)	0.25
Ag2	12j	m..	0.455(8)	0.6701(6)	0.4423(5)	0.25
Cu2	12j	m..	0.0758(14)	0.6701(6)	0.4423(5)	0.25
Ag3	12k	..m	0.23(2)	0.613(2)	0.613(2)	0.1951(9)
Cu3	12k	..m	0.039(3)	0.613(2)	0.613(2)	0.1951(9)
Ag4	12k	..m	0.336(11)	1	0.7770(12)	0.1880(4)
Cu4	12k	..m	0.056(2)	1	0.7770(12)	0.1880(4)
Ag5	24l	1	0.197(9)	0.6505(11)	0.5064(12)	0.1952(7)
Cu5	24l	1	0.033(2)	0.6505(11)	0.5064(12)	0.1952(7)
Ag6	24l	1	0.235(10)	0.569(2)	0.8723(12)	0.1871(5)
Cu6	24l	1	0.039(2)	0.569(2)	0.8723(12)	0.1871(5)
Ag7	24l	1	0.408(9)	1.1232(6)	0.8768(6)	0.1693(4)
Cu7	24l	1	0.0680(14)	1.1232(6)	0.8768(6)	0.1693(4)
Ag8	24l	1	0.398(9)	0.469(2)	0.5511(13)	0.1715(5)
Cu8	24l	1	0.066(2)	0.469(2)	0.5511(13)	0.1715(5)
Ag9	24l	1	0.325(9)	0.5827(11)	0.7873(10)	0.1669(2)
Cu9	24l	1	0.054(2)	0.5827(11)	0.7873(10)	0.1669(2)
Ag10	24l	1	0.237(10)	0.5407(12)	0.393(2)	0.1055(8)
Cu10	24l	1	0.040(2)	0.5407(12)	0.393(2)	0.1055(8)
Ag11	24l	1	0.389(7)	0.8773(6)	0.7977(6)	0.1141(3)
Cu11	24l	1	0.0649(12)	0.8773(6)	0.7977(6)	0.1141(3)

Ag12	24l	1	0.292(11)	0.7686(14)	0.549(2)	0.1199(11)
Cu12	24l	1	0.049(2)	0.7686(14)	0.549(2)	0.1199(11)
Ag13	24l	1	0.232(9)	0.5310(14)	0.419(2)	0.0729(7)
Cu13	24l	1	0.039(2)	0.5310(14)	0.419(2)	0.0729(7)
Ag14	24l	1	0.201(9)	0.7801(13)	0.5435(8)	0.0813(4)
Cu14	24l	1	0.034(2)	0.7801(13)	0.5435(8)	0.0813(4)
Ag15	12k	..m	0.538(9)	1	0.8151(5)	0.0600(2)
Cu15	12k	..m	0.090(2)	1	0.8151(5)	0.0600(2)
Ag16	24l	1	0.285(9)	0.6630(13)	0.5229(11)	0.0556(5)
Cu16	24l	1	0.048(2)	0.6630(13)	0.5229(11)	0.0556(5)

Table S11. Anisotropic displacement parameters of α -Ag₁₈Cu₃Te₁₁Cl₃ at 400 K.

Atom	U_{11}	U_{22}	U_{33}	U_{12}	U_{13}	U_{23}
Te1	0.0629(6)	0.0629(6)	0.0366(7)	0.0315(3)	0	0
Te2	0.0661(4)	0.0661(4)	0.0408(5)	0.0330(2)	0	0
Te3	0.0676(6)	0.0676(6)	0.0688(11)	0.0338(3)	0	0
Te4	0.0729(5)	0.0729(5)	0.0670(8)	0.0365(3)	0	0
Te5	0.0662(5)	0.0662(5)	0.0770(9)	0.0291(5)	-0.0011(4)	-0.0011(4)
Te6	0.0717(7)	0.0705(6)	0.0740(9)	0.0359(4)	0	-0.0012(4)
Te7	0.0971(13)	0.0959(13)	0.0711(10)	0.0480(6)	0	0
Te8	0.064(2)	0.051(2)	0.060(2)	0.012(2)	0	0
Te9	0.089(9)	0.15(2)	0.062(5)	0.078(11)	0	0
Ag1	0.107(4)	0.125(4)	0.149(5)	0.053(2)	0	0
Cu1	0.107(4)	0.125(4)	0.149(5)	0.053(2)	0	0
Ag2	0.240(5)	0.096(3)	0.098(3)	0.067(3)	0	0
Cu2	0.240(5)	0.096(3)	0.098(3)	0.067(3)	0	0
Ag3	0.23(2)	0.23(2)	0.114(11)	0.04(2)	0.021(7)	0.021(7)
Cu3	0.23(2)	0.23(2)	0.114(11)	0.04(2)	0.021(7)	0.021(7)
Ag4	0.216(14)	0.250(11)	0.110(6)	0.108(7)	0	-0.054(4)
Cu4	0.216(14)	0.250(11)	0.110(6)	0.108(7)	0	-0.054(4)
Ag5	0.139(9)	0.134(8)	0.33(2)	0.053(6)	0.004(10)	-0.091(11)
Cu5	0.139(9)	0.134(8)	0.33(2)	0.053(6)	0.004(10)	-0.091(11)
Ag6	0.37(2)	0.211(10)	0.154(8)	0.180(9)	0.085(8)	0.039(6)
Cu6	0.37(2)	0.211(10)	0.154(8)	0.180(9)	0.085(8)	0.039(6)
Ag7	0.125(4)	0.187(5)	0.136(6)	0.054(4)	0.001(2)	-0.003(3)
Cu7	0.125(4)	0.187(5)	0.136(6)	0.054(4)	0.001(2)	-0.003(3)
Ag8	0.231(12)	0.165(8)	0.181(9)	0.119(8)	0.106(9)	0.070(7)
Cu8	0.231(12)	0.165(8)	0.181(9)	0.119(8)	0.106(9)	0.070(7)
Ag9	0.135(6)	0.176(7)	0.092(4)	0.087(5)	-0.006(3)	0.007(3)
Cu9	0.135(6)	0.176(7)	0.092(4)	0.087(5)	-0.006(3)	0.007(3)
Ag10	0.155(9)	0.25(2)	0.63(3)	0.159(10)	0.160(11)	0.26(2)
Cu10	0.155(9)	0.25(2)	0.63(3)	0.159(10)	0.160(11)	0.26(2)
Ag11	0.116(4)	0.132(3)	0.54(2)	0.026(2)	0.061(4)	-0.048(5)
Cu11	0.116(4)	0.132(3)	0.54(2)	0.026(2)	0.061(4)	-0.048(5)
Ag12	0.156(9)	0.203(14)	0.91(5)	0.087(9)	0.13(2)	0.21(2)
Cu12	0.156(9)	0.203(14)	0.91(5)	0.087(9)	0.13(2)	0.21(2)
Ag13	0.198(9)	0.234(12)	0.194(12)	0.183(9)	0.119(7)	0.110(8)
Cu13	0.198(9)	0.234(12)	0.194(12)	0.183(9)	0.119(7)	0.110(8)
Ag14	0.171(9)	0.077(4)	0.272(10)	0.003(4)	-0.028(6)	-0.089(5)
Cu14	0.171(9)	0.077(4)	0.272(10)	0.003(4)	-0.028(6)	-0.089(5)
Ag15	0.449(10)	0.178(4)	0.175(4)	0.225(5)	0	0.048(2)

Cu15	0.449(10)	0.178(4)	0.175(4)	0.225(5)	0	0.048(2)
Ag16	0.197(12)	0.131(6)	0.145(6)	0.107(7)	-0.013(4)	-0.067(4)
Cu16	0.197(12)	0.131(6)	0.145(6)	0.107(7)	-0.013(4)	-0.067(4)

Table S12. Anharmonic displacement parameters of α -Ag₁₈Cu₃Te₁₁Cl₃ at 400 K.

Atom	C_{111}	C_{112}	C_{113}	C_{122}	C_{123}
Te7	-0.0110(8)	-0.0065(4)	0	-0.0065(4)	0
Te8	0.0018(6)	-0.0005(4)	0	0.0000(4)	0
Te9	-0.019(7)	-0.024(10)	0	-0.040(14)	0
Ag1	0	0.0101(13)	0	0.0101(13)	0
Cu1	0	0.0101(13)	0	0.0101(13)	0
Ag2	0.163(8)	0	0	-0.0171(13)	0
Cu2	0.163(8)	0	0	-0.0171(13)	0
Ag3	0	0.014(8)	-0.009(2)	0.014(8)	0
Cu3	0	0.014(8)	-0.009(2)	0.014(8)	0
Ag4	0	0	-0.018(2)	0	-0.0092(11)
Cu4	0	0	-0.018(2)	0	-0.0092(11)
Ag5	0	-0.015(3)	-0.014(2)	0	-0.013(2)
Cu5	0	-0.015(3)	-0.014(2)	0	-0.013(2)
Ag6	0.25(2)	0.21(2)	0.025(3)	0.144(14)	0.025(2)
Cu6	0.25(2)	0.21(2)	0.025(3)	0.144(14)	0.025(2)
Ag7	-0.005(2)	0	0.0035(5)	0.018(2)	0.0040(5)
Cu7	-0.005(2)	0	0.0035(5)	0.018(2)	0.0040(5)
Ag8	0.045(11)	0.025(7)	0.016(3)	0.033(7)	0.015(2)
Cu8	0.045(11)	0.025(7)	0.016(3)	0.033(7)	0.015(2)
Ag9	0.017(3)	0.010(2)	0	0	0.0013(3)
Cu9	0.017(3)	0.010(2)	0	0	0.0013(3)
Ag10	-0.014(7)	-0.035(9)	-0.025(5)	-0.068(13)	-0.039(6)
Cu10	-0.014(7)	-0.035(9)	-0.025(5)	-0.068(13)	-0.039(6)
Ag11	-0.012(2)	0	-0.0061(11)	-0.0052(11)	0
Cu11	-0.012(2)	0	-0.0061(11)	-0.0052(11)	0
Ag12	-0.064(10)	-0.016(6)	-0.016(5)	0.028(7)	0.021(4)
Cu12	-0.064(10)	-0.016(6)	-0.016(5)	0.028(7)	0.021(4)
Ag13	-0.048(8)	-0.059(8)	-0.018(2)	-0.075(10)	-0.025(3)
Cu13	-0.048(8)	-0.059(8)	-0.018(2)	-0.075(10)	-0.025(3)
Ag14	0.048(11)	-0.012(4)	-0.030(3)	0	0.0084(13)
Cu14	0.048(11)	-0.012(4)	-0.030(3)	0	0.0084(13)
Ag15	0	0.089(5)	0.084(4)	0.089(5)	0.042(2)
Cu15	0	0.089(5)	0.084(4)	0.089(5)	0.042(2)
Ag16	-0.031(8)	-0.039(7)	0.014(2)	-0.031(5)	0.0072(12)
Cu16	-0.031(8)	-0.039(7)	0.014(2)	-0.031(5)	0.0072(12)
	C_{133}	C_{222}	C_{223}	C_{233}	C_{333}
Te7	0.00013(5)	0	0	0	0
Te8	0.00013(4)	-0.0006(7)	0	-0.00036(5)	0
Te9	-0.0012(3)	-0.07(3)	0	-0.0017(5)	0
Ag1	0	0.015(3)	0	0	0
Cu1	0	0.015(3)	0	0	0
Ag2	-0.0016(2)	-0.021(2)	0	0	0
Cu2	-0.0016(2)	-0.021(2)	0	0	0
Ag3	0	0	-0.009(2)	0	0
Cu3	0	0	-0.009(2)	0	0

Ag4	0	-0.100(13)	0.010(2)	0	0
Cu4	0	-0.100(13)	0.010(2)	0	0
Ag5	0	-0.027(6)	0.015(3)	-0.017(2)	0.0089(14)
Cu5	0	-0.027(6)	0.015(3)	-0.017(2)	0.0089(14)
Ag6	0	0.073(10)	0.012(2)	0	0
Cu6	0	0.073(10)	0.012(2)	0	0
Ag7	0	0.034(4)	0.0112(9)	0	0.0014(2)
Cu7	0	0.034(4)	0.0112(9)	0	0.0014(2)
Ag8	0.0043(10)	0.035(7)	0.017(2)	0.0053(9)	0.0016(4)
Cu8	0.0043(10)	0.035(7)	0.017(2)	0.0053(9)	0.0016(4)
Ag9	-0.0009(2)	-0.009(3)	0.0057(6)	0	0
Cu9	-0.0009(2)	-0.009(3)	0.0057(6)	0	0
Ag10	-0.038(5)	-0.10(2)	-0.044(9)	-0.044(6)	-0.046(5)
Cu10	-0.038(5)	-0.10(2)	-0.044(9)	-0.044(6)	-0.046(5)
Ag11	-0.0180(13)	0	0.018(2)	-0.026(2)	-0.0143(12)
Cu11	-0.0180(13)	0	0.018(2)	-0.026(2)	-0.0143(12)
Ag12	0.021(5)	0.09(2)	0.051(7)	0.042(4)	0
Cu12	0.021(5)	0.09(2)	0.051(7)	0.042(4)	0
Ag13	-0.0033(7)	-0.092(12)	-0.032(3)	-0.0060(9)	0.0012(5)
Cu13	-0.0033(7)	-0.092(12)	-0.032(3)	-0.0060(9)	0.0012(5)
Ag14	-0.0033(10)	-0.013(3)	0.017(2)	-0.017(2)	0.0150(12)
Cu14	-0.0033(10)	-0.013(3)	0.017(2)	-0.017(2)	0.0150(12)
Ag15	0	0.063(4)	0.0204(10)	0.0015(2)	0
Cu15	0	0.063(4)	0.0204(10)	0.0015(2)	0
Ag16	0	-0.016(4)	0.0032(7)	0	0
Cu16	0	-0.016(4)	0.0032(7)	0	0

For a more realistic evaluation of atom positions and bond lengths in the case of anharmonic refinement, so called “mode positions” that represent the maximum of electron density were determined by calculating pdf (probability density functions). Mode positions of all refinements are given in **Table S13-S16**.

Table S13. Mode positions of anharmonic refined atoms in β -Ag₁₈Cu₃Te₁₁Cl₃ at 270 K.

Atom	<i>x</i>	<i>y</i>	<i>z</i>
AgCu1	0	0.8875	0.25
AgCu2	0.6527	0.4526	0.25
AgCu3	0.578	0.578	0.1924
AgCu4	0	0.799	0.193
AgCu5	0.634	0.5134	0.1944
AgCu6	0.5519	0.8487	0.185
AgCu7	0.123	0.8577	0.1606
AgCu8	0.4693	0.5512	0.1687
AgCu9	0.5843	0.7921	0.1641
AgCu10	0.5614	0.4156	0.1205
AgCu11	0.8866	0.8183	0.1172
AgCu12	0.7727	0.5178	0.114
AgCu13	0.5274	0.4213	0.0706

AgCu14	0.769	0.5622	0.0715
AgCu15	0	0.8024	0.0489
AgCu16	0.6718	0.5322	0.0483

Table S14. Mode positions of anharmonic refined atoms in α -Ag₁₈Cu₃Te₁₁Cl₃ at 330 K.

Atom	<i>x</i>	<i>y</i>	<i>z</i>
Te7	0.5666	0	0.25
Te8	0.3129	0.1225	0.25
Te9	0.3515	0.2026	0.25
AgCu1	0	0.8837	0.25
AgCu2	0.6511	0.4504	0.25
AgCu3	0.5829	0.5829	0.1926
AgCu4	0	0.7958	0.192
AgCu5	0.634	0.5228	0.1932
AgCu6	0.5492	0.8539	0.1857
AgCu7	0.1218	0.8671	0.162
AgCu8	0.4595	0.5435	0.1666
AgCu9	0.584	0.7882	0.1636
AgCu10	0.5526	0.4046	0.1138
AgCu11	0.884	0.8156	0.1172
AgCu12	0.7716	0.5206	0.1149
AgCu13	0.5412	0.4367	0.073
AgCu14	0.7789	0.5567	0.0715
AgCu15	0	0.8022	0.0517
AgCu16	0.6712	0.5324	0.0529

Table S15. Mode positions of anharmonic refined atoms in α -Ag₁₈Cu₃Te₁₁Cl₃ at 350 K.

Atom	<i>x</i>	<i>y</i>	<i>z</i>
Te7	0.566	0	0.25
Te8	0.3125	0.1218	0.25
Te9	0.3498	0.2011	0.25
AgCu1	0	0.8811	0.25
AgCu2	0.653	0.4512	0.25
AgCu3	0.5972	0.5972	0.1939
AgCu4	0	0.8002	0.1932
AgCu5	0.6399	0.5016	0.1941
AgCu6	0.5401	0.8506	0.1874
AgCu7	0.1202	0.8673	0.1607
AgCu8	0.4602	0.546	0.1652
AgCu9	0.5831	0.7861	0.1625
AgCu10	0.5542	0.408	0.1125
AgCu11	0.8873	0.8149	0.1171
AgCu12	0.7676	0.5208	0.1158
AgCu13	0.5359	0.4284	0.0726
AgCu14	0.7712	0.5612	0.0791
AgCu15	0	0.8033	0.0501
AgCu16	0.6736	0.5291	0.0514

Table S16. Mode positions of anharmonic refined atoms in α -Ag₁₈Cu₃Te₁₁Cl₃ at 400 K.

Atom	x	y	z
Te7	0.5594	0	0.25
Te8	0.3131	0.1204	0.25
Te9	0.3531	0.2034	0.25
AgCu1	0	0.8786	0.25
AgCu2	0.6549	0.4491	0.25
AgCu3	0.6079	0.6079	0.2001
AgCu4	0	0.7927	0.1892
AgCu5	0.6446	0.5038	0.1953
AgCu6	0.5482	0.8677	0.1877
AgCu7	0.17	0.8714	0.1631
AgCu8	0.4597	0.5488	0.1664
AgCu9	0.5825	0.7867	0.1652
AgCu10	0.5505	0.4045	0.1128
AgCu11	0.8873	0.8149	0.1171
AgCu12	0.7676	0.5208	0.1158
AgCu13	0.5359	0.4284	0.0726
AgCu14	0.7712	0.5612	0.0791
AgCu15	0	0.8033	0.0501
AgCu16	0.6736	0.5291	0.0514

EDX measurements.

Area measurements have been performed on one crystal facet of two different single crystals.

The average Ag:Cu ratio is 52.71:8.66, or 6.09:1, matching the initial composition of Ag₁₈Cu₃Te₁₁Cl₃.

Table S17. EDX data of two crystal faces of different Ag₁₈Cu₃Te₁₁Cl₃ single crystals. The estimated overall error of each data point is larger than +/- 1%.

	Ag [at%]	Cu [at%]	Te [at%]	Cl [at%]
Ag ₁₈ Cu ₃ Te ₁₁ Cl ₃ theoretical	51.43	8.57	31.43	8.57
crystal 1	51(1)	9(1)	30(1)	10(1)
crystal 2	54(1)	8(1)	29(1)	9(1)
Average	52.5	8.5	29.5	9.5

Bulk modulus determination

The bulk modulus was determined to $K_0 = 28.2(11)$ GPa by a 3rd order Birch-Murnaghan Equation of State fit. 2nd and 3rd order fits are given in **Figure S4**. Unit cell parameters determined from pressure dependent XRD are shown in **Table S18**.

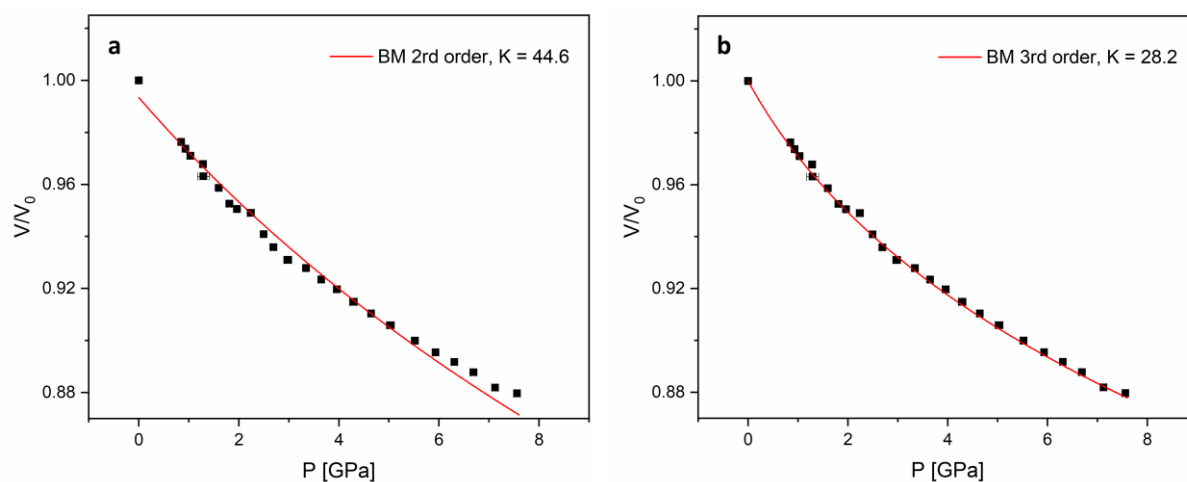


Figure S4. Data of bulk modulus measurements. 2nd (a) and 3rd (b) order Birch-Murnaghan Equation of State fit for $\text{Ag}_{18}\text{Cu}_3\text{Te}_{11}\text{Cl}_3$. Data according to **Table S18** are used. The error bars are located within the measurement points.

Table S18. Unit cell parameters determined from pressure-dependent XRD experiments. Pressure was applied via a Diamond-Anvil cell, and XRD data were collected at the Diamond Light Source, Ditcot, UK, using Synchrotron radiation.

Pressure [Gpa]	a [Å]	c [Å]	V [Å ³]	Profile R_p	Profile wR_p
0	13.5506(12)	30.772(2)	4893.4(7)	-	-
0.85	13.434(2)	30.5692(14)	4777(2)	0.0212	0.0621
0.93	13.4211(8)	30.543(2)	4764.4(9)	0.0106	0.0221
1.03	13.4103(14)	30.508(4)	4751(2)	0.0119	0.0308
1.28	13.3953(14)	30.475(4)	4735(2)	0.0125	0.0318
1.29	13.3753(12)	30.419 (3)	4712.7(13)	0.0111	0.0236
1.60	13.3542(14)	30.374(4)	4691(2)	0.0134	0.035
1.81	13.3281(13)	30.300(4)	4661(2)	0.0131	0.0301
1.96	13.319(2)	30.275(4)	4651(2)	0.0125	0.0282
2.24	13.3157(10)	30.242(4)	4643.6(14)	0.0151	0.0341
2.50	13.2841(12)	30.126(6)	4604(2)	0.0222	0.0415
2.69	13.2668(10)	30.044(4)	4579.3(14)	0.0226	0.0416
2.98	13.2418(11)	30.001(5)	4556(2)	0.0223	0.0418
3.34	13.2186(8)	30.004(4)	4540.1(12)	0.0205	0.0393
3.65	13.1974(2)	29.958(3)	4518.7(6)	0.0204	0.0391
3.96	13.1793(8)	29.917(3)	4500.1(11)	0.0207	0.0387
4.29	13.1560(9)	29.866(4)	4476.6(11)	0.021	0.0393
4.64	13.1347(9)	29.816(3)	4454.6(12)	0.0209	0.0384
5.03	13.1123(9)	29.770(3)	4432.5(11)	0.0208	0.0376
5.52	13.0836(9)	29.704(4)	4403.4(11)	0.0201	0.0365
5.93	13.0624(9)	29.653(4)	4381.6(11)	0.0201	0.0366
6.31	13.0448(9)	29.610(4)	4363.4(11)	0.0196	0.0348
6.69	13.0263(10)	29.562(4)	4344.0(13)	0.0197	0.035
7.12	12.9919(10)	29.523(4)	4315.4(12)	0.0191	0.0347
7.56	12.9848(2)	29.481(5)	4305(2)	0.0196	0.0354

Solid-state NMR

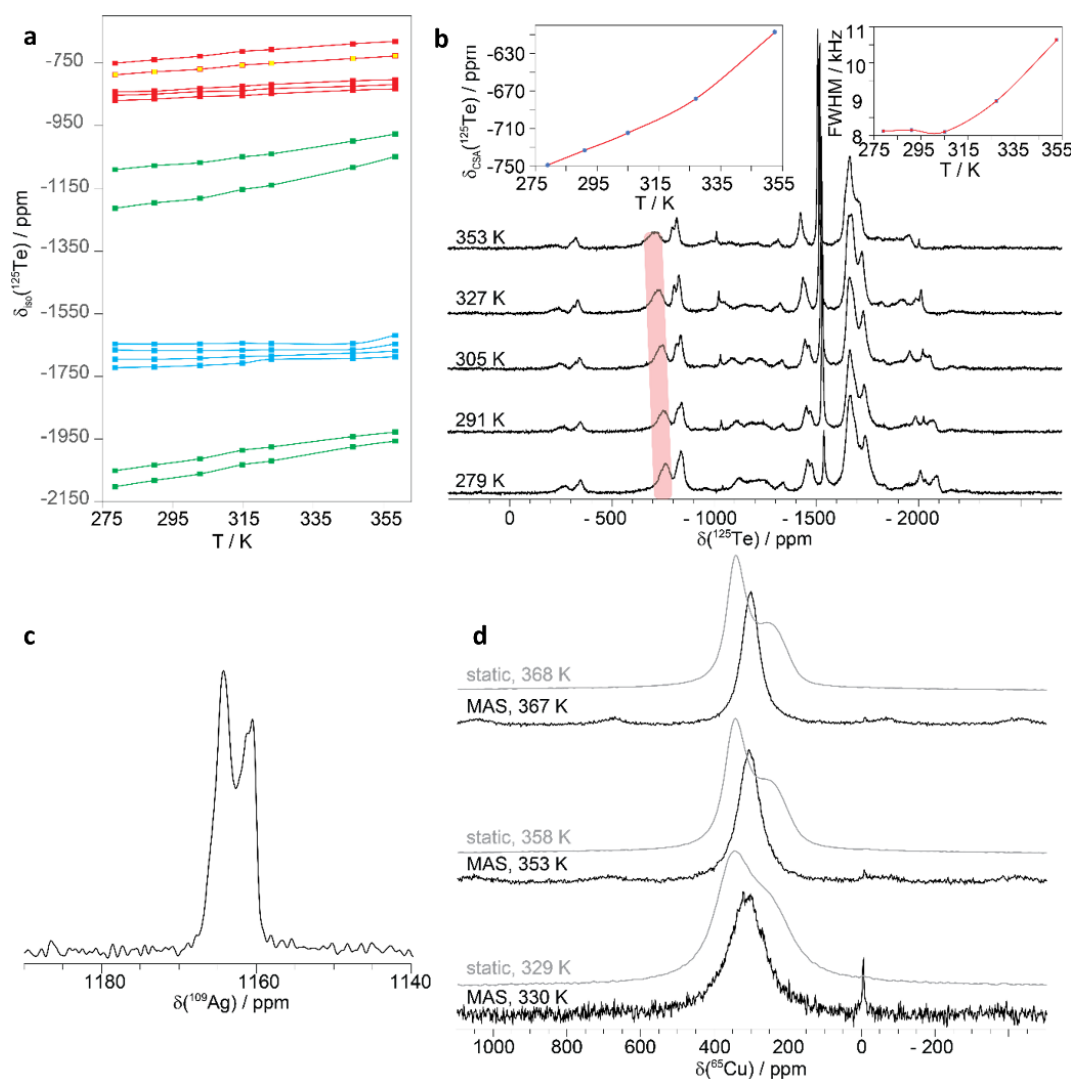


Figure S5. Solid-state NMR Data. a) Drift of the ^{125}Te isotropic chemical shifts with temperature, from the spectra shown in Figure 4. b) ^{125}Te MAS spectra ($\nu_{\text{rot}} = 62.5$ kHz) for the ^{125}Te -enriched $\text{Ag}_{18}\text{Cu}_3\text{Te}_{11}\text{Cl}_3$ sample at different temperature. The chemical shift anisotropy and full width at half maximum as a function of temperature are shown as insets. c) ^{109}Ag MAS spectrum ($\nu_{\text{rot}} = 40.0$ kHz) of $\text{Ag}_{18}\text{Cu}_3\text{Te}_{11}\text{Cl}_3$ acquired at room temperature. d) ^{65}Cu MAS spectrum (black, $\nu_{\text{rot}} = 62.5$ kHz) compared to the static spectra (grey) of $\text{Ag}_{18}\text{Cu}_3\text{Te}_{11}\text{Cl}_3$ at different temperatures.

U/I-measurements

In order to rule out the formation of Schottky diodes during the measurements, $\text{Ag}_{18}\text{Cu}_3\text{Te}_{11}\text{Cl}_3$ and AgCuS crystals were tested with tin-lead instead of indium contacts.^[14]

Figure S6a shows $\text{Ag}_{18}\text{Cu}_3\text{Te}_{11}\text{Cl}_3$ contacted with tin/lead solder. It was measured isothermally at 281 K (blue curve) and within a 295-308 K temperature gradient (red curve). At 281 K we observed an almost symmetric, ohmic behavior while a diode curve was found for the 295-308 K temperature gradient. The result indicates the successful preparation of a pn-junction independent from the solder material. The same set of experiments was performed with the pnp-switching material AgCuS (**Figure S6b**).^[14] This material shows a pn-transition at 361 K. An isothermal measurement was performed at 298(1) K. The temperature gradient, also leading to a diode curve was set to 333 to 365 K. The successful generation pn-junctions in the case of In (see main text) and tin/lead contacts substantiates that pnp-switching materials can be used for diodes in general.

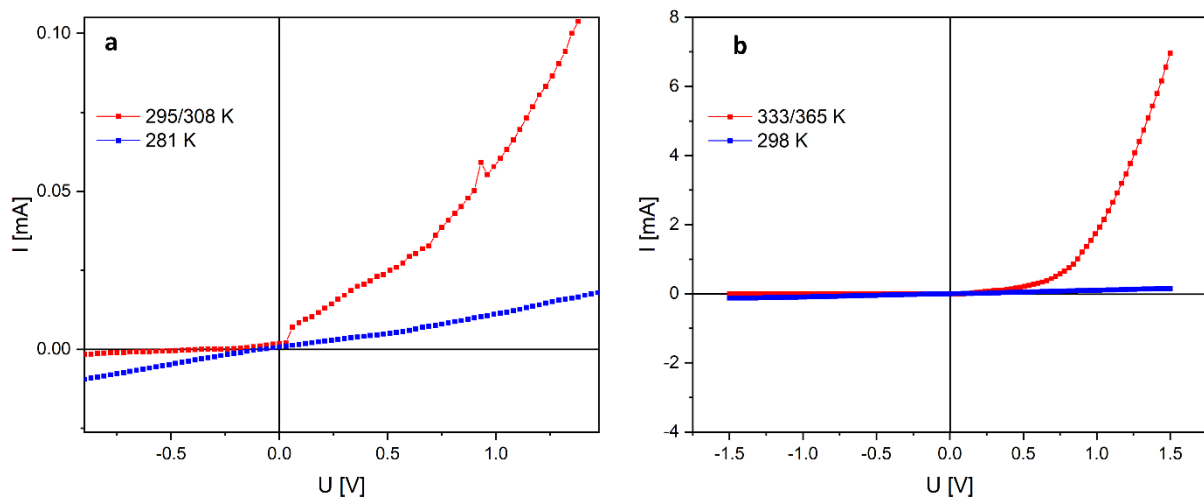


Figure S6. a) U/I measurements on $\text{Ag}_{18}\text{Cu}_3\text{Te}_{11}\text{Cl}_3$ contacted with tin/lead. Blue: isothermal at 281 K. Red: with a 295/308 K temperature gradient. b) U/I measurements on AgCuS .^[13] Blue: isothermal at 298 K. Red: with a 333/365 K temperature gradient.

Schockley-Queisser limit

In 2016, Rühle published a collection of data summarizing the solar cell performance at that time (**Figure S7**).^[14] $\text{Ag}_{18}\text{Cu}_3\text{Te}_{11}\text{Cl}_3$ shows an almost perfect bandgap for the realization of single junction solar cells as it is perfectly located in the efficiency maximum according to the Schockley-Queisser limit.^[15]

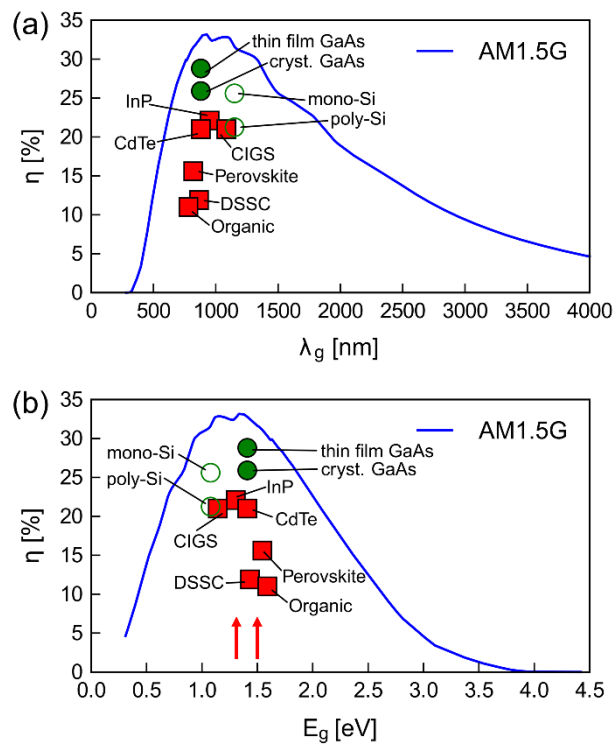


Figure S7. Schockley-Queisser limit or the maximum light to electric power conversion efficiency at 298.15K (AM1.5G source) with a) band gap wavelengths and b) energies. Red arrows denote the band gaps of 1.35 and 1.50 eV measured for $\text{Ag}_{18}\text{Cu}_3\text{Te}_{11}\text{Cl}_3$. Reprinted from *Solar Energy*, 130, Rühle, S., Tabulated values of the Shockley-Queisser limit for single junction solar cells, 139-147, Copyright (2016), with permission from Elsevier.^[14]

References (Supplement section)

- [1] A. Vogel, T. Nilges, *Inorg. Chem.* **2021**, 60(20), 15233.
- [2] S. Lange, T. Nilges, *Chem. Mater.* **2006**, 18(10), 2538.
- [3] S. Lange, M. Bawohl, D. Wilmer, H.-W. Meyer, H.-D. Wiemhöfer, T. Nilges, *Chem. Mater.* **2007**, 19(6), 1401.
- [4] A. Vogel, T. Miller, C. Hoch, M. Jakob, O. Oeckler, T. Nilges, *Inorg. Chem.* **2019**, 58(9), 6222.
- [5] R. Blachnik, H. A. Dreisbach, *J. Solid State Chem.* **1985**, 60(1), 115.
- [6] T. Nilges, S. Nilges, A. Pfitzner, T. Doert, P. Böttcher, *Chem. Mater.* **2004**, 16(5), 806.
- [7] J. Peters, O. Conrad, B. Bremer, B. Krebs, *Z. Anorg. Allg. Chem.* **1996**, 622(11), 1823.
- [8] T. Nilges, S. Lange, M. Bawohl, J. M. Deckwart, M. Janssen, H.-D. Wiemhöfer, R. Decourt, B. Chevalier, J. Vannahme, H. Eckert, R. Weihrich, *Nat. Mater.* **2009**, 8(2), 101.
- [9] W. F. Kuhs, *Acta Cryst A* **1992**, 48(2), 80.
- [10] T. Nilges, S. Reiser, J. H. Hong, E. Gaudin, A. Pfitzner, *PCCP* **2002**, 4(23), 5888.
- [11] S. Yanagisawa, M. Tashiro, S. Anzai, *J. Inorg. Nucl. Chem.* **1969**, 31(4), 943.
- [12] P. Böttcher, J. Getzschmann, R. Keller, *Z. Anorg. Allg. Chem.* **1993**, 619(3), 476.
- [13] S. N. Guin, J. Pan, A. Bhowmik, D. Sanyal, U. V. Waghmare, K. Biswas, *J. Am. Chem. Soc.* **2014**, 136(36), 12712.
- [14] S. Rühle, *Sol. Energy* **2016**, 130139.
- [15] W. Shockley, H. J. Queisser, *J. Appl. Phys.* **1961**, 32(3), 510.

3.2 AgCuS: A Single Material Diode with Fast Switching Times

Philipp Deng¹, Alfred Rabenbauer¹, Kathrin Vosseler¹, Janio Venturini¹, Tom Nilges¹

¹Technical University Munich, School of Natural Sciences (NAT), Department of Chemistry, Synthesis and Characterization of Innovative Materials Group, Lichtenbergstraße 4, 85748 Garching bei München, Germany

Adv. Funct. Mater. **2023**, 2213882

First published: February 20th 2023

After the discovery of its pnp-switchable ability in 2014, AgCuS was the material with the lowest switching temperature until our characterization of $\text{Ag}_{18}\text{Cu}_3\text{Te}_{11}\text{Cl}_3$. With 364 K (literature value), this temperature is located moderately above room temperature, and should also enable an easy access to pnp-switchable devices like diodes and transistors.¹¹ In this project, we re-assessed the electronic properties of pnp-switch in order to create a second one-compound diode. Furthermore, we compared the diode properties to the first representative of one-compound diode materials, namely $\text{Ag}_{18}\text{Cu}_3\text{Te}_{11}\text{Cl}_3$, and developed and characterized further switching applications of the newly created AgCuS diode. First of all, PXRD and DSC measurements are performed on freshly prepared samples of AgCuS to confirm the phase transition (orthorhombic β - to hexagonal α -phase) related to the conduction type switching. The electrical conductivity as well as the Seebeck coefficient are then measured in a temperature range of 300 – 390 K, showing a Seebeck coefficient drop from +648 to 393 $\mu\text{V K}^{-1}$ at ~360 K, accompanied by a slight increase in conductivity, which are both enabled by the aforementioned phase transition at 358(1) K (onset temperature, determined by own measurements). After the verification of those properties, different one-compound diode devices are created by mounting cut parts of AgCuS ingots on specially designed PCBs, enabling the contacting of the material at opposite sides with the possibility to independently control the temperature of those sides by resistive heating. By heating just one side to 368 K, slightly above the transition temperature, a one-compound pn-junction diode is created, perfectly showing rectifying behavior in the measured U/I curves, with a forward current around 75 times higher than the reverse current. In addition, the switching time is assessed, showing a total switching time t_s of 2.5 s, which is around 25 times faster in comparison to the 62.4 s of $\text{Ag}_{18}\text{Cu}_3\text{Te}_{11}\text{Cl}_3$. This is mainly caused by the massive reduction of the fall time, where excess minority carriers are discharged from the junction after switching the polarity, and is related to the higher thermal energy of the carriers at a temperature around 70 K higher than in $\text{Ag}_{18}\text{Cu}_3\text{Te}_{11}\text{Cl}_3$. Afterwards, the reversible formation and cancellation of a AgCuS one-compound diode is realized by reversible on- and off-switching of the temperature gradient. This results in the repeated creation of rectifying U/I curves, only slightly differing in their

conductivities as well as threshold voltages, due to slight fluctuations in the applied thermal gradient. In the last part of the work, the direction of current flow in the device is changed. This is facilitated by alternately heating the opposite side of the ingot with the second resistive heater. The p- and n regions in the ingot are inverted, leading to the change of the forward and reverse area of the diode, which would only be possible for classical diodes by resoldering of the contacts.

Author contributions: A.R. synthesized the compounds and performed the XRD and DSC measurements. A.R. and K.V. performed the EDX analysis. A.R. prepared all samples and characterized the thermoelectric performance of the material. A.R. and P.D. conducted the UI-measurements and different diode switching experiments. A.R., P.D. and T.N. wrote the manuscript. All authors discussed the results and revised the manuscript.

Reprint of Deng P.; Rabenbauer, A.; Vosseler, K.; Venturini, J.; Nilges, T.; ‚AgCuS: A Single Material Diode with Fast Switching Times‘, *Adv. Funct. Mater.* **2023**, 2214882. This work is licensed under the Creative Commons Attribution – Non Commercial - 4.0 International License. To view a copy of this license, visit <https://creativecommons.org/licenses/by-nc/4.0/legalcode> or send a letter to Creative Commons, PO Box 1866, Mountain View, CA 94042, USA.

AgCuS: A Single Material Diode with Fast Switching Times

Philipp Deng, Alfred Rabenbauer, Kathrin Vosseler, Janio Venturini, and Tom Nilges*

Pnp-switchable semiconductor materials are capable of switching their electronic properties from *p*- to *n*-type conduction. Observed in the handful of discovered compounds, this behavior is usually accompanied by a temperature-dependent phase transition. During this transition, the dynamical rearrangement of a certain substructure enables the change of the predominant charge carrier type. Considering the immense demand for compact and flexible electronic components, one possible approach is the construction of unconventional one-compound diodes using these pnp-switchable materials. In this study, pnp-switchable AgCuS is applied to realize a functional one-compound diode. AgCuS is accessible in large quantities as bulk material in a simple and short timeframe. Featuring an addressable pnp-switch at 364 K, this material is suitable for diode generation and usage in varied applications. The diode properties of AgCuS devices are reported and illustrate its reversibility and flexibility for diode operation. The material is fully characterized with regards to its electrical and thermal properties, as well as its diode performance. Properties of AgCuS are discussed in relation to the pnp-switchable material $\text{Ag}_{18}\text{Cu}_3\text{Te}_{11}\text{Cl}_3$, which is successfully used to fabricate the first one-compound diode operating close to room temperature.

single material that can switch between *p*- and *n*-type depending on its temperature and phase.^[7]

The first pnp-switchable material, $\text{Ag}_{10}\text{Te}_4\text{Br}_3$, was discovered in 2009. During heating, the material undergoes an order-disorder phase transition at 390 K, while at the same time a charge density wave (CDW) is created through the chain-like polytelluride substructure. This CDW results in the creation of mobile electrons, changing the predominant charge carrier type during the transition and therefore switching the semiconductor from *p*- to *n*-type conducting.^[7]

In principle, this pn-switch without any external doping of the compound is an intriguing property, which was never observed before in an inorganic material. Via substitution in the anion and cation substructures this pn-switching effect was shifted in temperature in a range of 400 to 380 K.^[8–10] Upon halide-substitution the pn-effect remains unchanged in

$\text{Ag}_{10}\text{Te}_4\text{Br}_3$ while any chalcogenide-substitution hinders a CDW formation and therefore the pn-switch. This discovery led to an intensive search for additional compounds capable to perform such kind of electronic structure manipulations. In principle, a reversible and addressable pn-switch can be used to fabricate diodes and transistors if the *p*- and *n*-type conduction can be controlled in an easy way, the creation of *p*- and *n*-areas are defined, and the electronic structure variation leads to a defined electronic response. For these purposes the pn-switch needs to be located in a suitable temperature range, e.g. close to room or application temperature, and the diode formation needs to be reliable and controllable.


In the following years, three other inorganic compounds were identified which perform a pn-switch. AgBiSe_2 shows this pn-switch at 580 K, $\text{Tl}_2\text{Ag}_{12}\text{Se}_7$ at 410 K, and finally AgCuS at 364 K.^[11–13] Evidently, the pn-transition temperature was lowered toward room temperature, where most devices and processes with diode or transistor contribution take place. Finally, with $\text{Ag}_{18}\text{Cu}_3\text{Te}_{11}\text{Cl}_3$ the first material was reported recently to show a pn-switch at room temperature. Using $\text{Ag}_{18}\text{Cu}_3\text{Te}_{11}\text{Cl}_3$, the first one-compound diode device was prepared and the diode formation and performance for this system were reported.^[14] Another interesting attempt to fabricate a diode via pn-junctions was the realization of an organic single molecule diode.^[15] Here, weakly coupled π -systems with donor and acceptor units that are attached to a rod can result in a diode-like U/I curve at 30 K.

The combination of *p*- and *n*-type semiconductors is not only used in electrical engineering, but also plays a key role in

1. Introduction

Diodes are basic building units which allow electrical current to pass in only one defined direction. They act as one-way switches and have become a prerequisite for almost every electronic device.^[1–5] To achieve this behavior, *n*- and *p*-type semiconductors have to be combined to form a pn-junction. This could either be addressed by the combination of two different materials, or at least by the defined creation of different doping levels within the device. As the continuous downscaling of diodes and transistors becomes more challenging, alternative designs for the construction of these electronic components are required.^[6] One approach is the realization of a diode using one

P. Deng, A. Rabenbauer, K. Vosseler, J. Venturini, T. Nilges
School of Natural Sciences (NAT)
Department of Chemistry
Synthesis and Characterization of Innovative Materials Group
Technical University of Munich
Lichtenbergstraße 4, 85748 Garching b. München, Germany
E-mail: tom.nilges@tum.de

 The ORCID identification number(s) for the author(s) of this article can be found under <https://doi.org/10.1002/adfm.202214882>.

© 2023 The Authors. Advanced Functional Materials published by Wiley-VCH GmbH. This is an open access article under the terms of the Creative Commons Attribution-NonCommercial License, which permits use, distribution and reproduction in any medium, provided the original work is properly cited and is not used for commercial purposes.

DOI: 10.1002/adfm.202214882

sensors, light emitting diodes (LEDs), catalytic processes and energy conversion system, e.g. solar cells, or thermoelectric devices.^[3,16–24] In each of those processes, the pn-junction needs to be formed at a certain place (or *p*- and *n*-type semiconductors are separated in thermoelectric applications). As conventional diodes are non-volatile, the position of the junction or the semiconductors itself is not flexible and in principle defined by the doping type and level in a given material.

With the realization of one-compound diode devices, like in the case of $\text{Ag}_{18}\text{Cu}_3\text{Te}_{11}\text{Cl}_3$, it has been shown that a diode can be generated on demand and position-independently.^[14] Once one-compound diodes are transferred into the aforementioned processes, this aspect may increase the flexibility of the device architecture drastically. With pnp-switching materials applied as one-compound diodes, more versatility can be achieved not only concerning the position, but in principle also in the direction of current flow. To realize a switch of the forward direction of the diode, only the temperature gradient has to be reversed in this one-compound diode device.

In this study we investigate the properties of AgCuS used as a one-compound diode. This mineral called stromeyerite was first characterized as a pnp-switchable material by Biswas et al.^[13,25,26] They reported on the polymorphism, thermoelectric, electronic and pnp-switching properties of this intriguing material. Also the pnp-switching mechanism has been reported in this study. Reduction of particle size down to the nanometer regime and a certain non-stoichiometry in the Cu substructure ($\text{AgCu}_{1-x}\text{S}$, $x = 0.01$ to 0.04) resulted in a loss of the pn-switching property.^[27,28] Defects in the silver substructure $\text{Ag}_{1-x}\text{CuS}$ of up to 10% ($\text{Ag}_{1-x}\text{CuS}$, $x = 0.01$ to 0.15) are less critical and the pn-switch still takes place, but is less pronounced than in AgCuS.

2. Results and Discussion

2.1. Phase Analysis and Characterization of AgCuS

All pnp-switchable materials known until now – $\text{Ag}_{10}\text{Te}_4\text{Br}_3$, $\text{Ag}_{18}\text{Cu}_3\text{Te}_{11}\text{Cl}_3$, $\text{Tl}_2\text{Ag}_{12}\text{Se}_7$, AgBiSe_2 , and the herein discussed AgCuS – show temperature dependent polymorphism.^[7,11–14] The crucial role of those transitions concerning the semiconduction type is discussed in detail later on in this manuscript. For AgCuS, three different polymorphs are reported in the range of 298 to 439 K (see **Figure 1**).^[13] Throughout those phase transitions, the cationic substructure becomes more and more disordered with increasing temperature. In the room temperature β -polymorph, crystallizing orthorhombically, in space group $Cmc2_1$ (36), Cu and Ag are completely ordered and therefore separated from each other on two different Wyckoff sites $4a$. In the first high temperature α -phase, that is stable above 358 K (onset value determined from our own DSC experiments, with literature values 361^[25] and 364 K^[13]) and crystallizes hexagonally, in space group $P6_3/mmc$ (194), partial disorder in the cation substructure takes place and 25% of the copper atoms mix with silver atoms on partially occupied $12k$ sites. Upon further heating, the δ -polymorph is formed at 439 K, crystallizing cubically, in space group $Fm\bar{3}m$ (223). In this modification, the cations are completely disordered, resulting in a partial and mixed occupancy of Cu and Ag on $8c$ and $32f$ sites.^[13,29] Representative structure sections including unit cells are depicted in **Figure 1**. Partial occupancy of sites is illustrated at the bottom part of **Figure 1**, bottom row, using open circles.

The powder XRD of our AgCuS sample synthesized via the method described by Biswas et al. is shown in **Figure 2a**.^[13]

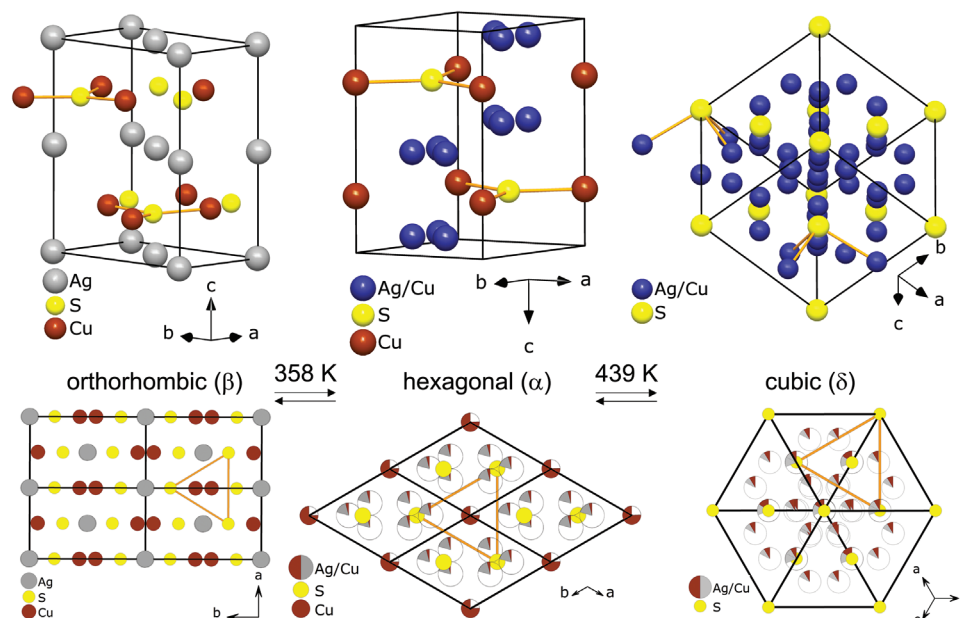


Figure 1. Top row: Selected structure motifs of the three different AgCuS polymorphs. Structure data taken from Biswas et al.^[13] The different unit cells and a representative $\text{S}-(\text{Cu}/\text{Ag})_3$ structure motif are displayed in the upper part. Bottom row: Changes in occupancy factors in the cation substructure. S_3 triangles are depicted in each polymorph to illustrate the changes in the crystal structure upon heating. A fully ordered cation substructure in the β -polymorph tends to disorder upon heating.

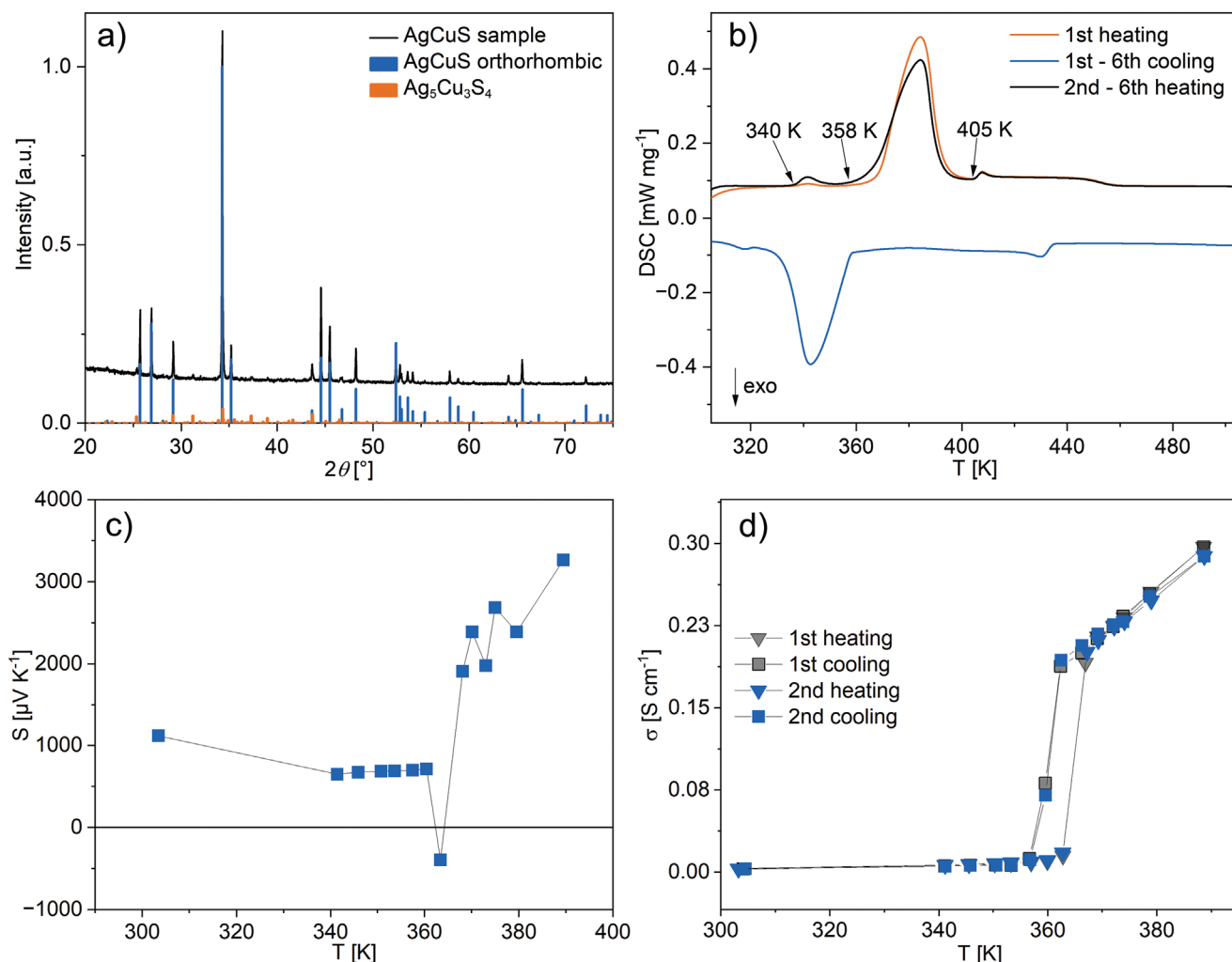


Figure 2. a) Powder XRD of the synthesized AgCuS sample, measured at 300 K. The theoretical patterns of AgCuS in the low-temperature orthorhombic phase (blue)^[13] and Ag₅Cu₃S₄ (orange)^[25] are depicted below. b) Differential scanning calorimetry curves of AgCuS sample for six consecutive cycles were measured. Two broad endothermic signals with onset points at 358 and 405 K are visible during first heating. An additional third very weak endothermic signal is already visible at an onset of 340 K which increases slightly in intensity in the second heating cycle. From 2nd to 6th cycle the thermal response is identical for heating and cooling. c) Seebeck coefficient measurement of AgCuS in a range of 303 to 388 K, displaying the pnp-switching ability of the material. d) Electrical conductivity measurement of AgCuS in a range of 303 to 388 K. Lines between the points are drawn to guide the eyes.

These reflections were indexed and refined using an orthorhombic symmetry, in the space group *Cmc2₁*, resulting in refined cell parameters of $a = 7.974(5)$ Å, $b = 6.627(4)$ Å, $c = 4.066(2)$ Å, and $V = 214.9(4)$ Å³. These values are nearly identical to those reported in the CIF data for the mineral stromeyerite ($a = 4.0673$ Å, $b = 6.6406$ Å, $c = 7.9711$ Å, $V = 215.3$ Å³).^[25] AgCuS reflections (blue lines in Figure 2a) were calculated on the basis of the room temperature data reported herein.^[25]

Besides the main phase, small impurities of the silver-rich phase Ag₅Cu₃S₄ can be recognized in the bulk material.^[29] This phase was identified as the mineral mckinstyrite, exhibiting a very similar crystal structure compared to stromeyerite in space group *Pnma*. The amount of the side phase was determined as 7% by a Rietveld refinement profile fit (see Figure S1, Supporting Information). No undefined reflections remained after identifying the two phases. EDX analysis resulted in a composition of 1.1(1):1.0(1):1.0(1) (Ag:Cu:S) for the main fraction AgCuS.

We compared our XRD data with the results from Biswas et al. and detected traces of our side phase in their temperature dependent AgCuS data, especially in their reported 333 K cooling sample.^[13] After this detailed phase analysis of our AgCuS sample it can be concluded that the product is sufficiently pure to create a single-material diode device.

In order to verify the thermal stability of AgCuS prior to our diode measurements we performed several heating and cooling cycles between room temperature and 500 K. Data from differential scanning calorimetry (DSC) experiments for six consecutive cycles are denoted in Figure 2b. Cycles 2 to 6 are fully identical and therefore only the 2nd cycle is plotted.

The DSC measurement shows one very intense endothermic signal at 358(1) K (onset value) in the heating cycle, representing the AgCuS transition from the orthorhombic room temperature β -polymorph to the hexagonal α -phase, which also represents the pn-switching transition. Between 405 and

440 K the thermal effect related to the α - δ transition takes place, when further disordering of the cations occurs. Upon cooling, an effect occurs at 433(2) K, marking the temperature at which the cations are again locked into the more ordered hexagonal phase. Those results exactly match the findings in the first heating cycle reported by Biswas et al. (see Supporting Information).^[13] The authors also described the additional signal at \approx 408 K associated to the low-temperature boundary of the two-phase hexagonal-cubic region.

In our study, we find an additional broad endothermic effect at 350(2) K (peak maximum), which gains intensity from the first to the second heating cycle but remains constant in the third one. In the cooling curve a related broad exothermic effect is visible at \approx 320(2) K. The DSC curve of Biswas et al. shows a similar exothermic effect in their cooling cycles, but this one is not explicitly explained in their study.^[13] Since an impurity of the silver-rich phase $\text{Ag}_5\text{Cu}_3\text{S}_4$ is identified by P-XRD, one might expect this side phase to create the two effects. Therefore, we synthesized a phase pure sample of $\text{Ag}_5\text{Cu}_3\text{S}_4$ in the same way as AgCuS and measured a DSC curve for the pure material. $\text{Ag}_5\text{Cu}_3\text{S}_4$ exhibits a phase transition at 369(1) K (onset value), and 407(1) K (onset value) (see Figure S2, Supporting Information). It is therefore most likely that the additional effects and the 408 K effect mentioned before are caused by $\text{Ag}_5\text{Cu}_3\text{S}_4$ or possibly by another non-crystalline phase. A secondary process during the final ordering in the cation substructure is also possible.

For the utilization of such a pn-switchable material as a one-compound diode, *p*- and *n*-type regions have to be created in the device simultaneously. To initiate this feature, a temperature gradient is a suitable method to generate both regions in a single crystal just by inducing the β - α phase transition from the *p*-type before and above the transition to the *n*-type conducting transition stage at the phase transition itself. Our group recently showed for the first time the feasibility of such a process using another pn-switchable material, $\text{Ag}_{18}\text{Cu}_3\text{Te}_{11}\text{Cl}_3$, in which a phase transition \approx 296 K is used to create both semiconductor types and therefore a one-compound diode out of only one material.^[14]

We compared the enthalpy of the two pnp phase transitions, of $\text{Ag}_{18}\text{Cu}_3\text{Te}_{11}\text{Cl}_3$ at 296 K, with the one of AgCuS at 358 K (see Figure S3, Supporting Information) and found only a very small transition enthalpy of 0.2 J g^{-1} for $\text{Ag}_{18}\text{Cu}_3\text{Te}_{11}\text{Cl}_3$ in contrast to 31.1 J g^{-1} for AgCuS .

The phase transition in $\text{Ag}_{18}\text{Cu}_3\text{Te}_{11}\text{Cl}_3$ is purely of second order, as no significant cell volume or property jump was reported in $\text{Ag}_{18}\text{Cu}_3\text{Te}_{11}\text{Cl}_3$. The *n*-type conduction occurs after the structural phase transition and is initiated by a partial disorder of Te atoms in the anionic substructure, accompanied by the creation of a partial 2D CDW. Neither a change in the space group nor a significant cell volume jump occurs during this β - α $\text{Ag}_{18}\text{Cu}_3\text{Te}_{11}\text{Cl}_3$ phase transition. Therefore, the amount of consumed heat is relatively low and the resulting endothermic DSC signal during heating is small. Evidently, AgCuS needs a larger amount of energy for a successful rearrangement or displacement of the cations during the pnp-switching β - α phase transition.

The pnp-switch itself was substantiated by Seebeck coefficient measurements for AgCuS . As illustrated in Figure 2c the

Seebeck coefficient changes its sign during the β - α phase transition. Between room temperature and up to 360 K, coefficients range from +648 to +1122 $\mu\text{V K}^{-1}$ while a drop to $-393 \mu\text{V K}^{-1}$ occurs at 363 K. At slightly higher temperatures the sign of the Seebeck coefficient is again switched to high positive values. This effect is reversible and has been observed in consecutive measurement cycles as illustrated in Figure S5 (Supporting Information).

During this β - α transition, we also observed a significant change in the electrical conductivity. The evolution of the temperature-dependent electrical conductivity measurement of a bulk AgCuS ingot is displayed in Figure 2d. At up to 363 K, only a small rise in conductivity from 3 to 10 mS cm^{-1} is visible with increasing temperature. Between 363 and 366 K, the conductivity suddenly rises to 0.2 S cm^{-1} and increases linearly up to 0.3 S cm^{-1} at 387 K. This jump occurs right at the β - α phase transition, enabling higher total electrical conductivities. It is most likely that the emerging cation disorder causes this phenomenon because of the enhanced cation mobility. In general, the increase in conductivity with temperature perfectly displays the behavior of a semiconducting material, and the determined values are in the same region reported by Biswas et al.. The only difference to the findings of Biswas et al. is that our samples do not show a significant conductivity increase at the phase transition temperature itself, which could have occurred due to the fact that we simply did not measure it within our temperature steps (see Figure S4, Supporting Information).

We therefore classify this β - α phase transition of mixed order with a significant first order contribution. The question of whether this first order contribution will affect the diode formation and performance will be addressed in the following part. It is not the purpose of this study to redetermine the pnp-switching mechanism. This mechanism was reported and perfectly described by Biswas et al. in their outstanding manuscript.^[13] The interested reader is asked to refer to the original literature or the supplement section where a brief summary of the underlying mechanism is given. All experiments reported so far were performed to evaluate the quality of AgCuS prior to the diode measurements and to verify the successful occurrence of the pnp-switch.

2.2. AgCuS Diode Fabrication and Performance

Crystals of AgCuS were mounted onto printed circuit boards (PCB), as shown in Figure 3a. Tin/lead solder was used as contact medium. The heating elements (56 Ω resistors) next to one contact can be activated independently from those on the other side, allowing for the creation of a thermal gradient in the device. If a current is applied to the paired resistors, heat is generated locally. The thermal gradient during this state was analyzed with a Micro-IR camera; the resulting image can be seen in Figure 3b. During this stage, the crystal is submitted to a temperature gradient of 333 to 368 K at the cold and hot contacts, respectively.

The electrical behavior of the produced device was characterized at two different temperature conditions, isothermally at a given temperature and operated within a certain temperature gradient.

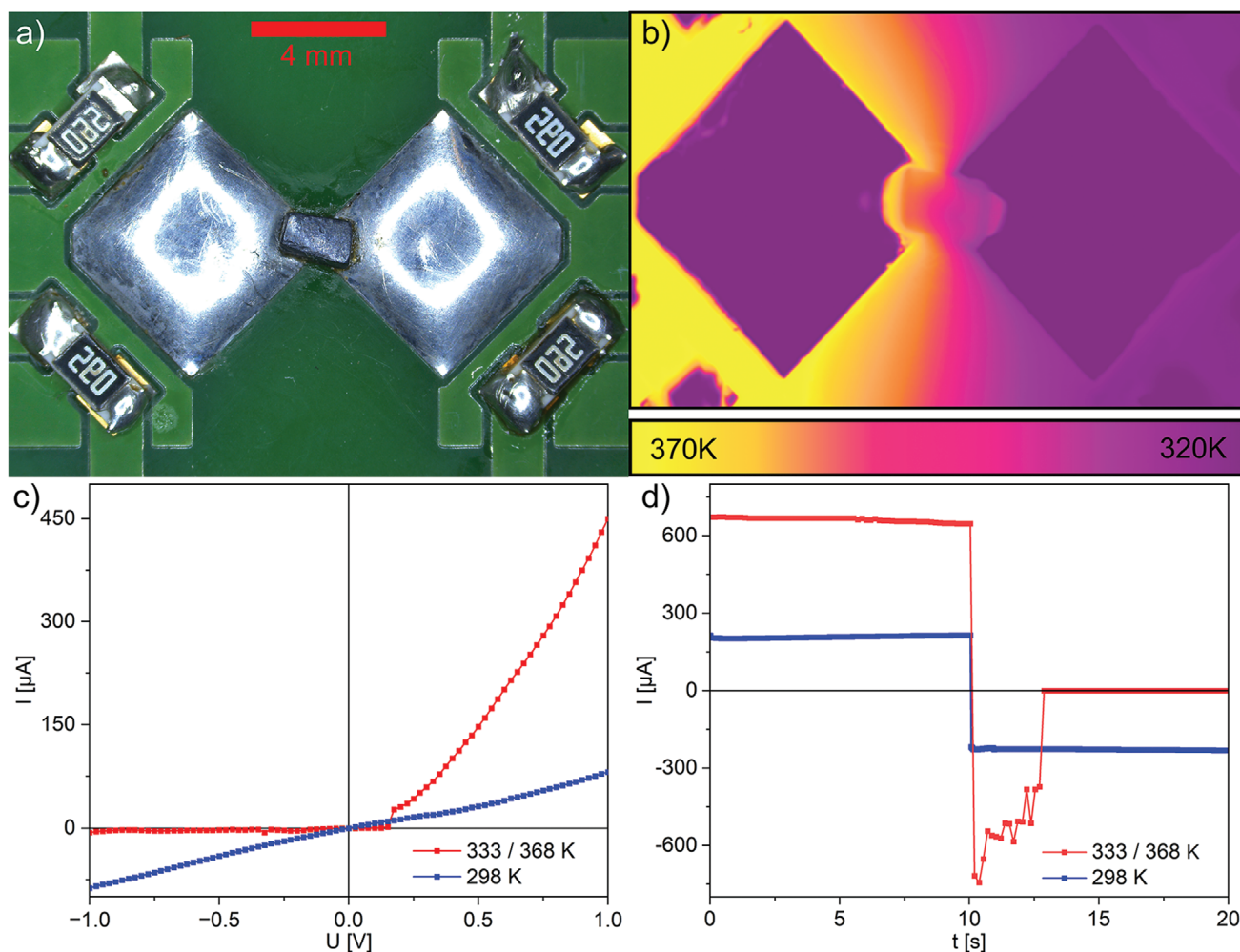


Figure 3. a) Optical microscope image of an AgCuS sample mounted onto a PCB. The contacts are produced with the aid of tin/lead solder to provide ohmic behavior between the gold pads and the crystal. Two 56Ω resistances per contact are used to specifically heat up alternating sides of the crystal to induce pn-regions across it. b) Thermal image of the device in a 333 to 368 K temperature gradient. c) U/I curves of the PCB-mounted crystal at 298 K (blue) and with a gradient of 333 to 368 K (red). d) Switching time of the produced devices under isothermal conditions (298 K) and with the application of a 333/398 K gradient. A potential of 1.0 V was applied to the device up to $t = 10$ s, after which the signal of the potential was inverted.

With the resistances turned off, the entire system operates isothermally at 298 K. The U/I curve measured between ± 1 V under these circumstances is that of a non-rectifying element, with a symmetrical character regardless of the applied potential. As shown in Figure 3c the isothermal conditions lead to the behavior expected of a regular resistive semiconductor with good ohmic contact, indistinguishable from a perfect resistance (blue curve). The linear dependence between potential and current also rules out the formation of a Schottky diode with the metallic contacts.

The second measurement condition includes the application of heat to the system via resistivity heating. Due to our experimental setup conditions the gradient starts at 320 K at the cold end. Evidently, room temperature would also work in this case. The system is thus led to the state described in Figure 3b, with a thermal gradient of 333/368 K through the crystal, encompassing both the *p*- and *n*-type regions of AgCuS. The heat dissipation is tuned in such a way that the β - α phase transition temperature and therefore also a pn-junction is localized exactly

within the mounted crystal. This results in a region where electrons are the majority charge carriers (*n*-type) on the hot side, while at the colder side the conductivity is dominated by holes (*p*-type). At a certain position between these regions, the created temperature profile should thus lead to the formation of a pn-junction. This new region is called ambijunction,^[14] to differ it from static pn-junctions formed by doped semiconductors.

The U/I curve of the system under these conditions is dramatically different, as denoted in Figure 3c (red curve). A classical diode behavior is observed, with a forward current 75 times higher than the reverse current at ± 1 V. The rectifying character confirms the formation of a pn-ambijunction in this device. The junction potential was determined from different ingots resulting in values between 0.15 and 0.6 V, likely due to the slightly different ingot sizes or thermal conditions, with the consequent varying charge carrier density. In the following we illustrate results on one selected system with a 0.15 V junction potential. The forward current for the AgCuS diode of 450 μ A is higher than that measured for $\text{Ag}_{18}\text{Cu}_3\text{Te}_{11}\text{Cl}_3$. Here the value

is 140 μA . The power transmitted through the present AgCuS diode at +1 V in the forward direction is therefore four times higher than that of its previously mentioned counterpart.

In order to confirm the formation of a pn-ambijunction, the switching time of these systems was also measured at the two different temperature conditions (see Figure 3d). In this study, the systems were polarized with a forward potential (+1.0 V) for 10 s, after which a reverse potential of the same magnitude was applied and held. The isothermal curves at 298 K (blue curve in Figure 3d) show no evidence of current rectification. Currents of same magnitude but inverse direction were obtained after switching the polarization of the system, indicating a purely resistive behavior.

When the experiments were repeated with the application of the thermal gradient (red curve in Figure 3d), a classical diode response was observed. Initially, a relatively stable and intense current is measured due to the discharge of the excess minority charge carriers that were injected during the forward regime.

The linear removal of these excess carriers leads to a rather stable current, with a switching time t_s of 2.5 s. This aspect can be found between 10 and 12.5 s in Figure 3d. At $t > t_s$, where the fall time regime t_f supposedly starts, the reverse current usually decays exponentially toward the saturation current of the diode. In the present case, the fall time t_f is faster than the resolution of our measurement setup, thus it could not be measured precisely. We only observed a sudden decrease of the current. Almost immediately after the linear phase, the AgCuS diode shuts off and current is mostly blocked from traveling through the device.

The total time involved with the switching of this diode is much faster than the one previously reported for $\text{Ag}_{18}\text{Cu}_3\text{Te}_{11}\text{Cl}_3$. Diodes created with this compound are reported to shut cur-

rent off after 62.4 s ($t_s + t_f$). On the other hand, AgCuS shows a much faster blocking speed, discharging excess charge carriers and creating a depletion region ≈ 25 times faster than its counterpart. The faster switching times could be associated to the different temperature regimes: while AgCuS shows the pnp-transition at ≈ 364 K, this phenomenon happens much closer to room temperature in $\text{Ag}_{18}\text{Cu}_3\text{Te}_{11}\text{Cl}_3$ (≈ 290 K). With more thermal energy, the charge carriers in AgCuS – both majority and minority – supposedly have increased mobility, diffusing much faster through the *p*- and *n*-regions and leading to faster switching times.

Moreover, the reversible formation and cancellation (or on- and off-switching) of a one-compound diode was analyzed in this study for the first time. The thermal gradient was consecutively introduced and removed from the system in order to analyze the reversibility and reliability of diode formation in these devices. Figure 4 shows the U/I curves created after application of three consecutive heating cycles over the same device. A heating cycle represents the application of a temperature gradient (333 to 368 K) and the switch to an isothermal stage (298 K) afterward. An initial heating step leads to the production of the diode for the first time in this system. When the heat source is turned off and the temperature gradient decays, the rectifying behavior starts to falter, dying off completely once the crystal cools down beyond the temperature where the *n*-type material exists. If the heating elements are turned on again to reapply a temperature gradient, the system starts to show hints of rectification. A full diode is established once the thermal conditions are back to their optimized state and the needed temperature gradient is present (333 and 368 K at the cold and hot sides, respectively). This experiment was repeated three times, as illustrated in Figure 4. AgCuS can be tuned by an external

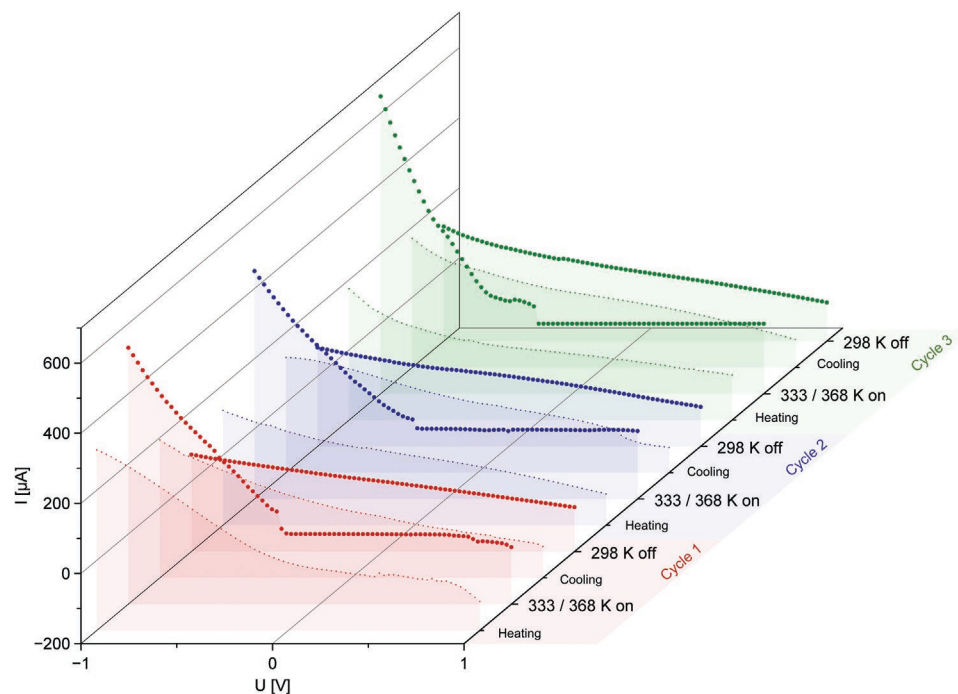


Figure 4. On/off-switching of the single-material diode. A thermal gradient was created and removed three consecutive times over the same device. The diode behavior is seen only when the *p*- and *n*-regions are present simultaneously.

temperature gradient and act as a one-compound diode where the diode formation and cancellation are fully reversible.

Certain differences in the U/I curves between Cycle 1 and Cycle 3, either in resistance or in the curve profile are most probably due to slight differences in the applied temperature gradient from measurement to measurement. It has to be stated that the measurements are performed against lab atmosphere and no shielding was applied to the PCB to avoid thermal convection. Since the temperature state in each of the cycles is not exactly the same and the n - or p -character is strongly dependent on temperature, the junction potential might also be affected, in the same manner it would if we changed the dopant concentration in a normal diode.

In Figure 2b one can observe a certain hysteresis in the DSC experiments between heating and cooling cycles during the pnp-switch phase transition. The formation of the diode was not affected by this hysteresis because we always illustrated the diode formation by heating of the system from room temperature to the transition temperature. The cancellation of the diode was not measured by us but it will take place once the T-gradient and therefore the pn-junction vanishes, most likely at slightly lower temperatures than for the formation.

Furthermore, this test showcases the flexible (volatile) diode formation potential of this new type of device. One-material

diodes are very different from all other types of applied diodes in the sense that they are non-permanent. The rectifying diode behavior is only displayed if the system is operated under a certain temperature gradient. Otherwise, the same system displays a regular resistive character. When requested, AgCuS may block the passage of current in one direction, remaining virtually oblivious to any directionality in passage of charge under different circumstances.

An extra degree of freedom in the utilization of one-compound diode materials in devices or processes is the possibility of choosing the direction of current flow. In principle, the forward direction of a diode is defined once it is fabricated. With the present reversible one-compound diode devices, the forward direction of the diode can be adjusted by the orientation of the applied temperature gradient. To prove this feature, we reversed the applied temperature gradient and measured the electronic response afterward. A first diode was formed by heating the system on the right side, as shown in Figure 5a,c. The previously described rectifying behavior was observed. The heating elements were then turned off and the system was cooled down to room temperature (Figure 5b). The linear U/I response of a resistance was measured, indicating that the initial diode was annihilated. Subsequently, after reversing the temperature gradient, a diode was again produced, but with a forward direction

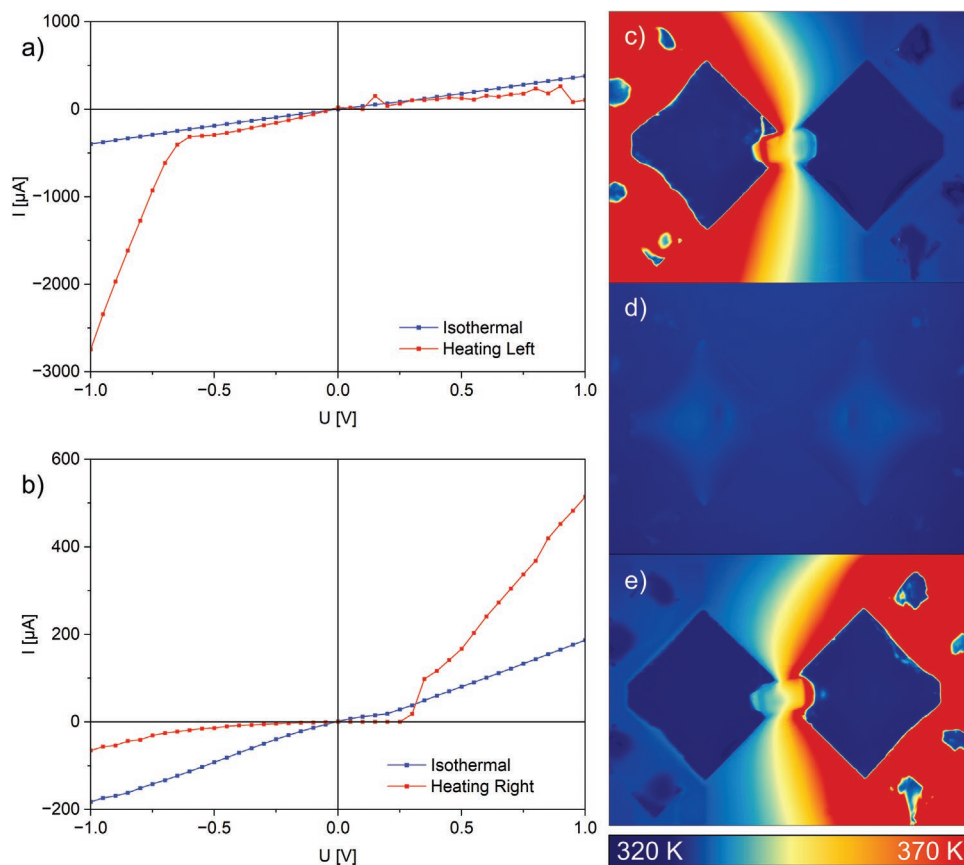


Figure 5. The forward direction of the diodes can be switched by alternating the direction of the heat gradient (a and b). When the left side is heated, the diode is blocking for positive voltages a). When the right side is heated, the diode is blocking for negative voltages b). The dissipation of the heat within the crystal was visualized via infrared imaging. With resistivity heating, the PCB and therefore the crystal can be independently heated at the left side c) or right side e). No temperature gradient is visible across the crystal under isothermal conditions at room temperature d).

opposite to that in the previous case, see Figure 5b,e. As the position of the *p*- and *n*-regions was reversed, the direction of the forward current was also inverted, and current is now allowed to pass only in the direction opposite to that of the previous configuration.

Differences in total current and junction potential are accounted by different temperature conditions and contact areas on the two sides of the crystal. The total time for this experiment was of ≈ 15 min, which was the time associated with the establishment of a stable thermal gradient; once the gradient is present, the diode behavior is displayed virtually instantaneously.

3. Discussion

In this study, two new processes for diodes are illustrated for the first time, a) the reversible on- and off-switching of a diode by a one-compound pnp-material via a temperature gradient (and without doping), and b) the variable definition of the forward direction of a diode by a simple modification of the temperature gradient orientation.

In state-of-the-art diodes, a) is not possible and b) could only be mimicked by manually reconnecting the diode contacts. After manufacturing of integrated circuits, this direction switch is virtually impossible without strenuous manipulation. In the case of our devices, the blocking direction can be chosen by tweaking the temperature gradient that is applied to the system. Careful thermal control thus also allows the definition of the direction in which these novel devices conduct current, and likewise the direction through which no transport is allowed.

The processes a) and b) are unique in regular semiconducting devices. Diodes created via pnp-switching compounds can be formed selectively at a position where they are needed. Commonly used diodes present switching in either forward or blocking modes in a pre-defined direction. One-material diodes allow the selection of the forward direction in devices by the simple application of an external temperature gradient. This unique feature allows completely new architectures for diode devices and generates alternative pathways for applications of diodes in different processes. On top of this extra degree of freedom, the described devices show another further switch, between pn and np characters. With the standard thermal gradient, the system has a specific forward direction. With the symmetric reversion of the thermal gradient through the device, the forward direction is also inverted, meaning that current can now be transmitted only in the opposite orientation.

A certain drawback of AgCuS seems to be the operation temperature needed for the pnp-switch which is ≈ 363 K, in relation to the switching temperature of $\text{Ag}_{18}\text{Cu}_3\text{Te}_{11}\text{Cl}_3$ at room temperature. Due to the very low thermal conductivity of $0.5\text{--}0.7\text{ W m}^{-1}\text{ K}^{-1}$ (data taken from^[13]) an external temperature pulse might be applied locally without a strong heat dissipation in the system. Therefore, the slightly higher T-gradient, or better, the high T-value of the gradient needed in AgCuS might be more energy consuming to generate but it also accelerates the necessary ion displacement and diffusion during the phase transition process.

4. Conclusion

The composition, polymorphism, and semiconducting properties of AgCuS were re-assessed in order to confirm the quality of AgCuS as pnp-switching compound and therefore its suitability for creating a single-material diode. In this work, AgCuS ingots were successfully used to create a one-compound diode and determine its switching abilities.

A stable diode could be created, outperforming $\text{Ag}_{18}\text{Cu}_3\text{Te}_{11}\text{Cl}_3$, the first reported one-compound diode material, in terms of switching time and forward current. Due to the pn-transition temperature of 364 K ensuring a certain thermal distance to ambient conditions, the formation and maintenance of the pn junction is easy to realize in practice. Furthermore, the orientation of the forward direction of the diode can be adjusted by selecting a suitable thermal gradient, which is not possible for classical diodes. Those findings not only substantiate the creation of position- and current direction-independent diodes, but also enable the usage of one-compound diode materials in electrocatalysis, photocatalysis, or energy conversion processes, where an already present temperature gradient could be utilized to create diodes locally. In a next step, we intend to fabricate flexible transistors, further pushing the opportunities toward single-material electronic devices.

5. Experimental Section

Synthesis of AgCuS: AgCuS was synthesized as described by Biswas et al.^[13] The material was prepared by a melting reaction directly from the elements using silver (CHEMPUR, 99.999%), copper (CHEMPUR, 99.999%), and sulphur (ALFA AESAR, 99.999%) on a 7 g scale. Stoichiometric amounts of the starting materials were sealed into evacuated silica glass ampules and heated slowly to 773 K for 12 h. Afterward the temperature was increased to 1223 K in 5 h and held for 24 h. The material was then quenched by quick removal of the ampoule from the oven and exposure to air. Small amounts of silver residue on the surface were removed by polishing, leading to black shiny ingots of AgCuS. The product was cut into mm-sized pieces prior to use.

Powder X-ray Diffraction (P-XRD): For phase analysis, small amounts of finely ground sample were placed between two stripes of SCOTCH Magic Tape. Powder XRD data was collected in the range of 5.00 to 79.09 2θ with a STOE STADI P powder diffractometer equipped with a position sensitive DECTRIS Mythen 1K detector using $\text{Cu K}\alpha_1$ radiation ($\lambda = 1.54060$ Å, curved Ge(111) monochromator). Phase analysis was carried out using the STOE WinXpow software package.^[30]

Thermal Analysis: A small piece of the ingot was transferred to an aluminum crucible under inert conditions and differential scanning calorimetry was performed with a NETZSCH DSC 200 F3 Maia device. The measurement was conducted under N_2 atmosphere in the temperature range of 298 to 523 K with a heating/cooling rate of 10 K min^{-1} . Thermal effects were derived from onset temperatures when possible. Data analysis was performed using the NETZSCH Proteus Thermal Analysis software package.^[31]

Semi-quantitative Phase Analyses and Scanning Electron Microscopy (SEM): The samples were fixed on a steel holder with a conductive adhesive polymer tape from Plano GmbH. Energy dispersive X-ray spectroscopy (EDX) was performed using a JEOL JSM-IT200 InTouchScope™ with an integrated JEOL JED-2300 EDX unit. The acceleration voltage was set to 10 kV. The EDX results were averaged from at least three different points, selected randomly on the crystal surface. An error of 10% was estimated for all composition values.

Thermal Imaging via a Microbolometer-based Camera: Thermal images were collected by a INFRA TEC VarioCam HD head 980 S microbolometer

system equipped with a JENOPTIK M = 1.0× precision microscopy objective. The images were processed with the Irbis 3.1 professional software package.^[32] Pictures were acquired with activated microscan unit resulting in a nominal resolution of 2048 × 1536 pixel. Temperature accuracy at 303 K ±1.5 °C, thermal resolution 0.03 K.

Measurements of Electrical Conductivity and Seebeck Coefficient: An as-prepared AgCuS ingot was cut into a bar of ≈14 × 10 × 3 mm. The Seebeck coefficient and the electric conductivity were measured simultaneously directly with a NETZSCH SBA 458 Nemesis under a continuous argon flow. The electrical conductivity was determined using a four-point probe measurement. The technical measurement error was ±7% for the Seebeck coefficient and ±5% for the electrical conductivity. Data analysis was performed with the NETZSCH SBA-measurement software package.^[33]

Diode Characterization: A cut sample of the AgCuS ingot was mounted onto a printed circuit board (PCB) by soldering it onto the gold-plated contacts with a tin/lead solder (STANNOL, composition Sn:Pb:Cu = 60:39:1 wt.%), see Figure 3a. For the application of directional heat gradients, a pair of 56 Ω resistances was placed next to each of the contacts. Those were used to independently heat up the contacts and therefore create a heat gradient through the ingot. A QJE PS6005 switching power supply was used to provide the electrical current for the resistive heating. For AgCuS, the measurements could be conducted at ambient conditions, since the β-phase was prominent up to 369 K. For the diode measurements, a heat gradient from 338 to 363 K was applied to the ingot. Temperature was controlled by an external thermocouple (RSPRO thermometer device, Ni/Cr/Ni type thermocouple, accuracy ±1 K) at the contacts during the measurements as well as by the aforementioned thermal imaging device. Conductivity measurements were performed using a KEITHLEY 2450 SourceMeter®. Voltage errors are ±0.015% and current errors are ±0.03%. This digital multimeter was operated with the aid of KickStart I-V Characterizer App. Measurements were performed at a scanning speed of 0.06 V s⁻¹. Data analysis was performed with the KEITHLEY Kickstart IV Characterizer App software package.^[34]

Supporting Information

Supporting Information is available from the Wiley Online Library or from the author.

Acknowledgements

P.D. and A.R. contributed equally to this work. K.V. conducted the SEM and EDX measurements. P.D., A.R., J.V., and T.N. wrote the manuscript. A.R., P.D., and K.V. thank the TUM Graduate School for support. J.V. thanks for a stipend funded by the TUM Talent factory program. This project was supported in part by the international graduate school ATUMS, IRTG 2020 funded by the German Science Foundation DFG, and by the DFG Grant NI1095/12.

Open access funding enabled and organized by Projekt DEAL.

Conflict of Interest

The authors declare no conflict of interest.

Data Availability Statement

The data that support the findings of this study are available from the corresponding author upon reasonable request.

Keywords

ambijunctions, ion conductors, one-compound diodes, pnp-switching, semiconductors

Received: December 21, 2022

Revised: January 17, 2023

Published online: February 20, 2023

- [1] J.-P. Colinge, C. A. Colinge, *Physics of semiconductor devices*, Springer, NY, USA **2006**.
- [2] U. V. Ghorpade, M. P. Suryawanshi, M. A. Green, T. Wu, X. Hao, K. M. Ryan, *Chem. Rev.* **2022**.
- [3] L. Heng, X. Wang, N. Yang, J. Zhai, M. Wan, L. Jiang, *Adv. Funct. Mater.* **2010**, *20*, 266.
- [4] K. Potje-Kamloth, *Chem. Rev.* **2008**, *108*, 367.
- [5] M. Y. Wong, C. Y. Tso, T. C. Ho, H. H. Lee, *Int. J. Heat Mass Transfer* **2021**, *164*, 120607.
- [6] J. P. Sun, G. I. Haddad, P. Mazumder, J. N. Schulman, *Proc. IEEE* **1998**, *86*, 641.
- [7] T. Nilges, S. Lange, M. Bawohl, J. M. Deckwart, M. Janssen, H.-D. Wiemhöfer, R. Decourt, B. Chevalier, J. Vannahme, H. Eckert, R. Wehrich, *Nat. Mater.* **2009**, *8*, 101.
- [8] T. Nilges, M. Bawohl, *Z. Naturforsch., B: Chem. Sci.* **2008**, *63*, 629.
- [9] T. Nilges, M. Bawohl, S. Lange, *Z. Naturforsch., B: Chem. Sci.* **2007**, *62*, 955.
- [10] O. Osters, M. Bawohl, J.-L. Bobet, B. Chevalier, R. Decourt, T. Nilges, *Solid State Sci.* **2011**, *13*, 944.
- [11] C. Xiao, X. Qin, J. Zhang, R. An, J. Xu, K. Li, B. Cao, J. Yang, B. Ye, Y. Xie, *J. Am. Chem. Soc.* **2012**, *134*, 18460.
- [12] Y. Shi, A. Assoud, C. R. Sankar, H. Kleinke, *Chem. Mater.* **2017**, *29*, 9565.
- [13] S. N. Guin, J. Pan, A. Bhowmik, D. Sanyal, U. V. Waghmare, K. Biswas, *J. Am. Chem. Soc.* **2014**, *136*, 12712.
- [14] A. Vogel, A. Rabenbauer, P. Deng, R. Steib, T. Böger, W. G. Zeier, R. Siegel, J. Senker, D. Daisenberger, K. Nisi, A. W. Holleitner, J. Venturini, T. Nilges, *Adv. Mater.* **2022**, 2208698, <https://doi.org/10.1002/adma.202208698>.
- [15] M. Elbing, R. Ochs, M. Koentopp, M. Fischer, C. von Hänisch, F. Weigend, F. Evers, H. B. Weber, M. Mayor, *Proc. Natl. Acad. Sci. USA* **2005**, *102*, 8815.
- [16] C. Dai, Y. Liu, D. Wei, *Chem. Rev.* **2022**, *122*, 10319.
- [17] M.-H. Fang, Z. Bao, W.-T. Huang, R.-S. Liu, *Chem. Rev.* **2022**, *122*, 11474.
- [18] J. Briscoe, M. Stewart, M. Vopson, M. Cain, P. M. Weaver, S. Dunn, *Adv. Energy Mater.* **2012**, *2*, 1261.
- [19] S. Hadke, M. Huang, C. Chen, Y. F. Tay, S. Chen, J. Tang, L. Wong, *Chem. Rev.* **2022**, *122*, 10170.
- [20] K. He, T. Tadesse Tsega, X. Liu, J. Zai, X.-H. Li, X. Liu, W. Li, N. Ali, X. Qian, *Angew. Chem., Int. Ed.* **2019**, *58*, 11903.
- [21] R. He, G. Schierning, K. Nielsch, *Adv. Mater. Technol.* **2018**, *3*, 1700256.
- [22] H. Li, C. Chen, Y. Yan, T. Yan, C. Cheng, D. Sun, L. Zhang, *Adv. Mater.* **2021**, *33*, 2105067.
- [23] P. V. Pham, S. C. Bodepudi, K. Shehzad, Y. Liu, Y. Xu, B. Yu, X. Duan, *Chem. Rev.* **2022**, *122*, 6514.
- [24] X.-L. Shi, J. Zou, Z.-G. Chen, *Chem. Rev.* **2020**, *120*, 7399.
- [25] D. Santamaria-Perez, A. Morales-Garcia, D. Martinez-Garcia, B. Garcia-Domene, C. Mühle, M. Jansen, *Inorg. Chem.* **2013**, *52*, 355.
- [26] D. M. Trots, A. Senyshyn, D. A. Mikhailova, M. Knapp, C. Baetz, M. Hoelzel, H. Fuess, *J. Phys.: Condens. Matter* **2007**, *19*, 136204.

- [27] M. Dutta, D. Sanyal, K. Biswas, *Inorg. Chem.* **2018**, *57*, 7481.
- [28] S. N. Guin, D. Sanyal, K. Biswas, *Chem. Sci.* **2016**, *7*, 534.
- [29] U. Kolitsch, *Mineral. Mag.* **2010**, *74*, 73.
- [30] Stoe, *WinXPOW*, version 3.05, Stoe & Cie GmbH Darmstadt, Germany **2011**.
- [31] Netzsch. GmbH, *Proteus Thermal Analysis*, version 5.2.0, Netzsch Gerätebau GmbH, Selb, Germany **2010**.
- [32] InfraTec., *IRBIS 3.1 professional*, version 3.1.114, InfraTec GmbH, Dresden, Germany **2022**.
- [33] Netzsch. GmbH, *Netzsch S. B. A.-M.*, version 2.0.7.0, Netzsch Gerätebau GmbH, Selb, Germany **2016**.
- [34] Keithley Instruments LLC, *Kickstart IV Characterizer App*, version 2.5.0, Tektronix Inc., Beaverton, USA **2021**.
- [35] <https://creativecommons.org/licenses/by/3.0/>

Supporting Information

AgCuS: A Single Material diode with Fast Switching Times

Philipp Deng, Alfred Rabenbauer, Kathrin Vosseler, Janio Venturini, Tom Nilges

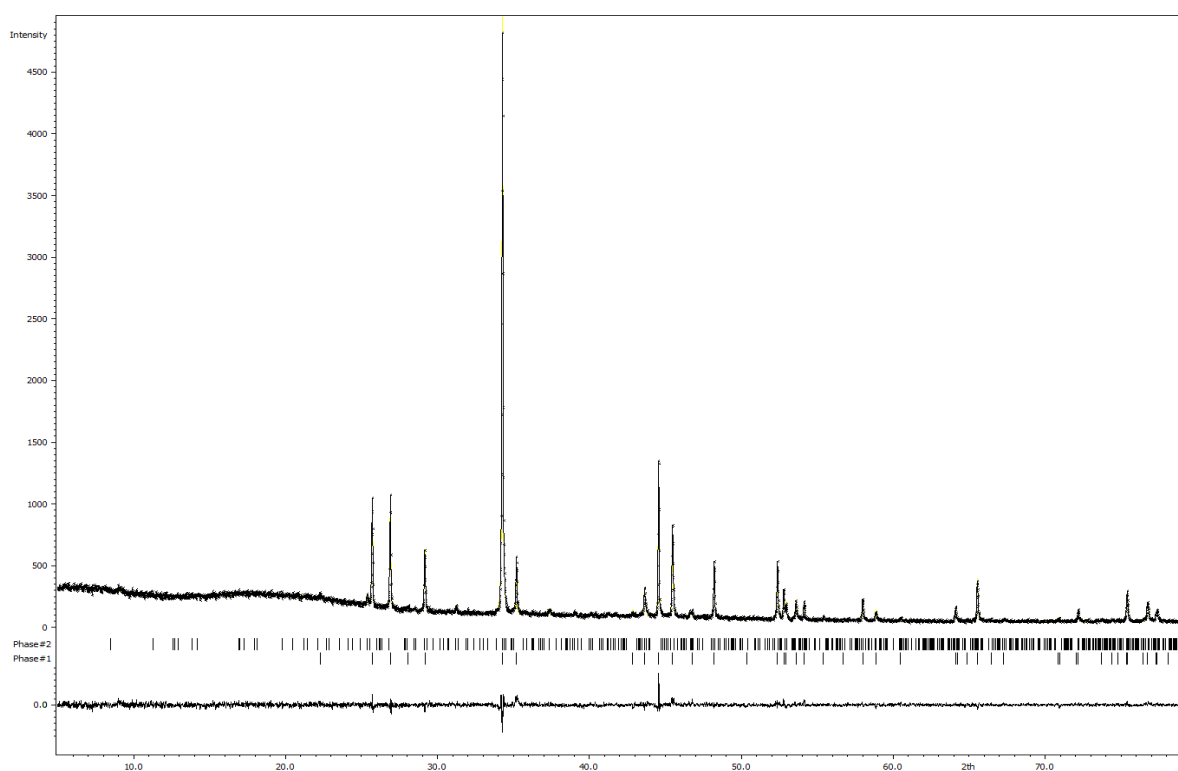


Figure S1: Rietveld refinement of AgCuS sample for the determination of phase composition between AgCuS (phase 1) and Ag₅Cu₃S₄ (phase 2). The difference plot shows a sufficient fit for both compounds, resulting in final values of $R_p = 5.67$, $wR_p = 7.54$, $wR2(\text{all}) = 4.33$ for phase 1 and $wR2(\text{all}) = 5.16$ for phase 2. The amount of Ag₅Cu₃S₄ is ~7%.

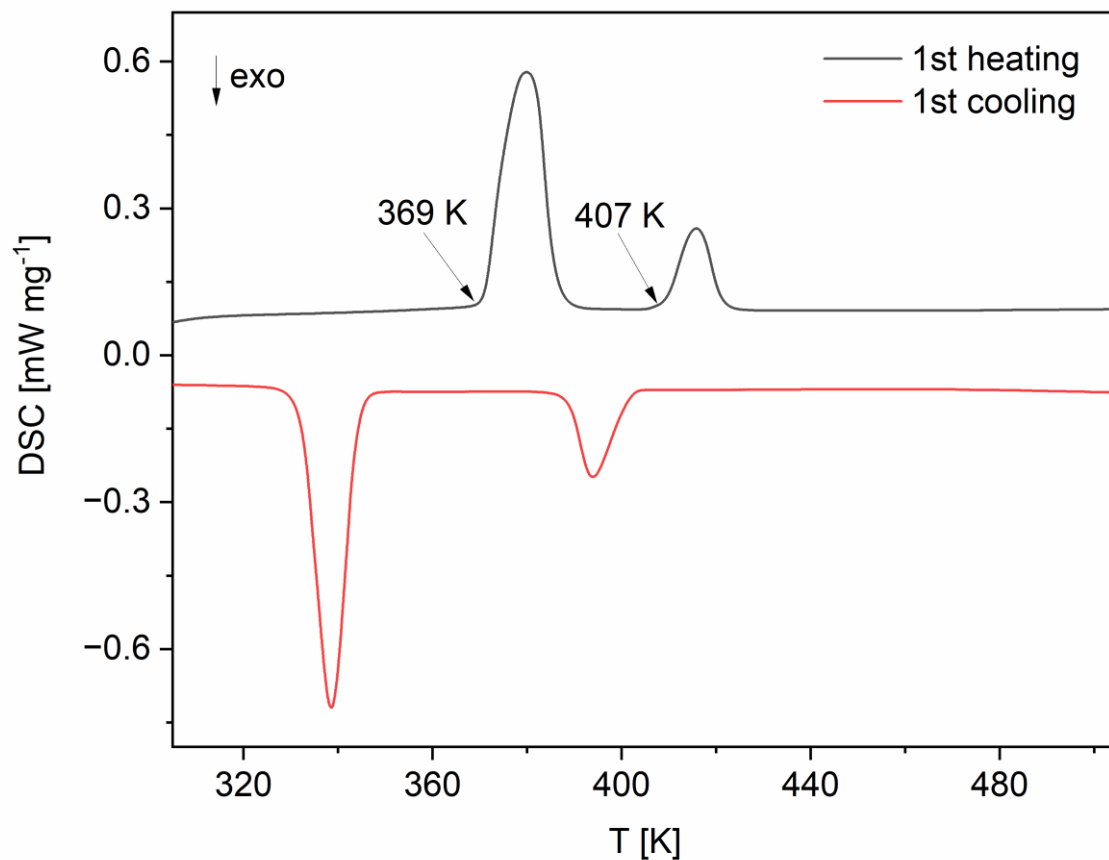


Figure S2: Differential Scanning Calorimetry curve for a pure $\text{Ag}_5\text{Cu}_3\text{S}_4$ sample. Two endothermal phase transitions are visible during heating, at 369 K and 407 K.

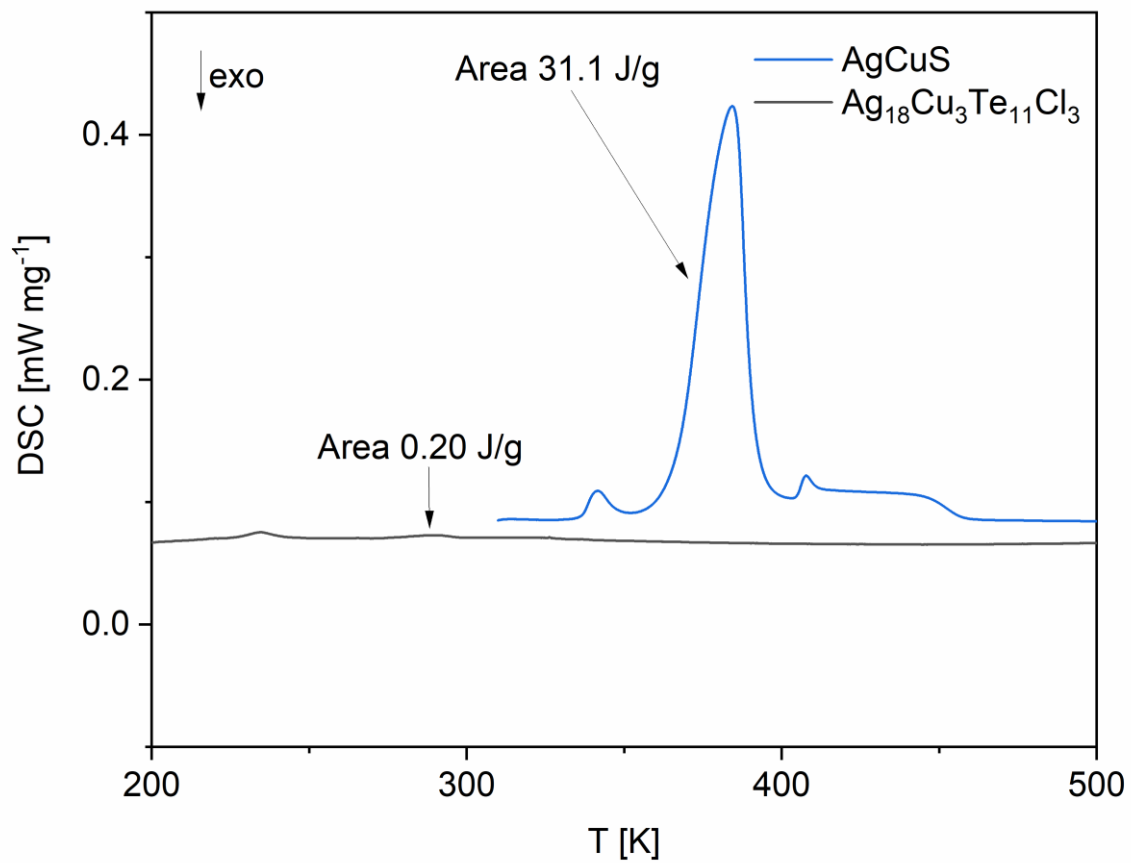


Figure S3: Differential Scanning Calorimetry of AgCuS in comparison to Ag₁₈Cu₃Te₁₁Cl₃ to demonstrate the difference between the second and first order type transitions.

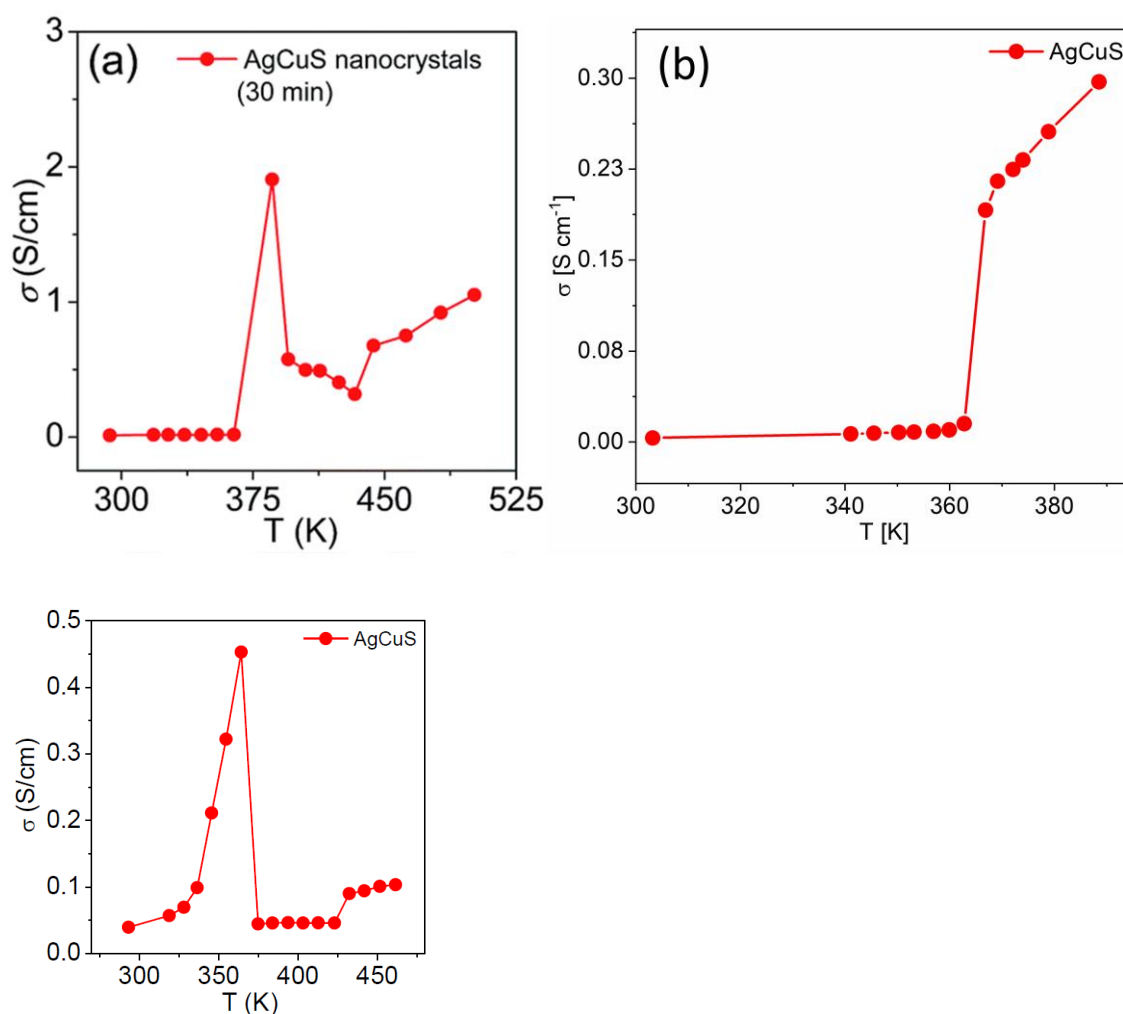


Figure S4: Electrical conductivities reported for nanoparticulate AgCuS (a) (cropped reprint from S. N. Guin, D. Sanyal, K. Biswas, *Chem. Sci.* **2016**, 7, 534.^[28] This work is licensed under a Creative Commons Attribution CC BY 3.0^[35] in relation with the conductivity determined in this study (b). In c the conductivity of AgCuS according to [13] is denoted. *In the case of acceptance the reprint permission from the author itself is needed because this figure is only shown in the supplement of the paper.*

Pnp-switching Mechanism in AgCuS

Biswas *et al.* extensively studied the reasons for this switch between p- and n-type conductivity. They performed positron annihilation spectroscopy as well as density functional theory

calculations in order to examine the electronic behavior of the material. In the β -phase, Ag vacancies are easily created, resulting in the dominant p-type conduction in the room temperature phase. In the α -phase, valence electrons are abundant, behaving as majority carrier in the n-type conducting state.

This phase transition is driven by an order-disorder phenomenon, associated with partial disordering of Ag/Cu in the rigid sulfur sublattice, as reported in ^[13]. During this transition Biswas *et al.* identified that the most abundant valence electrons in the system are the responsible n-type charge carriers overlying the p-type charge carriers (mostly defined by Ag vacancies) and that intermediate semi-metallic states occur during the transition. These states were identified by partial Density-Of-States calculations (P-DOS) at different steps in the transition path. Those are mainly responsible for the creation of free electrons in the conduction states brought closer to the Fermi level, therefore allowing the n-type conduction for a brief moment during the phase transition.

Our own measurements at higher temperatures show that the conduction type of our samples switches back to p-type, with much higher Seebeck coefficients than those displayed at the low-temperature p-region. The results substantiate the previous findings of Biswas *et al.* showing that this material undergoes pnp-switching in a narrow range of temperatures around 364 K.^[13] As it is shown that opposite charge carriers dominate conduction at different temperatures, the produced materials could be used to construct a thermally-controlled one-material diode.

Thermopower response of AgCuS

To verify the reversibility of the pnp-switch at the β - α phase transition in AgCuS we performed several measuring cycles. In Figure S5 three different cycles are denoted. In each cycle the pnp switch occurs around the β - α phase transition temperature of 363 K. It has to be taken into account that the absolute Seebeck values at a pnp-transition can vary drastically due to the measurement procedure applied to determine the coefficient. Commonly, a T-gradient is applied to generate the thermopower and one usually expects that the type of charge carrier does not change within this gradient. Dependent on the exact pnp-transition temperature as well as the phase transition broadness, its kinetics and other internal and external parameters the situation is rather complex at this point. In the case of AgCuS, the region where the pnp-switch occurs is rather small and an even a selected small T-gradient can sometimes lie exactly within this gradient. Often, this situation results in strong effects and sometimes an overestimation of Seebeck values. Therefore, the absolute values of the Seebeck coefficient needs to be handled with care.

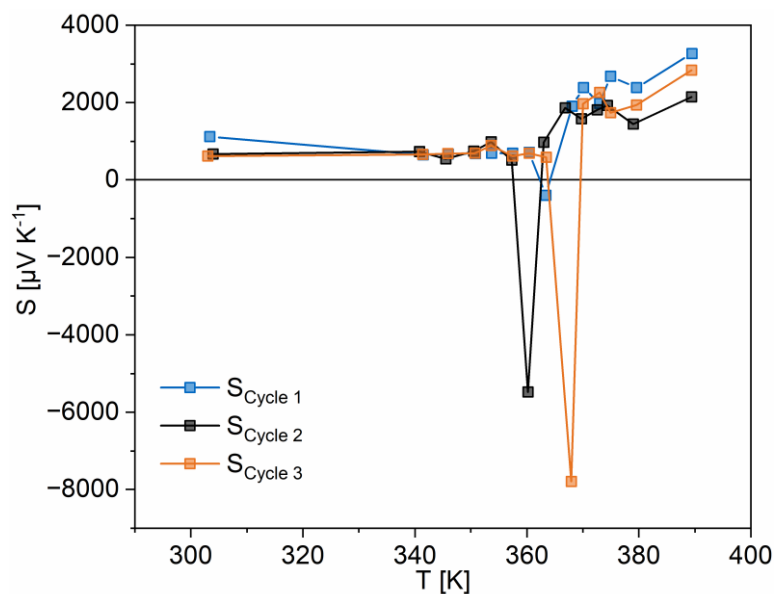


Figure S5: Consecutive Seebeck measurement cycles for AgCuS.

3.3 $\text{Cu}_{1.5}\text{Se}_y\text{Te}_{1-y}$ ($y = 0.2 - 0.7$): A Series of Narrow Band Gap Semiconductors with Low Thermal Conductivity at Ambient Temperature

Alfred Rabenbauer¹, Anna Vogel¹, Janio Venturini¹, Mahboubeh Moslemi², Oliver Oeckler², Dominik Daisenberger³, Tom Nilges¹

¹ Technical University Munich, School of Natural Sciences (NAT), Department of Chemistry, Synthesis and Characterization of Innovative Materials Group, Lichtenbergstraße 4, 85748 Garching bei München, Germany

² Leipzig University, Faculty of Chemistry and Mineralogy, Institute for Mineralogy, Crystallography and Materials Science, Scharnhorststraße 20, 04275 Leipzig, Germany

³ Diamond Light Source, Harwell Science and Innovation Campus, Didcot, OX11 0DE Oxfordshire, Great Britain.

Inorg. Chem., **2023**, 02037

First published: July 21st 2023

Thermoelectric materials offer a promising approach to harvest electrical energy from appearing waste heat via a direct conversion of a thermal gradient into an electrical potential. Promising materials are e.g. Bi_2Te_3 , Sb_2Te_3 , or GeTe-rich alloys due to their intrinsic high thermoelectric performance, which all contain chalcogenides.⁸⁶ But even coinage-metal chalcogenides and chalcogenide halides have been identified as possible candidates, due to their high ionic conductivity, paired with low thermal conductivities, and some of them in addition showed the unique ability to switch from p- to n-type semiconduction during a thermally induced phase transition.^{3, 4, 10} In this project, we tried to identify novel materials in this class, and were able to synthesize and characterize the new series $\text{Cu}_{1.5}\text{Se}_y\text{Te}_{1-y}$ ($y = 0.2 - 0.7$), which represent low-bandgap thermoelectrics.

The materials are synthesized in a classical solid-state synthesis with CuCl as transport agent, and the whole series from 20% to 70% selenium content in the chalcogenide part is realized. The crystal structure is identified by single crystal XRD for the composition $\text{Cu}_{1.5}\text{Se}_{0.3}\text{Te}_{0.7}$ and substantiated for the whole series by PXRD. The series crystallizes cubical, in space group $Pm\bar{3}n$, and shows a linear decrease in cell parameter with increasing selenium content according to Vegard's law.⁸⁷ Cu-positions are only partially occupied, enabling ionic conductivity within the material, as known for e.g. $\text{C}_{9.1}\text{Te}_4\text{Cl}_3$.³ The overall composition of the material is furthermore substantiated by EDX measurements, showing no significant deviations from the single crystal measurement, and proving the possibility of the varying chalcogenide

ratios. The thermoelectric characterization is performed for the two representatives $\text{Cu}_{1.5}\text{Se}_{0.5}\text{Te}_{0.5}$ ($y = 0.5$) and $\text{Cu}_{1.5}\text{Se}_{0.3}\text{Te}_{0.7}$ ($y = 0.3$) in a temperature range from 300 to 570 K. The materials shows sufficient electrical conductivities of up to $\sim 270 \text{ S cm}^{-1}$ for $y = 0.5$ and $\sim 420 \text{ S cm}^{-1}$ for $y = 0.3$. The Seebeck coefficients reach up to $97 \mu\text{V K}^{-1}$ for $y = 0.5$ and up to $57 \mu\text{V K}^{-1}$ for $y = 0.3$, and the temperature dependency of both values is used to estimate the band gaps in the further work. Thermal conductivity measurements revealed conductivities in a range from 0.7 to $1.0 \text{ W m}^{-1} \text{ K}^{-1}$ for annealed samples, which would result in quite low ZT values of < 0.1 . Due to their narrow band gaps, the materials could be applied in infrared sensing. In a last part, the material's stability against mechanical pressure is evaluated by high pressure P-XRD experiments in a range up to 10 GPa, and the bulk modulus is calculated.

Author contributions: A.R. synthesized the compounds and performed the XRD, DSC, SEM and EDX measurements. A.V. and A.R. solved the crystal structure. A.R. conducted the Seebeck and electrical measurements. A.R. M.M. and O.Oe. executed the LFA measurements and calculated the thermal conductivities. A.R. and D.D. measured pressure dependent powder XRD and assessed the bulk modulus. A.R and T.N. wrote the manuscript. All authors discussed the results and revised the manuscript.

Reprinted with permission from Rabenbauer, A.; Vogel, A.; Venturini, J.; Moslemi, M.; Oeckler, O.; Daisenberger, D.; Nilges, T.; *Inorg. Chem* **2023**, DOI: 10.1021/acs.inorgchem.3c02037. Copyright © 2023, American Chemical Society.

Cu_{1.5}Se_yTe_{1-y} (y = 0.2–0.7): A Series of Narrow Band Gap Semiconductors with Low Thermal Conductivity at Ambient Temperature

Alfred Rabenbauer, Anna Vogel, Janio Venturini, Mahboubeh Moslemi, Oliver Oeckler, Dominik Daisenberger, and Tom Nilges*



Cite This: <https://doi.org/10.1021/acs.inorgchem.3c02037>



Read Online

ACCESS |



Metrics & More

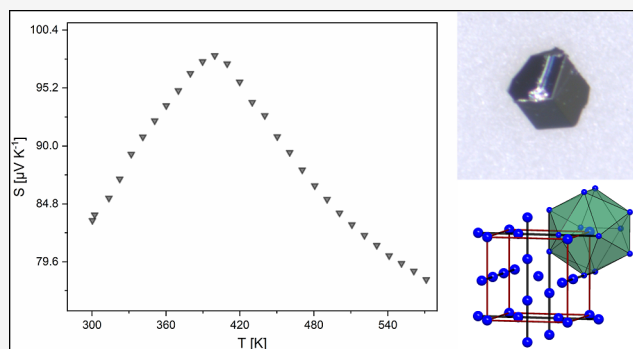


Article Recommendations



Supporting Information

ABSTRACT: Coinage metal chalcogenides offer ideal prerequisites for high thermoelectric performance and sensor applications, with their usually low lattice thermal and high electrical conductivity, as well as small band gaps. In the solid solution Cu_{1.5}Se_yTe_{1-y} we synthesized phase pure materials with y = 0.2–0.7 and characterized them concerning selected physical properties. X-ray crystal structure determination was performed for two representatives of the solid solution, Cu_{1.5}Se_{0.3}Te_{0.7} and Cu_{1.5}Se_{0.5}Te_{0.5}. The entire series crystallizes cubically, in space group *Pm3n*. No structural changes are observed between room temperature and the synthesis temperature of 723 K. The conductivity measurements and Seebeck coefficients of Cu_{1.5}Se_{0.3}Te_{0.7} and Cu_{1.5}Se_{0.5}Te_{0.5} indicate that the two representatives are narrow band gap semiconductors (*E_g* 0.06–0.08 eV). Both compounds show positive Seebeck coefficients and reasonably low thermal conductivities at moderate temperatures. Cu_{1.5}Se_{0.5}Te_{0.5} is characterized by a bulk modulus of 40.9 GPa.



INTRODUCTION

The continuous request for energy pushes society's demands for novel, more efficient power sources. One strategy that may help us maximize energy efficiency is the harvesting of waste thermal energy via the utilization of thermoelectric materials.¹ These compounds are able to convert a thermal gradient into an electrical potential difference. This phenomenon is called the Seebeck effect, and its magnitude is described by the Seebeck coefficient. The main properties defining a good thermoelectric material are high Seebeck coefficients, high electrical conductivity and poor thermal transport.² Semiconductors are therefore the most promising candidates for high *ZT* values, which characterize the overall performance of a thermoelectric material and are defined as

$$ZT = \frac{S^2 \sigma}{\kappa} T \quad (1)$$

where *ZT*, *S*, σ and κ are the thermoelectric figure of merit, the Seebeck coefficient, the electrical conductivity and the thermal conductivity at a specific temperature *T*.

A band gap may involve an asymmetry between the energy distribution of electrons and holes, i.e., the distance of the density of states (DOS) of cold and hot electrons (electrons below and above the Fermi level) increases, which enables high Seebeck coefficients.³ Mechanisms that affect the Seebeck

coefficient usually have a detrimental effect on the electrical conductivity, whereas the relation between thermal and electrical conductivity, described by the Wiedemann–Franz law, negatively influences the Seebeck coefficient.⁴ These complex dependences render the development of new thermoelectric materials non-trivial.

Most materials that display effective thermoelectric conversion are narrow band gap semiconductors.^{1–3,5} Several metal chalcogenides with narrow band gaps are known for their remarkable thermoelectric performance, with Bi₂Te₃ reaching high figures of merit *ZT* near room temperature.^{6–8} Starting with *ZT* values of around 0.5 in bulk Bi₂Te₃, nowadays *ZT* values of ~1.4 are reported in nano-engineered Bi₂Te₃ for temperatures up to 400 K.^{9,10} Other state-of-the-art candidates reach high *ZT* values (>1.5) only at elevated temperatures (e.g., over 800 K). Despite intensive research conducted over the last decades, no outperforming alternatives to Bi₂Te₃ for

Received: June 20, 2023

Table 1. Figure of Merit for Selected Copper Chalcogenides Over the Last Decade

composition	synthesis	temperature (in K)	ZT	year
Cu ₂ Se ²⁰	single-step arc melting	873	1.46	2019
Cu ₂ Se ²¹	reduction-precipitation process	623	0.45	2015
Cu ₂ Te ²²	solid-state synthesis under high pressure	575	0.043	2019
Cu _{1.97} S ²³	solid-state synthesis	1000	~1.9	2015
Cu ₂ S ²³	solid-state synthesis	1000	~1.05	2015
Cu _{1.8} Ag _{0.2} Se _{0.9} S _{0.1} ²⁴	melting, annealing and SPS	873	1.46	2019
Cu _{1.94} Se _{0.5} S _{0.5} ²⁵	solid-state synthesis and SPS	1000	~2.3	2017
Cu ₂ Se _{0.7} Te _{0.3} ²⁶	melting, annealing and SPS	1000	~1.4	2018
Cu ₂ Se _{1.9} Te _{0.1} ²⁷	ball milling and SPS	873	1.9	2016

low temperature applications have yet been found which can replace those ubiquitous devices.^{5,11,12}

Among thermoelectric materials, coinage metal chalcogenides are an interesting alternative to current materials due to their usually narrow band gaps and relatively high electrical conductivities.¹³ Particularly, the fact that they often are mixed electronic ionic conductors (MIECs) due to their high coinage metal ion mobility promotes them as possible candidates for high thermoelectric performance.^{14,15} Ag₂Se was extensively studied over the past decades.^{6,15–17} After a sequence of incremental improvements, ZT values of ~1 could be reached by combination of electrical conductivities up to 1.4×10^3 S cm⁻¹, high ion mobilities, and low thermal conductivity <1 W m⁻¹ K⁻¹, at 348 K.^{6,18} Nevertheless, the currently known copper chalcogenides still do not show high enough efficiencies and stabilities due to ion migration to promote them as possible substitutes for the Bi₂Te₃ devices.¹⁹ In Table 1, the thermoelectric figure of merit of selected copper chalcogenides over the last decade is reviewed.

Here we report a series of copper chalcogenides, Cu_{1.5}Se_yTe_{1-y}, with $y = 0.2$ to 0.7 . The crystal structures of these materials were determined and their thermal stability and thermoelectric performance have been assessed.

EXPERIMENTAL SECTION

Synthesis. Cu_{1.5}Se_yTe_{1-y} ($y = 0.2$ – 0.7) was prepared from a 17: x :11 – x :3 (molar ratio, $x = 2.2$ – 7.7) mixture of Cu (Chempur, 99.999%), Se (Chempur, 99.99%), Te (Chempur, 99.999%), and CuCl (Alfa Aesar, 97%) on a 750 mg scale per batch. CuCl was purified by recrystallization from aqueous hydrochloric acid as described elsewhere; the other starting materials were used without further purification.²⁸ The mixtures were sealed in evacuated silica glass ampoules, heated to 1223 K in a muffle furnace, held at this temperature for 8 h and then quenched in an ice bath. The crude product, a compact bulk residue containing all starting materials, was finely ground in a mortar, re-sealed into silica glass ampoules and annealed at 723 K for 1 week to obtain polycrystalline samples. For single crystal growth, the annealing time was extended to 3 weeks. The as-prepared product consists mainly of black Cu_{1.5}Se_yTe_{1-y} crystals at the hot end of the ampoule. A mixture of CuCl with binary copper selenides/tellurides is transported to the cold side of the ampoule. Cu_{1.5}Se_yTe_{1-y} (major phase, approx. 80 wt %) was separated from the minor phases (CuCl and residues) and used for further characterization. For $y \leq 0.2$ Cu₂₀Te₁₁Cl₃ appears as an additional side phase in the residue.²⁹ The black compounds are light-, air- and moisture stable and can be stored and handled under ambient conditions for several months. Samples for thermoelectric (TE) measurements were hot pressed to pellets and in some cases annealed at 573 K for 3 days after pressing (details see later on in the TE Characterization section).

Single Crystal X-ray Diffraction. Single crystals of Cu_{1.5}Se_{0.3}Te_{0.7} were fixed on a glass capillary prior to measurements. Data was collected on a STOE STADIVARI diffractometer equipped

with a DECTRIS PILATUS 300 K hybrid pixel detector using Mo K $\alpha_{1/2}$ radiation ($\lambda = 0.71073$ Å) at room temperature. The datasets were corrected for Lorentz and polarization effects and a numerical absorption correction based on symmetry-equivalent, reflection derived optimized crystal shapes was applied using STOE X-Area software.³⁰ The structures were solved by a charge-flipping algorithm³¹ implemented in the Jana 2006 program suite.³²

Powder X-ray Diffraction. Composition and phase purity were checked by powder X-ray diffraction. Finely ground bulk material was placed between SCOTCH Magic Tape and measured in a STOE STADI P X-ray powder diffractometer equipped with a DECTRIS Mythen 1 K Detector using Cu K α_1 radiation ($\lambda = 1.54051$ Å; curved Ge(111) monochromator). Data was collected from 5 to 79° 2 θ in 0.015° step. Phase analysis, indexing and cell parameter refinement were performed using the STOE WinXPOW program package.³³

Differential Scanning Calorimetry. Thermal analysis was performed in a NETZSCH DSC 200 F3 Maja calorimeter. About 50 mg of sample were sealed in an aluminum crucible. An empty sealed crucible served as reference. The measurement was performed under a nitrogen flow of 100 mL/min in a temperature range from 123 to 773 K with a rate of 10 K/min. The calibration of temperature and enthalpy was done with Bi, C₆H₁₂, Hg, In, KNO₃, Sn and Zn. The differential scanning calorimetry (DSC) data was processed using the PROTHEUS Thermal Analysis software.³⁴

TE Characterization. Measurement of Electrical Conductivity and Seebeck Coefficient. Finely ground samples of Cu_{1.5}Se_{0.5}Te_{0.5} and Cu_{1.5}Se_{0.3}Te_{0.7} were pressed into pellets of 13 mm diameter using a P/O/Weber 10 hot press tool with a TRG 1 temperature control unit. The sample was pressed under 4 t in a Massen MP150lab press while it was heated to 100 °C for 20 min, kept at this temperature for 1 h and cooled to room temperature reaching densities of up to 5.70 g/cm³/80% of the theoretical density. Electrical conductivity and Seebeck coefficient measurements were performed simultaneously with a NETZSCH SBA 458 Nemesis under a constant argon flow of 60 mL/min and in a temperature range of 298–573 K with 10 K steps. For the measurement of the electrical conductivity a DC current of 50 mV was applied and a heater voltage of 7 V was used for the determination of the Seebeck coefficient. Three full cycles were measured for each sample. The collected data was processed in the NETZSCH SBA-Measurement software package.³⁵ The Goldsmid-Sharp method was also used to estimate the band gap based on Seebeck measurements.³⁵

Thermal Diffusivity Measurements Via Laser Flash Analysis. Finely ground Cu_{1.5}Se_{0.5}Te_{0.5} and Cu_{1.5}Se_{0.2}Te_{0.8} crystals were hot pressed to a pellet of 10 mm diameter under 2 t as described above, reaching above 84% of the crystallographic density. The pellets were spray-coated with a graphite layer on both sides to enhance emissivity.

Thermal diffusivity of freshly prepared pellets was measured on a NETZSCH LFA 467 HyperFlash laser flash Aperture under pure Nitrogen atmosphere. The ignition voltage of the flash lamp was set to 250 V with a pulse width of 600 μ s. An improved version of the model of Cape and Lehman was used to calculate thermal diffusivity.^{36,37} The data was analysed by the aid of the NETZSCH Proteus Thermal Analysis software package.³⁸

Thermal diffusivity of an annealed sample (annealing temperature 573 K for 3 days) was measured across the pellet under static helium

atmosphere using a Linseis LFA1000 laser-flash device equipped with an InSb detector. A laser power of 280 W was applied. The pulse length was 2 ms after the laser power. Heat loss and finite pulse corrections were calculated applying Dusza's model.³⁹ The specific heat capacitance C_p was determined in a temperature range from RT to 573 K on the same equipment. Since CuS doesn't show any phase transition in the desired range, a CuS sample with the same geometry and thickness was used as C_p reference, and both samples were coated with graphite spray prior to measurement.

Scanning Electron Microscopy and Energy Dispersive X-ray Spectroscopy. The samples were fixed on a steel holder with a conductive adhesive polymer tape from Plano GmbH. The SEM images and EDX analysis were performed using a JEOL JSM-IT200 InTouchScope with an integrated JEOL JED-2300 EDX unit. The acceleration voltage was set to 20 kV.

X-ray Photoelectron Spectroscopy Measurement. X-ray photoelectron spectroscopy (XPS) spectra were acquired with a Kratos Axis Supra spectrometer using monochromatic Al K_{α} radiation ($h\nu = 1486.6$ eV) with a total power of 225 W under ultra-high vacuum ($<1.33 \times 10^{-7}$ Pa). The emission current was 15 mA and the pass energy for the detector was 160 eV for the wide scan and 40 eV for the detailed spectra. For the wide scan, a step size of 1 eV and a dwell time of 200 ms and for the region scans a step size of 0.1 eV and a dwell time of 300 ms was applied. The instrument's charge neutralizer was activated, using a filament current of 0.45 A, a filament bias of 1 V and a charge balance of 3 V (empirical values). The binding energy values were calibrated to the C 1s photoemission peak for adventitious hydrocarbons at 284.8 eV.

Bulk Modulus Determination Via High Pressure Experiments. A powdered sample of $\text{Cu}_{1.5}\text{Se}_{0.5}\text{Te}_{0.5}$ was selected for diamond anvil cell (DAC) high pressure X-ray experiments (HPXRD) in order to determine pressure dependent properties and the bulk modulus. Pressure dependent cell parameter determinations were performed at beamline I15 at Diamond Light Source, UK, with an X-ray energy of 25.0 keV (wavelength $\lambda = 0.4959$ Å). For DAC experiments, diamond anvils with 500 μm diameter culets were used, the pressure transmitting medium was a 4:1 mixture of methanol/ethanol (volume fraction) and the ruby fluorescence scale was used for pressure calibration.⁴⁰ The methanol/ethanol mixture is known to behave hydrostatically up to a pressure of approximately 10 GPa. The experiments were performed in a pressure range from ambient to 9.51 GPa. Above this pressure, a change from hydrostatic to non-hydrostatic conditions was detected in the data. For the DAC measurements a CdTe 2M Pilatus area detector was used, of which the sample-to-detector distance was calibrated prior to the experiment with a LaB₆ standard. The 2D detector files of all experiments were compiled to 1D HPXRD data by using DAWN.⁴¹ The ruby fluorescence modes were collected before and after each X-ray measurement, and an equilibration time of 10 min was set prior to each data acquisition. The ruby modes were fitted with a pseudo-Voigt profile in the FITYK software to determine the exact pressure data.⁴⁰ Pressure values used for calculation were averaged from the two pre- and post-measurement ruby data points. Each diffractogram has been analyzed using the JANA 2006 software routine and the unit cells were refined after profile fitting.³²

Pressure as a function of volume was fitted with a third order Birch–Murnaghan equation of state (EoS)⁴²

$$P = \frac{3}{2}K_0 \left[\left(\frac{V}{V_0} \right)^{-7/3} - \left(\frac{V}{V_0} \right)^{-5/3} \right] \left\{ 1 + \frac{3}{4}(K' - 4) \left[\left(\frac{V}{V_0} \right)^{-2/3} - 1 \right] \right\} \quad (2)$$

with P = applied pressure in GPa, K_0 = bulk modulus in GPa, K' = first pressure derivative of bulk modulus, V_0 = cell volume at ambient pressure in Å³, and V = cell volume at a given pressure P in Å³ to determine the bulk modulus K_0 . The software EoSFit7c was used for the fitting.⁴¹

In order to verify the significance of the fit, the Eulerian strain f

$$f = \frac{1}{2} \left[\left(\frac{V}{V_0} \right)^{-2/3} - 1 \right] \quad (3)$$

was plotted against the normalized pressure F

$$F = \frac{P}{3f \times (1 + 2f)^{5/2}} \quad (4)$$

RESULTS AND DISCUSSION

The first part of the discussion focuses on the crystal structure of $\text{Cu}_{1.5}\text{Se}_y\text{Te}_{1-y}$. Single crystal and powder X-ray measurements were used to determine the structure and phase purity of the investigated new compounds. SEM/EDX as well as XPS measurements are reported to verify the nominal composition of the crystals. In the second part, the physical properties are determined to designate possible fields of application. Assuming semiconducting behavior—as inferred from the optical appearance of the material, the stability and thermo-electric behavior are investigated by thermal analysis as well as electrical conductivity and Seebeck coefficient measurements. Furthermore, the compressibility of the material was discussed.

Powder X-ray Diffraction of $\text{Cu}_{1.5}\text{Se}_y\text{Te}_{1-y}$ with $y = 0.2$ – 0.7 . Finely ground polycrystalline samples with the nominal composition $\text{Cu}_{1.5}\text{Se}_y\text{Te}_{1-y}$ with selenium contents varying from $y = 0.2$ to 0.7 were used to determine the purity by powder X-ray diffraction. All samples show comparable diffraction patterns with well-defined reflections (Figure 1),

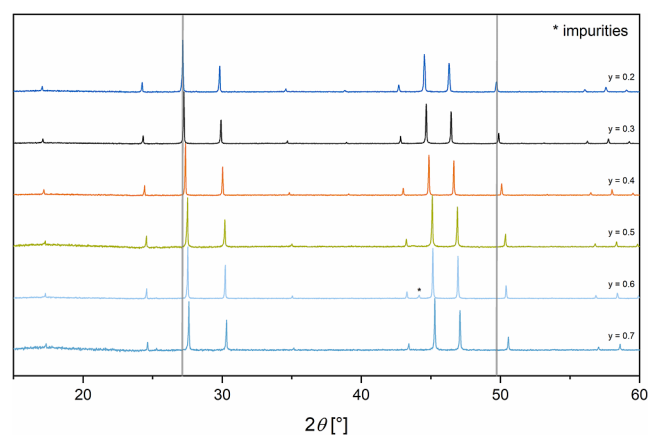


Figure 1. Powder XRD for $\text{Cu}_{1.5}\text{Se}_y\text{Te}_{1-y}$ with $y = 0.2$ – 0.7 . Impurities are marked with an asterisk, showing the main reflection of Cu_2Se . A clear shift to higher diffraction angles with higher selenium content is visible due to decreasing unit cell volume. Intensity is given in a.u.

leading to the assumption that a single phase is formed, crystallizing in an isotypic structure for all compositions. No side phases are observed in the diffractograms except for $y = 0.6$, where the main reflection of Cu_2Se is slightly visible (marked with an asterisk). For the determination of the crystal system and the lattice parameters, the powder XRDs were indexed for all compositions. $\text{Cu}_{1.5}\text{Se}_y\text{Te}_{1-y}$ representatives crystallize cubically, in space group $Pm\bar{3}n$ (no. 223), with lattice parameters of $a = 7.2100(4)$ Å, $y = 374.81(3)$ Å³ for $y = 0.7$ to $a = 7.3250(6)$ Å, $V = 393.03(6)$ Å³ for $y = 0.2$. Figure 2 shows a linear decrease of the cell volume with increasing selenium content, which is in good agreement with Vegard's law (taking the lattice parameter into account).⁴³ The adjusted

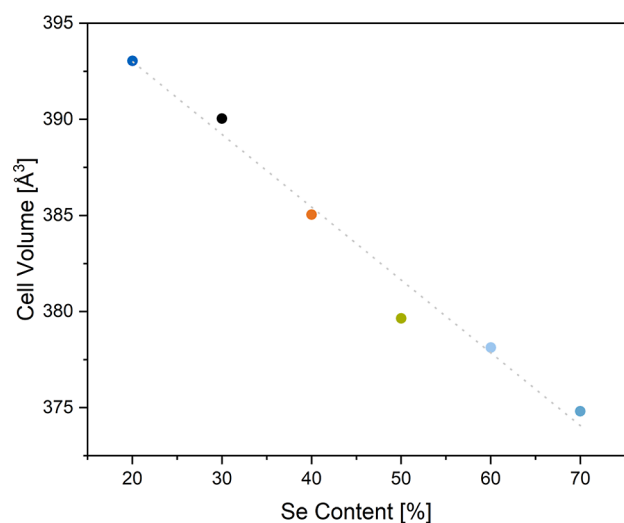


Figure 2. Cell volume as a function of selenium content in atom percent. The linear behavior is clearly visible ($R^2 = 0.974$).

R^2 value for the linear fit equals 0.974.⁴³ Lattice parameters are summarized in Table S1 in the supplement.

Single Crystal Structure Determination of $\text{Cu}_{1.5}\text{Se}_{0.3}\text{Te}_{0.7}$. Single crystals with a Se/Te ratio of 0.3:0.7 were used to perform single crystal X-ray structure determination. $\text{Cu}_{1.5}\text{Se}_{0.3}\text{Te}_{0.7}$ crystallize cubically, in space group $Pm\bar{3}n$; selected crystallographic data are summarized in Table 2. The lattice parameters for $\text{Cu}_{1.5}\text{Se}_{0.305}\text{Te}_{0.695}$ derived from single crystal data ($a = 7.2832(4)$ Å, $V = 386.34(4)$ Å³) deviate slightly from the powder data ($a = 7.3063(6)$ Å). This minor deviation may be explained by small compositional differences between single crystals and the bulk or a higher resolution in PXRD. Copper ions occupy 50% of the 24k position (0.8367(3), 0, 0.7031(5)), while selenium and

Table 2. Crystallographic Data and Structure Refinement Details for $\text{Cu}_{1.5}\text{Se}_{0.3}\text{Te}_{0.7}$

	$\text{Cu}_{1.5}\text{Se}_{0.3}\text{Te}_{0.7}$ 293 K
refined composition	$\text{Cu}_{1.5}\text{Se}_{0.305}\text{Te}_{0.695}$
molar mass (g mol ⁻¹)	208.1
crystal size (mm)	0.13
crystal shape/color	block/black
crystal system	cubic
space group	$Pm\bar{3}n$ (223)
Z	8
a (Å)	7.2832(4)
V (Å ³)	386.34(4)
ρ_{calc} (g cm ⁻³)	7.1552
diffractometer	STOE Stadivari
radiation (Å)	0.71073 (Mo K α 1/2)
μ (cm ⁻¹)	32.2
F(000)	720.0
θ range (°)	3.96–34.97
hkl range	0/+7, 0/+8, 1/+11
no. of reflections	305
R_{int}	0.0162
data/parameters	115/12
R/wR [$I > 3\sigma(I)$]	0.0423/0.0647
R/wR (all)	0.1102/0.0851
goodness of fit	1.31
res. elec. dens. max/min (e Å ⁻³)	-1.87/+1.27

tellurium are located on 2a (0, 0, 0) and 6d (0,5, 0, 0,75). On both anion sites the two different elements are randomly distributed. The refined ratio between them is 0.71(2):0.29 (Te/Se) in position 2a and 0.69(2):0.31 in position 6d, which in sum matches the starting ratio of 0.7:0.3. All atomic parameters are summarized in Table 3.

Table 3. Atomic Parameters of $\text{Cu}_{1.5}\text{Se}_{0.3}\text{Te}_{0.7}$

atom	Wyckoff position	atom site	S.O.F.	x/a	y/b	z/c
Te1	2a	m-3.	0.71(1)	0	0	0
Se1	2a	m-3.	0.29	0	0	0
Cu	24k	m..	0.5	0.8368(7)	0	0.7032(5)
Te2	6d	-4m.2	0.69(5)	1/2	0	3/4
Se2	6d	-4m.2	0.31	1/2	0	3/4

The anion substructure is isostructural to the A15-type (also called “ β -tungsten”) as illustrated in Figure 3a. Anions on 2a

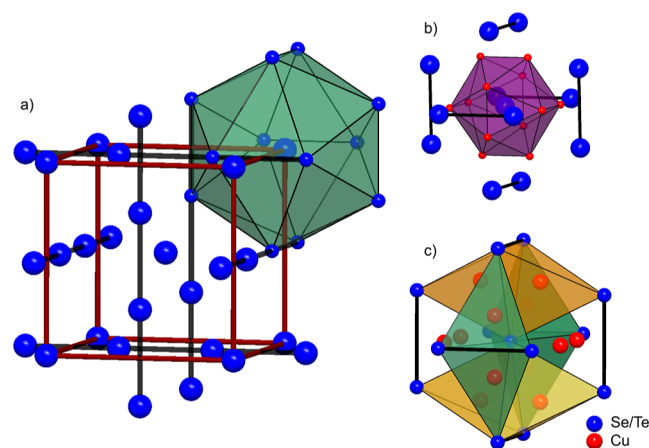


Figure 3. Crystal structure of $\text{Cu}_{1.5}\text{Se}_{0.3}\text{Te}_{0.7}$. (a) Anion substructure of $\text{Cu}_{1.5}\text{Se}_{0.3}\text{Te}_{0.7}$. The unit cell is depicted in red. Anions on position 2a form a body centered cubic atom arrangement and chains of anions, characterized by the shortest anion–anion distance of 3.642(1) Å, are located on each unit cell face (6d site). This motif is known from the A15-type structure.⁴⁴ The anions at the origin are icosahedrally coordinated, as illustrated by the green polyhedron. (b) Cation distribution in $\text{Cu}_{1.5}\text{Se}_{0.3}\text{Te}_{0.7}$. Each anion icosahedron accommodates 12 cation sites (24k) also forming an icosahedron. Each Cu site within the anionic icosahedron is half occupied. (c) Cu is distorted tetrahedrally coordinated by the anions. Two neighboring Cu-centered tetrahedra are interconnected via common faces (green and orange polyhedra) while neighboring double tetrahedra are connected via shared edges.

form a body centered cubic atom arrangement, in which chains of anions generated by the 6d site are located on each unit cell face. Anions on 2a are icosahedrally coordinated by anions located on 6d. Each anionic icosahedron is connected to neighboring icosahedra via a common edge that is defined by the shortest anion–anion distances within the linear anion chains (illustrated with black lines in Figure 3a–c). The cation substructure corresponds to a single cation site (24k). To illustrate the cation distribution, we use the aforementioned anion icosahedron. Cations are distributed icosahedrally within this anion icosahedron as shown in Figure 3b. The 24k site is half occupied which is a prerequisite due to the copper coordination (face-shared tetrahedra) within this anion icosahedron. The structure of $\text{Cu}_{1.5}\text{Se}_{0.3}\text{Te}_{0.7}$ can be regarded

as an anti-type of the β - $\text{UH}_3/\text{AuZn}_3$ structure.^{47,48} In UH_3 , the anions (hydride) occupy the $24k$ positions and the cations the $2a$ and $6d$ position (U in UH_3).

The copper atoms are coordinated by chalcogenide atoms to form distorted tetrahedra. This feature is illustrated in Figure 3c. As a result of the symmetry and the copper distribution, face-sharing double tetrahedra are present, leading to short Cu–Cu distances of 2.32(3) Å. As a consequence, only one of the two tetrahedral voids can be occupied. In Figure 3c we illustrate the double tetrahedra with similar colors (green and orange). Each set of double tetrahedra is connected to its neighbors via common edges. This edge sharing allows reasonable Cu–Cu distances of 2.77(2) Å.

Cu–Se/Te distances range from 2.467(2) to 2.630(3) Å. These values are very similar to the distances reported in copper chalcogenide minerals such as vulcanite (CuTe)—with Cu/Te distances of 2.604–2.763 Å and klockmannite (CuSe)—with Cu/Se distances of 2.200–2.318 Å.^{45,46} A distorted-tetrahedral coordination is also known from the latter mineral.

In comparison to the structure of $\text{Cu}_{1.5}\text{Te}$ determined from electron diffraction data by Willhammar et al., who reported Cu–Te distances of 2.51–2.70 Å, our single crystal data determination results in the same space group $Pm\bar{3}n$ and similar bond lengths.^{49a} Since $\text{Cu}_{1.5}\text{Te}$ could only be achieved as nanocrystals, we assume that the partial substitution of tellurium by selenium or the applied synthesis method is beneficial for crystal growth of millimeter-sized single crystals.

The title compound has nothing in common with the crystal structures of binary phases like Cu_3Se_2 or $\text{Cu}_{3-x}\text{Te}_2$ reported in the literature.^{49b,c}

Thermal Analysis by DSC of $\text{Cu}_{1.5}\text{Se}_y\text{Te}_{1-y}$ with $y = 0.2$ – 0.7 . The thermal properties and stabilities of $\text{Cu}_{1.5}\text{Se}_y\text{Te}_{1-y}$ with $y = 0.2$ – 0.7 were determined by DSC in sealed aluminium crucibles. No thermal effects were detected for the whole series between 173 and 723 K. As a representative example, data of $\text{Cu}_{1.5}\text{Se}_{0.5}\text{Te}_{0.5}$ is shown in Supporting Information Figure S1. To verify that no decomposition takes place up to 723 K, a powder diffractogram was collected after 2 consecutive cycles in the DSC. As Figure S2 shows, no changes could be detected.

After exposing $\text{Cu}_{1.5}\text{Se}_{0.5}\text{Te}_{0.5}$ for two cycles up to 773 K, a significant amount of Cu_2Se was formed, indicating that the decomposition of the material takes place above 723 K.

SEM/EDX/XPS on Selected $\text{Cu}_{1.5}\text{Se}_y\text{Te}_{1-y}$ Representatives. Quantitative energy-dispersive X-ray spectroscopy (EDX) measurements were performed to substantiate the composition derived from the single crystal structure determination and phase analysis (Table 4). Crystals of three different compositions, $\text{Cu}_{1.5}\text{Se}_{0.3}\text{Te}_{0.7}$, $\text{Cu}_{1.5}\text{Se}_{0.6}\text{Te}_{0.4}$ and $\text{Cu}_{1.5}\text{Se}_{0.5}\text{Te}_{0.5}$, were chosen to representatively verify the formation of a solid solution. For each sample, three independent spots were measured, and the average of these

Table 4. EDX Results for Three Different Compositions of $\text{Cu}_{1.5}\text{Se}_y\text{Te}_{1-y}$ ^a

nominal composition	Cu (at. %)	Se (at. %)	Te (at. %)	Cl (at. %)
$\text{Cu}_{1.5}\text{Se}_{0.3}\text{Te}_{0.7}$	64(2)	9.3(7)	24(1)	3.5(4)
$\text{Cu}_{1.5}\text{Se}_{0.5}\text{Te}_{0.5}$	60(1)	19.2(7)	18(2)	2.3(1)
$\text{Cu}_{1.5}\text{Se}_{0.6}\text{Te}_{0.4}$	58(1)	19.2(7)	18.6(3)	4.0(7)

^aAll values are averaged from three point measurements.

is used to calculate the composition. The crystals shown in Figure 4 show square facets with 90° angles between the faces,

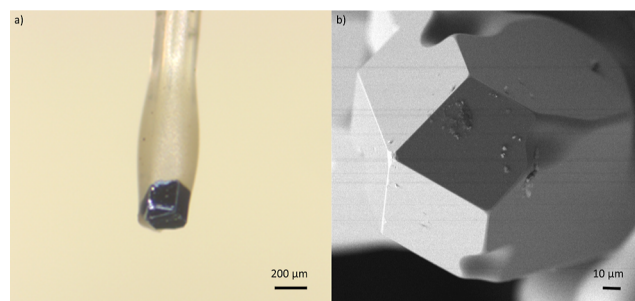


Figure 4. (a) Digital microscope image of a $\text{Cu}_{1.5}\text{Se}_{0.3}\text{Te}_{0.7}$ crystal mounted onto a single crystal pin holder. (b) SEM image (secondary electron detector) of a $\text{Cu}_{1.5}\text{Se}_{0.3}\text{Te}_{0.7}$ crystal at a 500 \times magnification and 20 kV acceleration voltage.

as expected for a cubic material. For $y = 0.3$ the composition in at. % calculated without considering chlorine is 65(1)% Cu, 9.6(1)% Se, and 25(1)% Te, resulting in a molar ratio of 1.5:0.22:0.57, thus showing a slight deficiency of the chalcogen atoms. Since a small amount of 1–2% chlorine is detected in every sample, this excess in copper could be explained by residual CuCl , the transport agent, present on the crystal surface. X-ray photoelectron spectroscopy (XPS, see below) on a fresh fracture surface of the crystals verifies the assumption, as chlorine was not detected within the crystal bulk.

For $y = 0.6$, 61(1)% Cu, 20(1)% Se, and 19.3(3)% (at. %) Te were detected. Here, the atomic ratio between copper and chalcogenide of Cu/Se/Te = 1.5:0.49:0.48 perfectly fits the one expected from the proposed chemical formula. The results confirm the presence of expected selenium and tellurium contents for $\text{Cu}_{1.5}\text{Se}_y\text{Te}_{1-y}$ representatives, as well as the adjustability of the ratio between these elements.

XPS measurements were performed on the fresh fracture face of a crystal to determine the role of chlorine in the synthesis as well as the oxidation state of copper. Therefore, a freshly prepared crystal was cut into two parts and directly transferred into the XPS under inert atmosphere. On the cleaved surface, no signals of chlorine could be detected. In the Cu 2p region, only the two signals for the $2p_{1/2}$ and $2p_{3/2}$ were observed, which can be fitted by two Lorentzian shaped curves, see Figure 5. The Cu $2p_{3/2}$ signal is slightly higher than the energy of metallic Cu (932.7 eV).⁵⁰ No satellites for higher-valent copper species were present, so the oxidation state in the crystal has to be the same for all copper positions. Taking the nominal composition of $\text{Cu}_{1.5}\text{X}$ (X = chalcogenide) with an expected oxidation state –II for the chalcogenide into account, a mixture of Cu^{II} and Cu^{I} would be needed to allow charge neutrality. The observation of only one copper valence indicates a non-ionic and more semi-metallic character of the material. We also checked anion–anion distances in order to verify the existence of attractive anion contacts. There is no hint of an anion dumbbell formation due to contacts exceeding 3.6 Å in $\text{Cu}_{1.5}\text{Se}_{0.3}\text{Te}_{0.7}$. Since XPS has a much lower depth resolution in contrast to EDX, these results mainly present the situation on the materials surface. All measurements were performed on mm-sized crystals. No $\text{Cu}_{1.5}\text{Se}_y\text{Te}_{1-y}$ formation featuring the afore mentioned structure could be achieved by various synthesis approaches such as synthesis in stoichiometric amounts in a common solid state melting and annealing

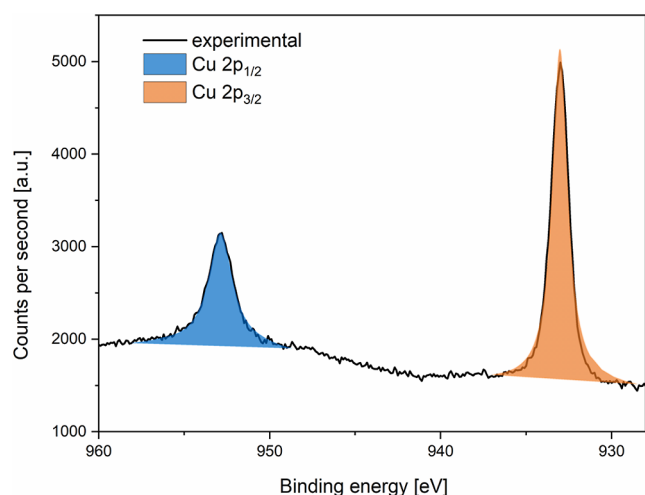


Figure 5. XPS spectrum of $\text{Cu}_{1.5}\text{Se}_{0.5}\text{Te}_{0.5}$ in the Cu 2p region. The two peaks at around 933 and 953 eV, fitted by a Lorentzian shaped curve, represent the $2p_{3/2}$ and $2p_{1/2}$ signals of only one valence state. No satellites for higher valent copper species were observed.

procedure, and via spark plasma sintering of the same, in the absence of copper chloride at different temperatures. This aspect illustrates the need of copper chloride as a transport agent to allow chemical transport in the gas phase; nevertheless, XPS results clearly show that no chlorine is present in the structure.

High Pressure Powder XRD $\text{Cu}_{1.5}\text{Se}_{0.5}\text{Te}_{0.5}$. The mechanical stability of $\text{Cu}_{1.5}\text{Se}_{0.5}\text{Te}_{0.5}$ under compressive stress was analyzed by high pressure powder X-ray diffraction (PXRD) measurements in a diamond anvil cell (DAC). The bulk modulus K as well as its pressure derivative K' were obtained by the fit of a 3rd order Birch–Murnaghan (BM) equation of state to the refined cell parameters. A pressure range from ambient to 9.51 GPa was applied as shown in Figure 6. A 2nd order BM equation of state (EOS) (see Figure S3 in the Supporting Information section) did not yield a reasonable fit, leading to a bulk modulus of 50.4(3) GPa. The obtained 3rd order fit results in a bulk modulus of $K = 40.9(1)$

GPa with a pressure derivative of $K' = 6.57(7)$. To substantiate the need of a 3rd order BM EOS, a f – F plot was performed. A linear fit of the resulting data indicates a bulk modulus of 41.3 GPa and a pressure derivative K' of 6.44, both agreeing reasonably well with the values of the third order BM EOS.

The obtained values show an intermediate compressive behavior between copper tellurides and selenides. CuSe and Cu_2Se present bulk moduli of 96 and 77 GPa, respectively.^{51,52} On the other side of the spectrum, CuTe has a low bulk modulus of 21 GPa.⁵³ These differences in stiffness are commonly explained by the difference in electronegativities between the chalcogenides. The difference between copper and selenium is quite pronounced ($\Delta\text{EN} = 0.7$), whereas the one for copper and tellurium is much smaller ($\Delta\text{EN} = 0.2$).⁵⁴ This variance leads to a different stiffness of the copper–chalcogenide bonds and ultimately results in the reported bulk moduli. For our mixed chalcogenides, the intermediate bulk modulus is a result of the averaged influence of both chalcogenides, leading to values between those ones of the binary compounds.

Thermoelectric Characterization of Selected $\text{Cu}_{1.5}\text{Se}_y\text{Te}_{1-y}$ Representatives. Coinage-metal chalcogenides are known as promising candidates for thermoelectric applications due to their typically high electrical conductivities, combined with a moderate thermal conductivities as well as the presence of mobile atoms. In the following section we evaluate the application potential of $\text{Cu}_{1.5}\text{Se}_y\text{Te}_{1-y}$ as thermoelectric materials. Seebeck measurements are not only used to determine the thermoelectric power of materials, but they are also suited to get an estimate of the band gap by using the Goldsmid–Sharp method.⁵⁵

The electrical behavior of two representative samples with different chalcogen ratios, $\text{Cu}_{1.5}\text{Se}_{0.5}\text{Te}_{0.5}$ and $\text{Cu}_{1.5}\text{Se}_{0.2}\text{Te}_{0.8}$, was investigated in a temperature range of 298–573 K. The Seebeck coefficient as well as the electrical conductivity as a function of temperature up to 573 K are shown in Figure 7a–d. To allow sintering of the samples the second cycle of each measurement is shown for a better comparison. Both curves for the Seebeck coefficient present only positive values over the whole temperature range, identifying the materials as p-type,

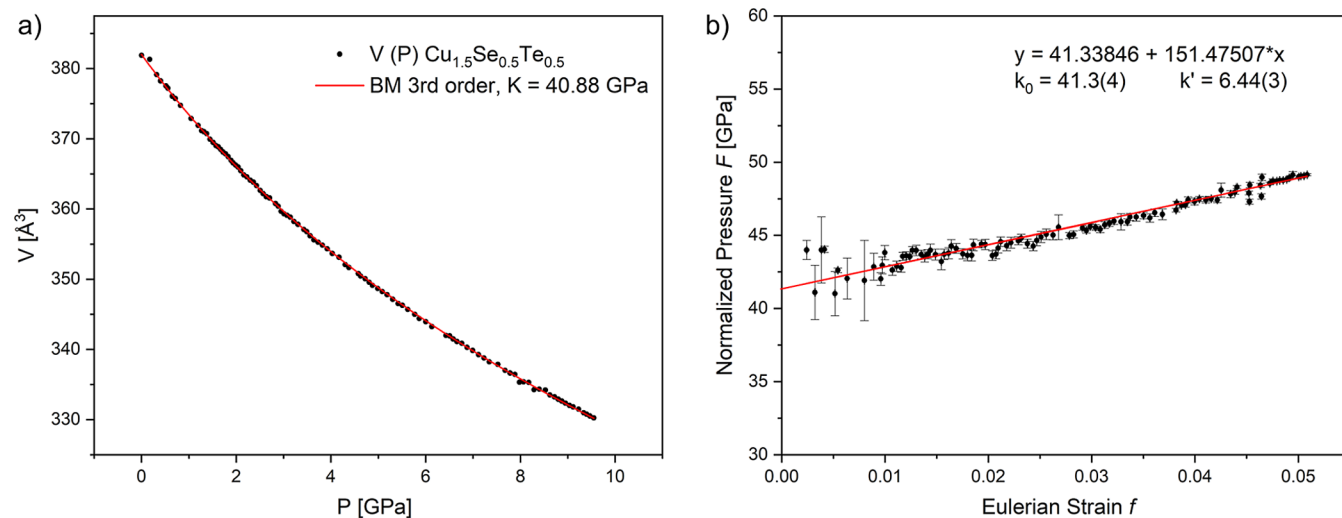


Figure 6. (a) High pressure cell volumes obtained from LeBail fitted P-XRD data as well as the third order Birch–Murnaghan (BM) fit for $\text{Cu}_{1.5}\text{Se}_{0.5}\text{Te}_{0.5}$. The obtained bulk modulus is 40.88 GPa. Data was collected in a diamond anvil cell via synchrotron radiation. (b) f – F plot with its linear fit resulting in $K = 41.3$ GPa and $K' = 6.44$, verifying the need of a third order BM fit.

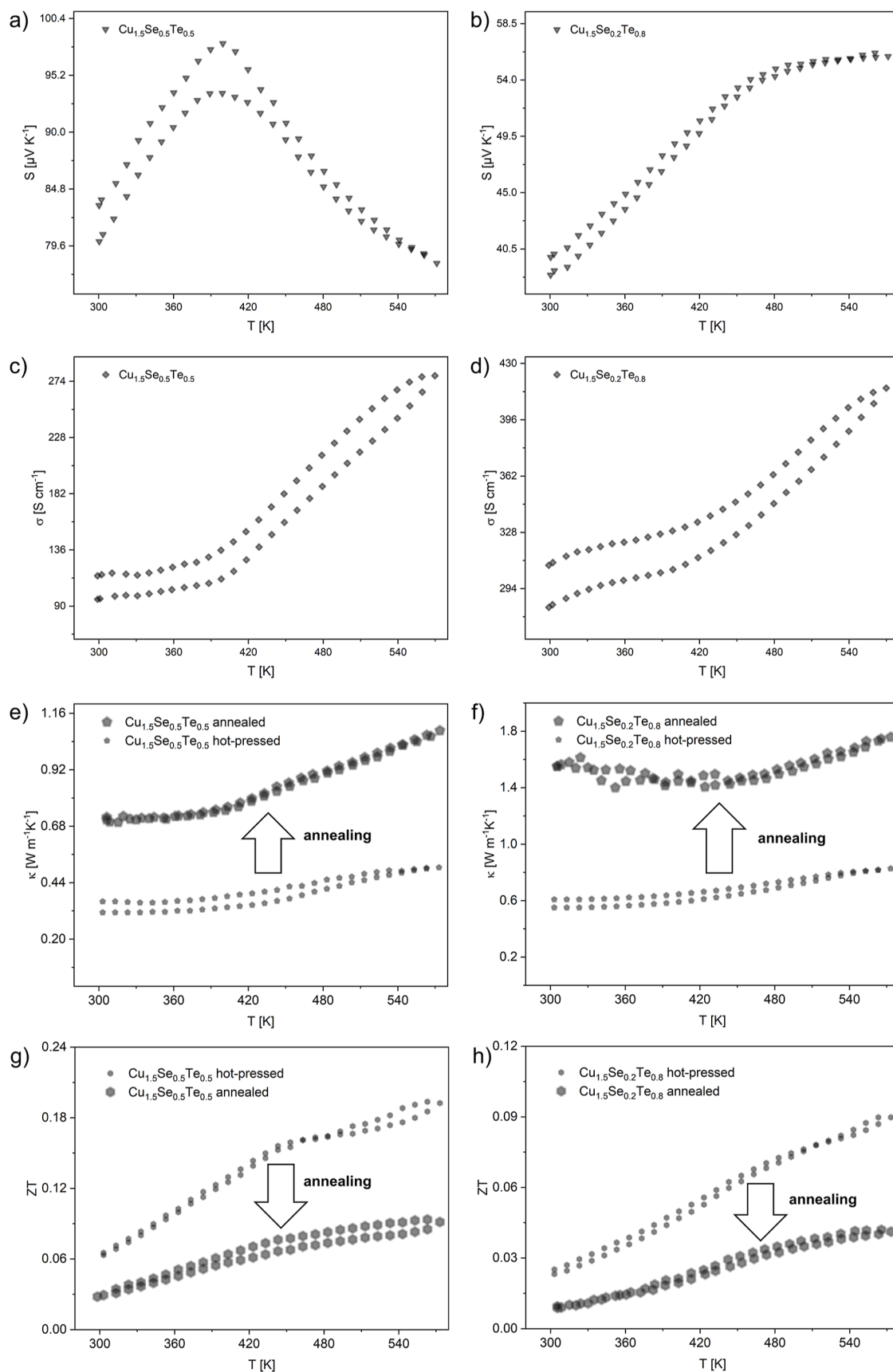


Figure 7. Seebeck coefficient values (a,b), electrical conductivity (c,d), thermal conductivity (e,f), and ZT (g,h) for $\text{Cu}_{1.5}\text{Se}_{0.5}\text{Te}_{0.5}$ and $\text{Cu}_{1.5}\text{Se}_{0.2}\text{Te}_{0.8}$ in a temperature range from 303 to 573 K.

i.e., predominantly hole-conducting semiconductors. Both compounds show moderate positive Seebeck coefficients below 100 $\mu\text{V}/\text{K}$ while $\text{Cu}_{1.5}\text{Se}_{0.5}\text{Te}_{0.5}$ almost reaches this value and $\text{Cu}_{1.5}\text{Se}_{0.2}\text{Te}_{0.8}$ keeps well below 60 $\mu\text{V}/\text{K}$ over the entire measuring range.

Starting from 83 $\mu\text{V}/\text{K}$ at room temperature, the Seebeck coefficient for $\text{Cu}_{1.5}\text{Se}_{0.5}\text{Te}_{0.5}$ reaches its maximum value of 98 $\mu\text{V K}^{-1}$ at 399 K. Afterwards, it decreases monotonically to 78 $\mu\text{V K}^{-1}$ at the maximum temperature of 673 K. The electrical conductivity is at the same time slightly increasing from 115 S cm^{-1} at room temperature to 135 S cm^{-1} at 393 K. Subsequently, it drastically rises to 278 S cm^{-1} at 573 K. The increase of electrical conductivity with increasing temperature characterizes the material as a low-gap semiconductor with a band gap of approx. 0.08 eV.

For $\text{Cu}_{1.5}\text{Se}_{0.2}\text{Te}_{0.8}$, both electrical conductivity and Seebeck coefficient behave in a similar way. In contrast to the sample with higher selenium content, Seebeck coefficients are slightly lower, starting from 40 $\mu\text{V K}^{-1}$ at room temperature. They increase constantly to 54 $\mu\text{V K}^{-1}$ at 453 K, but afterwards no decrease can be seen. Instead, a plateau-like behavior with only a slight increase to 55.9 $\mu\text{V K}^{-1}$ at the maximum of 573 K is observed. The electrical conductivity amounts to 283 S cm^{-1} at room temperature, which slightly increases to 317 S cm^{-1} at 428 K. Then, it rises further at a higher rate, up to 415 S cm^{-1} at 573 K. In Supporting Information Figure S4, three consecutive cycles of the Seebeck coefficient and electrical conductivity measurements for both materials are shown. After the first heating cycle, a slight increase in conductivity can be seen from cycle to cycle for both materials. For the Seebeck coefficients, the material behaves vice versa, showing a slight decrease of the measured values.

Comparing both materials, there is a clear difference in the behavior depending on the chalcogen ratio. $\text{Cu}_{1.5}\text{Se}_{0.2}\text{Te}_{0.8}$ shows an almost three times higher electrical conductivity over the whole temperature range, even if the rise after reaching the highest Seebeck values is not as pronounced as for $\text{Cu}_{1.5}\text{Se}_{0.5}\text{Te}_{0.5}$. An increase in electrical conductivity at higher tellurium content matches the expected results. Tellurium tends to behave more like a metal than selenium. On the other hand, the Seebeck coefficients only reach half the value achieved for the higher selenium amount, while also not showing an explicit maximum at a certain temperature.

Band gaps were derived from the temperature dependent conductivity measurements assuming Arrhenius-like behavior. The determined values are 0.08 eV for $\text{Cu}_{1.5}\text{Se}_{0.5}\text{Te}_{0.5}$ and 0.04 eV for $\text{Cu}_{1.5}\text{Se}_{0.2}\text{Te}_{0.8}$.

These values are confirmed from Seebeck measurements using the Goldsmid and Sharp method.⁵⁵ Seebeck curves show a specific change in slopes for one particular temperature, at approximately 373 K for $\text{Cu}_{1.5}\text{Se}_{0.5}\text{Te}_{0.5}$ and at 423 K for $\text{Cu}_{1.5}\text{Se}_{0.2}\text{Te}_{0.8}$ (a defined maximum is present in Figure S4d). It has to be stated at this point that for $\text{Cu}_{1.5}\text{Se}_{0.2}\text{Te}_{0.8}$ a defined maximum in the Seebeck coefficient is only present in the first measurement cycle and not in the curve in Figure 7b where a plateau is reached. The band gap of semiconductors could be calculated from the maximum Seebeck values by the method of Goldsmid and Sharp, using the equation

$$E_{\text{g}} = 2e \times S_{\text{max}} \times T_{\text{max}} \quad (5)$$

with E_{g} = band gap energy, e = charge of an electron, S_{max} = maximum Seebeck coefficient and T_{max} = temperature of highest Seebeck value.⁵⁵

The calculated band gap is 0.08 eV for $\text{Cu}_{1.5}\text{Se}_{0.5}\text{Te}_{0.5}$ and 0.06 eV for $\text{Cu}_{1.5}\text{Se}_{0.2}\text{Te}_{0.8}$, in good accordance to the values determined from conductivity measurements. Those values derived from two different methods identify both material as narrow band gap semiconductors. Unfortunately, a determination of the bandgap by photoluminescence measurements is not suitable for such low energies. Obviously, the variation of the Se/Te ratio in the material leads to a change in the band gap and therefore in the electronic structure of these solids.⁵⁷

To calculate the figure of merit ZT of a thermoelectric material, not only the power factor $S^2\sigma$, but also the thermal conductivity κ is needed. Its value can be calculated by

$$\kappa = \alpha \times C_{\text{p}} \times \rho \quad (6)$$

where α , C_{p} , and ρ are the heat diffusivity, the specific heat capacitance, and the density, respectively. The heat diffusivity was determined on freshly prepared, hot pressed (data see Supporting Information S5) and annealed (Supporting Information S6) pellet samples of $\text{Cu}_{1.5}\text{Se}_{0.5}\text{Te}_{0.5}$ and $\text{Cu}_{1.5}\text{Se}_{0.2}\text{Te}_{0.8}$ via LFA. It became obvious during our TE characterization the pretreatment of the samples has a certain influence on the TE performance. We decided to anneal some of the LFA pellet samples after preparation at 573 K for three days prior to the measurements. What we noticed for the annealed but also the freshly measured samples after the LFA measurements is a formation of additional side phases (see Figure S5) which is an indicator of a certain decomposition during the LFA measurements. Nevertheless, we found stable, invariant values for the thermal diffusivity in consecutive measurement cycles only for the annealed samples (see Figure S5a,b).

For hot-pressed $\text{Cu}_{1.5}\text{Se}_{0.5}\text{Te}_{0.5}$, α ranges from 0.13 to 0.21 $\text{mm}^2 \text{s}^{-2}$ between 303 and 573 K. C_{p} was determined to be 0.41 $\text{J g}^{-1} \text{K}^{-1}$ in the whole temperature range (see Supporting Information Figure S7a), revealing only slightly higher values than provided by the Dulong–Petit approximation that is most likely due to the errors during the C_{p} determination. Thermal conductivity calculated according to eq 6 amounts to 0.31 $\text{W m}^{-1} \text{K}^{-1}$ at 303 K and 0.50 $\text{W m}^{-1} \text{K}^{-1}$ at 573 K; the results are shown in Figure 7e. Those quite low values are around 1 order of magnitude lower than in the bulk binary copper telluride Cu_2Te (2–4 $\text{W m}^{-1} \text{K}^{-1}$ at RT)⁵⁸ and still half of the values for Cu_2Se (around 1 $\text{W m}^{-1} \text{K}^{-1}$ at RT and 400 K),^{18,59} whereas they are quite similar to the ones observed for coinage metal polytelluride halides like $\text{Ag}_{10}\text{Te}_4\text{Br}_3$ or $\text{Ag}_{18}\text{Cu}_3\text{Te}_{11}\text{Cl}_3$ (0.14–0.43 $\text{W m}^{-1} \text{K}^{-1}$)⁶⁰ and $\text{Cu}_{9,1}\text{Te}_4\text{Cl}_3$ (0.4–0.6 $\text{W m}^{-1} \text{K}^{-1}$).¹³ Taking the only stable values for annealed samples into account, the thermal conductivity reaches values between 0.7 and 1 $\text{W m}^{-1} \text{K}^{-1}$. Those values are slightly larger than observed for Cu_2Se (0.6 $\text{W m}^{-1} \text{K}^{-1}$ at 400 K)⁶¹

For the hot-pressed and non-annealed $\text{Cu}_{1.5}\text{Se}_{0.2}\text{Te}_{0.8}$ sample, we found lower values of α than for the annealed ones (see Figure 7f). C_{p} was determined to be 0.47–0.48 $\text{J g}^{-1} \text{K}^{-1}$ (see Supporting Information S7b). In the case of an annealed sample a thermal conductivity between 1.55 and 1.75 $\text{W m}^{-1} \text{K}^{-1}$ was detected. Also in this case we performed PXRD phase analyses for all samples before and after the LFA measurements and found traces of impurities after the treatment. We identified the formation of side phases (e.g., $\text{Cu}_{1.77}\text{Se}$) which indicates a certain lability of the title compounds during the LFA measurements. The electro-migration of copper is a well-known behavior of ion-

conducting thermoelectrics, unfortunately limiting their thermoelectric application potential.^{13,56}

Due to the fact that we observed hints of an unknown side phase formation after LFA measurements, as illustrated in Supporting Information Figure S5, we do not intend to discuss the resulting ZT values of the two samples in great detail. Nevertheless, taking the values of stable transport measurements into account, resulting ZT values are not competitive to other room temperature TE materials.

In the Seebeck and LFA measurements we realized that both materials tend to partially decompose during the experiments. This means that any application of these compounds as TE materials required an enhancement of stability. The sensibility against light treatment in LFA also explains our difficulties to measure Raman spectra (not shown) as well as photoluminescence, which all demand the excitation through intense laser light.

Assuming to overcome the stability issues and to perform an optimization of the thermal conductivity by reducing the lattice contribution to very low values, one can estimate the achievable ZT value for a given Seebeck value taking the following equation into account. Here the thermal conductivity is only expressed by the Wideman–Franz law $\kappa_e = \sigma \cdot L_0 \cdot T$ (with L_0 = Lorenz number)

$$ZT \sim \frac{S^2}{L_0} \quad (7)$$

According to eq 7 and using $L_0 = 1.99 \cdot 10^{-8} \text{ W } \Omega \text{ K}^{-2}$ for $\text{Cu}_{1.5}\text{Se}_{0.5}\text{Te}_{0.5}$ as well as $L_0 = 2.208 \cdot 10^{-8} \text{ W } \Omega \text{ K}^{-2}$ for $\text{Cu}_{1.5}\text{Se}_{0.2}\text{Te}_{0.8}$, calculated like described by Kang and Snyder, estimate the optimum ZT achievable for $\text{Cu}_{1.5}\text{Se}_{0.2}\text{Te}_{0.8}$ at 300 K ($40 \mu\text{V K}^{-1}$) to be 0.07(2), and for $\text{Cu}_{1.5}\text{Se}_{0.5}\text{Te}_{0.5}$ ($81 \mu\text{V K}^{-1}$) to be 0.32(2).⁶² With determined ZT values of 0.03 for $\text{Cu}_{1.5}\text{Se}_{0.2}\text{Te}_{0.8}$ and of 0.07 for $\text{Cu}_{1.5}\text{Se}_{0.5}\text{Te}_{0.5}$ at elevated temperatures (for annealed samples) we see that both compounds do not have reached their optimum performance at the moment and the calculated values are also out of bounce to indicate a certain application potential.

Besides thermoelectric applications, the narrow band gap identifies this class of materials as promising candidates for infrared sensing. The tunable band gap in the energy range of around $500\text{--}650 \text{ cm}^{-1}$ allows the material to absorb radiation starting from the far infrared area of the electromagnetic spectrum and enables a widespread field for further research.

CONCLUSIONS

With the solid solution $\text{Cu}_{1.5}\text{Se}_y\text{Te}_{1-y}$, a new family of coinage metal chalcogenides is established. Single crystal X-ray measurements reveal that the compound crystalizes cubically, in space group $Pm\bar{3}n$ (223). The anion substructure resembles the β -tungsten structure type and copper ions are coordinated in slightly distorted tetrahedral environment formed by the chalcogenide atoms. The material is thermally stable up to 723 K and the measured bulk modulus of $\text{Cu}_{1.5}\text{Se}_{0.5}\text{Te}_{0.5}$ of 40.9 GPa is located in an expected range between the ones of binary copper tellurides and selenides. Reasonable electrical conductivities as well as narrow band gaps of ~ 0.06 to 0.08 eV make these materials suitable for thermoelectric and IR sensing applications. A low thermal conductivity of $0.7\text{--}1.8 \text{ W m}^{-1} \text{ K}^{-1}$, ZT in combination with the narrow band gaps qualify them as suitable candidates for sensor applications. Unfortunately, the title compounds are less attractive for TE

applications unless the light and electronic stability is significantly increased.

ASSOCIATED CONTENT

Supporting Information

The Supporting Information is available free of charge at <https://pubs.acs.org/doi/10.1021/acs.inorgchem.3c02037>.

DSC and PXRD data prior and after DSC measurements of a $\text{Cu}_{1.5}\text{Se}_{0.5}\text{Te}_{0.5}$, PXRD data of $\text{Cu}_{1.5}\text{Se}_y\text{Te}_{1-y}$ with $y = 0.2$ to 0.7 , 2nd order Birch–Murnaghan equation of state fit, electrical conductivity, Seebeck measurements, thermal diffusivity, and PXRD data before and after measurements (PDF)

Accession Codes

CCDC 2195113 contains the supplementary crystallographic data for this paper. These data can be obtained free of charge via www.ccdc.cam.ac.uk/data_request/cif, or by emailing data_request@ccdc.cam.ac.uk, or by contacting The Cambridge Crystallographic Data Centre, 12 Union Road, Cambridge CB2 1EZ, UK; fax: +44 1223 336033.

AUTHOR INFORMATION

Corresponding Author

Tom Nilges – TU Munich, School of Natural Sciences (NAT), Department of Chemistry, Professorship for Synthesis and Characterization of Innovative Materials, TU Munich, 85748 Garching b. München, Germany; orcid.org/0000-0003-1415-4265; Email: tom.nilges@tum.de

Authors

Alfred Rabenbauer – TU Munich, School of Natural Sciences (NAT), Department of Chemistry, Professorship for Synthesis and Characterization of Innovative Materials, TU Munich, 85748 Garching b. München, Germany; orcid.org/0000-0002-4879-719X

Anna Vogel – TU Munich, School of Natural Sciences (NAT), Department of Chemistry, Professorship for Synthesis and Characterization of Innovative Materials, TU Munich, 85748 Garching b. München, Germany

Janio Venturini – TU Munich, School of Natural Sciences (NAT), Department of Chemistry, Professorship for Synthesis and Characterization of Innovative Materials, TU Munich, 85748 Garching b. München, Germany

Mahboubeh Moslemi – Faculty of Chemistry and Mineralogy, Institute for Mineralogy, Crystallography and Materials Science, Leipzig University, 04275 Leipzig, Germany

Oliver Oeckler – Faculty of Chemistry and Mineralogy, Institute for Mineralogy, Crystallography and Materials Science, Leipzig University, 04275 Leipzig, Germany; orcid.org/0000-0003-0149-7066

Dominik Daisenberger – Diamond Light Source, OX11 0DE Didcot, U.K.

Complete contact information is available at:

<https://pubs.acs.org/doi/10.1021/acs.inorgchem.3c02037>

Notes

The authors declare no competing financial interest.

ACKNOWLEDGMENTS

The support by the TUM Graduate School is gratefully acknowledged. Parts of this work are funded by the German Science Foundation (DFG) under grant no. Ni1095/12-1,

project no. 522732992. We also thank Diamond Light Source, UK, for the provision of beamtime at beamline I15 under proposal number CY30094. The authors kindly thank Rebecca Wilhelm (Chair of Technical Electrochemistry, TUM) for the XPS measurements.

REFERENCES

- (1) Riffat, S. B.; Ma, X. Thermoelectrics: a review of present and potential applications. *Appl. Therm. Eng.* **2003**, *23*, 913–935.
- (2) Rowe, D. M. *CRC Handbook of Thermoelectrics*; CRC Press, 2018.
- (3) Markov, M.; Rezaei, E.; Sadeghi, S.; Esfarjani, K.; Zebarjadi, M. Thermoelectric properties of semimetals. *Phys. Rev. Mater.* **2019**, *3*, 095401.
- (4) Snyder, G. J.; Toberer, E. S. Complex thermoelectric materials. *Nat. Mater.* **2008**, *7*, 105–114.
- (5) Gayner, C.; Kar, K. K. Recent advances in thermoelectric materials. *Prog. Mater. Sci.* **2016**, *83*, 330–382.
- (6) Hou, S.; Liu, Y.; Yin, L.; Chen, C.; Wu, Z.; Wang, J.; Luo, Y.; Xue, W.; Liu, X.; Zhang, Q.; Cao, F. High performance wearable thermoelectric generators using Ag₂Se films with large carrier mobility. *Nano Energy* **2021**, *87*, 106223.
- (7) Lai, C.-H.; Lu, M.-Y.; Chen, L.-J. Metal sulfide nanostructures: synthesis, properties and applications in energy conversion and storage. *J. Mater. Chem.* **2012**, *22*, 19–30.
- (8) Gao, M.-R.; Xu, Y.-F.; Jiang, J.; Yu, S.-H. Nanostructured metal chalcogenides: synthesis, modification, and applications in energy conversion and storage devices. *Chem. Soc. Rev.* **2013**, *42*, 2986–3017.
- (9) Goldsmid, H. J.; Douglas, R. W. The use of semiconductors in thermoelectric refrigeration. *Br. J. Appl. Phys.* **1954**, *5*, 458.
- (10) Goldsmid, H. J. Bismuth Telluride and Its Alloys as Materials for Thermoelectric Generation. *Materials* **2014**, *7*, 2577–2592.
- (11) Mao, J.; Chen, G.; Ren, Z. Thermoelectric cooling materials. *Nat. Mater.* **2021**, *20*, 454–461.
- (12) Bu, Z.; Zhang, X.; Hu, Y.; Chen, Z.; Lin, S.; Li, W.; Xiao, C.; Pei, Y. A record thermoelectric efficiency in tellurium-free modules for low-grade waste heat recovery. *Nat. Commun.* **2022**, *13*, 237.
- (13) Vogel, A.; Miller, T.; Hoch, C.; Jakob, M.; Oeckler, O.; Nilges, T. Cu₉Te₄Cl₃: A Thermoelectric Compound with Low Thermal and High Electrical Conductivity. *Inorg. Chem.* **2019**, *58*, 6222–6230.
- (14) Liu, H.; Shi, X.; Xu, F.; Zhang, L.; Zhang, W.; Chen, L.; Li, Q.; Uher, C.; Day, T.; Snyder, G. J. Copper ion liquid-like thermoelectrics. *Nat. Mater.* **2012**, *11*, 422–425.
- (15) Miyatani, S.-y. Ionic Conduction in β -Ag₂Te and β -Ag₂Se. *J. Phys. Soc. Jpn.* **1959**, *14*, 996–1002.
- (16) Jood, P.; Chetty, R.; Ohta, M. Structural stability enables high thermoelectric performance in room temperature Ag₂Se. *J. Mater. Chem. A* **2020**, *8*, 13024–13037.
- (17) Lee, M. H.; Yun, J. H.; Ahn, K.; Rhyee, J.-S. Thermoelectric properties and chemical potential tuning by Cu-doping in n-type ionic conductors Cu_xAg_{2-x}Se_{0.5}Te_{0.5}. *J. Phys. Chem. Solids* **2017**, *111*, 214–218.
- (18) Conn, J. B.; Taylor, R. C. Thermoelectric and Crystallographic Properties of Ag₂Se. *J. Electrochem. Soc.* **1960**, *107*, 977.
- (19) Qiu, P.; Agne, M. T.; Liu, Y.; Zhu, Y.; Chen, H.; Mao, T.; Yang, J.; Zhang, W.; Haile, S. M.; Zeier, W. G.; Janek, J.; Uher, C.; Shi, X.; Chen, L.; Snyder, G. J. Suppression of atom motion and metal deposition in mixed ionic electronic conductors. *Nat. Commun.* **2018**, *9*, 2910.
- (20) Butt, S.; Farooq, M. U.; Mahmood, W.; Salam, S.; Sultan, M.; Basit, M. A.; Ma, J.; Lin, Y.; Nan, C.-W. One-step rapid synthesis of Cu₂Se with enhanced thermoelectric properties. *J. Alloys Compd.* **2019**, *786*, 557–564.
- (21) Han, C.; Li, Z.; Lu, G. Q.; Xue, D.; Dou, S. Robust scalable synthesis of surfactant-free thermoelectric metal chalcogenide nanostructures. *Nano Energy* **2015**, *15*, 193–204.
- (22) Mukherjee, S.; Parasuraman, R.; Umarji, A. M.; Rogl, G.; Rogl, P.; Chattopadhyay, K. Effect of Fe alloying on the thermoelectric performance of Cu₂Te. *J. Alloys Compd.* **2020**, *817*, 152729.
- (23) Zhao, L.; Wang, X.; Fei, F. Y.; Wang, J.; Cheng, Z.; Dou, S.; Wang, J.; Snyder, G. J. High thermoelectric and mechanical performance in highly dense Cu_{2-x}S bulks prepared by a melt-solidification technique. *J. Mater. Chem. A* **2015**, *3*, 9432–9437.
- (24) Guan, M.; Zhao, K.; Qiu, P.; Ren, D.; Shi, X.; Chen, L. Enhanced Thermoelectric Performance of Quaternary Cu_{2-2x}Ag_{2x}Se_{1-x}S_x Liquid-like Chalcogenides. *ACS Appl. Mater. Interfaces* **2019**, *11*, 13433–13440.
- (25) Zhao, K.; Qiu, P.; Song, Q.; Blichfeld, A. B.; Eikeland, E.; Ren, D.; Ge, B.; Iversen, B. B.; Shi, X.; Chen, L. Ultrahigh thermoelectric performance in Cu_{2-y}Se_{0.5}S_{0.5} liquid-like materials. *Mater. Today Phys.* **2017**, *1*, 14–23.
- (26) Zhao, K.; Guan, M.; Qiu, P.; Blichfeld, A. B.; Eikeland, E.; Zhu, C.; Ren, D.; Xu, F.; Iversen, B. B.; Shi, X.; Chen, L. Thermoelectric properties of Cu₂Se_{1-x}Te_x solid solutions. *J. Mater. Chem. A* **2018**, *6*, 6977–6986.
- (27) Butt, S.; Xu, W.; Farooq, M. U.; Ren, G. K.; Zhang, Q.; Zhu, Y.; Khan, S. U.; Liu, L.; Yu, M.; Mohmed, F.; Lin, Y.; Nan, C.-W. Enhanced Thermoelectricity in High-Temperature β -Phase Copper(I) Selenides Embedded with Cu₂Te Nanoclusters. *ACS Appl. Mater. Interfaces* **2016**, *8*, 15196–15204.
- (28) Osterlof, J.; Carlsson, C. G.; Webb, M.; Rottenberg, M. Copper Compounds of Acetylene. I. Acetylene Compounds with Cuprous Chloride. *Acta Chem. Scand.* **1950**, *4*, 374–385.
- (29) Vogel, A.; Nilges, T. Ion Dynamics and Polymorphism in Cu₂₀Te₁₁Cl₃. *Inorg. Chem.* **2021**, *60*, 15233–15241.
- (30) Stoe & Cie. X-Area: Program for the Acquisition and Analysis of Data, Version 1.90; Stoe & Cie GmbH: Darmstadt, Germany, 2020.
- (31) Palatinus, L.; Chapuis, G. SUPERFLIP—a computer program for the solution of crystal structures by charge flipping in arbitrary dimensions. *J. Appl. Crystallogr.* **2007**, *40*, 786–790.
- (32) Petricek, V.; Dusek, M.; Palatinus, L. *The Crystallographic Computing System JANA 2006*, Version 15/01/2022; Institute of Physics: Praha, Czech Republic, 2022.
- (33) Stoe & Cie. WinXPow, Version 3.0.2.1; Stoe & Cie GmbH: Darmstadt, Germany, 2011.
- (34) NETZSCH Proteus GmbH. *Thermal Analysis*, Version 5.2.0; Netzsch Gerätebau GmbH: Selb, Germany, 2010.
- (35) Netzsch. SBA-Measurement, Version 2.0.7.0; Netzsch Gerätebau GmbH: Selb, Germany, 2016.
- (36) Cape, J. A.; Lehman, G. W. Temperature and Finite Pulse-Time Effects in the Flash Method for Measuring Thermal Diffusivity. *J. Appl. Phys.* **1963**, *34*, 1909–1913.
- (37) Blumm, J.; Opfermann, J. D. Improvement of the mathematical modeling of flash measurements. *High. Temp. -High. Press.* **2002**, *34*, 515–521.
- (38) NETZSCH Proteus GmbH. *LFA Analysis*; Netzsch Gerätebau GmbH: Selb, Germany, 2021.
- (39) Duszka, L. Combined solution of the simultaneous heat loss and finite pulse corrections with the laser flash method. *High. Temp. -High. Press.* **1995**, *27/28*, 467–473.
- (40) Syassen, K. Ruby under pressure. *High Pressure Res.* **2008**, *28*, 75–126.
- (41) Filik, J.; Ashton, A. W.; Chang, P. C. Y.; Chater, P. A.; Day, S. J.; Drakopoulos, M.; Gerring, M. W.; Hart, M. L.; Magdysyuk, O. V.; Michalik, S.; Smith, A.; Tang, C. C.; Terrill, N. J.; Wharmby, M. T.; Wilhelm, H. Processing two-dimensional X-ray diffraction and small-angle scattering data in DAWN 2. *J. Appl. Crystallogr.* **2017**, *50*, 959–966.
- (42) Birch, F. Finite Elastic Strain of Cubic Crystals. *Phys. Rev.* **1947**, *71*, 809–824.
- (43) Vegard, L. Die Konstitution der Mischkristalle und die Raumfüllung der Atome. *Z. Phys.* **1921**, *5*, 17–26.

- (44) Morcom, W. R.; Worrell, W. L.; Sell, H. G.; Kaplan, H. I. The preparation and characterization of beta-tungsten, a metastable tungsten phase. *Metall. Mater. Trans. B* **1974**, *5*, 155–161.
- (45) Pertlik, F. Vulcanite, CuTe: hydrothermal synthesis and crystal structure refinement. *Mineral. Petrol.* **2001**, *71*, 149–154.
- (46) Milman, V. Klockmannite, CuSe: structure, properties and phase stability from ab initio modeling. *Acta Crystallogr., Sect. B: Struct. Sci.* **2002**, *58*, 437–447.
- (47) Bartscher, W.; Boeuf, A.; Caciuffo, R.; Fournier, J. M.; Kuhs, W. F.; Rebizant, J.; Rustichelli, F. Neutron diffraction study of β -UD₃ and β -UH₃. *Solid State Commun.* **1985**, *53*, 423–426.
- (48) Gotzmann, K.; Burkhardt, U.; Ellner, M.; Grin, Y. Powder diffraction data for the intermetallic compounds RhAl_{2.63}, IrAl_{2.75} and AuZn₃. *Powder Diffr.* **1997**, *12*, 248–251.
- (49) (a) Willhammar, T.; Sentosun, K.; Mourdikoudis, S.; Goris, B.; Kurttepel, M.; Bercx, M.; Lamoen, D.; Partoens, B.; Pastoriza-Santos, I.; Pérez-Juste, J.; Liz-Marzán, L. M.; Bals, S.; Van Tendeloo, G. Structure and vacancy distribution in copper telluride nanoparticles influence plasmonic activity in the near-infrared. *Nat. Commun.* **2017**, *8*, 14925. (b) Heyding, R. D. The copper/selenium system. *Can. J. Chem.* **1966**, *44*, 1233–1236. (c) Schutte, W. J.; De Boer, J. L. Determination of the Incommensurately Modulated Structure of Cu_{3-x}Te₂. *Acta Crystallogr., Sect. B: Struct. Sci.* **1993**, *49*, 398–403.
- (50) Thompson, A. C. *X-ray Data Booklet*, 3rd ed.; Lawrence Berkeley National Laboratory, University of California, 2009.
- (51) Peiris, S. M.; Pearson, T. T.; Heinz, D. L. Compression of klockmannite, CuSe. *J. Chem. Phys.* **1998**, *109*, 634–636.
- (52) Das, A.; Kumar, A.; Banerji, P. First principles study of electronic structure and thermoelectric transport in tin selenide and phase separated tin selenide–copper selenide alloy. *J. Phys.: Condens. Matter* **2020**, *32*, 265501.
- (53) Kabra, K.; Arora, S.; Joshi, K. B.; Sharma, G. DFT investigation of mechanical and vibrational properties of CuTe. *Phys. B* **2021**, *620*, 413214.
- (54) Holleman, A. F.; Wiberg, E.; Wiberg, N. *Lehrbuch der Anorganischen Chemie*; Walter de Gruyter, 2007.
- (55) Goldsmid, H. J.; Sharp, J. W. Estimation of the thermal band gap of a semiconductor from seebeck measurements. *J. Electron. Mater.* **1999**, *28*, 869–872.
- (56) Bailey, T. P.; Hui, S.; Xie, H.; Olvera, A.; Poudeu, P. F. P.; Tang, X.; Uher, C. Enhanced ZT and attempts to chemically stabilize Cu₂Se via Sn doping. *J. Mater. Chem. A* **2016**, *4*, 17225–17235.
- (57) Gibbs, Z. M.; Kim, H.-S.; Wang, H.; Snyder, G. J. Band gap estimation from temperature dependent Seebeck measurement—Deviations from the $2e|S|_{\max}T_{\max}$ relation. *Appl. Phys. Lett.* **2015**, *106*, 022112.
- (58) He, Y.; Zhang, T.; Shi, X.; Wei, S.-H.; Chen, L. High thermoelectric performance in copper telluride. *NPG Asia Mater.* **2015**, *7*, No. e210.
- (59) Yu, B.; Liu, W.; Chen, S.; Wang, H.; Wang, H.; Chen, G.; Ren, Z. Thermoelectric properties of copper selenide with ordered selenium layer and disordered copper layer. *Nano Energy* **2012**, *1*, 472–478.
- (60) (a) Nilges, T.; Lange, S.; Bawohl, M.; Deckwart, J. M.; Janssen, M.; Wiemhöfer, H. D.; Decourt, R.; Chevalier, B.; Vannahme, J.; Eckert, H.; Wehrich, R. Reversible switching between p- and n-type conduction in the semiconductor Ag₁₀Te₄Br₃. *Nat. Mater.* **2009**, *8*, 101–108. (b) Vogel, A.; Rabenbauer, A.; Deng, P.; Steib, R.; Boger, T.; Zeier, W. G.; Siegel, R.; Senker, J.; Daisenberger, D.; Nisi, K.; Holleitner, A. W.; Venturini, J.; Nilges, T. A switchable one compound diode. *Adv. Mater.* **2023**, *35*, 2208698.
- (61) Liu, W.; Shi, X.; Hong, M.; Yang, L.; Moshwan, R.; Chen, Z.-G.; Zou, J. Ag doping induced abnormal lattice thermal conductivity in Cu₂Se. *J. Mater. Chem. C* **2018**, *6*, 13225–13231.
- (62) Kang, S. D.; Snyder, G. J. Transport property analysis method for thermoelectric materials: material quality factor and the effective mass model. **2017**, arXiv:1710.06896. arXiv preprint.

Supporting Information

Cu_{1.5}Se_yTe_{1-y} (y = 0.2 – 0.7): A Series of Narrow Band Gap Semiconductors with Low Thermal Conductivity at Ambient Temperature

Alfred Rabenbauer^{a)}, Anna Vogel^{a)}, Janio Venturini^{a)}, Mahboubeh Moslemi^{b)}, Oliver Oeckler^{b)},
Dominik Daisenberger^{c)} and Tom Nilges^{a),*}

corresponding author: Prof. Dr. Tom Nilges, Professorship for Synthesis and Characterization of Innovative Materials, TU Munich, Lichtenbergstraße 4, 85748 Garching bei München, E-Mail: tom.nilges@tum.de

a) TU Munich, School of Natural Sciences (NAT), Department of Chemistry, Professorship for Synthesis and Characterization of Innovative Materials, TU Munich, Lichtenbergstraße 4, 85748 Garching b. München, Germany

b) Faculty of Chemistry and Mineralogy, Institute for Mineralogy, Crystallography and Materials Science, Leipzig University, Scharnhorststraße 20, 04275 Leipzig, Germany

c) Diamond Light Source, Harwell Science Campus, Didcot OX11 0DE, UK

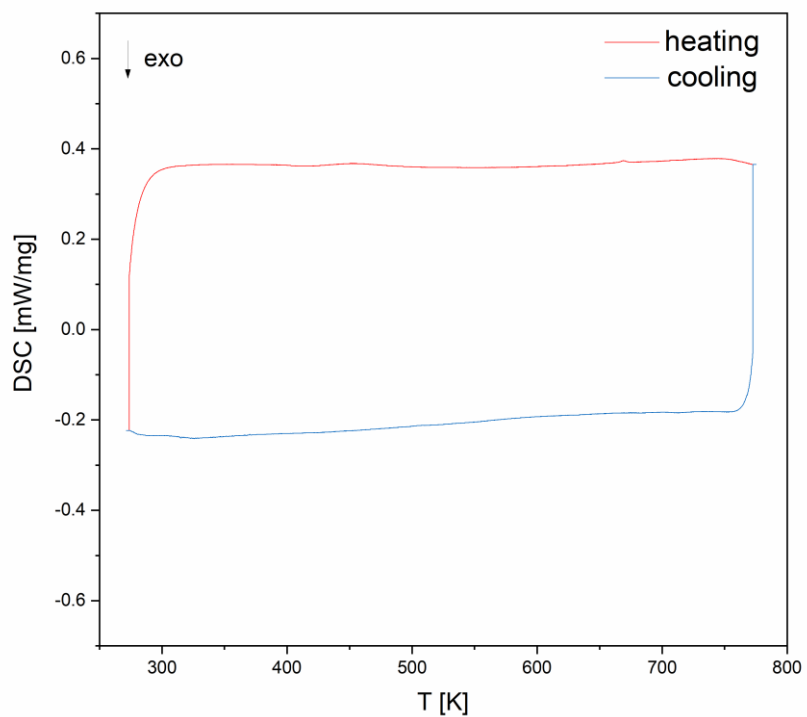


Figure S1: Differential scanning calorimetry of a $\text{Cu}_{1.5}\text{Se}_{0.5}\text{Te}_{0.5}$ sample. The second cycle with heating (red) and cooling (black) is shown. No thermal effects are observed up to 773 K.

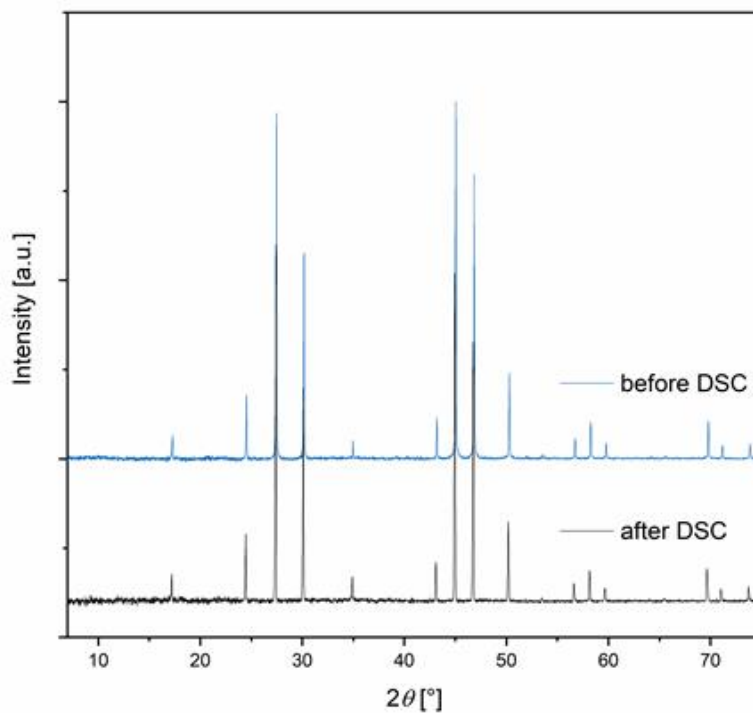


Figure S2: PXRD pattern of $\text{Cu}_{1.5}\text{Se}_{0.5}\text{Te}_{0.5}$ before (blue line) and after (black line) two consecutive cycles in the DSC up to 773 K. No decomposition or structural change was observed up to this temperature.

Table S1: Lattice parameters and cell volume determined by PXRD of $\text{Cu}_{1.5}\text{Se}_y\text{Te}_{1-y}$ with $y = 0.2$ to 0.7. Standard deviations are given in parentheses. Space group $Pm\bar{3}n$.

y in $\text{Cu}_{1.5}\text{Se}_y\text{Te}_{1-y}$	Lattice Parameter a (Å)	Cell Volume (Å ³)
0.2	7.3250(6)	393.03(6)
0.3	7.3063(6)	390.03(6)
0.4	7.2750(4)	385.04(4)
0.5	7.2409(6)	379.64(5)
0.6	7.2313(4)	378.13(4)
0.7	7.2100(4)	374.81(3)

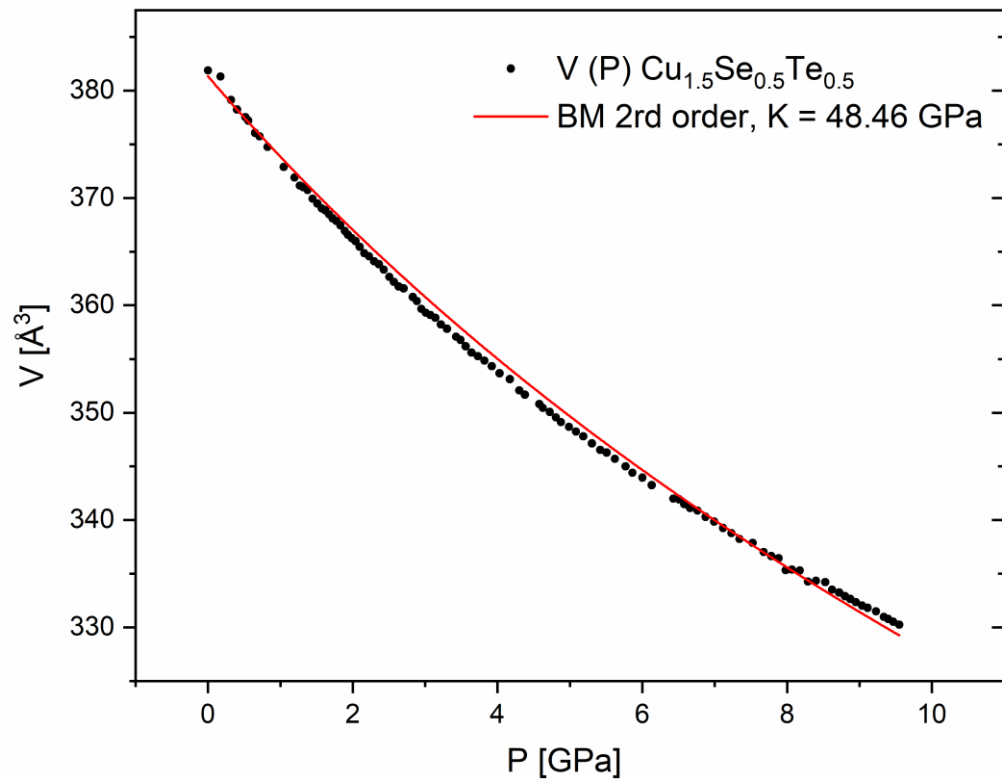


Figure S3: Cell volume as a function of pressure: experimental data with a 2nd order Birch-Murnaghan equation of state fit (BM EOS, red line). The deviation from the measured data substantiates the need for a 3rd order BM EOS which is also corroborated by the analysis of the f-F plot.

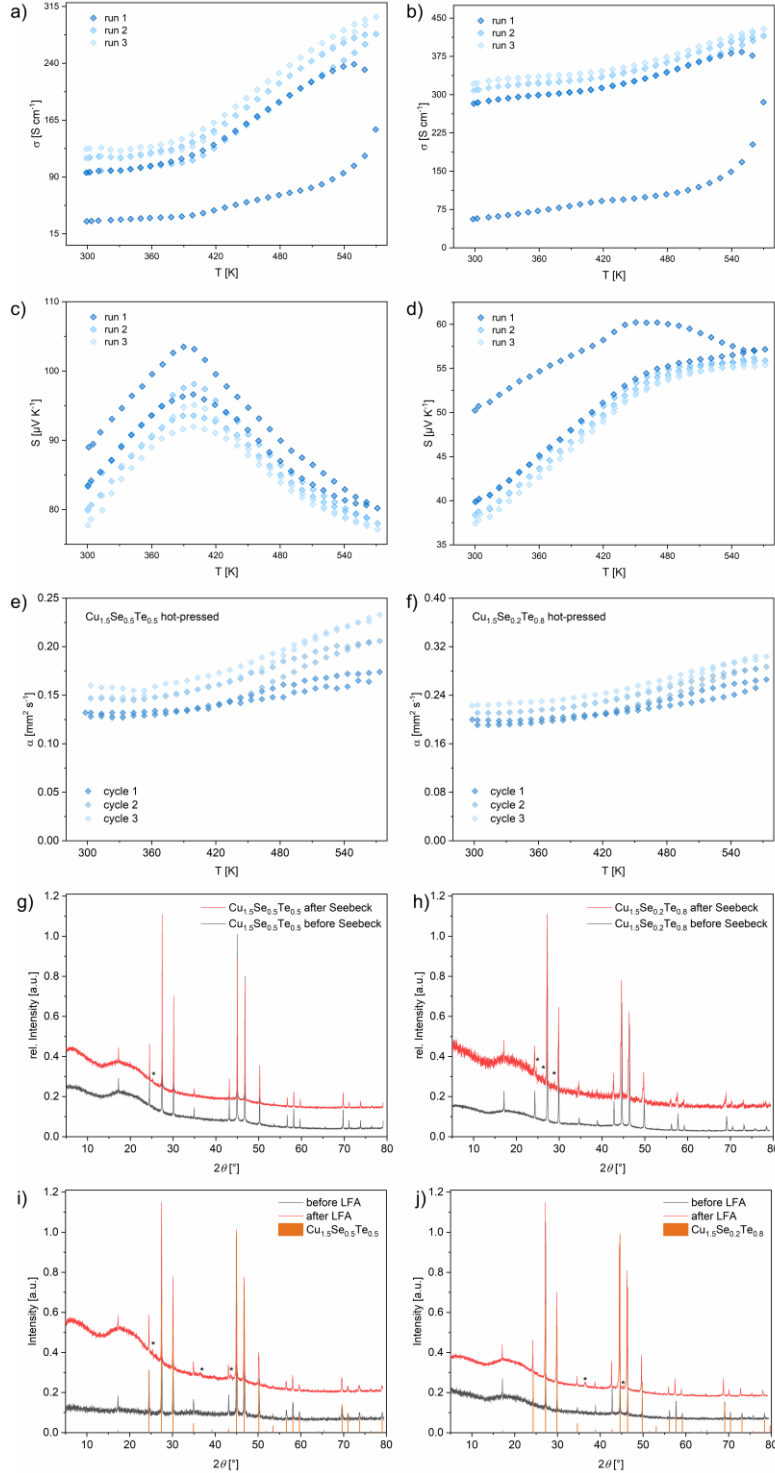


Figure S4: Electrical conductivity measurements for $\text{Cu}_{1.5}\text{Se}_{0.5}\text{Te}_{0.5}$ (a) and $\text{Cu}_{1.5}\text{Se}_{0.2}\text{Te}_{0.8}$ (b), Seebeck coefficient determinations for $\text{Cu}_{1.5}\text{Se}_{0.5}\text{Te}_{0.5}$ (c) and $\text{Cu}_{1.5}\text{Se}_{0.2}\text{Te}_{0.8}$ (d) and heat diffusivity of $\text{Cu}_{1.5}\text{Se}_{0.5}\text{Te}_{0.5}$ (e) and $\text{Cu}_{1.5}\text{Se}_{0.2}\text{Te}_{0.8}$ (f) measured on hot-pressed samples. A PXRD of the samples for $\text{Cu}_{1.5}\text{Se}_{0.5}\text{Te}_{0.5}$ (g) and $\text{Cu}_{1.5}\text{Se}_{0.2}\text{Te}_{0.8}$ (h) before and after Seebeck measurement as well as for $\text{Cu}_{1.5}\text{Se}_{0.5}\text{Te}_{0.5}$ (i) and $\text{Cu}_{1.5}\text{Se}_{0.2}\text{Te}_{0.8}$ (j) before and after LFA measurement is also depicted.

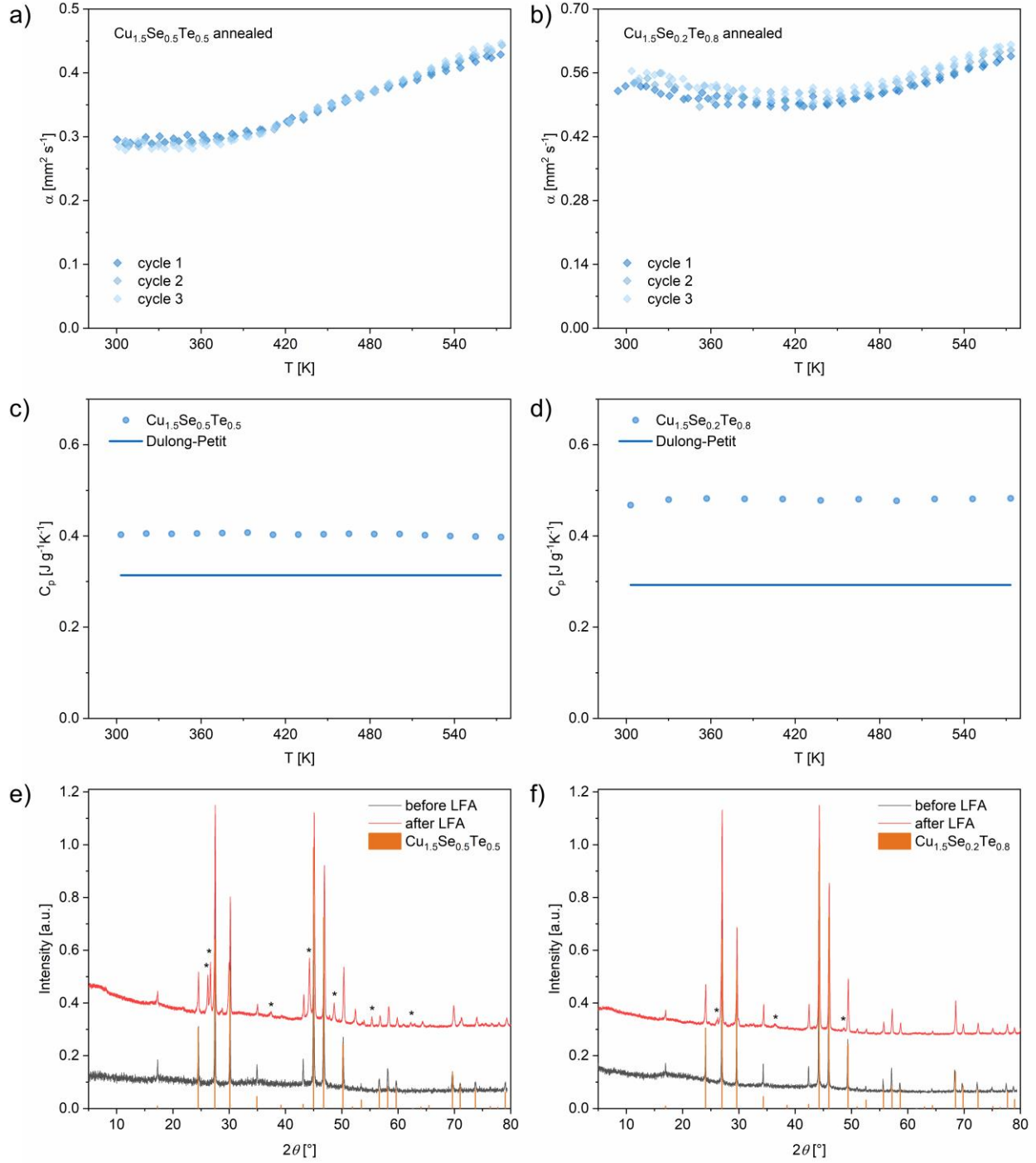


Figure S5: Thermal diffusivity α for an annealed (573 K, 3 days) $\text{Cu}_{1.5}\text{Se}_{0.5}\text{Te}_{0.5}$ (a) and $\text{Cu}_{1.5}\text{Se}_{0.2}\text{Te}_{0.8}$ (b) sample measured for three consecutive cycles. Averaged C_p values for $\text{Cu}_{1.5}\text{Se}_{0.5}\text{Te}_{0.5}$ (c) and $\text{Cu}_{1.5}\text{Se}_{0.2}\text{Te}_{0.8}$ (d), the value calculated by Dulong-Petit is added as a line. PXRD measurements before and after LFA are depicted for $\text{Cu}_{1.5}\text{Se}_{0.5}\text{Te}_{0.5}$ (e) and $\text{Cu}_{1.5}\text{Se}_{0.2}\text{Te}_{0.8}$ (f).

4 Summary

In this work, three different coinage metal chalcogenides or chalcogenide halides were synthesized and characterized regarding their polymorphism and thermoelectric properties. The series $\text{Cu}_{1.5}\text{Se}_{1-y}\text{Te}_y$ ($y = 0.2 - 0.7$) was produced in single- and polycrystalline form in a classical solid state synthesis. The materials crystallize cubically, in space group $Pm\bar{3}n$ (223), which was verified by X-ray diffraction studies. Those low band gap semiconductors don't show any polymorphism, but a sufficient electrical conductivity up to $\sim 400 \text{ S cm}^{-1}$ combined with a low thermal conductivity of $0.3 - 0.8 \text{ W m}^{-1} \text{ K}^{-1}$ allows ZT values up to 0.19 at ambient temperatures up to 450 K. Further improvements in the electrical conductivity, e.g. by doping, would enable the material to become high efficient thermoelectrics for low temperature applications such as regeneration of exhaust gas energy.

The new compound $\text{Ag}_{18}\text{Cu}_3\text{Te}_{11}\text{Cl}_3$, which was discovered through a cationic substitution in $\text{Cu}_{20}\text{Te}_{11}\text{Cl}_3$, shows similar polymorphism to the starting material, but the β - α phase transition is accompanied by a similar pnp-switch like in $\text{Ag}_{10}\text{Te}_4\text{Br}_3$. Besides its tremendous Seebeck coefficient drop of $\sim 4500 \mu\text{V K}^{-1}$, this material is the first one showing this switch already at 295 K, so right at room temperature. Single crystal X-ray diffraction as well as solid state NMR studies were performed to propose a possible mechanism causing the change in conductivity type, revealing two major contributions during the phase transition: An order-disorder phenomenon within the Te 6363 Kagomé net generating a two dimensional charge density wave through the compound, as well as attractive d^{10} - d^{10} interactions in the Cu substructure, which were shown to cause thermopower modulations in $\text{Ag}_5\text{Te}_2\text{Cl}$ before.²⁶⁻²⁹

Enabling those pn-switch close to room temperature, a one-compound diode was created by the simple application of a thermal gradient of 295/308 K onto single-crystalline samples. The rectifying behavior of the diode was substantiated by various UI-curve measurements, showing the possibility to reversibly create a rectifying device in an non-doped single material. The switching time in the range of up to ~ 8 s rules out the formation of a Schottky diode and clearly identifies the created diode as pn-junction device.

In addition, another pnp-switchable material, namely AgCuS , was tested for the use as one-compound diode. The compound was reassessed concerning its structural as well as thermoelectric properties during the pn-switching phase transition. Since the material can be synthesized as a homogeneous ingot in a simple melting process, the potential for industrial applications of this material in one-compound rectifying devices is even higher. The measurement of rectifying UI curves was successful for this material, showing even faster switching times of 2 – 3 s. To investigate and demonstrate the huge variability of those devices, further possibilities were shown by different switching experiments. The volatility was

not only shown by reversible on- and off switching of the diode by repetitive application and removal of the temperature gradient, but the forward direction can also be switched by changing the hot and cold end of the gradient without any physical changes in the measured system. For normal pn-junction diodes, this could only be achieved by a manual removal, re-orientation and re-soldering of the diode.

One-compound diode devices could enable various new applications. Inverting of the forward direction of commercially used diodes is impossible, but with this new kind of devices, the direction of current flow can be inverted by simply tweaking the applied temperature gradient. The temperature tuning could not only be performed by resistive heating, but locally by laser irradiation, allowing even smaller architecture sizes than used in present devices. Additionally, the combination of the two aforementioned points could be used for the creation of miniaturized current switches. Also the production of one compound bipolar or field effect transistors should be feasible. If a pn-junction can be reversibly created on purpose, this can also be used in various other processes where those junctions are used. Electrochemical water splitting for the generation of hydrogen, as well as other electrocatalytic applications can be realized by those pnp-switchable materials. A self-generated solar cell, where the heat gradient is produced right in place through the irradiation of the sun, might also be possible.

Publications

Articles

- Anna Vogel[†], **Alfred Rabenbauer**[†], Philipp Deng[†], Ruben Steib, Thorben Böger, Wolfgang Zeier, Renée Siegel, Jürgen Senker, Dominik Deisenberger, Katharina Nisi, Alexander Holleitner, Janio Venturini and Tom Nilges: A Switchable One-Compound Diode, *Adv. Mater.* **2022**, 2208698.
- Philipp Deng[†], **Alfred Rabenbauer**[†], Kathrin Vosseler, Janio Venturini and Tom Nilges: AgCuS: A Single Material Diode with Fast Switching Times, *Adv. Funct. Mater.* **2023**, 202214882.
- **Alfred Rabenbauer**, Anna Vogel, Janio Venturini, Mahboubeh Moslemi, Oliver Oeckler, Dominik Daisenberger and Tom Nilges: Cu_{1.5}Se_yTe_{1-y} (y = 0.2 – 0.7): A Series of Narrow Band Gap Semiconductors with Low Thermal Conductivity at Ambient Temperature, *Inorg. Chem.* **2023**.
- Nataliya L. Gulay, Jutta Kösters, Yaroslav M. Kalychak, Samir F. Matar, **Alfred Rabenbauer**, Tom Nilges and Rainer Pöttgen: Peierls distortion of the cobalt chain in the low-temperature structure of CoIn₂, *Z. Naturforsch. B*, **2022**, 237, 239-248.
- Christian Paulsen, Josef Maximilian Gerdes, Volodymyr Svitlyk, Maximilian Kai Reimann, **Alfred Rabenbauer**, Tom Nilges, Michael Ryan Hansen and Rainer Pöttgen: Trimorphic TaCrP – A diffraction and ³¹P solid state NMR spectroscopic study; *Z. Naturforsch. B*, **2023**, 238.
- Tobias Hölderle, Mykhailo Monchak, Volodymyr Baran, Armin Kriele, Martin Mühlbauer, Vadim Dyadkin, **Alfred Rabenbauer**, Alexander Schökel, Helmut Ehrenberger, Peter Müller-Buschbaum and Anatoliy Senyshyn: Thermal Structural Behavior of Electrochemically Lithiated Graphite (Li_xC₆) Anodes in Li-ion Batteries, **2023**, manuscript under review.

[†]: Those authors contributed equally to this work.

Posters:

- „Cu₃Se_yTe_{2-y}: A new representative of transition metal dichalcogenides”, 30th annual meeting of the German Crystallographic Society (DGK) Munich, Germany, March **2022**.
- „Cu_{1.5}Se_yTe_{1-y} (y = 0.2 – 0.7): Narrow Band Gap Thermoelectrics”, 21st Conference on Inorganic Chemistry of the Divisions Wöhler-Vereinigung & solid-state chemistry and materials research, Marburg, Germany, September **2023**.

Literature

- [1] Gayner, C.; Kar, K. K., Recent advances in thermoelectric materials. *Prog. Mater Sci.* **2016**, *83*, 330-382. DOI: <https://doi.org/10.1016/j.pmatsci.2016.07.002>
- [2] Nilges, T.; Bawohl, M.; Osters, O.; Lange, S.; Messel, J., Silver(I)-(poly)chalcogenide Halides – Ion and Electron High Potentials. *Z. Phys. Chem.* **2010**, *224* (10-12), 1505-1531. DOI: [doi:10.1524/zpch.2010.0032](https://doi.org/10.1524/zpch.2010.0032)
- [3] Vogel, A.; Miller, T.; Hoch, C.; Jakob, M.; Oeckler, O.; Nilges, T., Cu_{9.1}Te₄Cl₃: A Thermoelectric Compound with Low Thermal and High Electrical Conductivity. *Inorg. Chem.* **2019**, *58* (9), 6222-6230. DOI: [10.1021/acs.inorgchem.9b00453](https://doi.org/10.1021/acs.inorgchem.9b00453)
- [4] Vogel, A.; Nilges, T., Ion Dynamics and Polymorphism in Cu₂₀Te₁₁Cl₃. *Inorg. Chem.* **2021**, *60* (20), 15233-15241. DOI: [10.1021/acs.inorgchem.1c01764](https://doi.org/10.1021/acs.inorgchem.1c01764)
- [5] Lange, S.; Bawohl, M.; Wilmer, D.; Meyer, H.-W.; Wiemhöfer, H.-D.; Nilges, T., Polymorphism, structural frustration, and electrical properties of the mixed conductor Ag₁₀Te₄Br₃. *Chem. Mater.* **2007**, *19* (6), 1401-1410.
- [6] Lange, S.; Nilges, T., Ag₁₀Te₄Br₃: A new silver (I)(poly) chalcogenide halide solid electrolyte. *Chem. Mater.* **2006**, *18* (10), 2538-2544.
- [7] Sales, B. C., Critical Overview of Recent Approaches to Improved Thermoelectric Materials. *Int. J. Appl. Ceram.* **2007**, *4* (4), 291-296. DOI: <https://doi.org/10.1111/j.1744-7402.2007.02143.x>
- [8] Chen, Z.; Zhang, X.; Pei, Y., Manipulation of Phonon Transport in Thermoelectrics. *Adv. Mater.* **2018**, *30* (17), 1705617. DOI: <https://doi.org/10.1002/adma.201705617>
- [9] Rowe, D. M. *CRC handbook of thermoelectrics*, CRC press, **2018**, ISBN: 9780429956676.
- [10] Nilges, T.; Lange, S.; Bawohl, M.; Deckwart, J. M.; Janssen, M.; Wiemhöfer, H. D.; Decourt, R.; Chevalier, B.; Vannahme, J.; Eckert, H.; Wehrich, R., Reversible switching between p- and n-type conduction in the semiconductor Ag₁₀Te₄Br₃. *Nat. Mater.* **2009**, *8* (2), 101-8. DOI: [10.1038/nmat2358](https://doi.org/10.1038/nmat2358)

- [11] Guin, S. N.; Pan, J.; Bhowmik, A.; Sanyal, D.; Waghmare, U. V.; Biswas, K., Temperature dependent reversible p–n–p type conduction switching with colossal change in thermopower of semiconducting AgCuS. *J. Am. Chem. Soc.* **2014**, *136* (36), 12712-12720.
- [12] Nemir, D.; Beck, J., On the Significance of the Thermoelectric Figure of Merit Z. *J. Electron. Mater.* **2010**, *39* (9), 1897-1901. DOI: 10.1007/s11664-009-1060-4
- [13] Vining, C. B., An inconvenient truth about thermoelectrics. *Nat. Mater.* **2009**, *8* (2), 83-85. DOI: 10.1038/nmat2361
- [14] Beeken, R. B.; Beeken, E. M., Ionic conductivity in Cu-substituted Ag₃SBr. *Solid State Ion.* **2000**, *136-137*, 463-467. DOI: [https://doi.org/10.1016/S0167-2738\(00\)00564-6](https://doi.org/10.1016/S0167-2738(00)00564-6)
- [15] Nilges, T.; Bawohl, M.; Lange, S.; Messel, J.; Osters, O., Highly Dynamic Chalcogen Chains in Silver (I)(Poly) Chalcogenide Halides: a New Concept for Thermoelectrics? *J. Electron. Mater.* **2010**, *39*, 2096-2104.
- [16] Jonson, M.; Mahan, G., Mott's formula for the thermopower and the Wiedemann-Franz law. *Phys. Rev. B.* **1980**, *21* (10), 4223.
- [17] Xiao, C.; Qin, X.; Zhang, J.; An, R.; Xu, J.; Li, K.; Cao, B.; Yang, J.; Ye, B.; Xie, Y., High Thermoelectric and Reversible p-n-p Conduction Type Switching Integrated in Dimetal Chalcogenide. *J. Am. Chem. Soc.* **2012**, *134* (44), 18460-18466. DOI: 10.1021/ja308936b
- [18] Shi, Y.; Assoud, A.; Sankar, C. R.; Kleinke, H., Tl₂Ag₁₂Se₇: A New pnp Conduction Switching Material with Extraordinarily Low Thermal Conductivity. *Chem. Matter.* **2017**, *29* (21), 9565-9571. DOI: 10.1021/acs.chemmater.7b04015
- [19] Wen, T.; Wang, Y.; Li, N.; Zhang, Q.; Zhao, Y.; Yang, W.; Zhao, Y.; Mao, H.-k., Pressure-Driven Reversible Switching between n- and p-Type Conduction in Chalcopyrite CuFeS₂. *J. Am. Chem. Soc.* **2019**, *141* (1), 505-510. DOI: 10.1021/jacs.8b11269
- [20] Kitai, A. *Principles of Solar Cells, LEDs and Diodes: The role of the PN junction*; John Wiley & Sons, **2011**, ISBN: 9781119974543.

- [21] Giller, M.; Bawohl, M.; Gerstle, A. P.; Nilges, T., Copper substitution and mixed cation effect in $\text{Ag}_{10}\text{Te}_4\text{Br}_3$. *Z. anorg. allg. Chem.* **2013**, 639 (14), 2379-2381.
- [22] Nilges, T.; Bawohl, M.; Lange, S., $\text{Ag}_{10}\text{Te}_4\text{Br}_{3-x}\text{Cl}_x$ and $\text{Ag}_{10}\text{Te}_4\text{Br}_{3-y}\text{I}_y$: Structural and Electrical Property Tuning of a Mixed Conductor by Partial Anion Substitution. *Z. Naturforsch. B* **2007**, 62 (7), 955-964. DOI: doi:10.1515/znb-2007-0713
- [23] Nilges, T.; Bawohl, M., Structures and thermal properties of silver (I)(poly) chalcogenide halide solid solutions $\text{Ag}_{10}\text{Te}_{4-(q,p)}\text{Q}_{(q,p)}\text{Br}_3$ with Q= S, Se. *Z. Naturforsch. B* **2008**, 63 (6), 629-636.
- [24] Lange, S.; Bawohl, M.; Nilges, T., Crystal structures and thermal and electrical properties of the new silver (poly) Chalcogenide halides $\text{Ag}_{23}\text{Te}_{12}\text{Cl}$ and $\text{Ag}_{23}\text{Te}_{12}\text{Br}$. *Inorg. Chem.* **2008**, 47 (7), 2625-2633.
- [25] Nilges, T.; Nilges, S.; Pfitzner, A.; Doert, T.; Böttcher, P., Structure-Property Relations and Diffusion Pathways of the Silver Ion Conductor $\text{Ag}_5\text{Te}_2\text{Cl}$. *Chem. Mater.* **2004**, 16 (5), 806-812. DOI: 10.1021/cm031131c
- [26] Messel, J.; Nilges, T., Structure chemical aspects of silver (I) chalcogenide halides and preparation of the $x= 1$ member of the solid solution $\text{Ag}_5\text{Te}_2\text{Cl}_{1-x}\text{Br}_x$. *Z. Naturforsch. B* **2008**, 63 (9), 1077-1082.
- [27] Nilges, T.; Dreher, C.; Hezinger, A., Structures, phase transitions and electrical properties of $\text{Ag}_5\text{Te}_{2-y}\text{Se}_y\text{Cl}$ ($y= 0-0.7$). *Solid State Sci.* **2005**, 7 (1), 79-88.
- [28] Nilges, T.; Lange, S., $\text{Ag}_5\text{Te}_{2-y}\text{Se}_y\text{Cl}$ und $\text{Ag}_5\text{Te}_2\text{Cl}_{1-x}\text{Br}_x$: Struktureigenschaftsvariationen durch Anionenaustausch. *Z. anorg. allg. Chem.* **2004**, 630 (11), 1749-1749.
- [29] Nilges, T.; Lange, S., $\text{Ag}_5\text{Te}_2\text{Cl}_{1-x}\text{Br}_x$ ($x= 0-0.65$) and $\text{Ag}_5\text{Te}_{2-y}\text{S}_y\text{Cl}$ ($y= 0-0.3$): Variation of Physical Properties in Silver (I) Chalcogenide Halides. *Z. anorg. allg. Chem.* **2005**, 631 (15), 3002-3012.
- [30] Trots, D.; Senyshyn, A.; Mikhailova, D.; Knapp, M.; Baetz, C.; Hoelzel, M.; Fuess, H., High-temperature thermal expansion and structural behaviour of stromeyerite, AgCuS . *J. Condens. Matter Phys.* **2007**, 19 (13), 136204.

- [31] Santamaria-Perez, D.; Morales-Garcia, A.; Martinez-Garcia, D.; Garcia-Domene, B.; Mühle, C.; Jansen, M., Structural Phase Transitions on AgCuS Stromeyerite Mineral under Compression. *Inorg. Chem.* **2013**, *52* (1), 355-361. DOI: 10.1021/ic302116b
- [32] Guin, S. N.; Sanyal, D.; Biswas, K., The effect of order–disorder phase transitions and band gap evolution on the thermoelectric properties of AgCuS nanocrystals. *Chem. Sci.* **2016**, *7* (1), 534-543.
- [33] Dutta, M.; Sanyal, D.; Biswas, K., Tuning of p–n–p-type conduction in AgCuS through cation vacancy: thermopower and positron annihilation spectroscopy investigations. *Inorg. Chem.* **2018**, *57* (12), 7481-7489.
- [34] Mott, N. F., The basis of the electron theory of metals, with special reference to the transition metals. *Proc. Phys. Soc. A* **1949**, *62* (7), 416.
- [35] Tenny, K. M.; Keenaghan, M., Ohms Law; StatPearls Publishing, **2017**, PMID: 28722905.
- [36] Colinge, J.-P.; Colinge, C. A. *Physics of semiconductor devices*; Springer Science & Business Media, **2005**, ISBN: 9781402070181.
- [37] Muller, R. S.; Kamins, T. I. *Device electronics for integrated circuits*; John Wiley & Sons, **2002**, ISBN: 9780471593980.
- [38] Mott, N. F., The theory of crystal rectifiers. *Proc. Math. Phys. Eng. Sci.* **1939**, *171* (944), 27-38.
- [39] Braun, F., Über die Stromleitung durch Schwefelmetalle. *Ann. Phys.* **1875**, *229* (12), 556-563.
- [40] Van Zeghbroeck, B. J., *Principles of semiconductor devices*. Bart Van Zeghbroeck, **2011**.
- [41] Sah, C.-T.; Noyce, R. N.; Shockley, W., Carrier generation and recombination in pn junctions and pn junction characteristics. *Proc. IRE* **1957**, *45* (9), 1228-1243.
- [42] Shockley, W., The Theory of p-n Junctions in Semiconductors and p-n Junction Transistors. *Bell. Syst. Tech. J.* **1949**, *28* (3), 435-489.

- [43] Oldham, W. G.; Samuelson, R. R.; Antognetti, P., Triggering phenomena in avalanche diodes. *IEEE Trans. Electron Devices* **1972**, *19* (9), 1056-1060. DOI: 10.1109/T-ED.1972.17544
- [44] Laha, A.; Smart, D., A zener diode model with application to SPICE2. *IEEE J. Solid-State Circuits* **1981**, *16* (1), 21-22.
- [45] Hurkx, G. A. M.; Graaff, H. C. d.; Kloosterman, W. J.; Knuvers, M. P. G., A new analytical diode model including tunneling and avalanche breakdown. *IEEE Trans. Electron Devices* **1992**, *39* (9), 2090-2098. DOI: 10.1109/16.155882
- [46] Kingston, R. H., Switching time in junction diodes and junction transistors. *Proc. IRE* **1954**, *42* (5), 829-834.
- [47] Nandi, A.; Rana, K. S.; Bag, A., Design and Analysis of P-GaN/N-Ga₂O₃ Based Junction Barrier Schottky Diodes. *IEEE Trans. Electron Devices* **2021**, *68* (12), 6052-6058. DOI: 10.1109/TED.2021.3119261
- [48] Bourget, C. M., An Introduction to Light-emitting Diodes. *HortScience* **2008**, *43* (7), 1944-1946. DOI: 10.21273/hortsci.43.7.1944
- [49] Bergh, A. A.; Dean, P. J., Light-emitting diodes. *Proc. IEEE* **1972**, *60* (2), 156-223.
- [50] Hovel, H. J., Solar cells. *NASA STI/Recon Tech. Rep. A* **1975**, *76*, 20650.
- [51] Partain, L. D.; Fraas, L. M. *Solar cells and their applications*; John Wiley & Sons, **2010**, ISBN: 9780470446331.
- [52] STOE *WinXPOW*, version 3.0.2.1; Stoe & Cie GmbH, Darmstadt, Germany: **2011**.
- [53] Villars, P.; Cenzual, K.; *Pearson's Crystal Data: Crystal Structure Database for Inorganic Compounds*, version 2.3; Crystal Impact GbR, Bonn, Germany: **2019**.
- [54] STOE *X-AREA: program for the acquisition and analysis of data*, version 1.90; Stoe & Cie GmbH: Darmstadt, Germany: **2020**.
- [55] STOE *X-Red*, version 1.62.2; Stoe & Cie GmbH, Darmstadt, Germany: **2015**.

- [56] STOE *X-Shape*, version 2.18; Stoe & Cie GmbH, Darmstadt, Germany: **2015**.
- [57] Petříček, V.; Dušek, M.; Palatinus, L., The crystallographic computing system JANA 2006, Version 15/01/2022. Institute of Physics, Praha, Czech Republic: **2022**.
- [58] Palatinus, L.; Chapuis, G., SUPERFLIP—a computer program for the solution of crystal structures by charge flipping in arbitrary dimensions. *J. Appl. Crystallogr.* **2007**, *40* (4), 786-790.
- [59] Petříček, V.; Dušek, M.; Palatinus, L., Crystallographic computing system JANA2006: general features. *Z. Kristallogr. - Cryst. Mater.* **2014**, *229* (5), 345-352.
- [60] Willis, B., Lattice vibrations and the accurate determination of structure factors for the elastic scattering of X-rays and neutrons. *Acta Crystallogr. A* **1969**, *25* (2), 277-300.
- [61] Zucker, U. H.; Schulz, H., Statistical approaches for the treatment of anharmonic motion in crystals. I. A comparison of the most frequently used formalisms of anharmonic thermal vibrations. *Acta Crystallogr. A* **1982**, *38* (5), 563-568.
- [62] Zucker, U. H.; Schulz, H., Statistical approaches for the treatment of anharmonic motion in crystals. II. Anharmonic thermal vibrations and effective atomic potentials in the fast ionic conductor lithium nitride (Li₃N). *Acta Crystallogr. A* **1982**, *38* (5), 568-576.
- [63] Bachmann, R.; Schulz, H., Anharmonic potentials and pseudo potentials in ordered and disordered crystals. *Acta Crystallogr. A* **1984**, *40* (6), 668-675.
- [64] Kuhs, W., Generalized atomic displacements in crystallographic structure analysis. *Acta Crystallogr. A* **1992**, *48* (2), 80-98.
- [65] *Netzsch SBA 458 Manual*, Netzsch Gerätebau GmbH, Selb, Germany, **2016**.
- [66] Smits, F. M., Measurement of sheet resistivities with the four-point probe. *Bell Syst. Tech. J.* **1958**, *37* (3), 711-718.
- [67] Valdes, L. B., Resistivity measurements on germanium for transistors. *Proc. IRE* **1954**, *42* (2), 420-427.

- [68] *Netzsch SBA-Measurement*, 2.0.7.0; Netzsch Gerätebau GmbH, Selb, Germany, **2016**.
- [69] Roberts, G. G.; Apsley, N.; Munn, R. W., Temperature dependent electronic conduction in semiconductors. *Phys. Rep.* **1980**, *60* (2), 59-150. DOI: [https://doi.org/10.1016/0370-1573\(80\)90046-0](https://doi.org/10.1016/0370-1573(80)90046-0)
- [70] Dusza, L., Combined solution of the simultaneous heat loss and finite pulse corrections with the laser flash method. *High Temp. High Press.* **1995**, *27* (5), 467-473.
- [71] *Protheus LFA Analysis*, Netzsch Gerätebau GmbH, Selb, Germany, **2021**.
- [72] Cape, J. A.; Lehman, G. W., Temperature and Finite Pulse-Time Effects in the Flash Method for Measuring Thermal Diffusivity. *Journal of Applied Physics* **1963**, *34* (7), 1909-1913. DOI: 10.1063/1.1729711
- [73] Blumm, J.; Opfermann, J. D., Improvement of the mathematical modeling of flash measurements. *High Temp. High Press.* **2002**, *34*, 515-521.
- [74] Dulong, P. L.; Petit, A. T. *Recherches sur la mesure des températures et sur les lois de la communication de la chaleur*, De l'Imprimerie royale, **1818**.
- [75] *Kickstart IV Characterizer App*, version 2.5.0; Tektronix Inc., Beaverton, USA, **2021**.
- [76] *Eagle*, 9.5.0; Autodesk GmbH, München, Germany, **2023**.
- [77] *Fusion 360*, 2.0.15299; Autodesk GmbH, Munich, Germany, **2022**.
- [78] *IRBIS 3.1 professional*, version 3.0.2.1; InfraTec GmbH, Dresden, Germany, **2022**.
- [79] Richet, P.; Xu, J.-A.; Mao, H.-K., Quasi-hydrostatic compression of ruby to 500 kbar. *Phys. Chem. Miner.* **1988**, *16*, 207-211.
- [80] Syassen, K., Ruby under pressure. *High Press. Res.* **2008**, *28* (2), 75-126. DOI: 10.1080/08957950802235640
- [81] Jephcoat, A.; Hemley, R.; Mao, H., X-ray diffraction of ruby (Al₂O₃: Cr³⁺) to 175 GPa. *Physica B+ C* **1988**, *150* (1-2), 115-121.

- [82] Filik, J.; Ashton, A. W.; Chang, P. C. Y.; Chater, P. A.; Day, S. J.; Drakopoulos, M.; Gerring, M. W.; Hart, M. L.; Magdysyuk, O. V.; Michalik, S.; Smith, A.; Tang, C. C.; Terrill, N. J.; Wharmby, M. T.; Wilhelm, H., Processing two-dimensional X-ray diffraction and small-angle scattering data in DAWN 2. *J. Appl. Crystallogr.* **2017**, *50* (3), 959-966. DOI: doi:10.1107/S1600576717004708
- [83] Wojdyr, M., Fityk: a general-purpose peak fitting program. *J. Appl. Cryst.* **2010**, *43* (5), 1126-1128. DOI: doi:10.1107/S0021889810030499
- [84] Bruker *TopSpin*, 3.6.3; Bruker Cororation, Billerica, USA **2021**.
- [85] *Protheus Thermal Analysis*, version 5.2.0; Netzsch Gerätebau GmbH, Selb, Germany, **2010**.
- [86] Perumal, S.; Roychowdhury, S.; Biswas, K., High performance thermoelectric materials and devices based on GeTe. *J. Mater. Chem. C.* **2016**, *4* (32), 7520-7536. DOI: 10.1039/C6TC02501C
- [87] Vegard, L., Die Konstitution der Mischkristalle und die Raumfüllung der Atome. *Z. Phys.* **1921**, *5* (1), 17-26. DOI: 10.1007/BF01349680